

**A Thesis Submitted for the Degree of PhD at the University of Warwick**

**Permanent WRAP URL:**

<http://wrap.warwick.ac.uk/171367>

**Copyright and reuse:**

This thesis is made available online and is protected by original copyright.

Please scroll down to view the document itself.

Please refer to the repository record for this item for information to help you to cite it.

Our policy information is available from the repository home page.

For more information, please contact the WRAP Team at: [wrap@warwick.ac.uk](mailto:wrap@warwick.ac.uk)



# Boron Doped Diamond Electrochemical Sensors for the Environment; Towards *In-situ* Analysis

by

Nicole Elizabeth Reily-Horne

A thesis

Submitted in fulfilment of the requirements for the degree  
of

Doctor of Philosophy in Chemistry

University of Warwick  
Department of Chemistry

December 2021



Dedicated to Hannah and Eilidh,  
become whoever you want to be.

*'At first people refuse to believe that a strange new thing can be done, then they begin to hope it can be done, then they see it can be done - then it is done and all the world wonders why it was not done centuries ago.'*

*Frances Hodgson Burnett | The Secret Garden*

# 1 Table of Contents

---

<b>1</b>	<b>Introduction</b>	<b>1</b>
1.1	Overview	1
1.2	Methods of Electroanalysis	2
1.2.1	Dynamic electrochemistry	2
1.2.2	Scanning techniques and use in electroanalysis	6
1.2.3	Electrochemical Cell Setup	9
1.2.4	Electrode materials	10
1.3	Boron Doped Diamond	11
1.3.1	Electrochemical Properties	13
1.4	Heavy Metal Detection	16
1.4.1	Heavy Metal Speciation	18
1.4.2	Heavy Metal Detection Techniques	19
1.4.2.1	Inductively Coupled Plasma Mass Spectrometry	19
1.4.2.2	Anodic Stripping Voltammetry	21
1.4.2.3	X-ray Fluorescence Spectrometry	24
1.5	pH and Buffer Capacity	26
1.5.1	Methods of pH measurement	28
1.5.1.1	Optical	28
1.5.1.2	Glass pH probes	29
1.5.1.3	Metal oxides	31
1.5.1.4	Ion-Selective Field Effect Transistors	31
1.5.1.5	Quinone based pH sensing technologies	32
1.5.2	Methods of Alkalinity Measurement	34
1.6	Microbial Biofilms and the impact on sensors	35
1.6.1	Biofilm Formation	36
1.6.2	Biofouling	37
1.6.3	Quantification and visualisation of biofilms	38
1.6.3.1	Microbiological and molecular methods	38
1.6.3.2	Physical methods	39
1.6.3.3	Chemical methods	39
1.6.3.4	Optical and fluorescence microscopy	40
1.6.3.5	Electron Microscopy	41
1.6.3.6	Scanning Probe Microscopy	43
1.7	Aims and Objectives	44
1.8	References	45

<b>2</b>	<b>Experimental.....</b>	<b>61</b>
2.1	Chemicals.....	61
2.2	Materials.....	63
2.3	Fabrication of electrodes.....	64
2.3.1	Preparation of BDD.....	64
2.3.1.1	Hot acid clean and thermal anneal procedure.....	65
2.3.1.2	Incorporation of pH Sensitive BDD-Q.....	65
2.3.1.3	Formation of an Ohmic contact.....	65
2.3.2	Electrode Fabrication.....	66
2.4	Instrumentation.....	67
2.4.1	Potentiostats.....	67
2.4.2	3D Printers.....	67
2.4.3	X-ray Fluorescence.....	70
2.4.4	White Light Interferometry.....	70
2.5	Electrochemical Characterisation.....	70
2.5.1	Capacitance.....	70
2.5.2	Solvent Window.....	71
2.5.3	Redox Electrochemistry.....	71
2.5.4	Quinone surface coverage measurement.....	72
2.6	References.....	73
<b>3</b>	<b>Assessment of a boron doped diamond ring disc buffer capacity sensor .....</b>	<b>74</b>
3.1	Overview.....	74
3.2	Introduction.....	75
3.2.1	Buffer capacity measurements.....	77
3.2.2	Miniaturised pH sensors and alkalinity sensors.....	79
3.3	Experimental.....	84
3.3.1	Solution preparation.....	84
3.3.2	Fabrication of ring disc electrode.....	84
3.3.3	Experimental set up.....	87
3.3.4	Electrochemical characterisation.....	88
3.3.5	Reactive-transport Modelling.....	89
3.3.6	Data analysis for buffer capacity measurement.....	93
3.4	Results and Discussion.....	94
3.4.1	Electrochemical Characterisation.....	94
3.4.2	Proton Generation in electrolyte solutions.....	97
3.4.3	Proton generation and pH tracking in Phosphate buffer.....	99

3.4.4	Proton generation and pH tracking in hydroxide solutions and borate buffer solutions.....	102
3.4.5	Response of BDD-Q in multiple pH environments. ....	105
3.4.6	COMSOL modelling of the BDD-Q ring disc in phosphate buffer .....	108
3.4.7	The Role of Natural Convection.....	116
3.4.8	Response of trench BDD-Q disc electrode in phosphate buffer with proton generation on ring.....	117
3.4.9	Analysis of BDD ring disc as a buffer capacity sensor .....	120
3.5	Conclusions and future work .....	122
3.6	References.....	124
<b>4</b>	<b><i>In-situ</i> tracking of catalytically driven pH changes on boron doped diamond (BDD) versus copper nanoparticle modified BDD in unbuffered solutions.....</b>	<b>128</b>
4.1	Overview.....	128
4.2	Introduction .....	129
4.3	Experimental.....	134
4.3.1	Chemicals & solutions.....	134
4.3.2	Electrode Fabrication .....	134
4.3.3	Electrochemical Measurements .....	136
4.4	Results and Discussion .....	138
4.4.1	Electrochemical Characterisation.....	138
4.4.2	Electrochemical response of bare BDD .....	142
4.4.3	Electrochemical response of Cu NP-BDD electrode.....	143
4.4.4	Electrocatalytic effect of Cu.....	146
4.4.4.1	pH Tracking in Nitrate Electrolyte .....	148
4.4.4.2	pH Tracking in Sulfate Electrolyte.....	153
4.4.5	pH Tracking with a Cu-NP BDD Ring Electrode.....	155
4.4.5.1	pH Tracking with Cu nanoparticles in Nitrate electrolyte.....	157
4.4.5.2	pH Tracking with Cu NPs in Sulfate electrolyte .....	163
4.4.5.3	Comparison of electrocatalysed pH changes in nitrate and sulfate solutions on bare BDD and BDD decorated with copper nanoparticles .....	167
4.5	Conclusions and future work .....	168
4.6	References.....	170
<b>5</b>	<b>Electrochemical Copper Detection.....</b>	<b>174</b>
5.1	Overview.....	174
5.2	Introduction .....	175
5.2.1	Heavy metals, the environment, and health.....	175
5.2.2	Electrochemical Detection of Metals.....	176
5.3	Experimental.....	179

5.3.1	Solution Preparation.....	179
5.3.2	Electrochemical Characterisation.....	179
5.3.3	EC-XRF Rotating Disc Electrode Design and Measurements.....	180
5.3.3.1	EC-XRF Rotating Disc Electrode .....	180
5.3.3.2	EC-XRF Electrochemical Measurements .....	181
5.3.3.3	ED-XRF .....	182
5.3.4	Ring Disc Electrode Fabrication and Measurements.....	182
5.3.4.1	Blank Ring Disc electrodes.....	182
5.3.4.2	BDD-Q ring disc electrode fabrication .....	183
5.3.4.3	Ring Disc Electrochemical Measurements .....	184
5.3.4.4	Iridium Oxide Film deposition .....	184
5.4	Results and Discussion.....	185
5.4.1	EC-XRF Design and Experimental Variation.....	185
5.4.2	EC-XRF Electrode characterisation .....	185
5.4.3	Copper EC-XRF.....	188
5.4.3.1	Effect of deposition potential.....	189
5.4.3.2	Copper Calibration curve.....	193
5.4.3.3	Supporting Electrolyte/reducing variability.....	195
5.4.3.4	Analysis of EC-XRF Redesign and Functionality .....	196
5.4.4	Anodic Stripping Voltammetry under locally controlled pH environments 198	
5.4.5	Ring Disc Electrode Characterisation.....	199
5.4.5.1	BDD and BDD-Q Macroelectrodes .....	199
5.4.5.2	BDD Ring Disc Electrode Characterisation .....	200
5.4.5.3	BDD-Q Ring Disc Electrode Characterisation.....	201
5.4.6	Exploring BDD and BDD-Q electrodes for Cu detection and the effect of pH 203	
5.4.7	Anodic Stripping Voltammetry of copper in acidic bulk solutions on BDD and BDD-Q electrodes.....	204
5.4.8	Local pH change measurement.....	205
5.4.8.1	Iridium oxide thin film.....	205
5.4.8.2	BDD-Q Ring Disc Electrodes.....	207
5.4.9	Cu detection in locally acidic environment on BDD ring disc electrode	211
5.4.9.1	Effect of local pH decrease .....	211
5.4.9.2	Effect of water oxidation on the local environment.....	212
5.4.10	Effect of ring current on Cu ASV .....	216
5.5	Conclusions.....	217
5.6	References.....	218

<b>6</b>	<b>Low Potential Biofilm Control .....</b>	<b>222</b>
6.1	Overview.....	222
6.2	Introduction .....	223
6.2.1	Biofouling.....	223
6.2.2	Electrochemical control of bacteria and biofilms .....	223
6.2.2.1	Previous electrochemical studies on prevention of cell attachment .....	225
6.2.2.2	Previous electrochemical studies on prevention of biofilm formation 227	
6.2.2.3	The bioelectric effect.....	229
6.2.2.4	Project Aims and Objectives.....	229
6.3	Experimental.....	230
6.3.1	3D printing.....	230
6.3.2	BDD electrode fabrication.....	231
6.3.3	3D printed experimental set-up.....	232
6.3.4	Bacterial strain, media and growth conditions.....	232
6.3.5	Experimental set up with potential applied.....	233
6.3.6	Crystal violet assay .....	234
6.4	Results and Discussion .....	234
6.4.1	Material Testing and Experimental design.....	234
6.4.2	Optimisation of cell design and set up.....	237
6.4.3	Potentiostat testing .....	240
6.4.4	Membrane.....	242
6.4.5	Bacterial growth and crystal violet analysis conditions .....	243
6.4.6	Optimisation of experimental set up.....	244
6.4.7	Optimisation of Crystal Violet assay analysis .....	247
6.4.8	Effect of potential on <i>P. aeruginosa</i> biofilm formation .....	249
6.4.8.1	Determination of potential range .....	249
6.4.8.2	Effect of application of 0 mV to BDD.....	250
6.4.8.3	Comparison of applied potentials to biofilm formation on BDD .....	251
6.5	Conclusions and future work .....	262
6.6	References.....	264
<b>7</b>	<b>Conclusions and Future Work .....</b>	<b>271</b>
7.1	Conclusions.....	271
7.2	Future Work.....	274
7.3	References.....	276



# List of Figures

Figure 1.1 Double layer structure for negative and positively charged interfaces. The inner Helmholtz plane (IHP) is the centre of adsorbed species at the electrode surface, i.e. solvent molecules (teal) or ions (green/purple). Outer Helmholtz plane (OHP) is the closest approach of solvated ions. _____	4
Figure 1.2 Concentration diffusional profiles at a) macroelectrode, b) microelectrode and c) rotating disc electrode. The arrows represent the flux of electroactive reactant from bulk concentration (blue) and decreasing in concentration at the electrode surfaces (to red). <sup>28</sup> _____	5
Figure 1.3 a) A cyclic voltammogram waveform and resulting exemplar current outputs for a reversible reaction on a b) macroelectrode c) and microelectrode. _____	6
Figure 1.4 Square wave voltammogram waveform (black) and current decays (pink) showing sampling points ( $i_f$ and $i_r$ ) and resulting current output. _____	8
Figure 1.5 Three electrode cell set up. Working electrode, reference electrode and counter electrode from left to right. _____	9
Figure 1.6 Comparison of solvent windows in 0.1 M $\text{KNO}_3$ for BDD (blue), glassy carbon (pink) and platinum (green) electrodes. <sup>92</sup> _____	14
Figure 1.7 Schematic of an a) inner sphere reaction and an b) outer sphere reaction. _____	15
Figure 1.8 Solvent windows in 0.1 M $\text{KNO}_3$ for BDD (black; dashed) and $sp^2$ containing BDD (red; solid) arrows indicate increase in current associated with the oxygen reduction reaction (ORR) and the oxygen evolution reaction (OER). _____	16
Figure 1.9 The effect of element concentration for poisonous (blue), non-essential elements (green) and essential trace elements (pink) for organism growth and maintenance. The optimum concentration range for essential elements can be broad (solid line) or narrow (dashed line) depending on the element. _____	17
Figure 1.10 Schematic of ICP-MS measurement. _____	20
Figure 1.11 a) Exemplar cyclic voltammogram showing metal deposition (reduction) and stripping (oxidation). b) Exemplar current time trace for metal deposition and potential time waveform (inset). c) Exemplar metal stripping voltammogram and potential time waveform (inset). <sup>28</sup> _____	22
Figure 1.12 Principle of fluorescence produced by x-rays in XRF _____	25
Figure 1.13 Schematic of glass pH probe. _____	30
Figure 1.14 Quinone scheme of squares showing possible electron and proton transfer reactions. The proton coupled electron transfer regime is indicated by the pink dashed line. _____	32
Figure 1.15 Quinone deprotonation reactions showing $pK_{a1}$ and $pK_{a2}$ _____	33
Figure 1.16 Titration curve for a buffered solution (black solid line) and a less buffered solution (blue dashed line) _____	35
Figure 1.17 Schematic of the stages of biofilm formation. 1. Formation of a conditioning film, 2. Reversible adhesion, 3. Irreversible adhesion, 4. Microcolony formation and beginning of EPS excretion, 5. Mature biofilm and 6. Dispersal of daughter cells for further colonisation. _____	36

Figure 1.18 Schematic of a scanning electron microscope. _____	42
Figure 2.1 Schematic of fused deposition modelling printer based on the mechanism of a Lulzbot Taz 6. _____	68
Figure 2.2 Schematic of a stereolithographic printer based on the mechanism of a Formlabs Form 3 printer including the wash and cure steps. _____	69
Figure 3.1 Schematic of electrochemical generation of proton or hydroxide ions through the oxidation or reduction of water respectively, diffusion into solution and detection of pH change. _____	78
Figure 3.2 Schematic of modified ISFET for alkalinity measurements, modified from Ref 31. _____	80
Figure 3.3 Schematic of ion selective membrane alkalinity sensor modified from Ref 36. _____	81
Figure 3.4 Stages of BDD-Q ring disc electrode fabrication; a) an image of the intrinsic diamond ring disc support (diameter 2.2 mm) with holes for wire contacting. b) Two images of the BDD ring (ID 1.4 mm, OD 1.8 mm) and disc electrodes (1 mm diameter) from the front face and showing the Ti/Au contacts on the rear. c) An image of the BDD ring and disc in position in the support from the rear. d) An image of the BDD ring disc and support in the 3D printed electrode cap. _____	85
Figure 3.5 Image of fabricated ring disc electrode and optical microscopy image of BDD ring disc with microspot array. Central disc diameter is 1 mm. _____	87
Figure 3.6 Schematic of the electrode set up for buffer capacity measurements. From left to right, Pt coil counter electrode, SCE reference, ring disc electrode, the counter reference and disc are connected to the Autolab potentiostat. A constant current (70 $\mu\text{A}$ ) is applied between the ring of the ring disc and the second Pt coil counter. _____	88
Figure 3.7 Schematic of the boundaries in the COMSOL model; 1 is the disc, 2 the insulating epoxy, 3 the ring, 4 the bulk conditions and the dash dot line the axis of symmetry. _____	90
Figure 3.8 Cyclic voltammograms for electrochemical characterisation of blank BDD ring (dashed) and BDD-Q disc electrode (solid) for a) solvent window and b) capacitance and c) quinone surface coverage on the BDD-Q disc all undertaken with a 0.1 $\text{V s}^{-1}$ scan rate. _____	95
Figure 3.9 pH response of BDD-Q electrode a) SWV response of BDD-Q disc in pH 2 (orange), 4 (pink), 7 (teal) and 10 (purple) Carmody buffers. b) Calibration of SWV peak position against pH measured with glass probe in Carmody buffer solutions (pink; ●). c) SWV response of BDD-Q disc in unbuffered pH adjusted 0.1 M $\text{KNO}_3$ and d) Calibration of SWV peak against solution pH measure by glass pH probe (blue; ■) solutions and peak positions of buffered data shown in b (pink; ●). _____	97
Figure 3.10 a) SWV response on BDD-Q disc in 0.1 M $\text{KNO}_3$ with 70 $\mu\text{A}$ applied to the ring. b) pH measured by BDD-Q disc over time determined from the data presented in part a. Colours correspond between the two graphs. _____	98
Figure 3.11 Measured BDD-Q response with applied currents of 1.5 (■), 3 (●), 5 (▲), 10 (◆), 15 (◇), 30 (◆) and 50 (★) $\mu\text{A}$ on BDD ring in 0.1 M $\text{KNO}_3$ . _____	99
Figure 3.12 A selection of successive square wave voltammograms from BDD-Q disc with 70 $\mu\text{A}$ applied to the ring in phosphate concentrations of a) 1, b) 10, c) 15 and d) 25 mM, not all SWV	

included for clarity. Green to red indicates shift from bulk pH to the generated acidic pH. Bold black lines indicate the double peak feature or broadening as discussed in the main text. \_\_\_\_\_ 100

Figure 3.13 a) SWV response of BDD-Q disc in 5 mM phosphate buffer solution with 70  $\mu$ A applied to the ring, blue to pink, not all data shown for clarity. b) BDD-Q pH determined from peak position as analysed by NOVA (■) and manually (●), colours correspond between parts a and b. \_\_\_\_\_ 101

Figure 3.14 Graph showing pH change over time for 0.5 (■), 1 (●), 5 (▲), 10 (▼), 15 (◆), 20 (◀), 25 (▶), 30 (●), 35 (★), and 40 mM (◆) determined from manual peak picking of SWV data and conversion of peak potential to pH from buffered pH calibration line ( $E_p = -0.06093 \text{ pH} + 0.48977$ ). 102

Figure 3.15 SWV response on BDD-Q disc in potassium hydroxide solutions with 70  $\mu$ A applied to the ring at a) pH 6.05, b) pH 7.02, c) pH 9.08 and d) pH 11.29. \_\_\_\_\_ 103

Figure 3.16 SWV response of BDD-Q disc in borate buffer with 70  $\mu$ A applied to the ring at a) 0.1 mM, b) 5 mM, c) 15 mM and d) 30 mM. \_\_\_\_\_ 104

Figure 3.17 a) Calibration of two BDD-Q macroelectrodes together (■) and individually (● and ▲). SWV responses of the two BDD-Q electrodes in buffered solutions between pH 2.06 and 10.16 (solid line colours correspond roughly to pH indicator colours) with one electrode held at b) pH 2.06, c) pH 6.00 and d) pH 10.16, dashed lines are the SWV response with both electrodes in the same solution. \_\_\_\_\_ 106

Figure 3.18 COMSOL output (lines) of average pH across the disc with 70  $\mu$ A applied to the ring in phosphate buffer (0.5 mM – 40 mM) and experimental data at the same concentrations (symbols). \_\_\_\_\_ 108

Figure 3.19 COMSOL simulation output of pH generated in phosphate buffer with 70  $\mu$ A applied to the ring at 5, 10, 30 and 60 s for phosphate concentrations at 1, 5 and 15 mM. The outline of the ring electrode and the microspots of the BDD-Q electrodes are also indicated on each image. \_\_\_\_\_ 109

Figure 3.20 Modelled pH at edge of disc (green) and centre of disc (black) in 0.1 M  $\text{KNO}_3$  with 70  $\mu$ A applied to the ring over 80 s. The inset shows the profile over 20 s. \_\_\_\_\_ 110

Figure 3.21 COMSOL simulation output of pH generated in 15 mM phosphate buffer with 70  $\mu$ A applied to the ring at 30, 40, 50 and 60 s. The outline of the ring electrode and the microspots of the BDD-Q electrodes are also indicated on each image. \_\_\_\_\_ 111

Figure 3.22 SWV response of BDD-Q disc in 15 mM phosphate buffer with 70  $\mu$ A applied to the ring at 31 (purple; dash dot line), 42 (green; dashed line), 53 (orange; solid line) and 64 (pink; dotted line) s. \_\_\_\_\_ 112

Figure 3.23 The expected SWV response on the disc in 40 mM phosphate buffer with 70  $\mu$ A applied to the ring, estimated by assuming each spot showed a Gaussian SWV peak with a peak position given by  $E_p = -0.06 \text{ pH} + 0.54$ , a full width at half maximum (FWHM) of 75 mV and an amplitude (current) proportional to the number of spots in each ring. The response of each microspot group are shown individually, and summed together at 140, 147, 154 and 162 s. \_\_\_\_\_ 114

Figure 3.24 a) Modelled pH time graph at distribution of each group of microspots in 40 mM phosphate buffer with 70  $\mu$ A applied to the ring b) Simulated SWV response summing pH of each

group of spots across the disc over time for the same experimental conditions at 140, 147, 154 and 162 s as depicted in Figure 2.23. _____	115
Figure 3.25 COMSOL model output for experimental system measured in Figure 3.14 with the Amatore natural convection factor applied with a) a 400 $\mu\text{m}$ diffusion layer and b) a 200 $\mu\text{m}$ diffusion layer. _____	116
Figure 3.26 Optical microscopy image of BDD ring with inner diameter of 1.4 mm and outer diameter 1.8 mm and trench disc, trench inner diameter 0.8 mm and outer diameter 0.9 mm. _____	117
Figure 3.27 SWV response of trench disc in 10 mM phosphate with 70 $\mu\text{A}$ applied to the ring. _____	118
Figure 3.28 Measured pH values on BDD-Q ( $\diamond$ ) and trench ( $\bullet$ ) disc electrodes with 70 $\mu\text{A}$ applied to the ring in 5 mM (green), 10 mM (blue) and 15 mM (purple) phosphate buffer. _____	119
Figure 3.29 a) FEM output for trench disc data with 70 $\mu\text{A}$ applied to the ring in phosphate buffer at 0 (black), 0.5 (teal), 1 (orange), 5 (purple), 10 (pink), 15 (green) and 20 (yellow) mM, the solid lines are the average pH across the trench with the dashed line representing the maximum and the dotted line the minimum pH values. The inset is the same data over the initial 100 s where the majority of the pH change occurs. b) Compares the average pH value for the trench electrode (dashed line) and microspot electrode (solid line) when generating at the ring electrode at 70 $\mu\text{A}$ at the same phosphate buffer concentrations. _____	120
Figure 3.30 Rate of pH change from bulk pH (7.3) to first set of five SWV with a stable single peak position divided by the generation time between plotted against buffer concentration for BDD-Q ring disc in phosphate buffer generating $\text{H}^+$ at 70 $\mu\text{A}$ on the BDD ring. _____	121
Figure 3.31 Schematic of a suggested thin channel alkalinity sensor using BDD disc electrodes. _____	123
Figure 3.32 Dual proton generation alkalinity sensor designs; red generating electrodes and grey BDD-Q sensing electrodes a) bars that could be placed within a defined channel and b) ring-ring disc electrode configuration. _____	124
Figure 4.1 a) pH dependent speciation of Cu in water and b) Pourbaix diagram of Cu in water. Both at an ion concentration 0.001 m (mol/kg water). Temperature 25°C. _____	130
Figure 4.2 Images of ring disc electrode a) electrode body in final form, b) electrode face and c) optical microscopy image of BDD ring and BDD-Q disc (diameter 1 mm). Note the non-circular appearance of the disc electrode is due to a small amount of resin remaining on the surface of the disc. _____	136
Figure 4.3 Calibration graph for BDD-Q disc electrode at a) 10 $\mu\text{A V}^{-1}$ sensitivity in Carmody buffer solutions (solid line; $\blacksquare$ ; blue) and pH response in unbuffered solution (dashed line; $\blacktriangle$ ; pink) and b) 1 $\mu\text{A V}^{-1}$ sensitivities. Carmody buffer solutions (solid line; $\blacksquare$ ; green) and pH response in unbuffered solution (dashed line; $\blacktriangle$ ; purple). _____	139
Figure 4.4 a) SWV responses of BDD-Q disc in ring disc arrangement at 0.1 $\mu\text{A V}^{-1}$ (black dotted line) 1 $\mu\text{A V}^{-1}$ (blue dashed line) 10 $\mu\text{A V}^{-1}$ (pink solid line) and $i-t$ decay response over 0.246 to 0.230 V using STEP measurement to simulate SWV response at a) 10 $\mu\text{A V}^{-1}$ (pink solid line), c) 1 $\mu\text{A V}^{-1}$ (blue dashed line) and d) 0.1 $\mu\text{A V}^{-1}$ (black dotted line). Grey box covers first 'step' response is not	

representative in the first measurement. Dashed grey box shows 50 -100% region of one *i-t* decay, the region sampled by the potentiostat during a SWV measurement. \_\_\_\_\_ 141

Figure 4.5 (a) pH calibration SWV measurements in pH 4 (pink), 7 (green) and 10 (purple) Carmody buffers and (b) corresponding pH calibration lines under OCP (solid line; ▲), Cell On returning to start potential (dashed line; ●) and Cell on holding at final potential (dotted line; ■) \_\_\_\_\_ 142

Figure 4.6 LSV on bare BDD ring electrode in aerated 0.1 M KNO<sub>3</sub> (purple; dotted line) and 0.1 M K<sub>2</sub>SO<sub>4</sub> (green) solutions. Undertaken with a 0.1 V s<sup>-1</sup> scan rate. \_\_\_\_\_ 143

Figure 4.7 A cyclic voltammogram performed on the ring of the BDD ring disc electrode in 100 μM CuSO<sub>4</sub> deoxygenated acetate buffer, pH 3.1. Scan rate = 0.1 V s<sup>-1</sup>. \_\_\_\_\_ 144

Figure 4.8 Dashed line is Cu CV performed on the ring of the BDD ring disc electrode in 100 μM CuSO<sub>4</sub> deoxygenated acetate buffer overlaid by; a) ASV data from Cu deposition in deoxygenated 100 μM CuSO<sub>4</sub> in acetate buffer at -0.8 V for 10 s (green), 20 s (blue) and 30 s (pink) stripped in acetate buffer solution, b) ASV data from Cu deposition in deoxygenated 100 μM CuSO<sub>4</sub> in acetate buffer for 20 s at -0.5 V (orange), -0.6 V (purple), -0.7 V (green) and -0.8 V (blue). All undertaken at a scan rate of 0.1 V s<sup>-1</sup>. \_\_\_\_\_ 145

Figure 4.9 SEM image of Cu deposits (white spots) on ring of BDD-Q ring disc electrode, deposited from a deoxygenated 100 μM CuSO<sub>2</sub> acetate buffer solution by holding at -0.6 V vs. SCE for 20 s. 146

Figure 4.10 LSV responses in 0.1 M KNO<sub>3</sub> (a & c) and 0.1 M K<sub>2</sub>SO<sub>4</sub> (b & d) on ring electrode of ring disc (a & b) and a 1 mm macro electrode (c & d) without Cu NPs (dotted line), and with Cu NPs in; aerated solutions (solid line), deoxygenated solutions (dashed line) and oxygenated solutions (dot dash line). Undertaken with a 0.1 V s<sup>-1</sup> scan rate. \_\_\_\_\_ 147

Figure 4.11 Background response of BDD ring disc electrode in aerated 0.1 M KNO<sub>3</sub>. Dashed line is the bulk measurement on disc prior to applying a potential to the ring. 20 sequential SWV scans on disc electrode with -2.0 V applied to the ring. \_\_\_\_\_ 149

Figure 4.12 The measured pH change in an aerated 0.1 M KNO<sub>3</sub> on the disc electrode, unless otherwise stated, at ring potentials of -0.2 V (■), -0.4 V in deoxygenated solution (●), -0.4 V (▲), -1.0 V (◆) and -2.0 V (◆) normalised to measured bulk concentration. \_\_\_\_\_ 150

Figure 4.13 Background response of ring disc electrode in deoxygenated 0.1 M KNO<sub>3</sub>. Dashed line is the bulk measurement on disc prior to applying a potential to the ring. 20 sequential SWV scans on disc electrode with -0.4 V applied to the ring. \_\_\_\_\_ 151

Figure 4.14 Background response of ring disc electrode in aerated 0.1 M KNO<sub>3</sub>. Dashed line is the bulk measurement on disc prior to applying a potential to the ring. a) 20 sequential SWV scans on disc electrode with -0.2 V applied to the ring b) 20 sequential SWV scans on disc electrode with -0.4 V applied to the ring and c) 20 sequential SWV scans on disc electrode with -1.0 V applied to the ring. \_\_\_\_\_ 152

Figure 4.15 Background response of ring disc electrode in aerated 0.1 M K<sub>2</sub>SO<sub>4</sub>. Dashed line is the bulk measurement on disc prior to applying a potential to the ring. a) 20 sequential SWV scans on

disc electrode with -0.2 V applied to the ring b) 20 sequential SWV scans on disc electrode with -1.0 V applied to the ring. \_\_\_\_\_ 153

Figure 4.16 Background response of ring disc electrode in 0.1 M  $K_2SO_4$ . Dashed line is the bulk measurement on disc prior to applying a potential to the ring. a) 20 sequential SWV scans on disc electrode with -0.4 V applied to the ring in a deoxygenated solution b) 20 sequential SWV scans on disc electrode with -0.4 V applied to the ring in an aerated solution and c) 20 sequential SWV scans on disc electrode with -2.0 V applied to the ring in an aerated solution. \_\_\_\_\_ 154

Figure 4.17 The measured pH change in 0.1 M  $K_2SO_4$  on the disc electrode at ring potentials of -0.2 V (■), -0.4 V in deoxygenated solution (●), -0.4 V (▲), -1.0 V (◆) and -2.0 V (◆) normalised to measured bulk concentration. Unless stated all solutions are aerated. \_\_\_\_\_ 155

Figure 4.18 Bulk pH measurements in 0.1 M  $KNO_3$  on BDD-Q disc before Cu deposition (dashed line) and after Cu deposition returned to the original 0.1 M  $KNO_3$  solution (solid line) a) without rinsing, b) rinsed gently in static DI and c) rinsed in DI stirred with a magnetic flea. \_\_\_\_\_ 156

Figure 4.19 Response of ring disc electrode in aerated 0.1 M  $KNO_3$  with Cu NPs electrodeposited on the ring subsequently held at a) -1 V and b) -2 V. Dashed line is the bulk measurement on disc prior to deposition of Cu from a deoxygenated 100  $\mu M$   $Cu_2SO_4$  solution onto the ring. 20 sequential SWV scans on disc electrode at each potential are shown. Vertical solid lines indicate the shift of the pH peak from scan one (blue) to scan twenty (beige). \_\_\_\_\_ 159

Figure 4.20 Response of ring disc electrode in aerated 0.1 M  $KNO_3$  with Cu NPs electrodeposited on the ring. Dashed line is the bulk measurement on disc prior to deposition of Cu from a deoxygenated 100  $\mu M$   $Cu_2SO_4$  solution onto the ring. 20 sequential SWV scans on disc electrode with -0.2 V applied to the ring. Dashed vertical line indicates the peak position of the bulk pH measurement, solid vertical line indicates the stability of the pH peak potential during the measurement and the orange, dash dot vertical line indicates the stability of the second peak throughout the scans thought to be associated with some form of Cu deposition. \_\_\_\_\_ 160

Figure 4.21 Response of ring disc electrode in 0.1 M  $KNO_3$  with Cu NPs electrodeposited on the ring at -0.4 V. Dashed line is the bulk measurement on disc prior to deposition of Cu from a deoxygenated 100  $\mu M$   $Cu_2SO_4$  solution onto the ring. 20 sequential SWV scans on disc electrode with -0.4 V applied to the ring in a) deoxygenated 0.1 M  $KNO_3$  and b) in aerated 0.1 M  $KNO_3$ . Vertical solid lines indicate the shift of the pH peak from scan one (blue) to scan twenty (beige). Vertical dashed lines indicate the shift in potential of the Cu associated peak from scan one (blue) to scan twenty (beige). \_\_\_\_\_ 162

Figure 4.22 The measured pH change in 0.1 M  $KNO_3$  on the disc electrode at ring potentials of -0.2 V (■), -0.4 V in deoxygenated solution (●), -0.4 V in an aerated solution (▲), -1.0 V (◆) and -2.0 V (◆) normalised to measured bulk concentration for bare BDD ring (purple) and with Cu NPs (gold). \_\_\_\_\_ 163

Figure 4.23 Response of ring disc electrode in aerated 0.1 M  $K_2SO_4$  with Cu NPs electrodeposited on the ring subsequently held at a) -0.2 V and b) -0.4 V in a deoxygenated solution. Dashed line is the bulk measurement on disc prior to deposition of Cu from a deoxygenated 100  $\mu M$   $Cu_2SO_4$  solution

onto the ring. 20 sequential SWV scans on disc electrode at each potential are shown. Vertical solid lines indicate pH peak position. \_\_\_\_\_ 164

Figure 4.24 Response of ring disc electrode in aerated 0.1 M  $K_2SO_4$  with Cu NPs electrodeposited on the ring subsequently held at a)  $-0.4$  V and b)  $-1$  V. Dashed line is the bulk measurement on disc prior to deposition of Cu from a deoxygenated  $100 \mu M$   $Cu_2SO_4$  solution onto the ring. 20 sequential SWV scans on disc electrode at each potential are shown. Vertical solid lines indicate the shift of the pH peak from scan one (dark brown) to scan twenty (beige). \_\_\_\_\_ 165

Figure 4.25 Response of ring disc electrode in aerated 0.1 M  $K_2SO_4$  with Cu NPs electrodeposited on the ring subsequently held at  $-2.0$  V. Dashed line is the bulk measurement on disc prior to deposition of Cu from a deoxygenated  $100 \mu M$   $Cu_2SO_4$  solution onto the ring. 20 sequential SWV scans on disc electrode at each potential are shown. Vertical solid lines indicate the shift of the pH peak from scan one (dark brown) to scan twenty (beige). \_\_\_\_\_ 166

Figure 4.26 The measured pH change in 0.1 M  $K_2SO_4$  on the disc electrode at ring potentials of  $-0.2$  V (■),  $-0.4$  V in deoxygenated solution (●),  $-0.4$  V in an aerated solution (▲),  $-1$  V (◆) and  $-2$  V (◆) normalised to measured bulk concentration for bare BDD ring (grey) and with Cu NPs (orange). \_ 167

Figure 5.1 Rotating disc electrode design for EC-XRF studies in References 11 and 12. Left hand side shows the assembled of the electrode the right shows the components within the electrode. Schematic not to scale, BDD disc has a diameter of 25 mm. \_\_\_\_\_ 178

Figure 5.2 New rotating disc electrode design. Left hand side shows the assembly of the electrode cap and body, the figure on the right shows the rear of the electrode cap to highlight the ohmic contacts. Schematic not to scale, BDD diameter 21 mm. \_\_\_\_\_ 181

Figure 5.3 Stages of the fabrication process for a BDD ring disc electrode. a) Ti/Au sputtered ring and disc, sealed in epoxy resin as centrally as possible. b) Placement of copper wire (thick white) on disc and silver plated copper wire (red) on ring contacted with silver epoxy. c) and d) reverse and front of completed electrode, respectively. e) Image of ring disc taken by optical microscope, disc = 1 mm diameter ( $\phi$ ). \_\_\_\_\_ 183

Figure 5.4 Stages of the fabrication process for BDD-Q ring disc fabrication (disc  $\phi$  1 mm) using thermal grade diamond ( $\phi$  2.2 mm) support and 3D printed components. The microspots were infilled with HIPS during fabrication which can be seen in the final image. \_\_\_\_\_ 184

Figure 5.5 Cyclic voltammograms in 0.1 M  $KNO_3$  run at  $0.1 V s^{-1}$  for capacitance (a) and solvent window (b) measurements of EC-XRF electrode ( $\phi$  21 mm) in stationary solution. Measurements were undertaken under stationary conditions with a  $0.1 V s^{-1}$  scan rate. \_\_\_\_\_ 186

Figure 5.6 a) Randle-Sevcik analysis of EC-XRF electrode ai) CVs at various scan rates, the CV at  $0.1 V s^{-1}$  is highlighted by the dashed line. aii) shows the experimental peak current data from ai. and a second rotating disc electrode cap. b) Levich analysis of E-XRF electrode bi) Cyclic voltammograms at various rotation rates with the stationary CV at  $0.1 V s^{-1}$  for comparison (dashed line). bii) shows the experimental limiting current data from bi. \_\_\_\_\_ 187

Figure 5.7 XRF background spectra of two EC-XRF electrode caps in the region of interest using the Mo target.	188
Figure 5.8 CVs of 100 ppm Cu(NO <sub>3</sub> ) <sub>2</sub> in a) 0.1 M KNO <sub>3</sub> b) 0.2 M HNO <sub>3</sub> and c) pH 4.5 acetate buffer on the EC-XRF rotating disc electrode at 0.1 V s <sup>-1</sup> . Solid line is the first cycle and dashed line indicates the second cycle.	189
Figure 5.9 a) Average XRF count rate (n=3) of Cu Kα after electrodeposition of 1 ppm Cu at different potentials for 3600 s at 1200 rpm in 0.2 M HNO <sub>3</sub> (pink; circles; bi) and 0.1 M KNO <sub>3</sub> (navy; squares; bii). bi and bii are raw XRF spectra of one run in each condition at the deposition potentials tested.	190
Figure 5.10 Optical images (i) and SEM images (ii) of Cu deposits from solutions containing 10 ppm Cu(NO <sub>3</sub> ) <sub>2</sub> deposited for 1800 s at 1200 rpm at -0.2 V (a and b) and -0.7 V (c and d) in 0.1 M KNO <sub>3</sub> (a and c) and 0.2 M HNO <sub>3</sub> (b and d).	192
Figure 5.11 XRF spectra from Cu deposition in a 10 ppm Cu <sup>2+</sup> solution for 1800 s at 1200 rpm at -0.2 V (green lines) and -0.7 V (purple lines) in a) 0.2 M HNO <sub>3</sub> and b) 0.1 M KNO <sub>3</sub> .	193
Figure 5.12 a) Average XRF count rate (n=3) of Cu Kα after electrodeposition of Cu at different concentrations for 3600 s at 1200 rpm in at -0.7 V in 0.2 M KNO <sub>3</sub> (pink; circles; bi) and at -0.5 V in 0.1 M KNO <sub>3</sub> (navy; squares; bii). bi and bii are raw XRF spectra of one run for each concentration range, insets show the spectra for 5000 ppb.	194
Figure 5.13 Average XRF count rate (n=3) from depositions for 3600 s at 1200 rpm with 500 ppb Cu using a variety of supporting electrolytes, deposition potentials and other conditions to understand the variability observed.	195
Figure 5.14 XRF spectra of deposited metals from a sample of water from Hayle estuary (green; solid line), with 0.1 M KNO <sub>3</sub> (navy; dashed line) and 0.2 M HNO <sub>3</sub> (pink; dotted line) after deposition from 50 ml of solution at -1.0 V for 3600 s at 1200 rpm.	198
Figure 5.15 Characterisation data of BDD (navy) and BDD-Q (pink) glass sealed macroelectrodes for capacitance (a) and solvent window (b) in 0.1 M KNO <sub>3</sub> and QSC (c; BDD-Q only) in pH 2 Carmody Buffer. All undertaken with a 0.1 V s <sup>-1</sup> scan rate.	199
Figure 5.16 Characterisation data of BDD ring (dashed line) disc (solid line) electrode for capacitance (a), solvent window (b) in 0.1 M KNO <sub>3</sub> and ΔE <sub>p</sub> (c) in 1 mM Ru(NH <sub>3</sub> ) <sub>6</sub> <sup>3+</sup> in 0.1 M KNO <sub>3</sub> . All undertaken with a 0.1 V s <sup>-1</sup> scan rate.	200
Figure 5.17 Characterisation data of BDD-Q Disc (purple) and BDD ring (Black) electrode for capacitance (a) and solvent window (b) in 0.1 M KNO <sub>3</sub> and QSC (c; BDD-Q Disc only) in pH 2 Carmody Buffer. All undertaken with a 0.1 V s <sup>-1</sup> scan rate.	202
Figure 5.18 Optical Image of BDD-Q ring disc electrode. Pink rings denote the boundary of the ring electrode. Disc is 1 mm in diameter.	203
Figure 5.19 CV of 10 ppm Cu in an aerated solution on BDD (Blue) and BDD-Q (Pink) glass sealed macroelectrodes, at pH 2. Scan rate of 0.1 Vs	203



Figure 5.20 CV of 10 ppm Cu on BDD (Blue) and BDD-Q (Pink) electrodes, at pH 4.4 (a) and 5.2 (b). Scan rate of 0.1 V s <sup>-1</sup> .	204
Figure 5.21 Stripping step of ppb Cu in pH 2 solution on bare BDD (Blue) and BDD-Q (Pink) electrodes. Concentrations tested; 10 ppb (solid), 50 ppb (--) and 100 ppb (-..). Deposition parameters; -0.5 V, 5 mins. Undertaken with a 0.1 V s <sup>-1</sup> scan rate.	205
Figure 5.22 Iridium oxide calibration (navy) collected by running an OCP measurement (a) and changing the buffer solution approximately every 3-5 minutes once the response had stabilised. Overlaid is the response of the iridium oxide electrode on the disc in KNO <sub>3</sub> for approximately 5 minutes and whilst 50 µA is applied to the ring (pink). B) is the calibration line of the iridium oxide taken at the stable potentials in (a) and plotted against the pH measured by a glass probe.	206
Figure 5.23 Calibration of iridium oxide film before (black) and after (blue) generating on the ring to measure local pH shift at ring currents of 1.5, 3, 5, 8 and 10 µA. The calibration steps of iridium oxide film was collected by running an OCP measurement and changing the buffer solution approximately every 3-5 minutes once the response had stabilised, as in figure 5.22.	207
Figure 5.24 pH response BDD-Q disc in ring disc electrode configuration in Carmody buffers pH 2 – 10. Square wave voltammetry at 150 Hz, 0.1 V amplitude, 1 mV step between 0.5 and -0.5 V (a). Peak potential plotted vs. pH (b).	208
Figure 5.25 pH response of BDD-Q disc in ring disc electrode configuration in pH adjusted 0.1 M KNO <sub>3</sub> between pH 2 and 10. Square wave voltammetry at 150 Hz, 0.1 V amplitude, 1 mV step between 0.5 and -0.3 V (a) pH adjusted with KOH and H <sub>2</sub> SO <sub>4</sub> . Peak potential plotted vs. pH (b) with calibration line from measurement in pH 4, 7 and 10 Carmody buffers.	208
Figure 5.26 pH response of BDD-Q disc in ring disc electrode configuration in pH adjusted 0.1 M KNO <sub>3</sub> between pH 2 and 7. Square wave voltammetry at 150 Hz, 0.1 V amplitude, 1 mV step between 0.7 and -0.15 V (a) pH adjusted with KOH and H <sub>2</sub> SO <sub>4</sub> . Peak potential plotted vs. pH (b) with calibration line from measurement in pH 2, 3, 4, 5, 6 and 7 Carmody buffers.	209
Figure 5.27 pH response of BDD-Q Disc in ring disc electrode configuration in 0.1 M KNO <sub>3</sub> generating at 8 µA (a) and 70 µA (b) on the ring after 5 sweeps. Square wave voltammetry at 150 Hz, 0.1 V amplitude, 1 mV step between 0.7 and -0.15 V	210
Figure 5.28 Shift in peak position on BDD-Q disc with scan number whilst generating on the ring at different currents (a) (starting at scan 5) and associated pH value from calibration line once plateaued (b).	210
Figure 5.29 LSV of Cu in 0.1 M KNO <sub>3</sub> (green) and when applying 50 µA on ring (pink). At a) 10 ppm, b) 1 ppm and c) 0.1 ppm Sequential LSVs to ensure all deposits are removed, the first of which is shown for each condition (dashed line). Deposition -0.7 V for 5 mins, if generating, allowed to generate for 1 minute prior to deposition. All undertaken with a 0.1 V s <sup>-1</sup> scan rate.	212
Figure 5.30 LSV of 500 ppb Cu at bulk pH 2 (blue), and in 0.1 M KNO <sub>3</sub> with 50 µA applied to the ring in an aerated solution (green) and a deoxygenated solution (pink). Deposition -0.7 V for 5 mins, ring allowed to generate for 1 minute prior to deposition. All undertaken with a 0.1 V s <sup>-1</sup> scan rate.	213

<i>Figure 5.31 Sequential LSVs on BDD-Q disc (scan rate of 0.2 V s<sup>-1</sup>) in 0.1 M KNO<sub>3</sub> with 50 μA applied to the ring for 5 minutes with an LSV recorded every 15 s. Undertaken at a 0.1 V s<sup>-1</sup> scan rate.</i>	214
<i>Figure 5.32 LSVs on BDD-Q disc (scan rate of 0.2 V s<sup>-1</sup>) in 0.1 M KNO<sub>3</sub> with a number of currents applied to the ring electrode after 5 minutes. All undertaken with a 0.1 V s<sup>-1</sup> scan rate.</i>	215
<i>Figure 5.33 SWV on BDD-Q disc whilst generating at a) 10 μA and b) 30 μA for 70 seconds, sampling every 2 seconds. 150 Hz, 4 mV step, 1 mV amplitude.</i>	216
<i>Figure 5.34 LSV of 500 ppb Cu deposited under different ring currents in aerated 0.1 M KNO<sub>3</sub> solutions. Deposition at -0.7 V for 5 mins, ring allowed to generate for 1 minute prior to deposition. All undertaken with a 0.1 V s<sup>-1</sup> scan rate.</i>	216
<i>Figure 6.1 CAD model of 3D printed test wells</i>	231
<i>Figure 6.2 Deformed FDM printed test wells and lids in PET with 0.10, 0.18 and 0.25 mm layer thicknesses after autoclaving at 121°C for 15 minutes.</i>	235
<i>Figure 6.3 Test prints of a) High temp resin, b) clear resin and c) PLA from FDM printing after autoclaving sterilisation and dyeing PA01 growth with 0.1% Crystal violet.</i>	236
<i>Figure 6.4 CVA absorbance results of biofilm growth in wells printed in the test materials of interest against a standard 96-well plate. The five bars are the individual wells and the striped bar the mean value and the error bars indicate ± 1 standard deviation.</i>	237
<i>Figure 6.5 CAD model of the final biofilm design (left) and an optical image of set up in MSC (right). Nine outer wells connect to a central compartment isolated by a Nafion 212 membrane and sealed using rubber gaskets held in place using a hose clamp. Each of the outer wells have a lid through which the BDD electrode is placed. The central well lid has a central hole for the reference electrode and a small hole for the counter electrode and a hole for the thermometer.</i>	239
<i>Figure 6.6 Image of the 4 mm diameter BDD round in the clip and lid configuration.</i>	240
<i>Figure 6.7 Response of 1 mm BDD macroelectrode with 1 mM Ru(NH<sub>3</sub>)<sub>6</sub><sup>3+</sup> in 0.1 M KNO<sub>3</sub> on a) the same electrode on each of the 9 WE32 channels and b) of nine electrodes run simultaneously on the nine WE32 channels. Undertaken with a 0.1 V s<sup>-1</sup> scan rate.</i>	241
<i>Figure 6.8 a) Current response of nine 1 mm BDD macroelectrodes with 1 mM Ru(NH<sub>3</sub>)<sub>6</sub><sup>3+</sup> in 0.1 M KNO<sub>3</sub> with no offset (green), a potential offset of -200 mV (purple) and a potential offset of +200 mV (pink) b) shows the applied potential range for the three groups of electrodes, the Black vertical bars align with the redox potentials of Ru(NH<sub>3</sub>)<sub>6</sub><sup>3+</sup> in each case. Undertaken with a 0.1 V s<sup>-1</sup> scan rate.</i>	242
<i>Figure 6.9 a) Growth curve of PA01 with optical density readings taken at multiple time points. b) optical density plotted against colony forming units from serial dilutions of five samples taken during the growth curve. This plot can be used to calculate cell concentrations with relation to optical density.</i>	244
<i>Figure 6.10 Images show discolouration of solution where rusting had occurred and the typical location of the rusting on the Hirshmann clips, inside pink circle. The current time plot shows the large currents passed at 0 mV for nine electrodes in the nine individual wells with the 4 mm BDD rounds used as the electrode.</i>	245

Figure 6.11 image of comparison of the two BDD geometries used, top is the 4 mm round, bottom the 5 x 10 mm piece of diamond. The gold area on both shows the sputtered contact. The purple on the clip by the spring is the nail varnish applied to seal the brass. _____	246
Figure 6.12 Schematic to visualise the entrapment of air against the membrane _____	246
Figure 6.13 Image of unused outer well (left) and a stained outer well (right), height 32 mm. ____	247
Figure 6.14 Difference between positioning of BDD 4 mm round and 5x10 mm rectangle of BDD in the wells of a 96-well plate for crystal violet assay analysis. _____	248
Figure 6.15 Solvent windows (scan rate = $0.1 \text{ V s}^{-1}$ ) performed on a 1 mm diameter disc glass sealed BDD macroelectrode LB medium (yellow; solid line), $0.1 \text{ M KNO}_3$ (purple; dotted line) and NaCl at $10 \text{ mg ml}^{-1}$ (blue; dashed line) across the potential range a) $\pm 0.8 \text{ V vs. SCE}$ and b) $\pm 1.5 \text{ V vs. SCE}$ . ____	249
Figure 6.16 Individual results for CVA (top) and optical density (bottom) from wells with no applied potential and an applied potential of 0 mV, the striped column is the mean of the individual results and the error bars represent $\pm 1$ standard deviation. _____	250
Figure 6.17 a) image of PA01 grown on an LB Agar plate at $37^\circ\text{C}$ for 16 h and b) image of PA01 liquid culture after incubation in a rotating incubator for 72 h at $37^\circ\text{C}$ at 120 rpm. _____	252
Figure 6.18 Both images are of the contents of the outer wells after a 72 h experiment with PA01, the first and last cuvettes contain LB containing no cells for reference. The top image shows a green tint to the culture indicating pyocyanin product, whereas the cultures in the bottom image are not green and appear cloudy which indicates the presence of bacterial cells. _____	253
Figure 6.19 a) Current-time trace of BDD samples at applied potentials of 0 mV (navy), + 400 mV (green) and - 400 mV (pink) in PA01 cultures, inset is the same graph without the two samples at - 400 mV to provide more detail at the lower currents. b) The mean absorbance values of the CVA on the BDD samples averaged from the triplicate samples at each applied potential, error bars represent $\pm 1$ standard deviation. c) The mean $\text{OD}_{600}$ values averaged from the triplicate well cultures at each applied potential, error bars represent $\pm 1$ standard deviation. _____	254
Figure 6.20 a) Current-time trace of BDD samples at applied potentials of 0 mV (navy), + 50 mV (green) and - 50 mV (pink) in PA01 cultures. b) The mean absorbance values of the CVA on the BDD samples averaged from the triplicate samples at each applied potential, error bars represent $\pm 1$ standard deviation. c) The mean $\text{OD}_{600}$ values averaged from the triplicate well cultures at each applied potential, error bars represent $\pm 1$ standard deviation. _____	257
Figure 6.21 a) Current-time trace of BDD samples at applied potentials of 0 mV (navy), + 200 mV (green) and - 200 mV (pink) in PA01 cultures. b) The mean absorbance values of the CVA on the BDD samples averaged from the triplicate samples at each applied potential, error bars represent $\pm 1$ standard deviation. c) The mean $\text{OD}_{600}$ values averaged from the triplicate well cultures at each applied potential, error bars represent $\pm 1$ standard deviation. _____	258
Figure 6.22 a) The mean absorbance values of the CVA on the BDD samples averaged from the triplicate samples at each applied potential for the three experiments considered, pink $\pm 200 \text{ mV}$ , navy $\pm 50 \text{ mV}$ , green $\pm 400 \text{ mV}$ , error bars represent $\pm 1$ standard deviation b) The recorded	

temperature across the same three experimental runs pink  $\pm 200$  mV, navy  $\pm 50$  mV, green  $\pm 400$  mV.

---

259

Figure 6.23 a) Current-time trace with applied potential of 0 mV in PA01 cultures. b) Current-time trace of BDD samples at applied potentials of 0 mV (navy), + 400 mV (green) and - 400 mV (pink) in PA01 cultures

---

261

# List of Tables

<b>Table 2.1</b> List chemicals used with details of suppliers. _____	61
<b>Table 2.2</b> List of materials used with details of suppliers. _____	63
<b>Table 2.3</b> Potentiostats used in each chapter _____	67
<b>Table 3.1</b> Summary table of alkalinity sensor devices. _____	82
<b>Table 3.2</b> Diffusion coefficients applied in the FEM model _____	91
<b>Table 3.3</b> Chemical equilibria considered in FEM model _____	92
<b>Table 3.4</b> Local flux of species from equilibrium reactions _____	92
<b>Table 3.5</b> Speciation for simulations of the BDD-Q electrode (concentrations in mM) _____	93
<b>Table 3.6</b> Speciation for simulations of the trench electrode (concentrations in mM) _____	93
<b>Table 3.7</b> Peak position and corresponding pH detected by BDD-Q from peaks in Figure 3.17 in two buffer pH environments. _____	107
<b>Table 3.8</b> Groups of microspots and the number of microspots within each group relative the the microspot pattern on the BDD-Q disc. _____	113
<b>Table 4.1</b> Summary table of pH change measured on BDD-Q disc over ~ 30s in 0.1 M KNO <sub>3</sub> and K <sub>2</sub> SO <sub>4</sub> solutions when a range of potentials are applied to the bare BDD ring electrode. _____	155
<b>Table 4.2</b> Summary table of pH change measured on BDD-Q disc over ~ 30s in 0.1 M KNO <sub>3</sub> and K <sub>2</sub> SO <sub>4</sub> solutions when a range of potentials are applied to the bare BDD ring electrode and when Cu NPs are present on the BDD ring electrode. _____	167
<b>Table 5.1</b> Electrochemical Characterisation Values for BDD Ring Disc Electrode _____	200
<b>Table 5.2</b> Electrochemical Characterisation Values for BDD-Q Ring Disc Electrode _____	202

# Abbreviations

AFM	Atomic force microscopy
ASV	Anodic Stripping Voltammetry
BDD	Boron doped diamond
BDD-Q	Boron doped diamond with incorporated quinone groups
BiFE	Bismuth film electrode
CAD	Computer aided design
CE	Counter electrode
CFU	Colony forming unit
CLSM	Confocal laser scanning microscopy
CV	Cyclic voltammetry
CVA	Crystal violet assay
CVD	Chemical vapour deposition
EC-XRF	Electrochemical X-ray fluorescence
EDX	Energy dispersive X-ray
ED-XRF	Energy dispersive X-ray fluorescence
EPS	Extracellular polymeric substance
FDM	Fused deposition modelling
FEM	Finite element modelling
HER	Hydrogen evolution reaction
HF-CVD	Hot filament chemical vapour deposition
HIPS	High impact polystyrene
HPHT	High pressure high temperature
ICP-MS	Inductively coupled plasma mass spectrometry
IPA	Isopropyl alcohol
IrO <sub>x</sub>	Iridium oxide
ISFET	Ion-selective field effect transistor
LB	Luria-Bertani
LOD	Limit of Detection
LPU	Light processing unit
LSV	Linear sweep voltammetry

MSC	Microbiological safety cabinet
MV-CVD	Microwave chemical vapour deposition
NP	Nanoparticle
NRR	Nitrate reduction reaction
OCP	Open circuit potential
OD	Optical density
ORR	Oxygen reduction reaction
PCET	Proton coupled electron transfer
PEEK	Polyether ether ketone
PET	Polyethylene terephthalate
PLA	Poly(lactic acid)
PMMA	Polymethylmethacrylate
PZC	Point of zero charge
Q	Quinones
qPCR	Quantitative polymerase chain reaction
QSC	Quinone surface coverage
RE	Reference electrode
ROS	Reactive oxygen species
SCE	Saturated calomel electrode
SD	Standard deviation
SEM	Scanning electron microscopy
SLA	Stereolithographic
SWV	Square wave voltammetry
TEM	Transmission electron microscopy
TETA	Triethylenetetramine
TR-XRF	Total reflection X-ray fluorescence
UME	Ultramicroelectrode
UV	Ultraviolet
WD-XRF	Wavelength dispersive X-ray fluorescence
WE	Working electrode
WR	Water reduction
XRF	X-ray fluorescence

# Acknowledgements

I'd like to thank Prof. Julie Macpherson for her supervision, guidance, support and belief in me throughout the last 4 years. Thank you and NERC for the opportunity to push myself and learn a whole new set of skills. Thank you also to Prof. Pat Unwin for the many constructive discussions throughout this process. Also thanks to Prof. Liz Wellington for allowing me access to the microbiology facilities and sharing your knowledge with me.

Thank you to Dr. Ian Mcpherson, Dr. Tania Read, Dr. Anthony Lucio, Dr. Zoë Ayres, Dr. Chiara Borsetto and Dr. Rui Pereira for the guidance, input and support across these projects. Thank you to all WEIG members, past and present, who have provided a supportive, productive and fun environment for the past 4 years. A special mention goes to Joshua Tully for 3D printing, lasering and design wizardry, to Dr. Alexandra Borrill for imparting your electrochemistry wisdom and training me to be a 'proper chemist' and Dr. Lee Simcox for his help with the beasties, random office snacks and coffee breaks. Also a special thanks to my wonderful MChem student Sophie Webb for all her efforts in the lab during a very challenging year and being such a pleasure to supervise.

Thank you to my family for the support and encouragement, I hope this makes you proud.

And of course a huge thank you to Luke for being my taxi driver, chef, therapist, housemate, lockdown buddy and my own personal entertainer, 24/7. I'd definitely have gone more insane without you, but you've got a wife out of it so it's worked out OK for you too.



# Declarations

The work presented in this thesis is entirely original and my own work except where acknowledged in the text. I confirm that this thesis has not been submitted for a degree at another university. Collaborations are indicated below:

The work presented in Chapter 3 was in collaboration with Dr Ian McPherson who developed and ran the FEM COMSOL model. Shay Chaudhuri wrote the python code for data analysis. A publication of this work is in preparation.

The work presented in Chapter 4 was undertaken in collaboration with a MChem student, Sophie Webb. Some of the data is published in her Masters report. The majority of experimental work was undertaken by the author due to lab restrictions in place during the 20/21 academic year. Katie Levey wrote the multipotential step analysis to obtain raw i-t decays comparable to SWV behaviour. A publication of this work is in preparation.

The work in Chapter 5 on EC-XRF was undertaken in collaboration with Dr. Alexandra Borrill.

Some text in chapter 1 and chapter 5 is published in:

*Addressing the practicalities of anodic stripping voltammetry for heavy metal detection: A tutorial review* A. J. Borrill, N. Reily, J. Macpherson, *Analyst*, 2019, 144 (23), 6834-6849.

# Abstract

Environmental monitoring is hugely important to aid understanding of the natural processes of the planet and the impact of humans. Electrochemical sensors provide low cost, sensitive devices that could be operated at the source or *in-situ* due to their low power requirements and portability. Boron doped diamond (BDD) retains all the physical and mechanical properties of diamond with the added property of electrical conductivity. BDD is a relatively catalytically inert material making it an ideal sensor material due to low background currents across a large potential range. Through controlled introduction of a very robust and stable form of sp<sup>2</sup> carbon into the BDD surface, pH sensitive quinone groups (BDD-Q) are formed. Such electrodes can be utilised for voltammetric pH sensing.

In Chapter 3, BDD-Q sensors are incorporated into the disc of a ring disc dual electrode arrangement and used to track dynamic pH perturbations driven on the BDD ring electrode by water oxidation. The time-dependant pH changes are shown to vary depending on the buffer capacity of the solution and in this way a methodology for buffer capacity measurements is highlighted.

In Chapter 4, the BDD ring – BDD-Q disc electrode was again used but this time to track the local pH changes associated with the electrocatalytic reduction of dissolved oxygen, nitrate ions and water on both BDD and a Cu nanoparticle functionalised BDD electrode.

In Chapter 5, advancements in heavy metal detection were considered through (i) a new electrode design for electrochemical X-ray fluorescence (EC-XRF) and (ii) use of the BDD ring-disc electrode for at the source Cu detection. In particular, local acidification of the disc environment by water oxidation on the ring, to promote electrodeposition of metallic Cu, in the ppb concentration range.

Finally, in Chapter 6, the impact of bacterial biofilm formation on BDD is investigated under potential control conditions. One of the major barriers to long term *in-situ* measurements is biofilm formation on the electrode surface. Whilst BDD is a low fouling material with time biofilms will form. The application of low voltages to discourage cell adhesion was investigated as a method to prolong long-term sensor performance in aquatic systems. *Pseudomonas aeruginosa* was used as a model monospecies biofilm system.



# 1 Introduction

---

## 1.1 Overview

The human race is changing the natural cycles of our planet. Of which the hottest topic is increasing atmospheric CO<sub>2</sub> concentrations and the associated global temperature increase and ocean pH decrease.<sup>1-5</sup> But how do scientists know this is happening? Almost all scientific disciplines rely on analytical instruments to detect chemicals. The rising CO<sub>2</sub> example has relied on atmospheric and dissolved CO<sub>2</sub> sensors,<sup>6-9</sup> pH<sup>10</sup> and temperature measurements and detection of isotopes and organic proxies for historical temperature and CO<sub>2</sub> data.<sup>11</sup>

The natural environment has a relatively narrow range of optimum conditions for ecosystems which require accurate and precise measurements. However, these systems can be easily disrupted by anthropogenic activities, particularly in freshwater systems, *i.e.* chemical or nutrient inputs. External inputs can disrupt the balance, resulting in ecosystem collapse and potential implications for human health.<sup>12-16</sup>

In terms of water systems, most environmental sampling is conducted as point sampling. The UK Environmental Change Network has collected water data across 12 locations on a weekly basis since 1993.<sup>17</sup> Conductivity and pH are measured before the sample is filtered for further measurement of; Na<sup>+</sup>, K<sup>+</sup>, Ca<sup>2+</sup>, Mg<sup>2+</sup>, Fe<sup>2+</sup>, Al<sup>3+</sup>, NH<sub>4</sub><sup>+</sup>, Cl<sup>-</sup>, NO<sub>3</sub><sup>-</sup>, SO<sub>4</sub><sup>2-</sup>, PO<sub>4</sub><sup>3-</sup>, alkalinity and dissolved organic carbon. Most of this analysis is conducted away from the sampling site in a laboratory. However, some sites do have continuous monitoring in place. Cardiff Bay has 10 monitoring stations in the bay and its tributaries, monitoring dissolved oxygen, conductivity, salinity, temperature, pH and turbidity every 15 minutes.<sup>18</sup> This is particularly important during summer months, as Cardiff Bay is susceptible to thermal stratification when oxygen levels can drop to a critical point.<sup>19</sup> Continuous monitoring of oxygen concentrations allows aeration systems to be deployed when needed. Additional monitoring for metals, salts and nutrients requires sampling and analysis away from site.

Continuous real time measurement allows for a higher density of temporal sampling providing a better indication of environmental health. However, current commercial multiparameter sensors (sondes) are expensive and offer a limited range of parameters and thus are mostly used in targeted areas. Whilst continuous monitoring may be desirable, maintaining the instrumentation and calibrations *in-situ* is challenging. One of the major challenges for long term sensing is biofouling. Bacteria, algae and diatoms are abundantly present in the environment and will readily form biofilms on surfaces, including sensors. Biofilms negatively impact sensors by blocking the surface and impacting measurements.

A plethora of sensor technologies for multiple applications exist, utilising a variety of analytical techniques. Some techniques require a laboratory setting, whilst others can be used for at the source sensing. Optical sensors detect light intensity in a particular wavelength or spectral band and are currently used to measure dissolved oxygen in waters. Mass spectrometers detect quantities of ions with specific mass to charge ratios and are utilised heavily in chemical analysis for the detection of heavy metal ions in water systems. Electrochemical sensors use controlled electron transfer reactions to detect and quantify chemical species. The work in this thesis is on development towards environmental *in-situ* electrochemical sensors.

## 1.2 Methods of Electroanalysis

Electrochemical sensors provide an excellent opportunity to minimise the cost of data collection and size of equipment required for *in-situ* monitoring and increase the number of measurable parameters. Electrochemical sensors are compact, low cost, simplistic, readily automated, and highly sensitive making them ideal for such analysis. As a result electrochemical measurements are already used for a number of fields including medical diagnostics,<sup>20</sup> wastewater management,<sup>21</sup> energy generation<sup>22</sup> and environmental monitoring.<sup>23</sup>

### 1.2.1 Dynamic electrochemistry

Electrochemistry relies on the occurrence of a charge transfer event, and relates the flow of electrons to a chemical change,<sup>24,25</sup> as shown by Equation 1.1:



Where O and R represent the oxidised and reduced forms of an electroactive species, respectively. The standard electrode potential  $E^0$ , relates to the position of equilibrium under standard conditions. Applying an overpotential  $\eta, = E - E^0$  drives either the reduction ( $\eta$  is negative) or oxidation ( $\eta$  is positive) of species in solution. The exchange of electron(s) ( $e^-$ ) between the electroactive species and the electrode results in a current flow,  $i$ . According to the Butler-Volmer model, increasing the overpotential results in an exponential increase in the rate of electron transfer and a corresponding increase in the measured current. However, this only stands if there is a constant supply of species at the electrolyte/electrode interface.

Under transport controlled conditions, (where electron transfer is very fast) mass transport is rate limiting so  $i$  is proportional to the flux of species to the electrode surface as shown in Equation 1.2.

$$i = nAFj \quad \text{Equation 1.2}$$

Where  $i$  is current (A),  $n$  is the number of electrons transferred in the reaction,  $A$  is the area of the electrode ( $\text{cm}^2$ ),  $F$  is Faradays constant ( $96485 \text{ C mol}^{-1}$ ) and  $j$  is the flux ( $\text{mol cm}^{-2} \text{ s}^{-1}$ ). Under conditions where diffusion only contributes to the flux,  $j$  is a factor of the concentration gradient (between the bulk solution and the electrode surface) and the diffusion coefficient ( $D$ ;  $\text{cm}^2 \text{ s}^{-1}$ ) of the species as described by Equation 1.3.

$$j = -D \frac{\delta c}{\delta x} \quad \text{Equation 1.3}$$

The steeper the concentration gradient or the larger the diffusion coefficient the larger the corresponding current. For electrochemical measurements, migration is negated by the addition of an excess of supporting electrolyte. This acts to reduce solution resistance therefore compensating for ohmic drop and maintaining a compressed electrical double layer. A double layer forms at any interface in an electrolyte solution as the surface charge is countered by ions in solution, Figure 1.1.

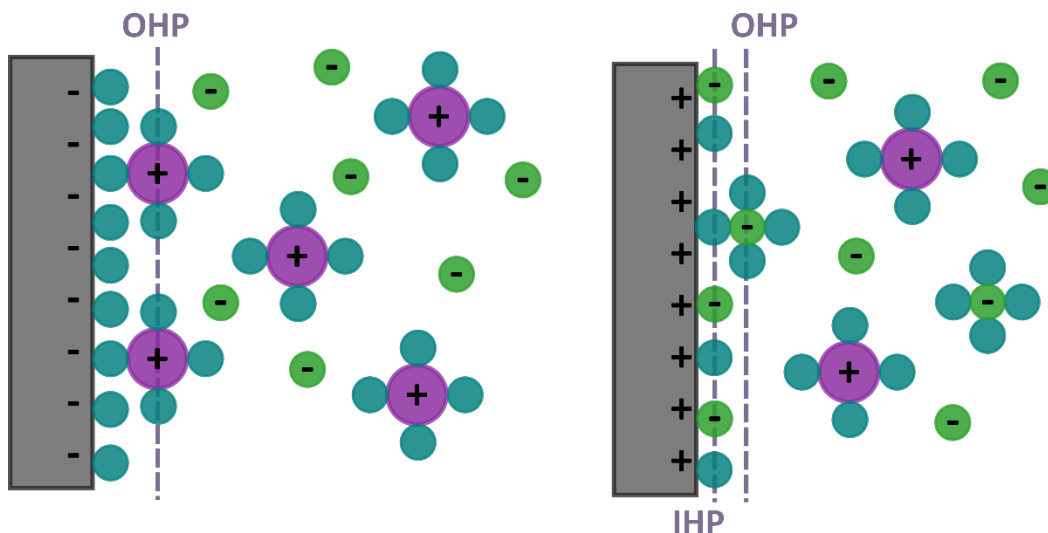


Figure 1.1 Double layer structure for negative and positively charged interfaces. The inner Helmholtz plane (IHP) is the centre of adsorbed species at the electrode surface, i.e. solvent molecules (teal) or ions (green/purple). Outer Helmholtz plane (OHP) is the closest approach of solvated ions.

In order to make electron transfer limiting it is important to sufficiently increase the rate of mass transfer. In diffusion only systems, one option is to use microelectrodes due to their more efficient hemispherical diffusional profile. However, the smaller electrode area means the currents are reduced. Forced convection, which is the combination of diffusion and solution convection, via electrode rotation or the use of flow cells, can also be used.

A planar macroelectrode, under planar diffusion-controlled conditions, gives a peak current ( $i_p$ ) for the electrolysis of a redox couple according to the Randles-Sevcik equation:<sup>26</sup>

$$i_p = 0.4463nFAC \left( \frac{nFvD}{RT} \right)^{\frac{1}{2}} \quad \text{Equation 1.4}$$

Where  $C$  is concentration,  $v$  is scan rate,  $R$  is the ideal gas constant and  $T$  is temperature. By substituting  $i_p$  for  $i$  in Equation 1.2 and using  $j = k_t C$  where  $k_t$  is the mass transport rate constant ( $\text{cm s}^{-1}$ ) then Equation 1.5 can be used to determine  $k_t$ .

$$k_t = 296000n^{\frac{1}{2}}D^{\frac{1}{2}}v^{\frac{1}{2}}F^{-1} \quad (\text{at } T = 298 \text{ K}) \quad \text{Equation 1.5}$$

For the exemplary case of a 1 mm diameter planar disc electrode (assuming  $n = 1$ ,  $D = 1 \times 10^{-5} \text{ cm}^2 \text{ s}^{-1}$  and  $v = 0.1 \text{ V s}^{-1}$ ),  $k_t = 0.0028 \text{ cm s}^{-1}$ . By moving to a

microelectrode the diffusional flux profile changes from planar, Figure 1.2a, to hemispherical Figure 1.2b.<sup>26</sup> Equation 1.6 describes the theoretical limiting current at a planar microdisc (or smaller) electrode in a quiescent solution:

$$i_{lim} = 4nrFDC \quad \text{Equation 1.6}$$

Where  $i_{lim}$  is the limiting current and  $r$  is the electrode radius ( $\text{cm}^2$ ). Under these conditions  $k_t = 4D/\pi r$ . By reducing the electrode diameter from 1 mm to 1  $\mu\text{m}$   $k_t = 0.25 \text{ cm s}^{-1}$  an increase of nearly two orders of magnitude. Microelectrodes are also useful in low conductivity solutions as ohmic drop effects ( $iR$ ) are not significant due to the smaller currents passed. In addition they suffer less from capacitive charging and can be used at fast scan rates.<sup>27</sup> If the measured currents are too small, microelectrode arrays can be used to amplify the signal.<sup>28</sup>

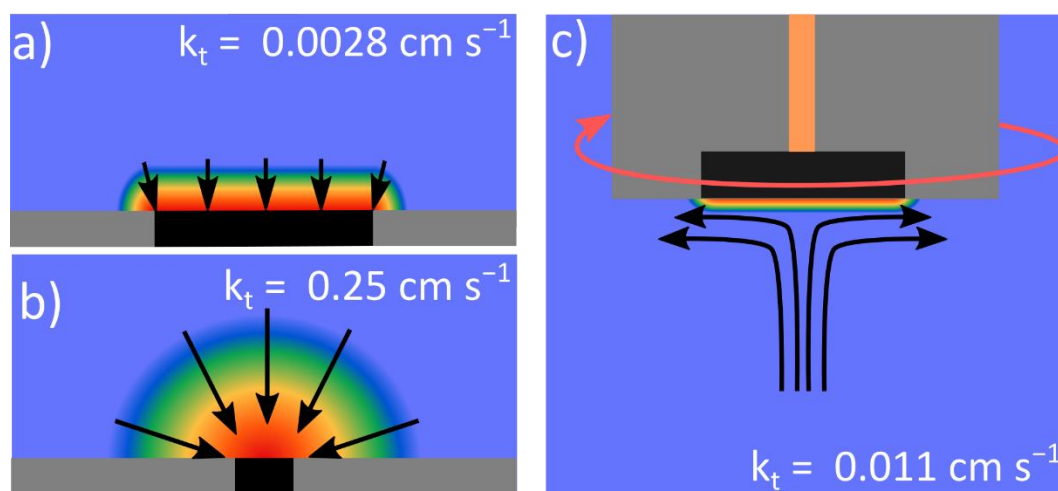


Figure 1.2 Concentration diffusional profiles at a) macroelectrode, b) microelectrode and c) rotating disc electrode. The arrows represent the flux of electroactive reactant from bulk concentration (blue) and decreasing in concentration at the electrode surfaces (to red).<sup>28</sup>

Mass transport can also be increased by using forced convection. A very commonly used forced convection set up is the rotating disc electrode,<sup>29,30</sup> the hydrodynamics of which were first characterised by Levich and Landau in 1942.<sup>31</sup> Rotation results in the compaction of the concentration gradient between the electrode and the bulk solution by creating a fluid flow to the surface, Figure 1.2c. The Levich Equation describes the relationship between current ( $i_{lim}$ ) and rotation frequency,  $\omega$  (Hz);



$$i_{lim} = 1.554nFAD^{\frac{2}{3}}\omega^{\frac{1}{2}}\nu^{\frac{-1}{6}}C \quad \text{Equation 1.7}$$

where  $\nu$  is kinematic viscosity. By rotating at 50 Hz (for  $D = 1 \times 10^{-5} \text{ cm}^2 \text{ s}^{-1}$  and  $\nu = 0.01 \text{ cm}^2 \text{ s}^{-1}$  for water at 298 K)  $k_t$  is almost an order of magnitude larger than a stationary disc of the same diameter ( $= 1 \text{ mm}$ ),  $k_t = 0.011 \text{ cm s}^{-1}$ . Other well defined hydrodynamic flow systems include the wall-jet electrode<sup>32</sup> and channel flow electrode,<sup>33</sup> although some less defined methods such as sonication,<sup>34</sup> vibration,<sup>35,36</sup> stirring<sup>37</sup> and bubbling<sup>38</sup> exist. Increasing mass transport can also aid electrochemical measurements by increasing sensitivity and reducing analysis times.

### 1.2.2 Scanning techniques and use in electroanalysis

Digital potentiostats are used to make electrochemical measurements either by voltammetric (controlled potential and measured current) or galvanostatic (controlled current and measured potential) methods.<sup>39</sup> Although not typically used for electroanalysis, cyclic voltammetry (CV) is a useful tool to inform about electrochemical reactions and electrode characteristics. CVs are conducted by sweeping, or more accurately stepping, the potential in one direction at a defined scan rate, and then reversing the direction to complete a cycle, Figure 1.3a. The resulting waveform, plotted as current vs. potential, can inform on the electrode characteristics and on the reaction of the electroactive species. Exemplar CVs for a macroelectrode, Figure 1.3b, and microelectrode or electrode under forced convection, Figure 1.3c reactions as discussed in Section 1.2.1 are presented.

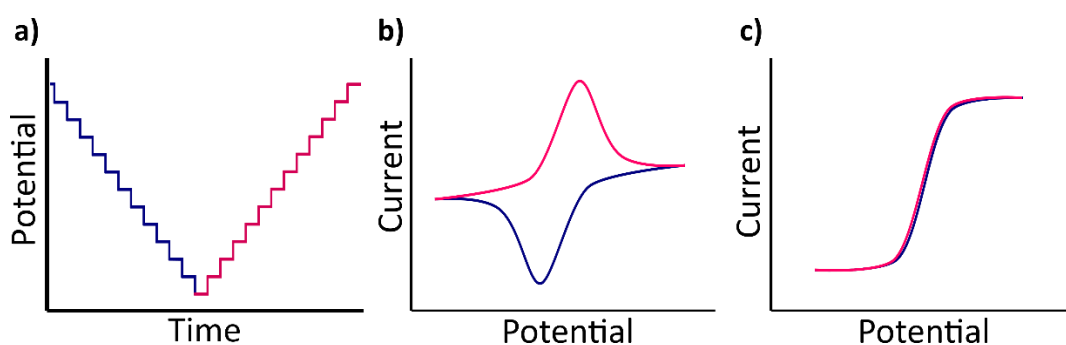


Figure 1.3 a) A cyclic voltammogram waveform and resulting exemplar current outputs for a reversible reaction on a b) macroelectrode c) and microelectrode.

At the planar macroelectrode, two current peaks are observed which correspond to the forward and back reaction, *i.e.* product generated in the forward reaction

is converted back to reactant in the back reaction. The peak to peak voltage separation is theoretically  $\Delta E_p = 57 \text{ mV}$  for a one electron transfer reaction.<sup>40</sup> By increasing the diffusional flux on the microelectrode, the product of the reaction diffuses away from the electrode so fast there is no product to detect in the reverse reaction. The current is also able to reach a limiting response. Under diffusion limited conditions, the  $\Delta E_p$  corresponding to  $\frac{3}{4}$  -  $\frac{1}{4}$  of the limiting current response is  $57 / n \text{ mV}$ .<sup>40</sup> In the absence of redox active species i.e. solutions containing only supporting electrolyte the CV can be used to inform on the double layer capacitance of an electrode and the potential window in which negligible solvent electrolysis occurs.<sup>41</sup> CVs can also be used to determine the electron transfer kinetics of a redox active species.

A further commonly used electrochemical technique is square wave voltammetry (SWV). SWV is a type of pulsed voltammetry. Pulsed techniques are often used to increase sensitivity and decrease measurement time. CV digital staircase measurements contain both faradaic (*i.e.* the redox reaction) and non-faradaic (*i.e.* double layer charging) current components. The desired faradaic current at low concentrations can be obscured by the non-faradaic contribution. The waveforms for SWV are shown in black in Figure 1.4.

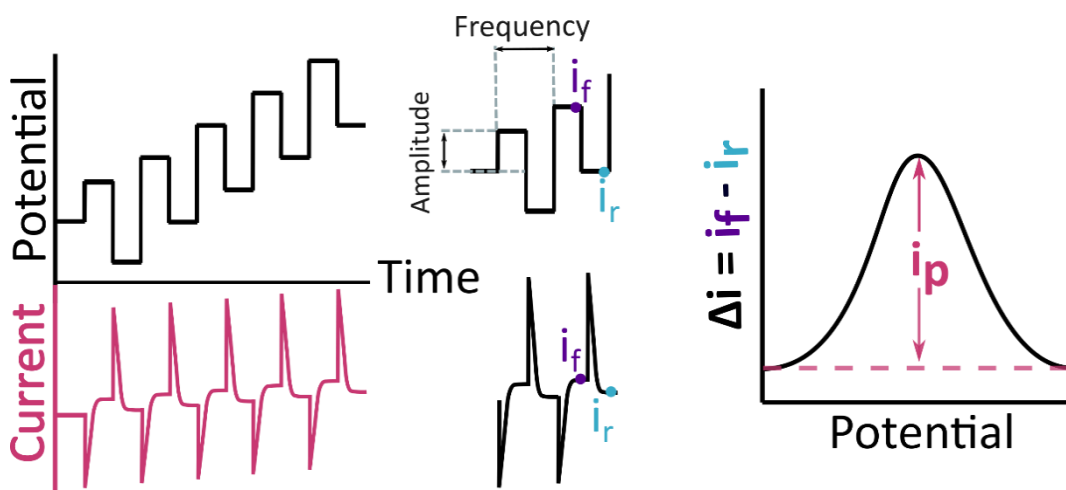
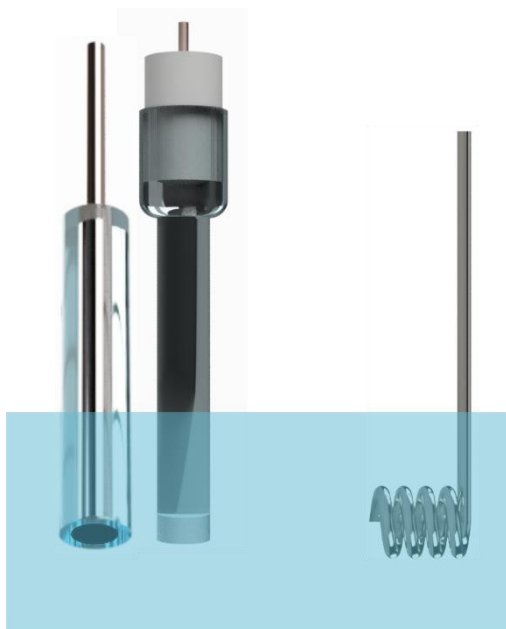


Figure 1.4 Square wave voltammogram waveform (black) and current decays (pink) showing sampling points ( $i_f$  and  $i_r$ ) and resulting current output.

The pulsed nature of SWV, means a current-time decay occurs at each pulse, shown in pink in Figure 1.4. The non-faradaic decay is proportional to  $e^{\frac{-t}{R_s C_{dl}}}$  where  $t$  is time,  $R_s$  is solution resistance and  $C_{dl}$  is the double layer capacitance, and the faradaic decay is proportional to  $t^{-\frac{1}{2}}$ . Therefore, the non-faradaic component decays faster than the faradaic and, depending on where the current is sampled, it is possible to exclude the non-faradaic component.<sup>42</sup> Typically the SWV pulses are measured over a proportion of the pulse, often the last 50-100% of the current decay, although this varies between potentiostat manufacturers. The forward current and the backward current are subtracted and the differential current ( $\Delta i$ ) plotted against the applied  $E$ , reflecting the faradaic component of the measurement. This sampling technique often results in a flatter baseline than for a non-pulsed technique.<sup>43</sup> Other pulsed techniques include normal pulse voltammetry and differential pulse voltammetry.<sup>44,45</sup> Choice of voltammetric technique is often application specific. In all cases a range of parameters should be tested in order to tailor the measurement, ensuring the best detection limits can be reached.

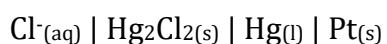
### 1.2.3 Electrochemical Cell Setup

In electroanalysis experiments, an electrochemical cell is employed consisting of a working electrode (WE) and a reference electrode (RE), the latter holding a constant potential. The potential between the WE and the RE is controlled using a potentiostat. For microelectrodes this two electrode cell is adequate due to the small currents passed through the RE. However, at the scale of macroelectrodes, the currents are too high and passing such currents through the RE will result in RE drift.<sup>39</sup> To mitigate against this a counter electrode (CE) should be introduced, typically a platinum coil or mesh, and current flows between WE and CE. This three electrode set up is depicted in Figure 1.5. The CE should have an area of at least ten times the WE to ensure no current limitations arise.



**Figure 1.5 Three electrode cell set up. Working electrode, reference electrode and counter electrode from left to right.**

The RE maintains a constant potential so the applied potential relative to the WE is always known. The saturated calomel electrode (SCE) is a commonly used RE with the following cell notation:



The SCE constitutes a mercury coated Pt wire covered by a thin layer of mercury(II) chloride immersed in a saturated potassium chloride solution. The potential of the SCE depends on activity of  $\text{Cl}^{-}$  ions present so by placement in a

saturated potassium chloride solution a constant potential is maintained. A porous frit serves as a junction between the RE and the solution.

#### 1.2.4 Electrode materials

An electrode can be made from any conductive material, provided it does not undergo reaction with the reactant or product of interest. In electroanalysis, the ideal material would have a large potential window, low background current, low ohmic resistance and would be non-toxic/biocompatible, inexpensive, easy to use, reproducible, stable and accurate.<sup>46</sup> Historically mercury was very commonly used, as it represents a homogenous electrode surface. In electroanalysis it proved especially useful for detecting metals at low concentrations. Due to its liquid state at room temperature, mercury forms homogenous metal amalgams. Alongside other very favourable properties mercury electrodes have low capacitance, minimal non-faradaic contributions, a highly reproducible and recoverable surface and a wide cathodic window due to the retardation of both the hydrogen evolution reaction<sup>47</sup> (HER; Equation 1.8) and water reduction<sup>48</sup> (Equation 1.9).



However, mercury now features in the top 10 chemicals of major public health concern<sup>49</sup> and is no longer considered a practically applicable electrode material.

Popular alternative electrode materials to mercury include gold, silver, platinum and sp<sup>2</sup>-bonded carbons such as glassy carbon.<sup>25,50</sup> Metal electrodes can come in bulk form or thin film, they are highly conductive and for many redox couples support fast electron transfer kinetics.<sup>24</sup> Metals show differing degrees of electrocatalytic activity towards water oxidation/reduction and HER and generally pass larger non-faradaic currents than carbon electrodes, due to oxidation/reduction of the metal surface or adsorption and desorption of protons and other ions. For example, ions such as chloride, can adsorb on the metal surface, block surface sites and alter reaction kinetics and mechanisms.<sup>51</sup>

Carbon materials are less expensive than the metals often used as electrodes and possess many desirable properties including; wider solvent windows than metal

electrodes, biocompatibility, and good electrocatalytic activity for many redox reactions.<sup>52,53</sup> Conductive carbon exists in many forms; glassy carbon,<sup>54</sup> screen printed carbon,<sup>55</sup> carbon fibres,<sup>56</sup> carbon nanotubes<sup>57</sup>, boron doped diamond,<sup>41,58</sup> and various forms of graphite and graphene.<sup>52,59</sup> The kinetics of electron transfer are typically dependent on the density of electronic states, which for carbon is determined by the carbon microstructure and by surface states.<sup>60</sup> Surface states are determined by the surface termination(s) and any structural defects. When the reactant undergoes inner sphere electron transfer carbon edge planes, *e.g.* edge plane pyrolytic graphite, are more reactive to electron transfer than basal plane graphite.<sup>53,60-62</sup>

Carbon materials are typically more heterogeneous in surface chemistry than metals and can be much more susceptible to effects from surface preparation techniques, so ensuring the presence of a reproducible surface can be challenging.<sup>60</sup> Surface modifications such as the addition of nanoparticles,<sup>63</sup> thin films,<sup>37,64</sup> self assembled monolayers,<sup>65,66</sup> coatings,<sup>67,68</sup> and microengineering<sup>69,70</sup> have been made to try and ensure electrode surfaces are reproducible and to aid sensitivity and selectivity.<sup>71,72</sup>

### 1.3 Boron Doped Diamond

Diamond is a remarkable material. Commercial diamond deposits are formed in the upper mantle, > 150 km below the Earth's surface, where temperatures are > 1050°C and pressures are > 4 GPa.<sup>73,74</sup> These critical temperature-pressure zones primarily occur in the stable interior of continental plates.<sup>73</sup> Deep-source volcanic eruptions, producing kimberlite and lamproite pipes, deliver diamonds from the upper mantle to the surface. These events are, however, extremely rare. Smaller diamonds can be formed at subduction zones and during asteroid impacts<sup>75-77</sup> and nanodiamonds have also been found in meteorites.<sup>78,79</sup>

Diamond however is more than just a gemstone due to its impressive range of chemical and physical properties. These include extreme hardness (*ca.* 90 GPa), a high thermal conductivity, a very high melting point, resistance to chemical erosion, a broad wavelength transparency (from deep ultraviolet to infrared) and an electrical insulator.<sup>41,58</sup> These properties make diamond useful for a range of industries, including; jewellery, cutting, grinding, drilling, and in cancer

treatments<sup>80</sup> and bionic eyes.<sup>81</sup> In order to make diamond a useful electrode material it has to be doped, typically with boron (p-type) to form boron doped diamond (BDD). At boron concentrations in the range of  $10^{16}$  – mid  $10^{19}$  atoms  $\text{cm}^{-3}$  the diamond becomes a p-type semiconductor. The boron atoms accept electrons from the valence band, creating electron ‘holes’. In order to become a ‘metal-like’ conductor the concentration must exceed  $10^{20}$  atoms  $\text{cm}^{-3}$ .<sup>3,41,58</sup> At these concentrations the electron ‘holes’ overlap forming a band. The dopant changes can be observed visually from colourless transparent insulating diamond to blue for a p-type semiconductor and black opaque diamond at metal-like conductivity.

Scientific advancement has led to the ability to produce quality synthetic diamonds. The two main methods are high-temperature high-pressure (HPHT) and chemical vapour deposition (CVD). The first synthetic diamond was produced in 1955 by HPHT which aims to mimic the conditions under which diamonds form naturally.<sup>82</sup> HPHT methods rely on the same process, but press designs can vary. Graphitic carbon is compressed to extreme pressures ( $\sim 5$  GPa) at elevated temperatures, in excess of 1800 K, in the presence of a metallic solvent.<sup>83</sup> Under these conditions graphite dissolves in the solvent metal and as the temperature is reduced, crystallises as  $\text{sp}^3$  diamond. HPHT is generally used to manufacture small diamonds ( $\mu\text{m}$  to  $\text{mm}$ ) which ultimately end up being used as abrasives for tools.<sup>58</sup> When growing diamonds using HPHT, nitrogen is unintentionally incorporated as an impurity resulting in the formation of yellow diamonds.<sup>84</sup> However, incorporation of boron at a high enough concentration and distribution for electrodes is challenging for HPHT.<sup>85,86</sup> Although using appropriate growth recipes this has recently been achieved.<sup>87</sup>

CVD occurs at much lower pressures and temperatures than HPHT, but still in the range where diamond is metastable compared to graphite.<sup>58</sup> First demonstrated in the 1960's by Eversole *et al.* of the Union Carbide Corporation in the USA, diamond produced from a hydrocarbon gas or CO/CO<sub>2</sub> mixture by CVD was deposited on a substrate.<sup>88</sup> However this produced a low yield of diamond. Since then processes to deposit  $\text{sp}^3$  bonded carbon whilst simultaneously suppressing  $\text{sp}^2$  bonded carbon formation have been refined. All

CVD diamond techniques are based on gas-phase non-equilibrium with supersaturated atomic hydrogen and hydrocarbon radicals.<sup>58</sup> Boron doping is better controlled during CVD than HPHT resulting in a more consistent product. A gaseous carbon source (typically CH<sub>4</sub>) and a gaseous boron source (*e.g.* B<sub>2</sub>H<sub>6</sub> or B(CH<sub>3</sub>)<sub>3</sub>)<sup>89,90</sup> is fed into the CVD reactor. A plasma is created either by hot filament (HF-CVD) or microwaves (MW-CVD). HF-CVD enables diamond to be grown over a larger area but MV-CVD can produce higher quality diamond faster.<sup>41</sup> Excess hydrogen in the reactor etches any non-diamond carbon during growth.<sup>91</sup>

CVD offers the possibility of growing either single crystal or polycrystalline diamond (or BDD) material from single or polycrystalline growth substrates, respectively. As crystallographic orientation affects boron uptake, for polycrystalline BDD there is a heterogeneity in dopant density between grains.<sup>41</sup> The growth conditions control the grain size which can range from ultrananocrystalline (<10 nm) to microcrystalline (>μm).<sup>41</sup> Microcrystalline films can be grown to a thickness of hundreds of microns by increasing the growth time. At this thickness they can be removed from the growth substrate and are referred to as freestanding wafers.<sup>41</sup> Due to the increased growth time the resulting grains are larger and fewer. The BDD used in this thesis was grown by MW-CVD as freestanding, polished on the growth face (~nanometre roughness), polycrystalline BDD, doped to a metal-like conductivity (> 10<sup>20</sup> atoms cm<sup>-3</sup>).

### 1.3.1 Electrochemical Properties

BDD has a very wide potential window (> 3 V in 0.1 M KNO<sub>3</sub>, within a ± 0.4 mA cm<sup>-2</sup> threshold)<sup>41</sup> and low background currents compared to other common electrode materials, Figure 1.6. The sp<sup>3</sup> structure of the diamond surface is much more electrocatalytically inert than sp<sup>2</sup> bonded carbon and metals due to a lack of binding sites.<sup>41</sup>



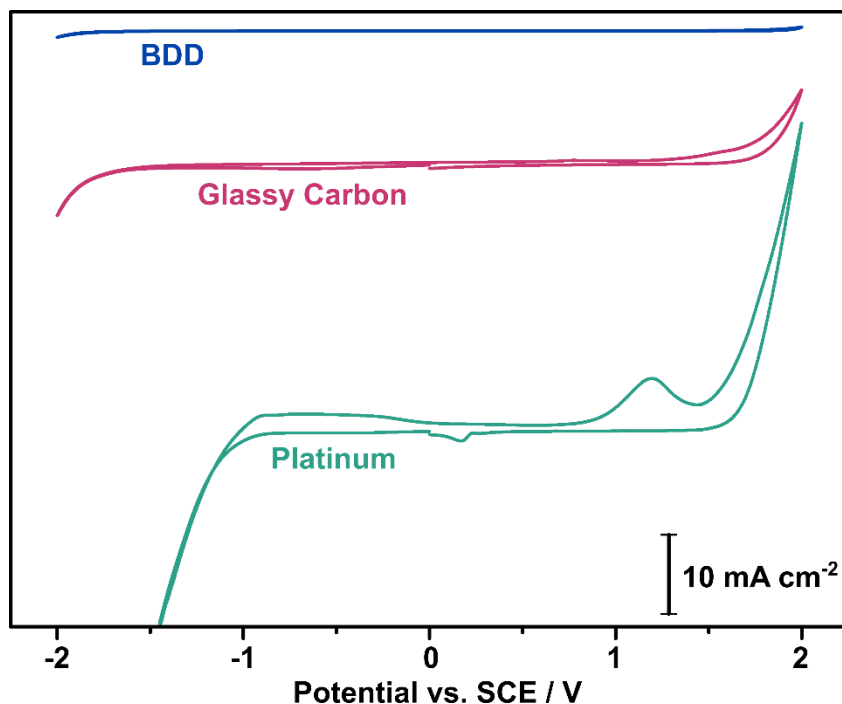


Figure 1.6 Comparison of solvent windows in 0.1 M  $\text{KNO}_3$  for BDD (blue), glassy carbon (pink) and platinum (green) electrodes.<sup>92</sup>

For inner sphere reactions, Figure 1.7a, such as water electrolysis and oxygen reduction, the lack of catalytic sites means the electron transfer processes are strongly retarded, and recorded electron transfer rate constants low. This gives rise to BDD's wide potential window and lack of oxygen signature, Figure 1.6. In contrast outer sphere reactions, where the reactant only needs to be in close proximity to the electrode surface, are less affected by the lack of catalytic sites on BDD, Figure 1.7b. The chemical stability of diamond, lack of surface processes and a lower density of states<sup>93</sup> results in low capacitive currents, giving rise to enhanced signal to noise ratios and allowing for more sensitive detection.<sup>41,58</sup> BDD maintains the extreme hardness, high thermal conductivity, very high melting point and resistance to chemical erosion of diamond. BDD is also considered a low biofouling material making it ideal for long term sensing applications.<sup>94-96</sup>

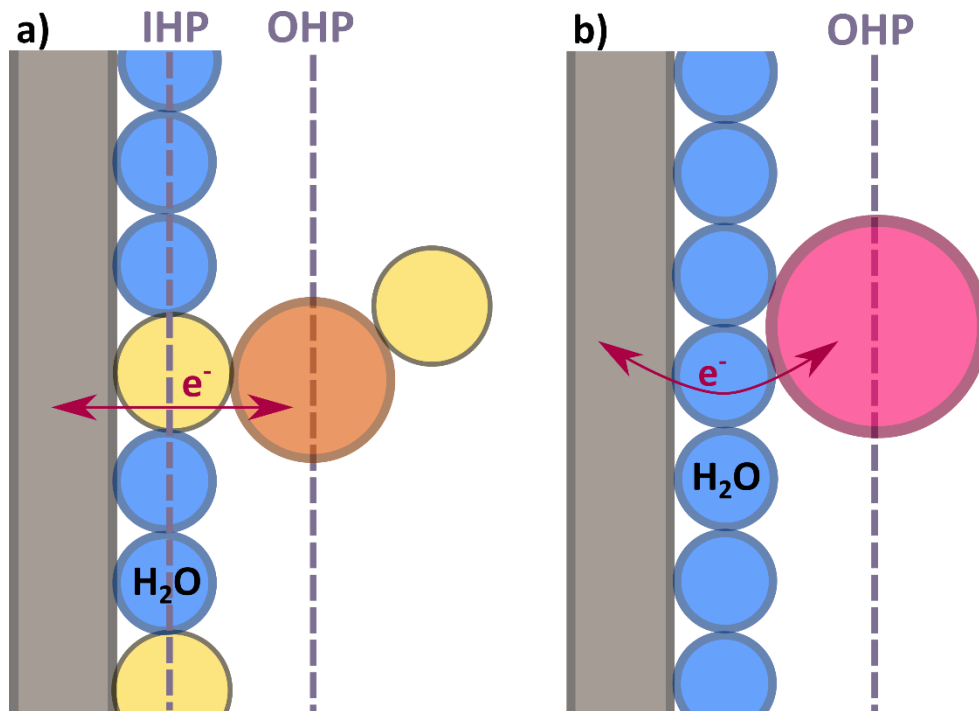


Figure 1.7 Schematic of an a) inner sphere reaction and an b) outer sphere reaction.

Ideally there would be no  $sp^2$  carbon present in a BDD electrode. However, it is very challenging, although not impossible, to exclude all  $sp^2$  carbon during diamond growth especially at high boron concentrations.<sup>41,92</sup>  $Sp^2$  carbon is commonly found at grain boundaries and for ultrananocrystalline and nanocrystalline films this can be a significant component of the electrochemical signal.<sup>97</sup> The presence of  $sp^2$  carbon increases the electrocatalytic activity of the surface<sup>98</sup> which is reflected in the electrochemical signatures observed, Figure 1.8. The potential window is reduced as water electrolysis is facilitated by the increase in electrocatalytic sites<sup>99</sup> and the capacitive current increases. The reductive window also shows reduction of oxygen on  $sp^2$  containing electrodes and oxidation of the  $sp^2$  can be observed in the oxidative window (Figure 1.8), both processes can further limit the potential window.<sup>41</sup>

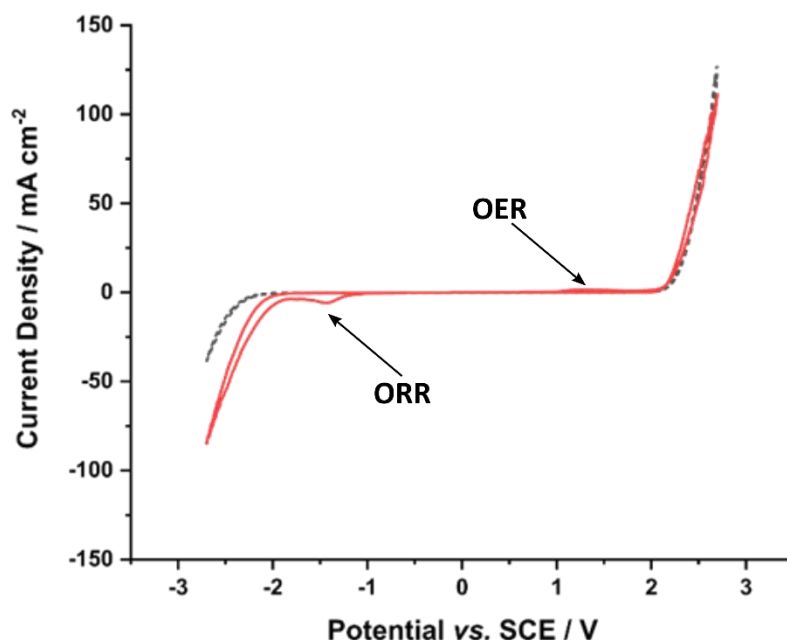


Figure 1.8 Solvent windows in 0.1 M  $\text{KNO}_3$  for BDD (black; dashed) and  $\text{sp}^2$  containing BDD (red; solid) arrows indicate increase in current associated with the oxygen reduction reaction (ORR) and the oxygen evolution reaction (OER).

For these reasons the presence of  $\text{sp}^2$  carbon in BDD was considered detrimental to the application of BDD electrodes. However, more recently the benefits of having  $\text{sp}^2$  carbon present in terms of increasing active adsorption, or redox active sites, has been shown to be beneficial for some applications. For example, previous work in the Macpherson group has shown that deliberate incorporation of  $\text{sp}^2$  carbon by laser micromachining can introduce pH sensitive quinone groups into the surface and enable simultaneous pH and oxygen measurements otherwise unachievable on BDD.<sup>69,100,101</sup>

## 1.4 Heavy Metal Detection

Heavy metals pose an interesting challenge for analytical chemistry. The term heavy metals is often used without proper definition, but is generally accepted as naturally occurring elements with a high atomic weight and density, at least five times greater than water.<sup>102</sup> Some less dense metals, non-metals and metalloids including aluminium, arsenic, beryllium and selenium are often grouped in with heavy metals as they can pose similar toxic effects.<sup>102</sup> Most heavy metals are believed to have a carcinogenic effect in the body.<sup>102,103</sup> Some heavy metals are

essential for life in small quantities,<sup>102,104</sup> but are toxic at levels above the optimum level required. The tolerable concentration of metals varies hugely depending on the element; the cut off values for Cu and Cr in blood are 1495 and 1.86  $\mu\text{g l}^{-1}$ , respectively.<sup>105</sup> Insufficient concentrations can also cause harm from deficiencies. Other heavy metals have no biological function and are toxic at low concentrations *i.e.* Pb which has a blood concentration cut off value of 2  $\mu\text{g dl}^{-1}$ .<sup>102,105</sup> This principle is shown visually in Figure 1.9. Detection, therefore, must be sensitive to sub ppb concentration and remain quantitative up to tens of ppm. Due to the widespread presence of heavy metals, analysis is undertaken from a range of samples including water, soil, pharmaceuticals<sup>106-108</sup> and food stuffs,<sup>109,110</sup> blood,<sup>111</sup> urine<sup>112</sup> and human hair.<sup>113</sup>

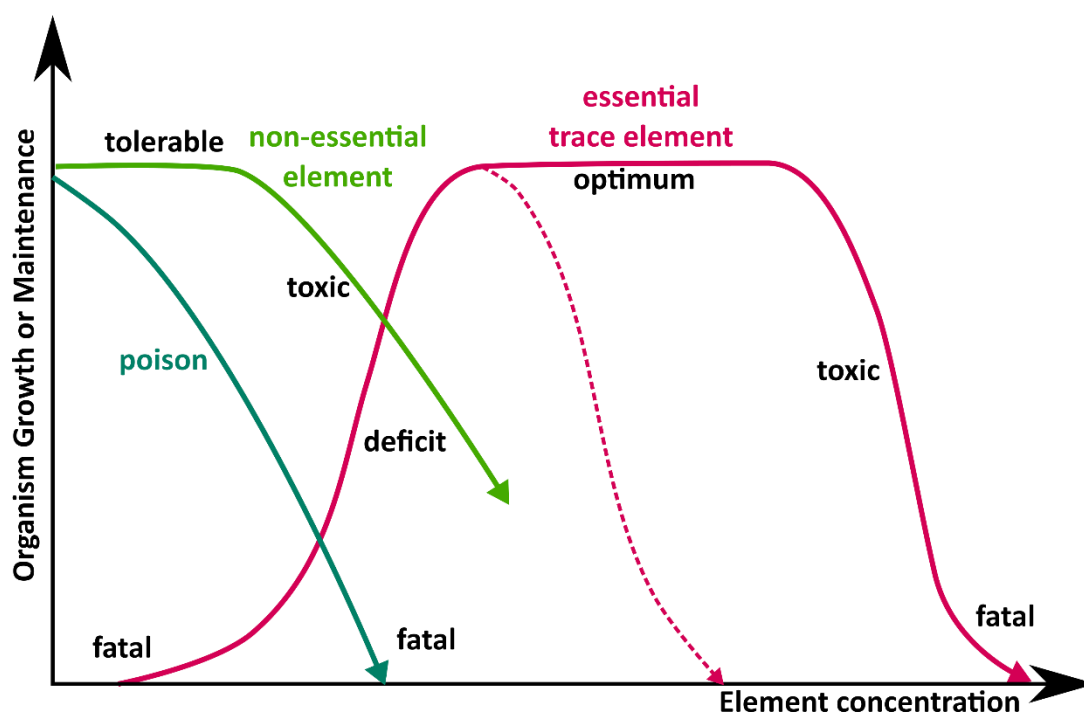


Figure 1.9 The effect of element concentration for poisonous (blue), non-essential elements (green) and essential trace elements (pink) for organism growth and maintenance. The optimum concentration range for essential elements can be broad (solid line) or narrow (dashed line) depending on the element.

Heavy metals occur naturally in the environment, it is possible for there to be naturally elevated background concentrations of metal species in soils and water bodies due to the local geology. Anthropogenic activities have led to an increase in the abundance of heavy metals within the natural system.<sup>102</sup> The most obvious source of metal pollution is from mining of metal ores and the associated refinement and waste disposal processes. Agricultural processes introduce

heavy metals from impurities in fertilisers, pesticides, wood preservatives and manure.<sup>114,115</sup> Industrial processes such as leather tanneries, paint production, battery manufacture, printing and corrosion of equipment can also cause metal pollution. Specific legacies can be observed such as elevated roadside lead concentrations from the use of leaded petrol in cars.<sup>116,117</sup> Water bodies, soils and sediments often act as pollutant sinks so monitoring is essential.

A number of heavy metals are found on the Environmental Quality Standards Directive List including As, Cd, Cu, Cr, Fe, Pb, Hg, Ni and Zn, which are highlighted as priority substances for assessment of water quality.<sup>118</sup> As heavy metals can bioaccumulate in plants and animals and bioconcentrate up the food chain analysis of primary sources remains a necessary indicator for entire ecosystem health.<sup>119</sup>

#### **1.4.1 Heavy Metal Speciation**

Ecochemical behaviour is determined by the physical and chemical state of an element. Properties are highly element specific and include solubility, mobilisation, sedimentation properties, bioavailability and toxicity. For example,  $\text{Cr}^{3+}$  is considered an essential trace element, required in the glucose tolerance factor essential for normal glucose metabolism.<sup>120</sup> In contrast,  $\text{Cr(VI)}$  is toxic as it is an oxidising agent and forms free radicals during reduction to  $\text{Cr}^{3+}$  inside cells.<sup>121</sup> Therefore presence of  $\text{Cr(VI)}$  is of significantly more concern than  $\text{Cr}^{3+}$ . As well as existing in different valence states metals can complex with other chemical species.

In natural environments heavy metals are found in a variety of forms. Whilst the simplest is the free hydrated metal ion, metals can also form complexes with organic and inorganic molecules, adsorb to colloidal organic and inorganic compounds, as well as being found in particulate mineral forms. For example, inorganic anions like  $\text{Cl}^-$ ,  $\text{SO}_4^{2-}$  and  $\text{HCO}_3^-$  and organic compounds such as humic and fulvic acids will complex with metal ions.<sup>122</sup> Al, Si, Mn and Fe oxides and clay minerals adsorb metals to their surface. Adsorbed metal – colloidal particles themselves have an environment dependent stability. Speciation is not only controlled by the presence of other chemical species but also by environmental

conditions such as water hardness, pH, oxygen availability, temperature, and microorganism metabolism.

Metal ions solvated with water molecules are generally more mobile, bioavailable and toxic.<sup>123</sup> Metals that are strongly bound to ligands or inorganic particles are often considered non-toxic or inert. Labile metal complexes have weakly coordinating ligands; the more labile the metal the higher the rate of ligand exchange. Understanding the speciation of the metal in the system of interest is important both from consideration of its toxicity and detection strategy.

### **1.4.2 Heavy Metal Detection Techniques**

Inductively Coupled Plasma Mass Spectrometry (ICP-MS) is the most commonly used heavy metal detection technique for freshwater environmental samples, whilst X-ray Fluorescence (XRF) is heavily used for geological samples, due to the much higher metal concentrations. Historically electrochemical techniques including anodic stripping voltammetry (ASV) with Hg electrodes showed significant promise for heavy metal detection.

#### **1.4.2.1 Inductively Coupled Plasma Mass Spectrometry**

ICP-MS is a hugely powerful analytical instrument with the ability to detect isotopes of 93 of the 118 elements, down to single ppt concentrations and across nine orders of magnitude.<sup>124</sup> Unsurprisingly, this capability comes from large, complex and expensive instrumentation that requires operation and maintenance by highly trained individuals in a laboratory setting.

ICP-MS analyses liquid samples, solid samples typically undergo an acid digestion process prior to analysis. An argon plasma is generated by passing argon gas through concentric quartz channels of an ICP torch wrapped at one end by a radio frequency induction coil. An electrical spark is applied to ionise the argon atoms, which in turn collide with more argon atoms, producing an inductively coupled plasma. The sample is introduced as an aerosol, produced in a nebuliser. When introduced to the plasma the sample is dried to a solid, heated to a gas and dissociated due to the extreme temperatures (~6000°C), as the atoms move through the plasma they are ionised. These ions are transferred into the mass spectrometer through a sampler cone, skimmer cone and, in newer models, a

hyper-skimmer cone. There is a significant pressure difference between the plasma, at atmospheric pressure, and the mass spectrometer. Creating a vacuum is essential to prevent collision with the ionised sample. Upon exiting the interface region the ion beam contains non ionised materials, neutral atoms and photons, it is necessary to separate the analyte ions before detection which is typically achieved using a quadrupole ion deflector. By placing the quadrupole at right angles to the ion beam, ions are transmitted to the mass spectrometer but neutrals and photons are removed. The mass spectrometer acts as a mass filter, separating the charged ions by their mass to charge ratio. Once exiting the quadrupole the ions strike the active surface of the detector, known as a dynode. The dynode releases an electron each time an ion strikes it, these are counted for each mass charge ratio considered, generating a measurable electronic signal.<sup>124</sup> This sequence is depicted in Figure 1.10.

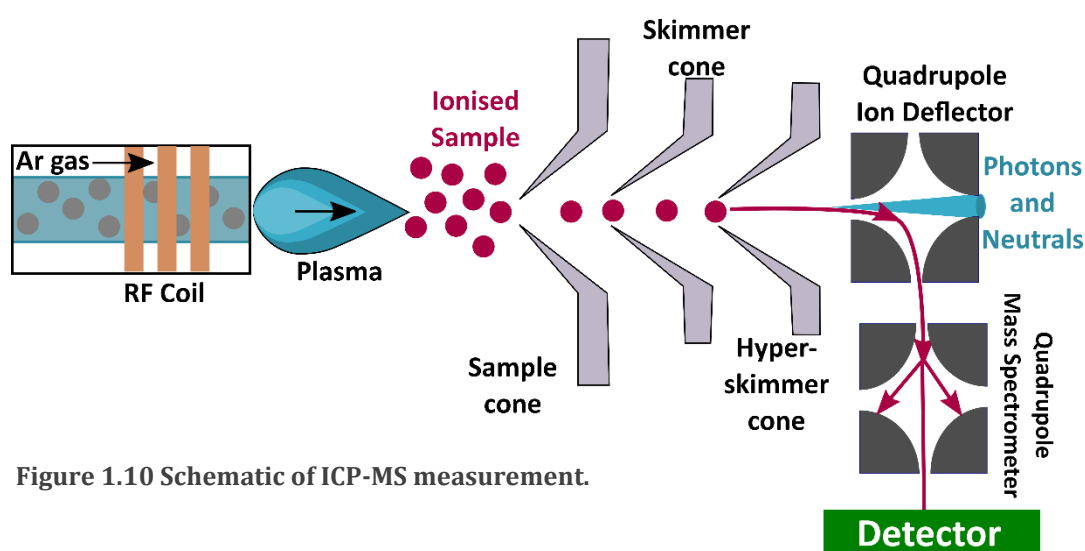


Figure 1.10 Schematic of ICP-MS measurement.

The sample matrix is important for ICP-MS analysis. The presence of dissolved solids can cause drift by precipitating in the nebuliser, overloading the plasma or blocking the sampling holes of the cones in the interface decreasing sensitivity and ultimately resulting in instrument down time. Therefore, all samples are filtered, typically through a 0.2  $\mu\text{m}$  filter, prior to analysis. Even in water, the simplest matrix for elemental analysis, problems can occur. For example, poorly soluble hydroxides and oxides can accumulate on internal components of the ICP-MS. This results in false readings and potential damage to the instrument.<sup>125</sup> Therefore, nitric acid at concentrations between one and five percent is typically

used for metal dissolution and stabilisation for ICP-MS analysis.<sup>125</sup> Such a low pH puts the metal ion in the hydrated water form. By coupling ICP-MS to other separation techniques such as gas chromatography, liquid chromatography or capillary electrophoresis speciation can be determined.<sup>126</sup> Development of sector field ICP-MS and multicollector ICP-MS are also advancing this field.<sup>127,128</sup>

#### 1.4.2.2 Anodic Stripping Voltammetry

ASV uses the ability to deposit ions onto the electrode surface and remove them again for detection purposes, Figure 1.11. A reducing potential is applied to the electrode for a defined period to reduce soluble metal ions in solution to metal on the electrode surface, Figure 1.11b. By using high mass transfer rates and prolonged deposition times even at trace levels, there is sufficient metal on the surface for subsequent detection.<sup>129,130</sup> This is termed pre-concentration. The detection step for ASV is also electrochemical. Ideally all the deposited metal atoms are oxidised from the electrode through the application of an increasingly positive (anodic) potential resulting in a peak shaped current response, Figure 1.11c. Peak position can be related to specific metals through consideration of the  $E^0$  of the redox couple, although this can be influenced by electrode material.<sup>47</sup> The peak area, for standard linear sweep waveforms, equates to charge passed and thus amount of metal on the surface,<sup>30,131</sup> but commonly peak height is used as the quantitative measure. Calibrations are determined either by plotting peak height (current) or peak area (charge) vs. concentration, allowing unknown concentrations to be determined.



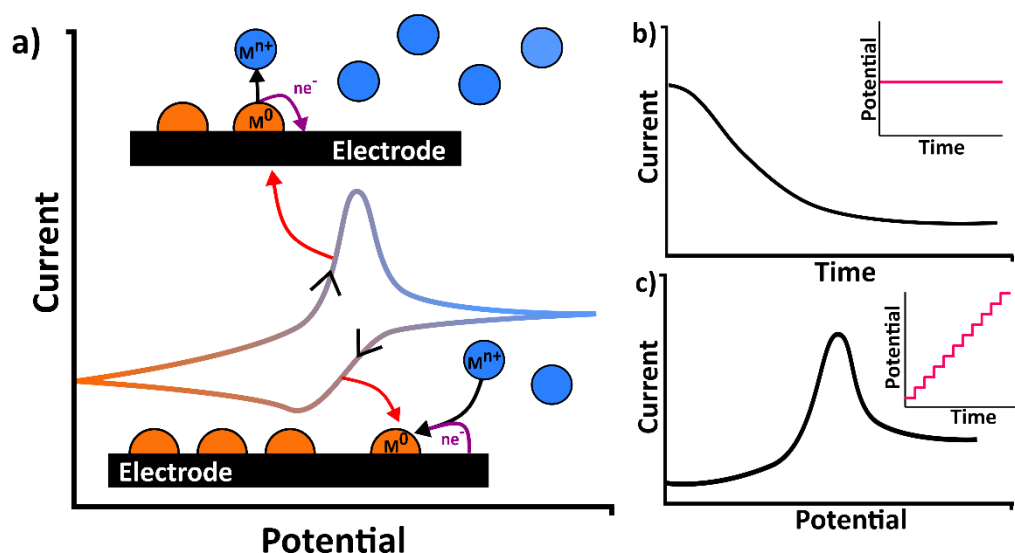


Figure 1.11 a) Exemplar cyclic voltammogram showing metal deposition (reduction) and stripping (oxidation). b) Exemplar current time trace for metal deposition and potential time waveform (inset). c) Exemplar metal stripping voltammogram and potential time waveform (inset).<sup>28</sup>

A large amount of work on ASV was undertaken with Hg electrodes, which resulted in narrow, symmetrical stripping peaks, the response of which could be analytically described.<sup>40,132,133</sup> As Hg can no longer be used, solid electrodes have been sought which possess as many of the favourable attributes of Hg as possible, including; retarded HER, low background currents, a reproducible surface and narrow stripping peaks whilst also exhibiting low toxicity. No general theory for metal stripping from solid electrodes has been found as the system is far more complex and experimental data often deviates from theory. Unlike Hg, which typically maintains its electrochemical characteristics upon electrodeposition,<sup>134,135</sup> the deposition of metals on solid electrode surfaces changes the surface characteristics to a combination of the original electrode properties and the properties of the deposited metal.<sup>28</sup> The potentials for deposition, HER and water reduction are altered, often occurring at less negative potentials. A range of morphologies can also be deposited due to the heterogeneous electrode surface. It is also important to consider alloying of metal electrodes with metal deposits, and intermetallic deposits between multiple deposited metals.<sup>136</sup> Different deposit morphologies can result in broader or multiple stripping peaks due to the slightly different potentials of oxidative dissolution.<sup>137</sup> Too much metal on the surface can also result in non-exhaustive

stripping, resulting in an underestimation of the metal present.<sup>28</sup> Such factors make interpretation of the stripping signatures challenging. However, a number of solid electrode materials have been investigated.

The Bi based electrode is one of the most popular metal electrode materials used for ASV.<sup>138</sup> Bi is typically used in thin film format, the Bi film electrode (BiFE), and is considered to be very similar in electrode characteristics to Hg, but importantly with lower toxicity. BiFE's give narrow, well resolved, reproducible stripping peaks, due to the ability of Bi to form solid metal alloys with a range of metals. Similar results have also been observed for Sb films.<sup>139</sup> The Bi film is typically generated by electrodepositing or co-depositing Bi with the analyte ions onto a carbon support electrode. The reason BiFEs are preferred over bulk Bi electrodes is most likely due to the film deposition/co-deposition process being an easy, reliable way of obtaining a reproducible surface. Bulk Bi has a slightly lower HER overpotential than the BiFE because of the differences in crystallinity between film and bulk, resulting in a smaller usable potential range.<sup>140</sup> Reproducibility is best when a new film is deposited each time.<sup>72</sup>

Carbon materials such as glassy carbon, carbon nanotubes, graphite (including highly ordered pyrolytic graphite, edge plane pyrolytic graphite, graphene and pencil lead) and carbon paste are also good electrode materials for ASV.<sup>53,141-143</sup> Carbon electrodes are more inert than metals and have low background currents, allowing them to also achieve lower limits of detection (LOD).<sup>41,144</sup> They are non-toxic so again are attractive for in vivo or general environmental and biological studies. Modification of carbon electrodes to improve sensitivity or selectivity in ASV is common place.<sup>144,145</sup> For example, conducting polymer layers containing surface molecules that chemically complex metal ions have enabled the simultaneous detection of Pb, Cu and Hg in the range  $10^{-7}$  to ca.  $10^{-10}$  M.<sup>146,147</sup> Useful ASV metal electrodes, such as Bi and Au have also been added to the carbon surface, typically as nanoparticles or a film by either electrodeposition<sup>71</sup> or chemical reduction methods.<sup>148</sup> However, the background signals are reduced as a result of a reduced amount of active metal on the surface leading to improved signal to noise ratios. The use of modified carbon electrodes for ASV applications has been extensively reviewed,<sup>53,141</sup> but one specific type of carbon electrode

worth further discussion is BDD for the characteristics already discussed in Section 1.3. Studies have shown that the stripping potentials for the metals Zn, Cd and Pb were not significantly shifted on BDD relative to Hg. Both electrodes were capable of metal detection over a concentration range of 3–4 orders of magnitude, with LODs in the low ppb range.<sup>142</sup>

ASV can be a very powerful tool for heavy metal detection reaching sub-ppb detection limits requiring less complex, smaller and low cost instrumentation. ASV has the capability of detecting around thirty elements, the bulk of which are metals.<sup>130,134</sup> In contrast to ICP-MS, ASV can provide information of the concentration of free and labile metals at the measurement pH of the solution; ICP-MS solutions require acidification. However measurement optimisation is often still required to ensure meaningful results are collected.<sup>28</sup>

#### 1.4.2.3 X-ray Fluorescence Spectrometry

XRF is a fast, accurate, non-destructive analytical technique applicable to solid, liquid, powder or thin layer samples requiring minimal preparation. XRF instruments range from large scale to benchtop to handheld devices offering highly accurate laboratory results to *in-situ* analysis. XRF has been used to study the elemental composition of a wide range of substrates from mineral composition,<sup>149–151</sup> crude oil,<sup>152</sup> fuels,<sup>153</sup> archaeological artefacts,<sup>151,154–156</sup> pharmaceuticals,<sup>157,158</sup> food tracability<sup>159</sup> and paint pigmentation.<sup>160,161</sup> Two spectrometer systems exist; energy dispersive (EDXRF) and wavelength dispersive (WDXRF), the main difference being in the detector systems.

X-rays are typically produced by X-ray tubes containing a filament and anode. The filament is heated by an electric current and electrons are emitted. X-rays are electromagnetic waves or beams of photons with an associated energy. When X-rays interact with matter there are three main paths; transmission, absorption or scatter. Scatter occurs with or without loss of energy, known as Compton or Rayleigh scatter, respectively. An X-ray photon with energy greater than the binding energy of an electron can expel an electron from an inner shell. This produces an unstable atom in an excited state due to the electron vacancy. To restabilise, an electron from a higher energy shell moves into the lower energy

vacancy and emits an X-ray photon (fluorescence) to balance the energy surplus. This process is depicted in Figure 1.12.

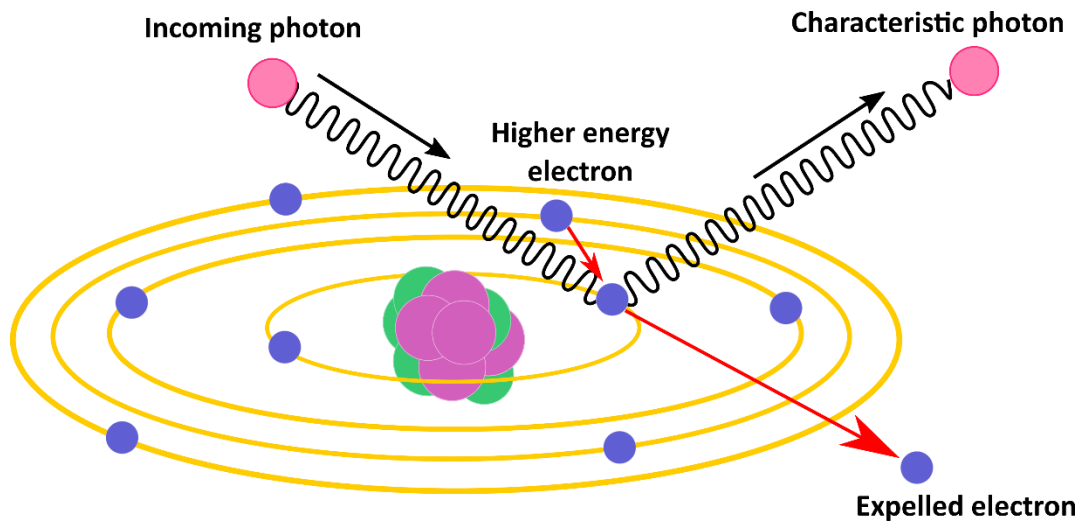


**Figure 1.12 Principle of fluorescence produced by x-rays in XRF**

Elements have specific energy levels, so the energy of the emitted photon is element specific and informs on the electron shells involved. Any electron can be expelled and replaced by an higher energy electron in the atomic structure resulting in a fingerprint of signals for each element. Absorption of radiation depends on the energy of the radiation, depth of atoms in the sample and sample density. Absorption can be so high only surface layers are analysed by this technique. For this reason thin, homogenous solid samples are best suited to XRF analysis.<sup>162</sup>

XRF has mostly been employed for analysis of solid samples. Liquid samples often have high background signals due to high x-ray scatter resulting in a poor signal to noise ratio. Typical limits of detection are in the parts per million range for conventional direct XRF systems, lacking the required sensitivity for some applications.<sup>162</sup> Sensitivity can be improved by the use of total reflection (TR)-XRF spectrometry, by using a low glancing angle ( $0.1^\circ$ ) the scatter and hence the background signal is reduced.<sup>163</sup> The detector can also be placed closer to the sample aiding sensitivity down to parts per billion.<sup>163,164</sup> However this can only be used on microliters of a sample. Another method to aid sensitivity with liquids is during the sample treatment or by using a preconcentration step. Preconcentration steps can be physical; evaporation<sup>165</sup> and freeze drying,<sup>166</sup> or

chemical; chelating ion exchange,<sup>167</sup> precipitation,<sup>168</sup> liquid-liquid extraction<sup>169</sup> and liquid-solid extraction.<sup>170</sup>

The concept of electrodeposition as a preconcentration technique for XRF analysis was first introduced in 2001 analysed by TR-XRF, but the focus was to interrogate deposition morphologies and distribution of the metals across the surface of an electrode rather than quantification.<sup>171</sup> As described in Section 1.4.2.2, electrodeposition uses a reductive potential to pre-concentrate metal atoms onto an electrode surface from metal ions in a solution. Previous work from the Macpherson group utilised this technique, termed electrochemical (EC)-XRF, to improve detection capabilities of XRF for metal ions in liquid samples. Forced convection methods i.e. rotating disc<sup>172</sup> and wall jet flow<sup>173</sup> were used to reduce pre-concentration times. This technique has also been applied to detection of palladium, a common catalyst used to synthesise pharmaceutical active ingredients, in pharmaceutical media.<sup>174</sup> BDD provides an excellent electrode for XRF analysis as the composition of boron and carbon atoms is undetectable, maintaining low background signals. However, the experimental systems used for the previous studies were extremely delicate and challenging to manipulate.

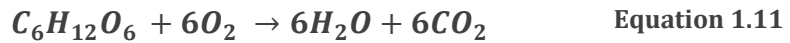
## 1.5 pH and Buffer Capacity

pH relates to the activity of protons in solution by Equation 1.10 providing a logarithmic scale for the effective acidity ( $\text{pH} < 7$ ) or basicity ( $\text{pH} > 7$ ) of a solution.

$$\text{pH} = -\log a\text{H}^+ \quad \text{Equation 1.10}$$

pH is an important factor for several reasons. Most natural systems have an optimal pH range within which an ecosystem can be sustained. Freshwater pH is generally between pH 6 and 9. Local geology can influence the pH of water, water bodies in limestone areas are more alkaline than those in sandstone areas. pH variation can also occur naturally, one example is diurnal pH fluctuations.<sup>175,176</sup> Aerobic respiration of flora and fauna in water bodies releases carbon dioxide into the water (Equation 1.11) which reacts with water molecules (Equation 1.12) and dissociates (Equation 1.13), decreasing solution pH. Rainfall is

naturally slightly acidic ~ pH 5 due to the interaction of raindrops with CO<sub>2</sub> and other acid forming chemicals naturally found in the air.

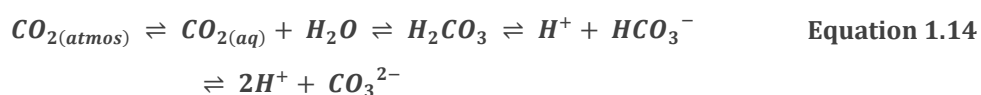


During the day, photosynthetic flora and algae remove CO<sub>2</sub> from water bodies resulting in a consumption of protons, (Equation 1.12 and Equation 1.13) and a corresponding increase in pH. This effect is more pronounced in some water bodies than others depending on rates of respiration and decomposition and on buffer capacity.<sup>175</sup>

Buffer capacity, also known as alkalinity or acid neutralising capacity, is the ability of a solution to resist a change in pH. It is an important property of water systems, those with a higher buffer capacity are more resilient to pH changes and therefore protect the ecosystem within the water body. Waters from anthropogenic sources can introduce pH changing ions, typically pollution related events including agricultural or industrial runoff, wastewater discharge, combustion of fossil fuels or mining and smelting. Acid mine drainage is a huge challenge for the environment around old mining sites. Water is pumped out of mines to allow access to material for mining by lowering the water table. When mines are no longer viable the pumps are shut off allowing the water table to rebound back to its natural level, thus exposing minerals to oxygen and water. Sulfide-bearing minerals, of which pyrite is the most commonly used example, are oxidised which results in release of protons and acidic water can enter streams and groundwater reserves.<sup>15</sup> Acid rain is formed from the release of sulfur dioxide and nitrogen oxides into the atmosphere through the combustion of fossil fuels and smelting of sulfide ores.<sup>177</sup> Once in the atmosphere sulfur dioxide and nitrogen oxides react with hydroxide radicals ultimately forming sulfuric and nitric acids. Sulfur dioxide can also dissolve in water droplets and dissociate to sulfuric acid. One of the lowest recorded acid rain values is pH 2.4 measured during a storm in Scotland in 1974.<sup>177</sup> Rapid acidification of aquatic environments, due to acid rain, was widespread in the late 20<sup>th</sup> century with

some severely affected waters retaining very limited buffer capacity after large acid inputs, increasing their vulnerability to significant pH changes in further acid rainfall events.<sup>178</sup>

One of the most alarming anthropogenically driven pH changes observed is that in the global oceans. Average surface oceanic pH prior to the industrial revolution was 8.2. As with most environmental systems, the ocean is predominantly buffered by carbonate. Oceans have absorbed roughly 40 per cent of emitted CO<sub>2</sub> since the industrial era,<sup>179,180</sup> and uptake rates have been increasing over the last decade due to changes in ocean circulation,<sup>181</sup> perturbing the carbonate buffer equilibrium (Equation 1.16);



This results in increased proton concentrations, causing ocean acidification. The average surface oceanic pH is now 8.1 with projections of a further 0.3-0.4 pH drop by the end of the 21<sup>st</sup> century.<sup>4</sup> Increasing proton concentrations result in the conversion of carbonate ions to bicarbonate, which also has implications for calcifying marine life due to a reduction in abundance of carbonate and the potential for shell dissolution.<sup>3,4</sup>

### 1.5.1 Methods of pH measurement

Measuring solution pH accurately is not only extremely important from an environment viewpoint but has a huge influence on other solution chemical processes, such as chemical speciation. pH can be measured by a variety of techniques.

#### 1.5.1.1 Optical

Optical pH sensors rely on a pH dependent response towards the absorbance, luminescence or fluorescence of a colorimetric reagent.<sup>182-184</sup> pH indicator dyes used for optical pH sensing are typically weak acids or bases with distinct optical properties in their protonated and deprotonated forms. The relative concentrations of the protonated and deprotonated forms are measured and used to determine the pH of the solution.<sup>182</sup> Colorimetric pH indicators include phenol red,<sup>185</sup> phenolphthalein<sup>186</sup> and bromocresol green.<sup>187</sup> Fluorescent pH indicators such as fluorescein<sup>188</sup> and 1-hydroxypyrene-3,6,8-trisulfonic acid<sup>189</sup>

offer better sensitivity and selectivity than colorimetric indicators.<sup>184</sup> Most optical pH sensors immobilise the indicator in a proton-permeable solid matrix.<sup>184</sup>

Optical pH sensors can be miniaturised, do not require a RE, offer high selectivity and sensitivity, potential for continuous measurements, low energy consumption and low production costs. However, the sigmoidal response of these dyes over a narrow working range, commonly 2 pH units, limits their applicability. They are commonly used for physiological investigations, including *in vivo* studies, where only a narrow working range is required.<sup>182</sup> Work is on-going to increase the range by the use of polyprotic dyes,<sup>190</sup> pH-triggered aggregation induced emission,<sup>191</sup> multilayer adsorption of indicators<sup>192</sup> or mixtures of indicators across different pH ranges.<sup>193</sup> Optical pH sensors have a limited long term stability due to photobleaching or leaching of the dye, making them best suited to single use sensors.<sup>184</sup> Temperature and ionic strength variations can also cause errors.<sup>182,184</sup>

#### 1.5.1.2 Glass pH probes

Glass pH probes are the most prevalent pH sensor and are based on electrochemical principles. Fundamentally, the glass pH probe is a hydrogen ion selective electrode, allowing a large measurement range (pH 2 – 12), high sensitivity and a fast response time. Glass probes consist of a glass bulb membrane which separates two silver/silver chloride REs. One is placed in the internal filling solution, the other in the solution of interest (Figure 1.13). The thin glass membrane is comprised of amorphous silicon oxide embedded with oxides of alkali metals. When exposed to water a hydrated layer forms and the silicon oxide groups become protonated, achieving equilibrium with the pH of the inner filling solution and outer test solution (Figure 1.13). The potential difference across the glass membrane, Equation 1.17, relates to the pH of the test solution.<sup>194</sup>



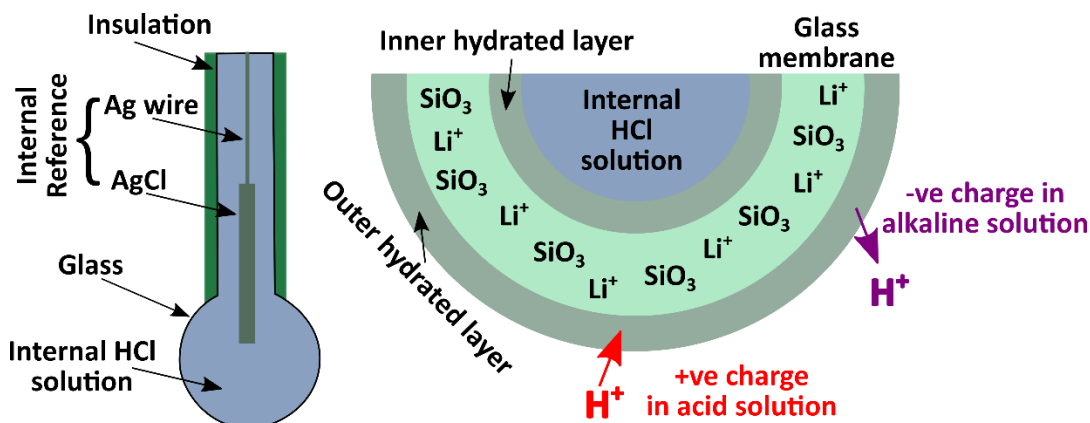


Figure 1.13 Schematic of glass pH probe.

A predicted Nernstian response of 59 mV per pH unit is expected at  $T = 298 \text{ K}$  (Equation 1.17). As temperature is important to an accurate measurement most pH probes have an in-built temperature probe and automatically correct for temperature.

$$E = E^0 - \frac{2.303 RT}{nF} pH \quad \text{Equation 1.15}$$

The glass electrode, however, has several limitations. The thin glass membrane is highly fragile and relatively large limiting its usefulness in some applications. The membrane must be hydrated prior to use, although less complex maintenance of modern probes is required than for historical probes. Interferences from alkali metals, due to their similar charge and size to protons, can cause erroneous measurements. In solutions of concentrated alkali hydroxides activity of protons is reduced meaning equilibrium takes a while to establish. Strong alkaline solutions and fluoride ions can etch and permanently damage the glass. Proteins can adsorb onto the glass, and metal ions could reduce and deposit onto the glass surface, both altering the membrane surface. Whilst the glass pH probe has had some refinements, little has changed in the hundred years since its development.

### 1.5.1.3 Metal oxides

Various proton sensitive metal oxide probes have emerged for pH sensing, of which ruthenium oxide and iridium oxide have received the greatest attention showing a close to Nernstian response and high degree of accuracy.<sup>195-200</sup> Sensitivity of metal oxide sensors depends on the composition and deposition method as porosity, surface homogeneity, film thickness and crystalline structure of the material affect the performance. Metal oxide sensors are low cost, easy to miniaturise but can be slow to respond, show large drift, can be difficult to handle and may require some form of hydration before use.<sup>200</sup>

Metal-metal oxide based pH sensors have also been trialled based on antimony and bismuth, utilising a pH sensitive redox equilibrium but they have a limited sensing range, are sensitive to redox agents and oxygen and show poor reproducibility and stability.<sup>38,200-202</sup>

### 1.5.1.4 Ion-Selective Field Effect Transistors

In ion-Selective Field Effect Transistors (ISFET), two semiconductor electrodes, a drain and a source, are connected by a third electrode, the gate electrode which is in contact with the solution and contains a proton sensitive chemical layer. Protons reside at the surface of the gate electrode in equilibrium with the solution. The presence of the protons produces an electric field that controls the current flowing between the source and the drain.<sup>203,204</sup> The resulting potential has a Nernstian dependency on pH (Equation 1.15). ISFETs are more structurally stable than glass pH probes, can be stored dry, are small, have a fast response time and show reduced alkaline errors. However, there remain some inherent issues with the ISFET technology, for example, voltage instability, which has limited the commercial viability of ISFETs,<sup>205</sup> exposure to chlorine and other aggressive chemicals can permanently damage the ISFET device and sediment rich samples can block the IFSET.<sup>206</sup>

### 1.5.1.5 Quinone based pH sensing technologies

Quinones (Q) are a class of oxidised derivatives of aromatic compounds that undergo proton coupled electron transfer (PCET). The different possible PCET pathways reaction can be summarised by the general scheme of squares displayed in Figure 1.14.<sup>207</sup>

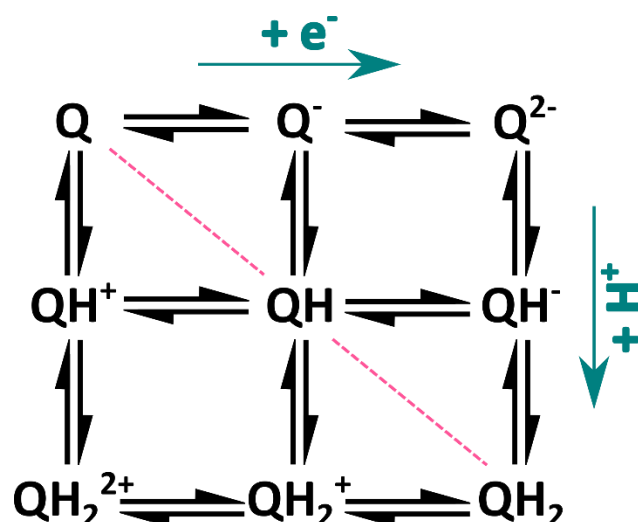


Figure 1.14 Quinone scheme of squares showing possible electron and proton transfer reactions. The proton coupled electron transfer regime is indicated by the pink dashed line.

In aprotic solvents only electron transfer is possible *i.e.*  $Q + 2e^- \rightleftharpoons Q^{2-}$ , showing two well defined redox peaks.<sup>208</sup> In buffered aqueous media, PCET of  $2e^-$ ,  $2H^+$  results in formation of hydroquinone as the final product.<sup>207</sup> Due to the inclusion of protons in the redox process the redox potential is pH dependent with peak potentials increasingly negative as pH increases. PCET can occur either in a stepwise manner with either electron or proton transfer occurring first or as one concerted step.<sup>207,209</sup> The transfer of the second electron and proton is thermodynamically more favourable than the first, known as potential inversion.<sup>210</sup> This potential inversion, causing the relative instability of QH in aqueous media, results in the observation of a single redox peak. Under PCET conditions the pH dependent voltammetric shift is  $59 \text{ mV pH}^{-1}$  as calculated by the Nernst equation (Equation 1.16) provided the first  $pK_{a1}$  is not exceeded;

$$E = E^0 + \frac{0.0592}{2} pH \frac{[Q]}{[QH_2]} - 0.0592 pH \quad \text{Equation 1.16}$$

As pH increases beyond  $pK_{a1}$ , and  $QH^-$  is the final product, the quinone undergoes a  $2 e^-$ ,  $1 H^+$  reaction and the voltammetric shift is  $30 \text{ mV pH}^{-1}$ . When  $pK_{a2}$  is exceeded resulting in the product  $Q^{2-}$ , the reaction is pH independent, as in the case with aprotic solvents.<sup>207</sup> This reaction scheme is shown in Figure 1.15. For pH sensing the PCET reaction is preferable, as this shows the highest sensitivity. In unbuffered solutions PCET can alter the local pH, as protons are locally removed (or released) during the electrochemical measurement, which can lead to erroneous measurements.<sup>207</sup>

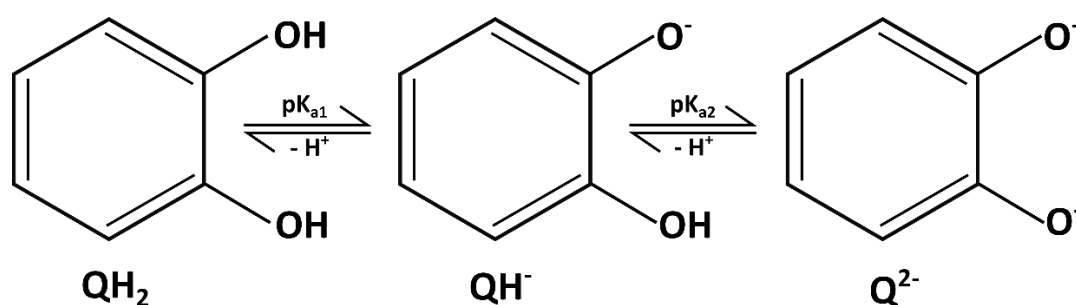


Figure 1.15 Quinone deprotonation reactions showing  $pK_{a1}$  and  $pK_{a2}$

Carbon electrodes, that are otherwise not pH sensitive, can be functionalised to contain pH sensitive groups, such as quinones by chemical oxidation, covalent bonding, physical absorption, film formation or using composite electrodes (immobilisation of graphite with a binder material onto the surface of carbon electrodes).<sup>211</sup> However quinones introduced by these mechanisms can be removed easily *e.g.* during cleaning the electrode via mechanical abrasion.<sup>211</sup> Furthermore, functionalisation is often time consuming and complex requiring numerous reagents.<sup>211</sup>

An alternative approach is to use  $sp^2$  bonded carbon electrodes which contain quinone groups naturally integrated into the surface, such as glassy carbon, edge plane pyrolytic graphite, and screen printed electrodes.<sup>212–214</sup> One emerging technology, developed by the Macpherson group, is a BDD pH sensitive sensor where the  $sp^2$  bonded carbon has been integrated into the surface using laser micromachining and subsequent chemical oxidation. The BDD-Q electrodes display a Nernstian pH sensitive response across the buffered pH range 2 – 12,<sup>69</sup> due to the high  $pK_{a1}$  of the surface bound quinones.<sup>100</sup> Figure 1.15 depicts a 1,2-benzoquinone, the exact form of quinone on the BDD-Q electrode is unknown. By

optimising the potential scanning waveform and quinone surface density, the sensor has also been utilised for pH sensing in unbuffered conditions with convincing linearity.<sup>100</sup>

### 1.5.2 Methods of Alkalinity Measurement

Alkalinity is the measurement of buffer capacity which relies on precise pH measurement. Measurement of alkalinity involves monitoring the pH change of a solution whilst a form of pH adjustment is employed. The most utilised measure of alkalinity is a standard titration. A measured volume of a known concentration of acid or base is controllably added to a known volume of the solution of interest. The pH change is monitored using a colorimetric indicator or measured using a glass pH probe.<sup>215</sup> For titrations two different end points are commonly used to identify the contribution of carbonate alkalinity ( $\text{CO}_3^-$  and  $\text{OH}^-$ ) and total alkalinity ( $\text{HCO}_3^-$ ); phenolphthalein or a measured pH of 8.3 is used as a measure of carbonate alkalinity, methyl orange or a measured pH of 4.5 is used as a measure of total alkalinity.<sup>216</sup> Spectrophotometric analysis alongside colorimetric pH sensitive indicators have also been demonstrated for single point and monitored titrations in seawater.<sup>217-219</sup>

Titrations where the pH change is measured with the addition of acid or base are more accurate than colorimetric indicators as they measure the pH of the sample rather than an optical response to pH. Depending on the indicator a colour or fluorescence change may be subtle, and therefore harder to detect. Measured pH changes can be closely monitored and this is, therefore, the standard procedure. A typical titration curve for measured pH against added proton concentration is shown in Figure 1.16. The plateau where pH remains stable shows the solution remains well buffered. Once the buffer capacity is overcome, a rapid pH change is observed. The more acid added before the pH change the greater the buffer capacity and higher the alkalinity. Titration data is most commonly handled by the Gran method<sup>220</sup> or a nonlinear least sum of squares.<sup>215,218</sup>

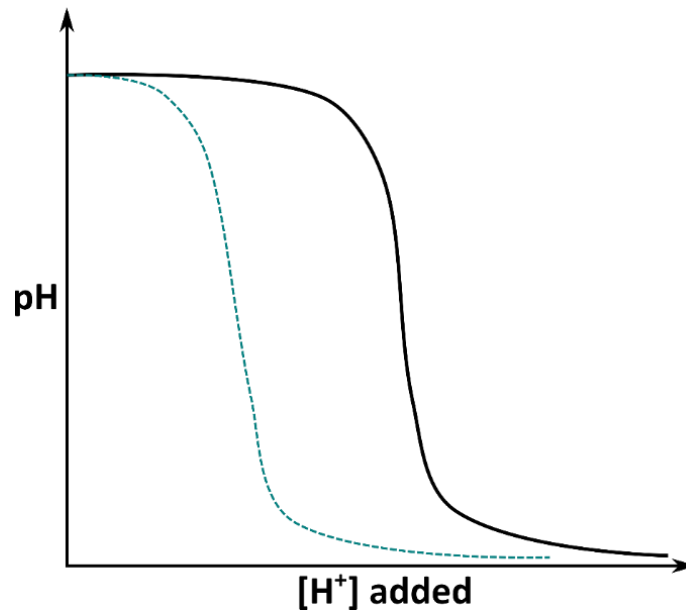


Figure 1.16 Titration curve for a buffered solution (black solid line) and a less buffered solution (blue dashed line)

## 1.6 Microbial Biofilms and the impact on sensors

Microorganisms play a key role in the global ecosystem through cycling of nutrients. Microbes have been found in every corner of the planet, from desert soils in the Antarctic Dry Valleys<sup>221,222</sup> and the Atacama Desert<sup>223</sup> to glaciers<sup>224</sup> and deep sea sediments.<sup>225</sup> Microorganisms were long thought of as planktonic, freely suspended cells. However, this is an artefact of pure culture microbiological studies in nutrient rich media selecting uncoated mutants.<sup>226</sup> Many bacteria have the ability to form an assemblage of microbial cells, enclosed in an extracellular polymeric substance (EPS), composed of polysaccharides,<sup>227</sup> attached to a surface, known as a biofilm. Van Leeuwenhoek is credited with discovering the first microbial biofilm from tooth surfaces using a light microscope.<sup>228</sup> Subsequently, observations of enhanced bacterial growth on surfaces compared to the surrounding media were reported.<sup>229,230</sup> However, it was not until the invention of electron microscopes that a detailed examination of biofilms could be performed.<sup>228</sup>

### 1.6.1 Biofilm Formation

In 1990 Characklis and Marshal described the formation of a biofilm to maturity, as depicted in Figure 1.17.<sup>231</sup>

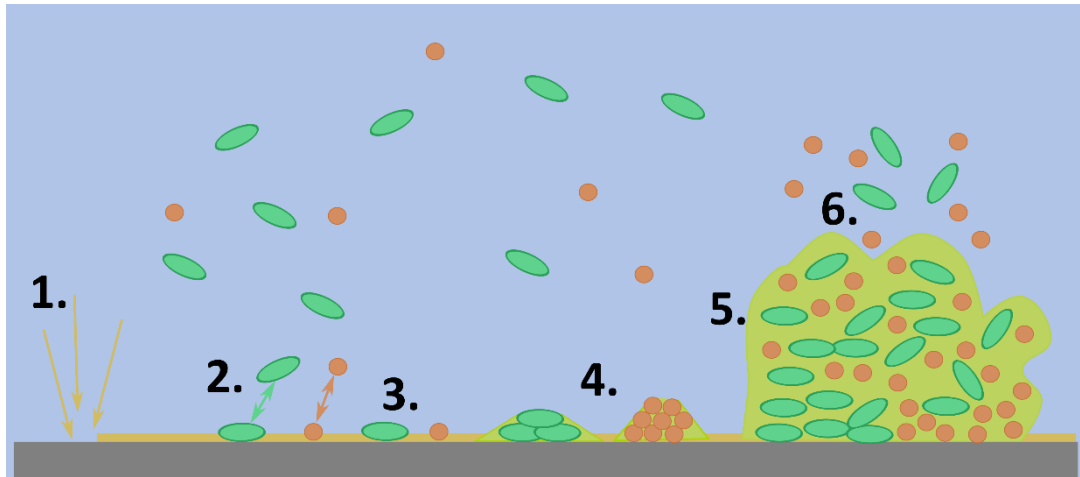


**Figure 1.17 Schematic of the stages of biofilm formation. 1. Formation of a conditioning film, 2. Reversible adhesion, 3. Irreversible adhesion, 4. Microcolony formation and beginning of EPS excretion, 5. Mature biofilm and 6. Dispersal of daughter cells for further colonisation.**

Prior to any microbial interaction with a surface a conditioning layer is formed consisting of adsorbed (macro)molecules, both organic and inorganic, derived from the liquid media in which they are submerged. This layer provides nutrients for the biofilm but can also modify the surface properties of the substrate.<sup>232</sup> Hydrophobicity, surface roughness, charge and functional groups can all affect biofilm formation.<sup>228,232-235</sup>

Planktonic cells are transported to the surface from the bulk liquid either by physical forces, including Brownian motion, convective mass transport and sedimentation, or by motility using bacterial appendages such as flagella.<sup>235</sup> Once the cells are close to the surface initial attachment occurs through Van der Waals forces, electrostatic forces and hydrophobic interactions.<sup>236-238</sup> Bacteria sense their proximity to a surface and appear to ‘explore’ the surface with species specific behaviours.<sup>239-242</sup> At this stage cells can easily be removed by fluid shear forces, hence the term reversible adhesion.<sup>243</sup> Cells then either detach or initiate irreversible adhesion by overcoming repulsive forces which prevent the main body of the bacterial cell making contact with the surface. Contact can be made through cellular appendages; flagella, fimbriae, pili and EPS fibrils. As a result, stronger interactions between the cell and the surface are formed, including

dipole-dipole interactions, covalent, ionic and hydrogen bonding as well as hydrophobic interactions.<sup>244</sup> Poortinga *et al.* observed electron transfer between the cell and the substrate surface which resulted in stronger cell adhesion.<sup>245</sup>

Once irreversibly attached the bacterial cells grow and divide laterally and vertically forming cell clusters.<sup>246</sup> Nutrients from the surrounding liquid and the conditioning film are utilised.<sup>235</sup> Microcolonies enlarge and coalesce with other microcolonies to form a layer of cells covering the surface. During the period of growth EPS is produced, helping anchor the colony to the surface and stabilise the environment. EPS is initially observed as thin fibres which increase in thickness over time to form the biofilm matrix. Other inorganic or organic substances and particulate matter become entrapped in the EPS alongside microbial products and microorganisms.<sup>244</sup>

The final stage of biofilm formation is dispersal, where cells return to the planktonic state for further colonisation. Daughter cells are released individually, triggered by decreases in nutrient levels or by quorum sensing. Larger aggregates can also be removed by flow effects.<sup>228,239,244</sup>

Understanding of biofilms has advanced significantly in the last 50 years and the advantages of this life form are multifaceted. The 3D structure of the EPS protects cells against desiccation and predation, whilst allowing nutrients and oxygen into the biofilm and a waste removal route. Steep gradients of electron acceptors and producers, pH and redox conditions exist in biofilms due to the heterogeneity of activities, producing a diverse range of habitats, and therefore a diverse community, within a very small area. Extracellular enzymes are stored within the EPS effectively acting as an external digestive system for the cells.<sup>247</sup>

### **1.6.2 Biofouling**

Biofilms are a major cause of biofouling, which is the accumulation of unwanted biological material. Biofouling is a significant obstacle to long term *in-situ* sensing in water based systems in the environment. This is particularly problematic for electrochemical sensors where electrode-solution interactions govern the measurement. Using low fouling materials with properties that make bacterial adhesion more difficult, *i.e.* smooth hydrophilic surfaces, can increase the time period before biofouling has detrimental effects. A recent study showed that



polished, free-standing, O-terminated, hydrophilic BDD slowed down biofilm growth the most compared to roughened or H-terminated, hydrophobic diamond and other common sensor and packaging materials over the same time period.<sup>95</sup> This concurs with other biofouling studies on BDD making it an interesting substrate to explore further.<sup>94,96</sup>

### **1.6.3 Quantification and visualisation of biofilms**

Technological advances in experimental methodology over the last 50 years has enabled our understanding of biofilms to develop. Biofilm composition, viability and quantification can be analysed by physical, chemical, microbiological and molecular techniques. Visualisation of biofilms using microscopy is also very common and is sometimes used in conjunction with quantification techniques to provide a better understanding of the structure.

#### **1.6.3.1 Microbiological and molecular methods**

The most widely used microbiological technique for estimation of biofilm cell viability is the determination of colony forming units (CFUs) on agar media. Utilising the universal dilution series approach to quantify cell numbers, any microbiological laboratory can run CFUs with relatively little expense. This method selects culturable species that will grow on agar, however viable but non-culturable cells could be present and therefore not represented. Additionally the sample plated may not be representative of the complex biofilm structure.<sup>248</sup> Flow cytometry coupled with fluorophores has been used to determine biofilm cell viability by allowing differentiation between total, dead and viable but non-culturable cells.<sup>249,250</sup> This method is significantly faster and more accurate than CFUs.

Molecular methods including quantitative polymerase chain reaction (qPCR) can be utilised to estimate the number of viable cells. To avoid overestimation, the extracellular DNA in the matrix and DNA in dead cells can be bound by propidium monoazide, prior to extraction, to ensure only DNA from viable cells is amplified.<sup>251</sup> Recent work on RNA based qPCR proposes not only quantification of species but also gene expression within the biofilm.<sup>252</sup> qPCR methods are fast and enable quantification of all species from one sample but they are expensive to conduct.<sup>248</sup>

### 1.6.3.2 Physical methods

Total biofilm biomass measurement can be obtained from dry or wet weight measurements. The difference in weight between the clean dried substrate before biofilm formation and the dried substrate with biofilm can be attributed to biofilm biomass. Volumetric biofilm density can be calculated as a unit of dried biofilm mass per unit of wet volume.<sup>253</sup> Alternatively, substrates with attached cells were vortexed to release the biofilm components, the liquid was filtered and the weight of the filter measured and compared to an unused sterile filter.<sup>254</sup> However this assumes all of the biofilm is removed and none is lost through the filter. Both methods are time consuming and have low sensitivity and accuracy.<sup>248</sup>

### 1.6.3.3 Chemical methods

Chemical methods utilise dyes or fluorophores that bind to or adsorb onto biofilm components. Crystal violet staining is the most frequently used quantification technique in microtitre plate assays.<sup>255-257</sup> In aqueous environments the crystal violet stain dissociates to CV<sup>+</sup> and Cl<sup>-</sup> ions that can penetrate through the wall and membrane of eukaryotic cells. The CV<sup>+</sup> ion interacts with negatively charged molecules within the cell including DNA and proteins.<sup>258</sup> This interaction can occur in both live and dead cells and any negatively charged molecules in the matrix. Therefore, crystal violet staining is applicable to total biofilm biomass measurements.<sup>259,260</sup>

Classically, biofilms are grown in the wells of polystyrene microtitre plates. Wells are emptied and washed to remove planktonic cells at various time points. Adhered cells are stained with crystal violet, and quantification can be achieved by detachment or stain solubilisation. Whilst crystal violet staining is an indirect measurement method three main advantages are offered: (1) the stain is compatible with a broad range of bacterial species and eukaryotic cells; (2) microorganisms can be analysed in the wells avoiding any bias with detachment or viable but non-culturable cells; and (3) high throughput capabilities allowing for rapid testing and assessment of many different conditions simultaneously. Though there are some limitations to the technique. The washing steps are critical, whilst they may introduce some bias by removing loose biofilm, washing

is necessary to remove sedimented or adhered planktonic cells which are not part of the biofilm. Therefore, there can be some inherent variability and a lack of reproducibility with the method. Despite being so frequently used there is no standard procedure for the crystal violet assay making comparison between studies difficult.<sup>248</sup>

Quantitative analysis of cellular metabolic activity can be probed by alternative dyes such as XXT, TTC and resazurin (also known as Alamar Blue).<sup>248</sup> Resazurin has advantages over the other salts mentioned such as ease of visualisation with spectrophotometric or spectrofluorescent techniques, low cost, low toxicity to eukaryotic cells, relatively rapid protocols and good correlation of results with CFU counts. However the limit of quantification is quite high which reduces its sensitivity, and there is variation in the metabolism of resazurin between species requiring optimisation of incubation periods for multispecies films.<sup>248,261-263</sup> Colourimetric methods to quantify EPS, total proteins and carbohydrates have been applied, however EPS components do not necessarily correlate with biofilm biomass.<sup>248</sup>

#### 1.6.3.4 Optical and fluorescence microscopy

Optical microscopy refers to techniques utilising the visible light range of the electromagnetic radiation spectrum to illuminate an object and magnify the image through optical lenses. Low magnification and resolution of optical microscopes allow for imaging of larger areas of sample providing an extensive analysis of coverage. Although sample preparation for optical microscopy is simple the cells do require staining and discriminatory detail is lacking.<sup>248,264</sup>

In fluorescence microscopy an external light source is used to stimulate secondary illumination by the sample itself, either by natural fluorescence or by fluorescent stains. Fluorescence is the property of a molecule to emit light of a longer wavelength when irradiated by a light of a shorter wavelength. Four staining procedures have been extensively used in biofilm research. (1) Fluorescent *in situ* hybridisation probes are single stranded DNA or RNA fragments with a fluorescent marker attached. The fragments hybridise with the complimentary sequence in a microbial cell. For biofilm analysis this requires immobilisation of the biofilm in epoxy resin which is subsequently sliced thinly

before the probe is added and analysed by fluorescence microscopy. (2) Fluorescent proteins isolated from naturally fluorescent organisms are added to cells on a plasmid, commonly with an antibiotic resistance gene. Genetic encoding is used to tag specific microorganisms with fluorescence of a specific colour. For study of suspended microorganisms the cells are cultured on agar containing the antibiotic the plasmid has a resistance gene to ensure any cells that grow can express the fluorescence protein. For biofilms, and mixed cultures this becomes more challenging, as all the microorganisms would have to be tagged with antibiotic resistance. Fluorescent proteins also require oxygen to fold properly, another issue for their use in biofilms. Therefore the use of fluorescent proteins for biofilm analysis is limited. (3) Live/dead staining provides the opportunity to assess the viability of cells *in-situ* in the biofilm. A dye that will stain all cells is added *i.e.* Acridine orange which emits a green fluorescence when bound to nucleated cells. A second stain that can only enter cells with damaged membranes, such as dead cells, is also added *i.e.* propidium iodide which emits red fluorescence. The fluorescence of the dead cell stain will quench the universal stain allowing for identification of live and dead cells in the matrix. (4) Fluorescence staining to investigate EPS has been used. However, there is no universal stain as the biofilm matrix is a complex mixture of compounds. Therefore analysis of matrix compounds or combinations of compounds are the best that can be achieved.<sup>264</sup>

Confocal laser scanning microscopy (CLSM), although not inherently a fluorescence microscope, is often used in conjunction with fluorescent dyes and probes for biofilm analysis. CLSM only detects fluorescence from the focal plane of the microscope lens thus avoiding the out of focus blur of conventional microscopes. The depth of the focal plane can be changed by moving the stage vertically and the raster image of each focal plane combined to build a 3D picture of a sample, however this process is slow. This 3D imaging has been particularly beneficial to the understanding of biofilms.<sup>248,264,265</sup>

#### 1.6.3.5 Electron Microscopy

Electron microscopy uses beams of electrons to illuminate a sample instead of light. There are two main types of electron microscopy; transmission electron

microscopy (TEM) and scanning electron microscopy (SEM). Both utilise an electron gun, equipped with a heated tungsten or lanthanum hexaboride element, to produce the primary electrons. In TEM the electron beam is condensed and focused through a series of lenses and accelerated towards the sample, the electrons penetrate the sample. Some collide with atoms in the sample and scatter, producing dark areas, and others remain unscattered and produce bright areas. In SEM the electrons are accelerated into an energetic beam as they pass an anode, an electromagnetic coil acts like a lens to focus the beam and another coil steers the beam across the sample, effectively scanning the surface (Figure 1.18). Although considered a surface analysis technique the electrons do penetrate the surface of the sample producing secondary electrons, backscattered electrons or X-ray photons depending on penetration depth.<sup>264</sup>

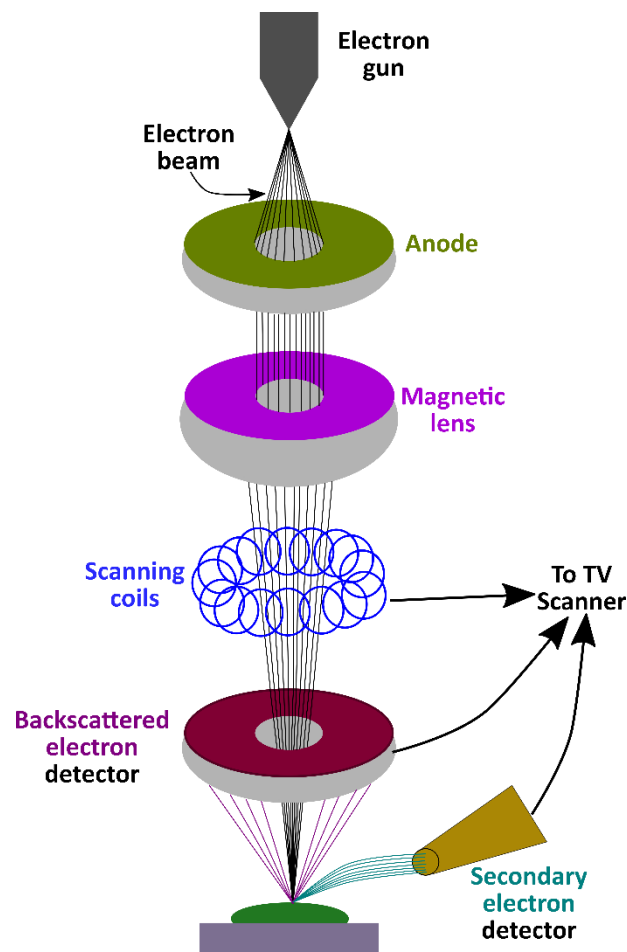


Figure 1.18 Schematic of a scanning electron microscope.

Secondary electrons have low energies and form a noncoherent wave so have to be attracted and accelerated towards the detector, which is usually placed at the

side of the sample. Secondary electron images provide information on the surface topography. Backscattered electrons and X-ray photons are not as sensitive to surface topography and provide more information on the sample composition.<sup>264</sup> SEM micrographs have a large depth of field and a wide range of magnification, useful for understanding 3D surface structures. SEM allows the visualisation of biofilms as the spatial structure and presence of EPS can be observed.<sup>248</sup>

Both techniques require a high vacuum to remove gas particles that could interact with the electron beam. Therefore, samples need to be dehydrated and/or fixed before analysis, which can alter the structural composition and result in loss of EPS. Although an environmental SEM can be used at ambient pressure in the sample chamber. TEM image quality depends on sample thickness, the thinner the sample the better, which poses challenges for biofilm and microorganism analysis. SEM requires the sample to be on a conductive material to dissipate the electrical charge on the surface during imaging.<sup>248,264</sup>

#### 1.6.3.6 Scanning Probe Microscopy

Atomic force microscopy (AFM) is the most commonly used scanning probe technique applied to microorganism and biofilm studies. AFM is a powerful technique for imaging biological samples at nanometre to micrometre scales under non-destructive conditions. A flexible cantilever, with a sharp tip, is raster scanned over the surface of the sample using a piezoelectric scanner. The interaction, caused by overlapping electron clouds, between the sample and the probe tip is measured. If an attracting force is sensed the cantilever bends, the deflection of the cantilever is measured using a laser beam and photodiode, an image of surface topography is outputted.<sup>266</sup> AFM is useful for looking at the initial stages of adhesion before the surface is covered in EPS. Quantification of the adhesion force between living cells, and cells and surface has been achieved by AFM.<sup>267</sup> However the scan area is often small (maximum of 150 x 150  $\mu\text{m}$ ), imaging of the side-walls of bacterial cells is difficult due to the tip geometry and cells must be immobilised for imaging.<sup>248,264</sup>

## 1.7 Aims and Objectives

This thesis aims to develop electroanalytical sensors with capabilities to function at source for environmentally relevant measurement. This thesis has a particular focus on buffer capacity and dynamic pH measurements and heavy metal detection. The work focusses on the use of BDD as a platform electrode technology. Multifunctional devices are introduced which provide added benefits over single function electrodes. Chapters 3, 4 and 5 utilise individually addressable ring disc electrode geometries. The ring electrode is used to conduct a pH changing reaction through water oxidation (chapters 3 and 5) or reduction of oxygen, nitrate and water (chapter 4). The disc electrode is a BDD-Q pH sensitive electrode which is used to track the pH change in the local environment over the disc. Chapter 3 utilises this electrode arrangement to probe solution buffer capacity. The mechanism and action is elucidated through experiments and finite element modelling. Chapter 4 considers the catalytic nature of BDD and Cu nanoparticles, deposited on the ring, and the associated pH changes with oxygen, nitrate and water reduction in unbuffered electrolyte solution.

Chapter 5 explores two techniques for electrochemical heavy metal detection. The ring disc electrode format was used to locally acidify the environment over the disc, through water oxidation on the ring, to encourage preconcentration of Cu in a metallic form. Effective use of ASV requires metallic deposits as oxides and hydroxides are more challenging to remove from the electrode surface and can make interpretation difficult. The second technique considered for heavy metal detection is EC-XRF. Here an electrochemical preconcentration step occurs and the resulting deposit is quantified on the electrode surface using XRF. The chemical oxidation state of the deposited metal is not important here as the XRF will detect the presence of the metal regardless of the oxidation state.

For any BDD sensor placed in direct contact with real life measurement solutions bacterial biofouling is an issue, particularly for long term sensing. The feasibility of extending the functional lifetime of BDD sensors through application of low voltages in the presence of bacteria is explored in Chapter 6.

Finally, Chapter 7 concludes the work presented in the thesis and discusses some directions for future work.

## 1.8 References

- 1 G. A. Florides and P. Christodoulides, *Environ. Int.*, 2009, **35**, 390–401.
- 2 J. Houghton, *Reports Prog. Phys.*, 2005, **68**, 1343–1403.
- 3 J. C. Orr, V. J. Fabry, O. Aumont, L. Bopp, S. C. Doney, R. A. Feely, A. Gnanadesikan, N. Gruber, A. Ishida, F. Joos, R. M. Key, K. Lindsay, E. Maier-Reimer, R. Matear, P. Monfray, A. Mouchet, R. G. Najjar, G. K. Plattner, K. B. Rodgers, C. L. Sabine, J. L. Sarmiento, R. Schlitzer, R. D. Slater, I. J. Totterdell, M. F. Weirig, Y. Yamanaka and A. Yool, *Nature*, 2005, **437**, 681–686.
- 4 S. C. Doney, V. J. Fabry, R. A. Feely and J. A. Kleypas, *Ann. Rev. Mar. Sci.*, 2009, **1**, 169–192.
- 5 S. C. Doney and R. A. Feely, *Oceanography*, 2009, **22**, 16–25.
- 6 J. C. Pales and C. D. Keeling, *J. Geophys. Res.*, 1965, **70**, 6053–6076.
- 7 C. D. Keeling, R. B. Bacastow and A. E. Bainbridge, *Tellus*, 1976, **28**, 538–551.
- 8 C. D. Winn, Y. H. Li, F. T. MacKenzie and D. M. Karl, *Mar. Chem.*, 1998, **60**, 33–47.
- 9 U. Schuster, A. Hannides, L. Mintrop and A. Körtzinger, *Ocean Sci.*, 2009, **5**, 547–558.
- 10 A. G. Dickson, *Mar. Chem.*, 1993, **44**, 131–142.
- 11 G. M. Henderson, *Earth Planet. Sci. Lett.*, 2002, **203**, 1–13.
- 12 D. Harper, *Eutrophication of Freshwaters: Principles, Problems and restoration*, Chapman & Hall, London, 1992.
- 13 D. A. Burns, J. Aherne, D. A. Gay and C. M. B. Lehmann, *Atmos. Environ.*, 2016, **146**, 1–4.
- 14 D. M. DeNicola and M. G. Stapleton, *Environ. Pollut.*, 2002, **119**, 303–315.
- 15 A. Akcil and S. Koldas, *J. Clean. Prod.*, 2006, **14**, 1139–1145.
- 16 P. Amoatey and M. S. Baawain, *Water Environ. Res.*, 2019, **91**, 1272–1287.
- 17 S. Rennie, C. Andrews, S. Atkinson, D. Beaumont, S. Benham, V. Bowmaker,



- J. Dick, B. Dodd, C. McKenna, D. Pallett, R. Rose, S. M. Schäfer, T. Scott, C. Taylor and H. Watson, *Earth Syst. Sci. Data*, 2020, **12**, 87–107.
- 18 YSI Environmental, *Water Quality is the Key to Success at Cardiff Bay*, 2011.
- 19 D. Andrews and J. Gulson, *Proc. Inst. Civ. Eng. Water Marit. Eng.*, 2002, **154**, 89–92.
- 20 Y. Wang, H. Xu, J. Zhang and G. Li, *Sensors*, 2008, **8**, 2043–2081.
- 21 G. Chen, *Sep. Purif. Technol.*, 2004, **38**, 11–41.
- 22 S. P. S. Badwal, S. S. Giddey, C. Munnings, A. I. Bhatt and A. F. Hollenkamp, *Front. Chem.*, 2014, **2**, 1–28.
- 23 G. Hanrahan, D. G. Patil and J. Wang, *J. Environ. Monit.*, 2004, **6**, 657–664.
- 24 C. M. A. Brett and A. M. O. Brett, *Electrochemistry Principles, Methods and Applications*, University Press Oxford, New York, 1993.
- 25 N. Elgrishi, K. J. Rountree, B. D. McCarthy, E. S. Rountree, T. T. Eisenhart and J. L. Dempsey, *J. Chem. Educ.*, 2018, **95**, 197–206.
- 26 A. J. Bard and L. R. Faulkner, *Electrochemical Methods: Fundamentals and Applications*, Wiley, New York, 2 edition., 2000.
- 27 J. Heinze, *Angew. Chemie Int. Ed. English*, 1993, **32**, 1268–1288.
- 28 A. J. Borrill, N. E. Reily and J. V. Macpherson, *Analyst*, 2019, **144**, 6834–6849.
- 29 M. L. Tercier and J. Buffle, *Electroanalysis*, 1993, **5**, 187–200.
- 30 T. R. Copeland and R. K. Skogerboe, *Anal. Chem.*, 1974, **46**, 1257A–1268a.
- 31 L. Landau and B. Levich, *Acta Physicochim. URSS*, 1942, **XVII**, 141–153.
- 32 H. Gunasingham and B. Fleet, *Anal. Chem.*, 1983, **55**, 1409–1414.
- 33 R. G. Compton, R. A. W. Dryfe, J. A. Alden, N. V. Rees, P. J. Dobson and P. A. Leigh, *J. Phys. Chem.*, 1994, **98**, 1270–1275.
- 34 N. A. Madigan, T. J. Murphy, J. M. Fortune, C. R. S. S. Hagan and L. A. Coury, *Anal. Chem.*, 1995, **67**, 2781–2786.
- 35 C. S. Chapman and C. M. G. Van Den Berg, *Electroanalysis*, 2007, **19**, 1347–

- 1355.
- 36 Z. Bi, C. S. Chapman, P. Salaün and C. M. G. Van Den Berg, *Electroanalysis*, 2010, **22**, 2897–2907.
- 37 G. Kefala, A. Economou, A. Voulgaropoulos and M. Sofoniou, *Talanta*, 2003, **61**, 603–610.
- 38 G. Edwall, *Med. Biol. Eng. Comput.*, 1978, **16**, 661–669.
- 39 A. W. Colburn, K. J. Levey, D. O’Hare and J. V. Macpherson, *Phys. Chem. Chem. Phys.*, 2021, **23**, 8100–8117.
- 40 R. S. Nicholson and I. Shain, *Anal. Chem.*, 1964, **36**, 706–723.
- 41 J. V Macpherson, *Phys. Chem. Chem. Phys.*, 2015, **17**, 2935–2949.
- 42 L. Ramaley and M. S. Krause, *Anal. Chem.*, 1969, **41**, 1362–1365.
- 43 J. G. Osteryoung and R. A. Osteryoung, *Anal. Chem.*, , DOI:10.1021/ac00279a789.
- 44 J. Osteryoung, *J. Chem. Educ.*, 1983, **60**, 296.
- 45 O. A. Farghaly, R. S. Abdel Hameed and A. A. H. Abu-Nawwas, *Int. J. Electrochem. Sci.*, 2014, **9**, 3287–3318.
- 46 G. M. S. Alves, L. S. Rocha and H. M. V. M. Soares, *Talanta*, 2017, **175**, 53–68.
- 47 R. G. Compton and C. E. Banks, *Understanding Voltammetry*, IMPERIAL COLLEGE PRESS, 2010.
- 48 F. Scholz, *Electroanalytical Methods*, 2nd edn., 2010.
- 49 World Health Organisation, *Trace elements in human nutrition and health*, 1996.
- 50 A. Dekanski, J. Stevanović, R. Stevanović, B. Ž. Nikolić and V. M. Jovanović, *Carbon N. Y.*, 2001, **39**, 1195–1205.
- 51 C. G. Zoski, *Handbook of electrochemistry*, 2007.
- 52 D. Chen, L. Tang and J. Li, *Chem. Soc. Rev.*, 2010, **39**, 3157–3180.
- 53 W. Zhang, S. Zhu, R. Luque, S. Han, L. Hu and G. Xu, *Chem. Soc. Rev.*, 2016, **45**, 715–752.

- 54 W. E. Van der Linden and J. W. Dieker, *Anal. Chim. Acta*, 1980, **119**, 1–24.
- 55 M. Li, Y. T. Li, D. W. Li and Y. T. Long, *Anal. Chim. Acta*, 2012, **734**, 31–44.
- 56 T. E. Edmonds, *Anal. Chim. Acta*, 1985, **175**, 1–22.
- 57 J. Wang, *Electroanalysis*, 2005, **17**, 7–14.
- 58 J. H. T. Luong, K. B. Male and J. D. Glennon, *Analyst*, 2009, **134**, 1965–1979.
- 59 Y. Shao, J. Wang, H. Wu, J. Liu, I. A. Aksay and Y. Lin, *Electroanalysis*, 2010, **22**, 1027–1036.
- 60 R. L. McCreery, *Chem. Rev.*, 2008, **108**, 2646–2687.
- 61 L. M. Gonçálves, C. Batchelor-Mcauley, A. A. Barros and R. G. Compton, *J. Phys. Chem. C*, 2010, **114**, 14213–14219.
- 62 Q. Li, C. Batchelor-Mcauley and R. G. Compton, *J. Phys. Chem. B*, 2010, **114**, 7423–7428.
- 63 K. Pungjunun, S. Chaiyo, I. Jantrahong, S. Nantaphol, W. Siangproh and O. Chailapakul, *Microchim. Acta*, 2018, **185**, 324.
- 64 G. P. Keeley, N. McEvoy, S. Kumar, N. Peltekis, M. Mausser and G. S. Duesberg, *Electrochem. commun.*, 2010, **12**, 1034–1036.
- 65 V. M. Mirsky, *TrAC - Trends Anal. Chem.*, 2002, **21**, 439–450.
- 66 E. Scavetta, A. G. Solito, M. Demelas, P. Cosseddu and A. Bonfiglio, *Electrochim. Acta*, 2012, **65**, 159–164.
- 67 A. Malinauskas, R. Garjonyte, R. Mažeikiene and I. Jurevičiute, *Talanta*, 2004, **64**, 121–129.
- 68 U. A. Aregueta-Robles, A. J. Woolley, L. A. Poole-Warren, N. H. Lovell and R. A. Green, *Front. Neuroeng.*, 2014, **7**, 1–18.
- 69 Z. J. Ayres, A. J. Borrill, J. C. Newland, M. E. Newton and J. V. Macpherson, *Anal. Chem.*, 2016, **88**, 974–980.
- 70 C. Lu, Y. Gao, G. Yu, M. Xu, J. Tan and F. Xuan, *Sensors Actuators, A Phys.*, 2018, **281**, 124–129.
- 71 A. Economou, *Sensors (Switzerland)*, 2018, **18**, 1–23.

- 72 Y. Lu, X. Liang, C. Niyungeko, J. Zhou, J. Xu and G. Tian, *Talanta*, 2018, **178**, 324–338.
- 73 F. R. Boyd, J. J. Gurney and S. H. Richardson, *Nature*, 1985, **315**, 387–389.
- 74 G. P. Bulanova, *J. Geochemical Explor.*, 1995, **53**, 1–23.
- 75 L. F. Dobrzhinetskaya, R. Wirth and H. W. Green, *Proc. Natl. Acad. Sci. U. S. A.*, 2007, **104**, 9128–9132.
- 76 L. M. Barron, S. R. Lishmund, G. M. Oakes, B. J. Barron and F. L. Sutherland, *Aust. J. Earth Sci.*, 1996, **43**, 257–267.
- 77 V. L. Masaitis, *Meteorites Planet. Sci.*, 1998, **359**, 349–359.
- 78 U. Ott, *J. Achiev. Mater. Manuf. Eng.*, 2009, **37**, 779–784.
- 79 T. L. Daulton, D. D. Eisenhour, T. J. Bernatowicz, R. S. Lewis and P. R. Buseck, *Geochim. Cosmochim. Acta*, 1996, **60**, 4853–4872.
- 80 C. Gupta, D. Prakash and S. Gupta, *Front. Biosci. - Sch.*, 2017, **9**, 62–70.
- 81 K. Ganesan, D. J. Garrett, A. Ahnood, M. N. Shivdasani, W. Tong, A. M. Turnley, K. Fox, H. Meffin and S. Praver, *Biomaterials*, 2014, **35**, 908–915.
- 82 F. Bundy, H. Hall, H. Strong and R. Wentorf, *Nature*, 1955, **176**, 51–55.
- 83 F. G. Celii and J. E. Butler, *Annu. Rev. Phys. Chem.*, 1991, **42**, 643–684.
- 84 I. Kiflawi, H. Kanda and S. C. Lawson, *Diam. Relat. Mater.*, 2002, **11**, 204–211.
- 85 J. Q. Zhang, H. A. Ma, Y. P. Jiang, Z. Z. Liang, Y. Tian and X. Jia, *Diam. Relat. Mater.*, 2007, **16**, 283–287.
- 86 F. M. Shakhov, A. M. Abyzov, S. V. Kidalov, A. A. Krasilin, E. Lähderanta, V. T. Lebedev, D. V. Shamshur and K. Takai, *J. Phys. Chem. Solids*, 2017, **103**, 224–237.
- 87 G. F. Wood, C. E. Zvoriste-Walters, M. G. Munday, M. E. Newton, V. Shkirskiy, P. R. Unwin and J. V. Macpherson, *Carbon N. Y.*, 2021, **171**, 845–856.
- 88 *ACM SIGGRAPH Comput. Graph.*, 1962, 4.
- 89 X. Gao, W. Li, R. Mei, C. Zhu, B. Zhou, L. Ma, Q. Wei and T. Liu, *J. Electroanal.*

- Chem.*, 2019, **832**, 247–253.
- 90 S. Morooka, T. Fukui, K. Semoto, T. Tsubota, T. Saito, K. Kusakabe, H. Maeda, Y. Hayashi and T. Asano, *Diam. Relat. Mater.*, 1999, **8**, 42–47.
- 91 J. E. Butler, Y. A. Mankelevich, A. Cheesman, J. Ma and M. N. R. Ashfold, *J. Phys. Condens. Matter*, , DOI:10.1088/0953-8984/21/36/364201.
- 92 L. A. Hutton, J. G. Iacobini, E. Bitziou, R. B. Channon, M. E. Newton and J. V. Macpherson, *Anal. Chem.*, 2013, **85**, 7230–7240.
- 93 H. V. Patten, K. E. Meadows, L. A. Hutton, J. G. Iacobini, D. Battistel, K. McKelvey, A. W. Colburn, M. E. Newton, J. V. MacPherson and P. R. Unwin, *Angew. Chemie - Int. Ed.*, 2012, **51**, 7002–7006.
- 94 R. Trouillon and D. O'Hare, *Electrochim. Acta*, 2010, **55**, 6586–6595.
- 95 L. J. Simcox, R. P. A. Pereira, E. M. H. Wellington and J. V. Macpherson, *ACS Appl. Mater. Interfaces*, 2019, acsami.9b07245.
- 96 R. E. Wilson, I. Stoianov and D. O'Hare, *Electrochem. commun.*, 2016, **71**, 79–83.
- 97 O. A. Williams, *Diam. Relat. Mater.*, 2011, **20**, 621–640.
- 98 T. Watanabe, Y. Honda, K. Kanda and Y. Einaga, *Phys. Status Solidi Appl. Mater. Sci.*, 2014, **211**, 2709–2717.
- 99 H. B. Martin, A. Argoitia, U. Landau, A. . Anderson and J. Angus, *J. Electrochem. Soc.*, 1996, **143**, 133–136.
- 100 S. J. Cobb, Z. J. Ayres, M. E. Newton and J. V Macpherson, *J. Am. Chem. Soc.*, 2019, **141**, 1035–1044.
- 101 T. L. Read, S. J. Cobb and J. V. Macpherson, *ACS Sensors*, 2019, **4**, 756–763.
- 102 P. B. Tchounwou, C. G. Yedjou, A. K. Patlolla and D. J. Sutton, 2012, **101**, 1–30.
- 103 H. S. Kim, Y. J. Kim and Y. R. Seo, *J. Cancer Prev.*, 2015, **20**, 232–240.
- 104 M. A. Zoroddu, J. Aaseth, G. Crisponi, S. Medici, M. Peana and V. M. Nurchi, *J. Inorg. Biochem.*, 2019, **195**, 120–129.

- 105 S. E. Cusick, E. G. Jaramillo, E. C. Moody, A. S. Ssemata, D. Bitwayi, T. C. Lund and E. Mupere, *BMC Public Health*, 2018, **18**, 1–8.
- 106 M. Kazemipour, M. Ansari, A. Mohammadi, H. Beitollahi and R. Ahmadi, *J. Anal. Chem.*, 2009, **64**, 65–70.
- 107 S. M. Rosolina, J. Q. Chambers, C. W. Lee and Z. L. Xue, *Anal. Chim. Acta*, 2015, **893**, 25–33.
- 108 S. M. Rosolina, J. Q. Chambers and Z. L. Xue, *Anal. Chim. Acta*, 2016, **914**, 47–52.
- 109 G. Hughes, K. Westmacott, K. C. Honeychurch, A. Crew, R. M. Pemberton and J. P. Hart, *Biosensors*, 2016, **6**, 1–39.
- 110 A. Giacomino, A. Ruo Redda, S. Squadrone, M. Rizzi, M. C. Abete, C. La Gioia, R. Toniolo, O. Abollino and M. Malandrino, *Food Chem.*, 2017, **221**, 737–745.
- 111 A. . Jaiswal, S. Das, V. Kumar, M. Gupta and N. Singh, *Int. J. Eng. Res.*, 2015, **4**, 235–239.
- 112 A. Sani and I. L. Abdullahi, *Toxicol. Reports*, 2017, **4**, 72–76.
- 113 G. Liang, L. Pan and X. Liu, *Int. J. Environ. Res. Public Health*, 2017, **14**, 1–10.
- 114 F. A. Nicholson, S. R. Smith, B. J. Alloway, C. Carlton-Smith and B. J. Chambers, *Sci. Total Environ.*, 2003, **311**, 205–219.
- 115 C. Seiler and T. U. Berendonk, *Front. Microbiol.*, 2012, **3**, 1–10.
- 116 B. E. Davies and P. L. Holmes, *J. Agric. Sci.*, 1972, **79**, 479–484.
- 117 M. Kayhanian, *Environ. Pollut.*, 2012, **160**, 169–177.
- 118 Council Directive 2008/105/EC on environmental quality standards in the field of water policy, *Off. J. Eur. Union*, 2008, **L348/84**, 84–97.
- 119 H. Ali and E. Khan, *Hum. Ecol. Risk Assess.*, 2019, **25**, 1353–1376.
- 120 E. Nieboer and A. Jusys, in *Chromium in Natural and Human Environments*, eds. J. Nriagu and E. Nieboer, Wiley Interscience, New York, 1988, pp. 21–81.

- 121 J. Kotaš and Z. Stasicka, *Environ. Pollut.*, 2000, **107**, 263–283.
- 122 E. Tipping, *Cation Binding by Humic Substances*, Cambridge University Press, Cambridge, 1st edn., 2002.
- 123 D. de Paiva Magalhães, M. R. da Costa Marques, D. F. Baptista and D. F. Buss, *Environ. Chem. Lett.*, 2015, **13**, 69–87.
- 124 E. Perkin, 2001, 1–8.
- 125 R. S. Pappas, *Spectroscopy*, 2012, **27**, 20–31.
- 126 J. A. Caruso and M. Montes-Bayon, *Ecotoxicol. Environ. Saf.*, 2003, **56**, 148–163.
- 127 M. Moldovan, E. M. Krupp, A. E. Holliday and O. F. X. Donard, *J. Anal. At. Spectrom.*, 2004, **19**, 815–822.
- 128 H. Küpper, S. N. H. Bokhari, N. Jaime-Pérez, L. Lyubenova, N. Ashraf and E. Andresen, *Anal. Chem.*, 2019, **91**, 10961–10969.
- 129 T. M. Florence, *Talanta*, 1982, **29**, 345–364.
- 130 T. M. Florence, *Analyst*, 1986, **111**, 489–505 ST-Electrochemical Approaches to Trace-.
- 131 W. D. Ellis, *J. Chem. Educ.*, 1973, **50**, A131.
- 132 C. M. A. Brett and A. M. C. F. Oliveira Brett, *J. Electroanal. Chem.*, 1989, **262**, 83–95.
- 133 K. Z. Brainina, *Talanta*, 1971, **18**, 513–539.
- 134 J. Wang, *Stripping analysis: principles, instrumentation, and applications*, VCH, 1985.
- 135 O. Mikkelsen and K. H. Schroder, *Electroanalysis*, 2003, **15**, 679–687.
- 136 M. B. Gumpu, M. Veerapandian, U. M. Krishnan and J. B. B. Rayappan, *Talanta*, 2017, **162**, 574–582.
- 137 S. E. Ward Jones, F. G. Chevallier, C. A. Paddon and R. G. Compton, *Anal. Chem.*, 2007, **79**, 4110–4119.
- 138 J. Wang, *Electroanalysis*, 2005, **17**, 1341–1346.

- 139 E. Tesarova, L. Baldrianova, S. B. Hocevar, I. Svancara, K. Vytras and B. Ogorevc, *Electrochim. Acta*, 2009, **54**, 1506–1510.
- 140 R. Pauliukaite, S. B. Hočevár, B. Ogorevc and J. Wang, *Electroanalysis*, 2004, **16**, 719–723.
- 141 N. Y. Stozhko, N. A. Malakhova, M. V. Fyodorov and K. Z. Brainina, *J. Solid State Electrochem.*, 2008, **12**, 1185–1204.
- 142 E. A. McGaw and G. M. Swain, *Anal. Chim. Acta*, 2006, **575**, 180–189.
- 143 S. Sharma, *J. Electrochem. Soc.*, 2020, **167**, 037501.
- 144 J. Wang, *Analytical Electrochemistry*, 2006.
- 145 D. W. M. Arrigan, *Analyst*, 1994, **11**, 1953–1966.
- 146 A. Mandil, L. Idrissi and A. Amine, *Microchim. Acta*, 2010, **170**, 299–305.
- 147 M. A. Rahman, M.-S. Won and Y.-B. Shim, *Anal. Chem.*, 2003, **75**, 1123–1129.
- 148 L. Cui, J. Wu and H. Ju, *Chem. - A Eur. J.*, 2015, **21**, 11525–11530.
- 149 S. Dai, J. Liu, C. R. Ward, J. C. Hower, D. French, S. Jia, M. M. Hood and T. M. Garrison, *Int. J. Coal Geol.*, 2016, **166**, 71–95.
- 150 T. R. Knott, M. K. Reichow, M. J. Branney, D. R. Finn, R. S. Coe, M. Storey and B. Bonnichsen, *Bull. Volcanol.*, **78**, 23.
- 151 C. Perreault, M. T. Boulanger, A. M. Hudson, D. Rhode, D. B. Madsen, J. W. Olsen, M. L. Steffen, J. Quade, M. D. Glascock and P. J. Brantingham, *J. Archaeol. Sci. Reports*, 2016, **5**, 392–399.
- 152 A. Doyle, A. Saavedra, M. L. B. Tristão, M. Nele and R. Q. Aucélio, *Spectrochim. Acta - Part B At. Spectrosc.*, 2011, **66**, 368–372.
- 153 M. F. Gazulla, M. Orduña, S. Vicente and M. Rodrigo, *Fuel*, 2013, **108**, 247–253.
- 154 H. W. Nørgaard, *Open Archaeol.*, 2017, **3**, 101–122.
- 155 R. Fernandes, B. J. H. van Os and H. D. J. Huisman, *Herit. Sci.*, 2013, **1**, 1–7.
- 156 J. Zhu, Y. Yang, W. Xu, D. Chen, J. Dong, L. Wang and M. D. Glascock, *X-Ray Spectrom.*, 2012, **41**, 363–366.



- 157 R. S. Ortiz, K. C. Mariotti, N. V. Schwab, G. P. Sabin, W. F. C. Rocha, E. V. R. de Castro, R. P. Limberger, P. Mayorga, M. I. M. S. Bueno and W. Romão, *J. Pharm. Biomed. Anal.*, 2012, **58**, 7–11.
- 158 N. Lewen, M. Soumeillant, J. Qiu, J. Selekman, S. Wood and K. Zhu, *Org. Process Res. Dev.*, 2015, **19**, 2039–2044.
- 159 D. Rajapaksha, V. Waduge, R. Padilla-Alvarez, M. Kalpage, R. M. N. P. Rathnayake, A. Migliori, R. Frew, S. Abeysinghe, A. Abraham and T. Amarakoon, *X-Ray Spectrom.*, 2017, **46**, 220–224.
- 160 M. Alfeld, J. V. Pedroso, M. Van Eikema Hommes, G. Van Der Snickt, G. Tauber, J. Blaas, M. Haschke, K. Erler, J. Dik and K. Janssens, *J. Anal. At. Spectrom.*, 2013, **28**, 760–767.
- 161 M. Sawczak, A. Kamińska, G. Rabczuk, M. Ferretti, R. Jendrzewski and G. Śliwiński, *Appl. Surf. Sci.*, 2009, **255**, 5542–5545.
- 162 E. Marguá, B. Zawisza and R. Sitko, *TrAC - Trends Anal. Chem.*, 2014, **53**, 73–83.
- 163 C. Streli, *Appl. Spectrosc. Rev.*, 2006, **41**, 473–489.
- 164 M. A. Barreiros, M. L. Carvalho, M. M. Costa, M. I. Marques and M. T. Ramos, *X-Ray Spectrom.*, 1997, **26**, 165–168.
- 165 A. Cinosi, N. Andriollo, G. Pepponi and D. Monticelli, *Anal. Bioanal. Chem.*, 2011, **399**, 927–933.
- 166 D. Klopfenstein and E. Nussbaum, *Proc. Indiana Acad. Sci.*, 1975, **85**, 339–342.
- 167 C. W. Blount, D. E. Leyden, T. L. Thomas and S. M. Guill, *Anal. Chem.*, 1973, **45**, 1045–1050.
- 168 R. Panayappan, D. L. Venezky, J. V. Gilfrich and L. S. Birks, *Anal. Chem.*, 1978, **50**, 1125–1126.
- 169 S. Igarashi, A. Takahashi, Y. Ueki and H. Yamaguchi, *Analyst*, 2000, **125**, 797–798.
- 170 X. Hou, H. L. Peters, Z. Yang, K. A. Wagner, J. D. Batchelor, M. M. Daniel and

- B. T. Jones, *Appl. Spectrosc.*, 2003, **57**, 338–342.
- 171 N. V. Alov, K. V. Oskolok, A. Wittershagen, M. Mertens, C. Rittmeyer, P. Rostam-Khani and B. O. Kolbesen, *Spectrochim. Acta - Part B At. Spectrosc.*, 2001, **56**, 2117–2126.
- 172 L. A. Hutton, G. D. O’Neil and T. L. Read, *Anal. Chem.*, 2014, **86**, 4566–4572.
- 173 G. D. O’Neil, M. E. Newton and J. V. Macpherson, *Anal. Chem.*, 2015, **87**, 4933–4940.
- 174 Z. J. Ayres, M. E. Newton and J. V. Macpherson, *Analyst*, 2016, **141**, 3349–3357.
- 175 B. Y. R. J. Whitney, *J. Exp. Biol.*, 1942, **19**, 92–99.
- 176 R. Christian Jones and A. P. Graziano, *Inl. Waters*, 2013, **3**, 421–436.
- 177 G. E. Likens, R. F. Wright, J. N. Galloway and T. J. Butler, *Sci. Am.*, 1979, **241**, 43–51.
- 178 D. W. Schindler, *Science*, 1988, **239**, 149–157.
- 179 S. Khatiwala, T. Tanhua, S. Mikaloff Fletcher, M. Gerber, S. C. Doney, H. D. Graven, N. Gruber, G. A. McKinley, A. Murata, A. F. Ríos and C. L. Sabine, *Biogeosciences*, 2013, **10**, 2169–2191.
- 180 T. DeVries, *Global Biogeochem. Cycles*, 2014, **28**, 631–647.
- 181 T. DeVries, M. Holzer and F. Primeau, *Nature*, 2017, **542**, 215–218.
- 182 M. J. P. Leiner and P. Hartmann, *Sensors Actuators B. Chem.*, 1993, **11**, 281–289.
- 183 J. Lin, *TrAC - Trends Anal. Chem.*, 2000, **19**, 541–552.
- 184 D. Wencel, T. Abel and C. McDonagh, *Anal. Chem.*, 2014, **86**, 15–29.
- 185 E. Wang, K. F. Chow, V. Kwan, T. Chin, C. Wong and A. Bocarsly, *Anal. Chim. Acta*, 2003, **495**, 45–50.
- 186 Z. Liu, F. Luo and T. Chen, *Anal. Chim. Acta*, 2004, **510**, 189–194.
- 187 F. Ismail, C. Malins and N. J. Goddard, *Analyst*, 2002, **127**, 253–257.
- 188 B. M. Weidgans, C. Krause, I. Klimant and O. S. Wolfbeis, *Analyst*, 2004, **129**,

- 645–650.
- 189 Q. Zhu, R. C. Aller and Y. Fan, *Environ. Sci. Technol.*, 2005, **39**, 8906–8911.
- 190 G. Nishimura, Y. Shiraishi and T. Hirai, *Chem. Commun.*, 2005, **1**, 5313–5315.
- 191 S. Chen, J. Liu, Y. Liu, H. Su, Y. Hong, C. K. W. Jim, R. T. K. Kwok, N. Zhao, W. Qin, J. W. Y. Lam, K. S. Wong and B. Z. Tang, *Chem. Sci.*, 2012, **3**, 1804–1809.
- 192 J. Goicoechea, C. R. Zamarreño, I. R. Matías and F. J. Arregui, *Sensors Actuators, B Chem.*, 2008, **132**, 305–311.
- 193 R. Gotor, P. Ashokkumar, M. Hecht, K. Keil and K. Rurack, *Anal. Chem.*, 2017, **89**, 8437–8444.
- 194 P. Vanýsek, *Electrochem. Soc. Interface*, 2004, **13**, 19–20.
- 195 M. Wang, S. Yao and M. Madou, *Sensors Actuators, B Chem.*, 2002, **81**, 313–315.
- 196 E. Prats-Alfonso, L. Abad, N. Casañ-Pastor, J. Gonzalo-Ruiz and E. Baldrich, *Biosens. Bioelectron.*, 2013, **39**, 163–169.
- 197 W. D. Huang, H. Cao, S. Deb, M. Chiao and J. C. Chiao, *Sensors Actuators, A Phys.*, 2011, **169**, 1–11.
- 198 Y. H. Liao and J. C. Chou, *Sensors Actuators, B Chem.*, 2008, **128**, 603–612.
- 199 S. Zhuiykov, *Sensors Actuators, B Chem.*, 2009, **136**, 248–256.
- 200 L. Manjakkal, D. Szwagierczak and R. Dahiya, *Prog. Mater. Sci.*, 2020, **109**, 100635.
- 201 D. O'Hare, K. H. Parker and C. P. Winlove, *Med. Eng. Phys.*, 2006, **28**, 982–988.
- 202 S. Głáb, A. Hulanicki, G. Edwall, F. Folke, I. Ingman and W. F. Koch, *Crit. Rev. Anal. Chem.*, 1989, **21**, 29–47.
- 203 J. C. Dutta, *Proc. - 2012 2nd Natl. Conf. Comput. Intell. Signal Process. CISP 2012*, 2012, 185–191.
- 204 T. M. Abdolkader, A. G. Alahdal, A. Shaker and W. Fikry, *Int. J. Chem. Eng.*

- Appl.*, 2015, **6**, 346–351.
- 205 W. Y. Chung, F. S. He, C. H. Yang and M. C. Wang, *J. Med. Biol. Eng.*, 2006, **26**, 29–34.
- 206 V. K. Khanna, *Sens. Rev.*, 2007, **27**, 233–238.
- 207 M. Quan, D. Sanchez, M. F. Wasylkiw and D. K. Smith, *J. Am. Chem. Soc.*, 2007, **129**, 12847–12856.
- 208 P. S. Guin, S. Das and P. C. Mandal, *Int. J. Electrochem.*, 2011, **2011**, 1–22.
- 209 C. Costentin, *Chem. Rev.*, 2008, **108**, 2145–2179.
- 210 R. S. Kim and T. D. Chung, *Bull. Korean Chem. Soc.*, 2014, **35**, 3143–3155.
- 211 H. Kahlert, *J. Solid State Electrochem.*, 2008, **12**, 1255–1266.
- 212 M. Lu and R. G. Compton, *Analyst*, 2014, **139**, 4599–4605.
- 213 M. Lu and R. G. Compton, *Analyst*, 2014, **139**, 2397–2403.
- 214 F. E. Galdino, J. P. Smith, S. I. Kwamou, D. K. Kampouris, J. Iniesta, G. C. Smith, J. A. Bonacin and C. E. Banks, *Anal. Chem.*, 2015, **87**, 11666–11672.
- 215 A. G. Dickson, J. D. Afghan and G. C. Anderson, *Mar. Chem.*, 2003, **80**, 185–197.
- 216 L. Van Vooren, P. Lessard, J. P. Ottoy and P. A. Vanrolleghem, *Environ. Technol. (United Kingdom)*, 1999, **20**, 547–561.
- 217 Q. Li, F. Wang, Z. A. Wang, D. Yuan, M. Dai, J. Chen, J. Dai and K. A. Hoering, *Environ. Sci. Technol.*, 2013, **47**, 11139–11146.
- 218 T. R. Martz, A. G. Dickson and M. D. DeGrandpre, *Anal. Chem.*, 2006, **78**, 1817–1826.
- 219 R. S. Spaulding, M. D. Degrandpre, J. C. Beck, R. D. Hart, B. Peterson, E. H. De Carlo, P. S. Drupp and T. R. Hammar, *Environ. Sci. Technol.*, 2014, **48**, 9573–9581.
- 220 G. Gran, *Analyst*, 1952, **77**, 661–671.
- 221 D. D. Wynn-Williams, *Biodivers. Conserv.*, 1996, **5**, 1271–1293.
- 222 S. C. Cary, I. R. McDonald, J. E. Barrett and D. A. Cowan, *Nat. Rev. Microbiol.*,

- 2010, **8**, 129–138.
- 223 N. Stivaletta, R. Barbieri and D. Billi, *Orig. Life Evol. Biosph.*, 2012, **42**, 187–200.
- 224 A. M. Anesio, S. Lutz, N. A. M. Christmas and L. G. Benning, *npj Biofilms Microbiomes*, 2017, **3**, 0–1.
- 225 R. Parkes, B. Cragg, S. Bale, J. Getilff, K. Goodman, P. Rochelle, J. Fry, A. Weightman and S. Harvey, *Lett. to Nat.*, 1994, **371**, 410–413.
- 226 J. W. Costerton, G. G. Geesey and K. J. Cheng, *Sci. Am.*, 1978, **238**, 86–95.
- 227 H. C. Jones, I. L. Roth and W. M. Sanders, *J. Bacteriol.*, 1969, **99**, 316–325.
- 228 R. M. Donlan, *Emerg. Infect. Dis.*, 2002, **8**, 881–890.
- 229 H. Heukelekian and A. Heller, *J. Bacteriol.*, 1940, **40**, 547–558.
- 230 C. E. Zobell, *J. Bacteriol.*, 1943, **46**, 39–56.
- 231 W. G. Characklis and K. C. Marshall, in *Biofilms*, John Wiley & Sons Ltd, New York, 1990, pp. 3–16.
- 232 G. S. Lorite, C. M. Rodrigues, A. A. de Souza, C. Kranz, B. Mizaikoff and M. A. Cotta, *J. Colloid Interface Sci.*, 2011, **359**, 289–295.
- 233 R. Oliveira, J. Azeredo and P. Teixeira, in *Biofilms in wastewater treatment: an interdisciplinary approach*, IWA Publishing, London, 2003, pp. 211–231.
- 234 R. P. Schneider, *J. Adhes. Sci. Technol.*, 1997, **11**, 979–994.
- 235 J. Palmer, S. Flint and J. Brooks, *J. Ind. Microbiol. Biotechnol.*, 2007, **34**, 577–588.
- 236 M. C. van Loosdrecht, J. Lyklema, W. Norde, G. Schraa and A. J. Zehnder, *Appl. Environ. Microbiol.*, 1987, **53**, 1898–1901.
- 237 P. Gilbert, D. J. Evans, E. Evans, I. G. Duguid and M. R. W. Brown, *J. Appl. Bacteriol.*, 1991, **71**, 72–77.
- 238 B. Carpentier and O. Cerf, *J. Appl. Bacteriol.*, 1993, **75**, 499–511.
- 239 G. O. Toole, H. B. Kaplan and R. Kolter, *Annu. Rev. Microbiol.*, 2000, **54**, 49–79.

- 240 J. W. Costerton, *Int. J. Antimicrob. Agents*, 1999, **11**, 217–221.
- 241 J. K. Teschler, D. Zamorano-Sánchez, A. S. Utada, C. J. A. Warner, G. C. L. Wong, R. G. Linington and F. H. Yildiz, *Nat. Rev. Microbiol.*, 2015, **13**, 255–268.
- 242 G. A. O’Toole and G. C. L. Wong, *Curr. Opin. Microbiol.*, 2016, **30**, 139–146.
- 243 K. C. MARSHALL, R. STOUT and R. MITCHELL, *J. Gen. Microbiol.*, 1971, **68**, 337–348.
- 244 C. G. Kumar and S. K. Anand, *Int. J. Food Microbiol.*, 1998, **42**, 9–27.
- 245 A. T. Poortinga, R. Bos and H. J. Busscher, *Biophys. Chem.*, 2001, **91**, 273–279.
- 246 P. Stoodley, K. Sauer, D. G. Davies and J. W. Costerton, *Annu. Rev. Microbiol.*, 2002, **56**, 187–209.
- 247 H. C. Flemming, J. Wingender, U. Szewzyk, P. Steinberg, S. A. Rice and S. Kjelleberg, *Nat. Rev. Microbiol.*, 2016, **14**, 563–575.
- 248 J. Azeredo, N. F. Azevedo, R. Briandet, N. Cerca, T. Coenye, A. R. Costa, M. Desvaux, G. Di Bonaventura, M. Hébraud, Z. Jaglic, M. Kačániová, S. Knøchel, A. Lourenço, F. Mergulhão, R. L. Meyer, G. Nychas, M. Simões, O. Tresse and C. Sternberg, *Crit. Rev. Microbiol.*, 2017, **43**, 313–351.
- 249 F. Cerca, G. Trigo, A. Correia, N. Cerca, J. Azeredo and M. Vilanova, *Can. J. Microbiol.*, 2011, **57**, 850–856.
- 250 F. Oliveira, C. A. Lima, S. Brás, Â. França and N. Cerca, *FEMS Microbiol. Lett.*, 2015, **362**, 1–7.
- 251 S. Tavernier and T. Coenye, *PeerJ*, , DOI:10.7717/peerj.787.
- 252 A. P. Magalhães, Â. França, M. O. Pereira and N. Cerca, *Sci. Rep.*, 2019, **9**, 1–12.
- 253 M. G. Trulear and W. G. Characklis, *IEE Conf. Publ.*, 1980, **54**, 1288–1301.
- 254 S. Jackson, L. Coulthwaite, Z. Loewy, A. Scallan and J. Verran, *J. Prosthet. Dent.*, 2014, **112**, 988–993.
- 255 J. H. Merritt, D. E. Kadouri and G. A. O’Toole, *Curr. Protoc. Microbiol.*, 2015,

- 1–29.
- 256 G. A. O’Toole, *J. Vis. Exp.*, 2010, 10–11.
- 257 S. M. Kwasny and T. J. Opperman, *Curr. Protoc. Pharmacol.*, 2010, 1–27.
- 258 A. C. Smith and M. A. Hussey, *Am. Soc. Microbiol.*, 2005, **1**, 14.
- 259 G. D. Christensen, W. A. Simpson, J. J. Younger, L. M. Baddour, F. F. Barrett, D. M. Melton and E. H. Beachey, *J. Clin. Microbiol.*, 1985, **22**, 996–1006.
- 260 B. Pitts, M. A. Hamilton, N. Zilver and P. S. Stewart, *J. Microbiol. Methods*, 2003, **54**, 269–276.
- 261 E. Peeters, H. J. Nelis and T. Coenye, *J. Microbiol. Methods*, 2008, **72**, 157–165.
- 262 M. E. Sandberg, D. Schellmann, G. Brunhofer, T. Erker, I. Busygin, R. Leino, P. M. Vuorela and A. Fallarero, *J. Microbiol. Methods*, 2009, **78**, 104–106.
- 263 F. Van den Driessche, P. Rigole, G. Brackman and T. Coenye, *J. Microbiol. Methods*, 2014, **98**, 31–34.
- 264 Z. Lewandowski and H. Beyenal, *Fundamentals of Biofilm Research*, CRC Press, Boca Raton, 2nd Editio., 2017.
- 265 N. S. Claxton, T. J. Fellers and M. W. Davidson, *SpringerReference*, 2011.
- 266 Y. F. Dufrêne, *J. Bacteriol.*, 2002, **184**, 5205–5213.
- 267 A. Beaussart, S. El-Kirat-Chatel, R. M. A. Sullan, D. Alsteens, P. Herman, S. Derclaye and Y. F. Dufrêne, *Nat. Protoc.*, 2014, **9**, 1049–1055.

## 2 Experimental

### 2.1 Chemicals

All solutions were prepared using ultra-pure water with a resistivity of  $\geq 18.2 \text{ M}\Omega \text{ cm}$  at  $25^\circ\text{C}$  (Millipore, Watford, UK). All reagents were used as received, Table 2.1, and weighed using an analytical balance (A200S, Sartorius, Göttingen, Germany).

Table 2.1 List of chemicals used with details of suppliers.

Chemical	Supplier	Details
Acetic acid $\text{CH}_3\text{COOH}$	Sigma Aldrich	99 %
	Fisher Scientific	$\geq 97 \%$
Anhydrous potassium carbonate $\text{K}_2\text{CO}_3$	Fisher Scientific	Extra Pure
Argon Gas	BOC	Pureshield 99.998 %
Boric acid $\text{H}_3\text{BO}_3$	Scientific Lab Supplies	$> 99 \%$
Citric acid $\text{C}_6\text{H}_8\text{O}_7$	Fisher Chemicals	$\geq 99.5 \%$
Copper nitrate $\text{Cu}(\text{NO}_3)_2$	Aldrich	$\geq 99.999 \%$
Copper sulphate $\text{CuSO}_4$	Merck	ACS Reagent grade, 99 – 102 %
Crystal violet solution $\text{C}_{25}\text{H}_{30}\text{N}_3\text{Cl}$	Sigma-Aldrich	1 % in $\text{H}_2\text{O}$
Ethanol absolute $\text{C}_2\text{H}_5\text{OH}$	VWR Chemicals	Reagent grade $\geq 99.8 \%$
Hexaammineruthenium(III) chloride $[\text{Ru}(\text{NH}_3)_6^{3+}]\text{Cl}_3$	Strem Chemicals	99 %
Hydrogen peroxide $\text{H}_2\text{O}_2$	Sigma Aldrich	30 % W/w
Iridium tetrachloride $\text{IrCl}_4$	Alfa Aesar	99.8 %



<b>Nitric acid</b> <b>HNO<sub>3</sub></b>	Honeywell	ACS Reagent, 70 % concentration
<b>Oxalic acid dehydrate</b> <b>C<sub>2</sub>H<sub>2</sub>O<sub>4</sub></b>	Aldrich	98 %
<b>Potassium hydroxide</b> <b>KOH</b>	Fisher Scientific	85 %
<b>Potassium nitrate</b> <b>KNO<sub>3</sub></b>	Acros Organics	≥ 99.0 %
<b>Potassium sulphate</b> <b>K<sub>2</sub>SO<sub>4</sub></b>	Sigma Aldrich	≥ 99 %
<b>Silicon tubing</b>	RS Components	0.8 mm inner diameter
<b>Sodium acetate</b> <b>CH<sub>3</sub>COONa</b>	Fisher Chemicals	99 %
<b>Sodium hydroxide</b>	Sigma Aldrich	> 99.99 %
<b>Sodium phosphate dibasic</b> <b>heptahydrate</b>	Sigma Aldrich	≥ 98 %
<b>Sodium phosphate</b> <b>monobasic monohydrate</b>	Calbiochem, Merck	≥ 98 %
<b>Sulphuric acid</b> <b>H<sub>2</sub>SO<sub>4</sub></b>	Fisher Scientific	≥ 95 %
<b>Tertiary sodium phosphate</b> <b>Na<sub>3</sub>PO<sub>4</sub></b>	Acros Organics	≥ 99.0 %

## 2.2 Materials

Materials used for sensor fabrication and experimental set up in this thesis are given in Table 2.2.

Table 2.2 List of materials used with details of suppliers.

Material	Supplier	Details
<b>3D printer filaments</b>	Innofil3D (PET)	-
	Filamentive (PLA, HIPS)	-
<b>96-Well plate</b>	Corning	-
<b>Alumina micropolish</b>	Buehler	0.05 $\mu\text{m}$
<b>Boron Doped Diamond</b>	Element Six	Electroanalytical grade Electrochemical processing grade
<b>Carbimet paper</b>	Buehler	-
<b>“Clear” Resin</b>	FormLabs	-
<b>Conductive adhesive Ag epoxy</b>	Chemtronics, Circuitworks	-
<b>Copper Wire</b>	R.S. Components	0.8 mm diameter
<b>Epoxy Resin</b>	Araldite	5 minute epoxy
	Robnor Resins	Epoxy Resin RX771C/NC, Aradur Hardener HY1300GB, Robnor Resins
<b>Ethylene polypropylene rubber</b>	RS Components	1.5 mm thick
<b>Glass capillaries</b>	Harvard Apparatus Ltd.	O.D. 2 mm, I.D. 1.16 mm
	Harvard Apparatus Ltd.	O.D 1.2 mm, I.D 0.6 mm

<b>“High-Temp” resin</b>	FormLabs	-
<b>Hirshmann clip</b>	RS Components	-
<b>Intrinsic diamond</b>	Element Six	Optical grade
<b>Isopropanol</b>	Fisher Chemicals	Analytical Grade
<b>Jubilee clip</b>	RS Components	JCS HI-GRIP 60 -80 mm
<b>Nafion 212 membrane</b>	Alfa Aersar	
<b>pH Buffer Solutions</b>	Mettler Toledo	pH 4, 7, 10
<b>Polyvinyl acetate</b>	Wilkinsons	Craft Glue
<b>Pt Gauze</b>	-	-
<b>Pt Wire</b>	-	-
<b>Saturated calomel electrode</b>	IJ Cambria	-
	CH Instruments	-
<b>Silver coated copper wire</b>	RS Components	450 $\mu\text{m}$ diameter
<b>Superglue</b>	Loctite 406	-

## 2.3 Fabrication of electrodes

### 2.3.1 Preparation of BDD

All work in this thesis was undertaken using freestanding BDD in the form of a 6 inch freestanding polycrystalline BDD electroanalytical grade wafer (boron dopant density  $>10^{20}$  B atoms  $\text{cm}^{-3}$ ; minimal  $\text{sp}^2$  carbon content, Element Six) unless otherwise stated.<sup>1,2</sup> The BDD thickness was 357  $\mu\text{m}$  with nanometre scale roughness of the growth face, achieved through polishing. A 355 nm Nd:YAG 34 ns laser micro-machining system (E-355H-ATHI-O system, Oxford Lasers) was used to ablate BDD in order to remove material or cut desired geometries from a freestanding wafer using a laser beam. A variety of geometries were used depending on the experiment.

The BDD used for work on electrochemical X-Ray fluorescence in Chapter 5 was freestanding electroprocessing grade, also produced by Element Six, and was supplied as 21 mm diameter discs polished to 250  $\mu\text{m}$  thickness and nm roughness on the growth face.

The BDD used in Chapter 6 was also freestanding electrochemical processing grade BDD, polished on both sides to nanometre scale roughness and a thickness of 500  $\mu\text{m}$ . Both 4 mm rounds and rectangular cuboids of 10 mm by 5 mm were machined. The top 1 mm of both geometries was laser roughened using a 532 nm Nd:YAG laser micromaching system (A-Series, Oxford Lasers Ltd. UK) with a nominal pulse length of 15 ns and a fluence of  $\sim 20 \text{ J cm}^{-1}$  to improve the adhesion of the Ti/Au sputtered contact.

#### 2.3.1.1 Hot acid clean and thermal anneal procedure

Once laser cut the BDD was subjected to a hot acid cleaning procedure to remove any loose  $\text{sp}^2$  carbon material and ensure the surface was oxygen-terminated.<sup>2</sup> The BDD was placed in a solution of 0.75 g  $\text{KNO}_3$  per ml of concentrated  $\text{H}_2\text{SO}_4$  and heated to  $\sim 250^\circ\text{C}$  for 30 minutes. The BDD was removed and placed in concentrated  $\text{H}_2\text{SO}_4$  and heated again for an additional 30 minutes.<sup>3</sup> The BDD was then rinsed multiple times with ultra-pure water and left to dry on lint-free cloth. To remove any further  $\text{sp}^2$  carbon a thermal anneal at  $600^\circ\text{C}$  in air for 5 hours was performed, unless otherwise stated.

#### 2.3.1.2 Incorporation of pH Sensitive BDD-Q

For pH sensing in Chapters 3, 4 and 5 prior to the addition of an electrical contact a further laser micro-machining process is undertaken to produce patterned regions of  $\text{sp}^2$  carbon into the BDD surface.<sup>4,5</sup> The  $\text{sp}^2$  carbon features were produced by rastering the laser beam in a circular pattern with a nominal pulse density of  $1 \times 10^6$  pulses per  $\text{cm}^2$  with a pulse fluence of  $14 \text{ J cm}^{-2}$ .<sup>6</sup> Followed by the same hot acid cleaning procedure as previously described. The patterned BDD do not undergo the thermal anneal, as the desire is to utilise the properties of the  $\text{sp}^2$  carbon introduced.

#### 2.3.1.3 Formation of an Ohmic contact

To provide an electrical contact Ti (10 nm) / Au (400 nm) was sputtered (Moorfields MiniLab 060 platform sputter/evaporator) onto the lapped

(nucleation face) side of the BDD substrate. To form an ohmic contact these were annealed at 400°C for 5 hours in air, forming a titanium carbide contact between the carbon and titanium layers. For EC-XRF studies a Ti (10 nm) / Pt (400 nm) contact was used as Au was previously studied by this technique.

### **2.3.2 Electrode Fabrication**

For initial conceptual work 1 mm cylinders, with or without incorporated  $sp^2$  patterns, were sealed in pulled glass capillaries (O.D. 2 mm; I.D. 1.16 mm, Harvard Apparatus Ltd., Kent, UK) with the back side, with its sputtered contact, facing the open end of the capillary. A vacuum was then applied and the edges of the BDD cylinders were heat sealed (Narishige PB-7) within the capillaries. Once sealed the BDD surface was exposed by polishing away the excess glass on CarbiMet grit paper with increasingly fine grains and finally alumina (0.05  $\mu\text{m}$ ) paste (Buehler, Germany) until the BDD face was exposed, verified with optical microscopy (Olympus BH-2-HLSH). Care must be taken to ensure polishing is parallel to the BDD surface to avoid exposure of the cylinder sides which may still contain some  $sp^2$  carbon. The back of the capillary was filled with conductive silver epoxy (Chemtronics, Circuitworks, UK) and a 0.8 mm diameter copper wire (polished flat) inserted in contact with the back side of the BDD cylinder. Finally, epoxy resin is added at the top of the capillary to seal the conductive epoxy and stabilise the copper wire. Bespoke electrodes are discussed in more detail in the relevant chapters.

## 2.4 Instrumentation

### 2.4.1 Potentiostats

A number of potentiostats were used throughout this thesis, Table 2.3.

Table 2.3 Potentiostats used in each chapter

Chapter	Potentiostat(s)
3. Assessment of a boron doped diamond ring disc buffer capacity sensor	Autolab PGSTAT101 CHI 750 A
4. In-situ tracking of catalytically driven pH changes on boron doped diamond (BDD) versus copper nanoparticle modified BDD in unbuffered solutions	CHI 760 E CHI 750 A
5. Electrochemical Copper Detection	CHI 760 C Autolab PGSTAT101
6. Low Potential Biofilm Control	Ivium Compactstat with WE32 module

### 2.4.2 3D Printers

Work throughout this thesis has been aided by custom made components from 3D printers. Two 3D printers were used, a Lulzbot Taz 6 (Lulzbot, North Dakota, USA) and a Form3 (Formlabs, Massachusetts, USA).

The Lulzbot Taz 6 is a fused deposition modelling (FDM) printer, also termed fused filament fabrication. FDM printers use materials in the form of a plastic filament which unwinds from a coil as it is fed through the extrusion nozzle, Figure 2.1. The material is heated in the extrusion nozzle and extrudes the heated

filament onto a build platform. Most prints were made from polylactic acid (PLA) or polyethylene terephthalate (PET) thermoplastics. The build platform is controlled in the Y dimension and the extruder in the X and Z dimensions. A computer-aided design (CAD) model is used to design the object to be printed. The CAD model is converted to a .STL file before sending to the printer software (Lulzbot Cura, Ultimaker), which determines where support features are required and incorporates these into the model before sending cross sectional instructions to the 3D printer. A layer is extruded from the nozzle onto the build platform, the thin layer of plastic cools and hardens binding to the layer beneath it, once a layer is completed, the Z dimension is increased, and the next layer is deposited. Layer thickness can be determined and will impact the length of time required for a print. Once completed support material can be removed leaving the final object. This printer is better suited to larger objects or more rapid prototyping than the Form 3.

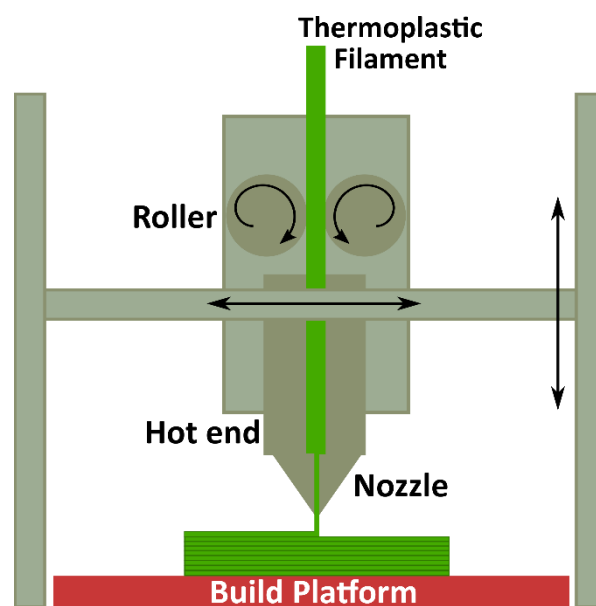


**Figure 2.1 Schematic of fused deposition modelling printer based on the mechanism of a Lulzbot Taz 6.**

The Form 3 is a stereolithographic (SLA) 3D printer. Rather than printing from a coil of thermoplastic, SLA printers use a photosensitive thermoset polymer resin set by an ultraviolet (UV) laser beam, Figure 2.2. Photopolymerisation occurs as the monomer carbon chains are activated by the light of the UV laser and become solid as strong unbreakable bonds are formed. The laser beam is focussed according to the CAD model using a light processing unit (LPU) which controls

the X direction. The LPU contains a UV laser, the beam is positioned in the Y direction by a galvanometer, passed through a spatial filter and is directed by a fold mirror and a parabolic mirror to deliver the beam perpendicular to the build plane. The build platform is positioned one layers height from the surface of the liquid and is raised with every layer. Once the model has been printed it requires post-processing including removal of excess resin through washing in isopropyl alcohol (IPA) before a final UV cure to ensure the bonding of the resin is complete. All FormLabs resins are Polymethylmethacrylate (PMMA) based with a 405 nm photoinitiator. Two resin formulations were used in this thesis, a Clear and a High Temp. To achieve the high temperature properties of the high temp resin a further cure at 180°C for 5 hours was undertaken. SLA prints are better suited to those with smaller details or a requirement to be watertight.

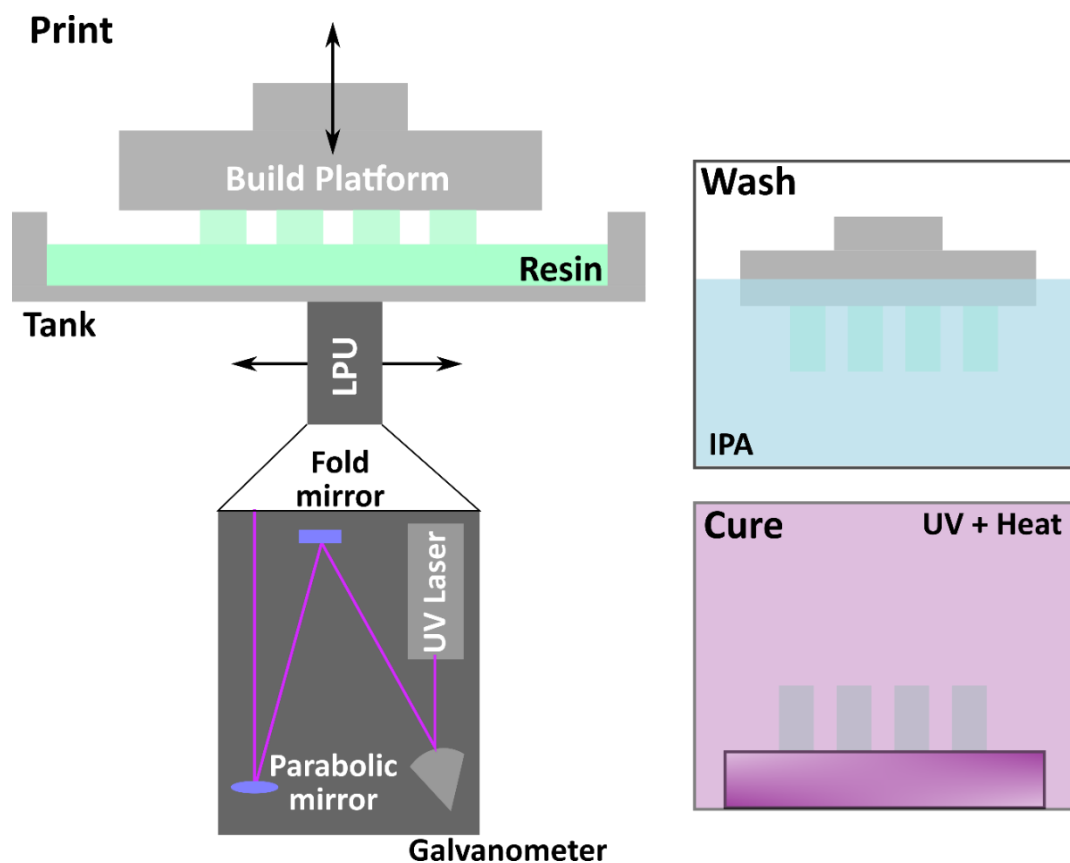


Figure 2.2 Schematic of a stereolithographic printer based on the mechanism of a Formlabs Form 3 printer including the wash and cure steps.



### 2.4.3 X-ray Fluorescence

A Rigaku NEX-CG: 50 kV Pd X-ray tube secondary carousel system with Cu, Mo, Al and RX9 (polarising target) was used with a Zr collimator, an irradiated 24 x 22 mm (oval) spot size was interrogated. All XRF analysis was undertaken with the following parameters: vacuum, Mo target, 300 s live time, automatic current, 1.6  $\mu$ s shaping time. Cu excitation was most efficient on the molybdenum secondary target providing the best signal to noise ratio.

### 2.4.4 White Light Interferometry

White light interferometry is used to measure topography of a surface through optical interference. A broad-spectrum light source is used that is collimated using a condenser lens. The light is split into two beams, one reflected from a reference mirror and the other scattered by the sample. The reflected beams are relayed to a charge coupled detector, forming an interference pattern.<sup>7</sup> From this, topographical information from the sample can be determined with sub-nm resolution. A Bruker ContourGT (Bruker, USA) was used to determine surface area of BDD-Q electrodes used in this thesis.

## 2.5 Electrochemical Characterisation

To ensure the BDD was sufficiently doped and the electrode manufacture had created a decent electrical contact a series of electrochemical measurements were undertaken.

### 2.5.1 Capacitance

The BDD electrode was polished with alumina rinsed and placed in a 0.1 M KNO<sub>3</sub> solution to ensure a clean surface was measured. In a three electrode set up, alongside an SCE as a reference and Pt wire as a counter electrode, a CV was employed between - 0.1 V and 0.1 V starting at 0 V at 0.1 V s<sup>-1</sup> until a stable response was observed to measure the capacitance. The final CV was analysed according to Equation 2.1;

$$C_{dl} = \frac{i_{av}}{\nu A}$$

Equation 2.1

Where  $C_{dl}$  is the capacitance of the double layer ( $\mu$ F cm<sup>-2</sup>),  $i_{av}$  is the average current (A) of the forward and reverse cycle at 0 V,  $\nu$  is the scan rate (V s<sup>-1</sup>) and

A is electrode area (cm<sup>2</sup>). High quality BDD is expected to have a capacitance value <10 μF cm<sup>-2</sup>.<sup>8</sup>

### 2.5.2 Solvent Window

A solvent window is the potential range within which an electrode material could be used for analytical measurements before solvent oxidation and reduction dominate the current response. A CV is measured across a large potential range, up to ± 2.5 V, in a three electrode set up in 0.1 M KNO<sub>3</sub> for 3 cycles. The current of the second CV was converted to current density (mA cm<sup>-2</sup>). The potential range within ± 0.4 mA cm<sup>-2</sup> is taken as the solvent window.<sup>8</sup> For high quality metal-like BDD the solvent window is expected to exceed 3 V, any incorporated sp<sup>2</sup> material will reduce this range.<sup>8</sup>

### 2.5.3 Redox Electrochemistry

A well-defined redox mediator, in this case ruthenium hexamine (Ru(NH<sub>3</sub>)<sub>6</sub><sup>3+</sup>), is used to probe the material and contact quality. This particular mediator on BDD is advantageous as it shows fast, outer sphere electron transfer and is electroactive in a region challenging for semiconductive BDD.<sup>8</sup> A CV is run between + 0.2 V and - 0.5 V in 1 mM Ru(NH<sub>3</sub>)<sub>6</sub><sup>3+</sup> with 0.1 M KNO<sub>3</sub> at a variety of scan rates between 0.05 V s<sup>-1</sup> and 0.25 V s<sup>-1</sup>. The voltage separation (ΔE<sub>p</sub>) between the reductive and oxidative peaks at 0.1 V s<sup>-1</sup> can be compared to theory; a value < 70 mV is expected for a well doped BDD electrode with a good ohmic contact under standard conditions, although the theoretical value is 57/n mV.<sup>9</sup> Additionally the reductive peak current (i<sub>p</sub>) at the different scan rates can be correlated to theory through the Randles-Sevcik equation (Equation 2.2).

$$i_p = 0.4463nFAC \left( \frac{nFvD}{RT} \right)^{\frac{1}{2}} \quad \text{Equation 2.2}$$

Where  $n$  is the number of electrons transferred,  $F$  is Faradays Constant,  $C$  is concentration of redox couple,  $D$  is the diffusion coefficient,  $R$  is the ideal gas constant and  $T$  is temperature (K). For a rotating disc electrode, such as the one

used in Chapter 5, using the same redox mediator but varying the rotation speed the hydrodynamics can be compared to the Levich equation (Equation 2.3).

$$i_l = (0.620)nFAD^{2/3}\omega^{1/2}v^{-1/6}C \quad \text{Equation 2.3}$$

Where  $i_l$  is the limiting current and  $\omega$  is rotation speed in rpm.

#### 2.5.4 Quinone surface coverage measurement

For electrodes with deliberate  $sp^2$  carbon incorporation measurement of the relative amount of  $sp^2$  carbon can be useful to compare electrode behaviours. An indirect measure using quinone electrochemistry can be used to infer the  $sp^2$  carbon content.<sup>4</sup> A CV is run in 0.1 M  $H_2SO_4$  at 0.1  $V s^{-1}$  between 0 V to - 2 V to + 2 V and back to 0 V for 20 cycles in the three electrode set up. The electrodes are rinsed and placed into a pH 2 Carmody buffer solution. Carmody buffers were prepared as previously described using boric acid (99% Scientific Lab Supplies, UK), citric acid (>99.5%, Fisher Chemical, UK), and tertiary sodium phosphate (extra pure, Arcos Organics, UK).<sup>10</sup> Quinone surface coverage (QSC) analysis was undertaken in a pH 2 Carmody buffer using CV between 0 and 0.7 V vs. SCE at 0.1  $V s^{-1}$ .<sup>10</sup> The peak between 0.25 and 0.6 V is baselined with a straight line and integrated to give the area under the peak ( $A_p$ ). The quinone surface coverage ( $\Gamma$ ) is calculated by

$$\Gamma = \frac{A_p}{nAFv} \quad \text{Equation 2.4}$$

where  $n$  is the number of electrons transferred,  $A$  is the electrode surface area and  $F$  is Faradays Constant and  $v$  is scan rate in  $V s^{-1}$ .

## 2.6 References

- 1 L. A. Hutton, M. E. Newton, P. R. Unwin and J. V. Macpherson, *Anal. Chem.*, 2009, **81**, 1023–1032.
- 2 L. A. Hutton, J. G. Iacobini, E. Bitziou, R. B. Channon, M. E. Newton and J. V. Macpherson, *Anal. Chem.*, 2013, **85**, 7230–7240.
- 3 S. J. Cobb, F. H. J. Laidlaw, G. West, G. Wood, M. E. Newton, R. Beanland and J. V. Macpherson, *Carbon N. Y.*, 2020, **167**, 1–10.
- 4 Z. J. Ayres, S. J. Cobb, M. E. Newton and J. V. Macpherson, *Electrochem. commun.*, 2016, **72**, 59–63.
- 5 Z. J. Ayres, A. J. Borrill, J. C. Newland, M. E. Newton and J. V. Macpherson, *Anal. Chem.*, 2016, **88**, 974–980.
- 6 T. L. Read, S. J. Cobb and J. V. Macpherson, *ACS Sensors*, 2019, **4**, 756–763.
- 7 P. Hariharan, *Acad. Press*, Basics of Interferometry, 2006.
- 8 J. V. Macpherson, *Phys. Chem. Chem. Phys.*, 2015, **17**, 2935–2949.
- 9 R. S. Nicholson and I. Shain, *Anal. Chem.*, 1964, **36**, 706–723.
- 10 W. R. Carmody, *J. Chem. Educ.*, 2009, **40**, A386.

## 3 Assessment of a boron doped diamond ring disc buffer capacity sensor

---

### 3.1 Overview

This chapter considers the feasibility of using a boron doped diamond (BDD) based ring disc electrode for buffer capacity measurements. The ring disc electrode consisted of a BDD ring used to oxidise water to produce protons ( $H^+$ ) and a quinone functionalised BDD disc (BDD-Q) for voltammetric pH measurement. Water oxidation was driven galvanostatically on the ring, in a range of different buffer capacity solutions whilst sequential pH measurements were made on the BDD-Q disc. A shift in the BDD-Q peak potential to more positive potentials is observed with time in both unbuffered and buffered solutions indicating an increasingly acidic local environment due to proton generation on the ring. As buffer capacity increased the time taken to reach a uniform acidic environment increased. Double peaks or broadened peaks were observed within the time-dependent voltammetric scans during the measurement in the presence of buffer. With the aid of finite element modelling it is shown that a pH gradient is formed across the BDD-Q disc during the measurement, the pH gradient is prolonged in the presence of buffer. The spatial arrangement of quinone groups on the BDD-Q disc was explored and found to affect the timescale and end point of the measurement. This technology shows promise for use as a buffer capacity sensor although sensitivity decreases significantly above buffer concentrations of 20 mM. However, the range is likely adequate for environmental water sampling. Some design improvements that could improve the sensitivity are also suggested.

## 3.2 Introduction

Buffers are typically composed of a weak acid or base and its conjugate salt;



When  $H^+$  ions are added, the equilibrium is shifted according to Le Chatelier's Principle, consuming the excess  $H^+$  and increasing the concentration of HA, Equation 3.1, favouring the reverse reaction.<sup>1</sup> When  $OH^-$  ions are added, in the presence of buffer species,  $H^+$  neutralise the  $OH^-$ , which acts to decrease the proton concentration forcing HA to dissociate, Equation 3.1. Additionally  $H_2O$  can undergo autoionisation to  $H_3O^+$  and  $OH^-$ , thus in itself water has some buffer capacity.  $K_w$  is the autoionisation constant for water, which is pH and temperature dependent.

There is a finite concentration of buffering species in a solution. Once the acid species are fully deprotonated, or the base species protonated, the pH will change in response to excess  $H^+$ , or  $OH^-$  ions. Buffer capacity, often used interchangeably with alkalinity, is a measure of the efficiency of a buffer to withstand a pH change. Typically, buffer capacity ( $\beta$ ) is expressed as the amount of strong acid or base added ( $\Delta B$ ) to change the pH of 1 L of solution by one unit, Equation 3.2.<sup>2</sup>

$$\beta = \frac{\Delta B}{\Delta pH} \quad \text{Equation 3.2}$$

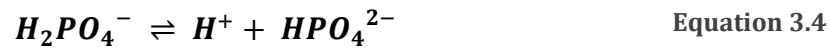
The buffer capacity depends on two factors; the total buffer concentration and the ratio of acid or base to conjugate salt. Buffer capacity is optimal when the ratio of acid or base to conjugate salt is 1:1, in other words when  $pH = pK_a$ .<sup>2</sup> The relationship between buffer capacity and buffer concentration is described by the Van Slyke equation:<sup>3</sup>

$$\beta = 2.3C \frac{K_a [H_3O^+]}{(K_a + [H_3O^+])^2} \quad \text{Equation 3.3}$$

Where  $C$  is the total buffer concentration and is equivalent to the molar concentration sum of acid and salt, and  $K_a$  is the acid dissociation constant.

Buffer capacity is important for a variety of situations. Biologically most enzymes only function within a narrow pH range. Phosphoric acid ( $H_3PO_4$ ) is triprotic and thus has three theoretical  $pK_a$  values, 2.16, 7.21 and 12.32.<sup>4</sup> Phosphate buffer,

consisting of hydrogen phosphate ( $\text{HPO}_4^{2-}$ ) and dihydrogen phosphate ( $\text{H}_2\text{PO}_4^-$ ) ions in equilibrium, Equation 3.4, is commonly used in biological sciences as it buffers well between pH 6.4 and 7.4, the physiological range, and doesn't interfere with biological processes.<sup>5</sup>



pKa values are theoretically derived assuming a very dilute solution containing water and no other ions.<sup>6</sup> In reality, weak acids dissociate more readily in aqueous solutions due to solvation of the ions dampening attraction between the dissociated ions. Ionic solutions further act to dampen the attraction as the dissociated ions can be surrounded by ions of opposite charge. These effects act to encourage dissociation and act to lower the solution pKa compared to the theoretical pKa. This effect is greater for multivalent ions such as phosphate, a polyprotic acid.

Environmental systems are also buffered, to varying extents, dependent on a number of factors. Natural water systems (fresh and saline) contain dissolved  $\text{CO}_2$  from the atmosphere. Water bodies found in areas with limestone ( $\text{CaCO}_3$ ) geology will contain additional dissolved carbonate ions so will have a higher buffer capacity. Due to the  $\text{Ca}^{2+}$  and  $\text{Mg}^{2+}$  cations commonly associated with carbonate minerals, areas with hard water generally have more buffer capacity. Soft water areas, generally where water flows over sandstone or granites, usually show reduced alkalinity. As such water hardness can be a good indicator of buffer capacity. However, dissolved potassium and sodium carbonate whilst not adding to water hardness do increase buffer capacity so hardness should only be used as a rough guide.<sup>7,8</sup> Carbonate is the dominant buffer species found in the environment, as described in Equation 3.5:



Other species that can contribute to buffer capacity include borate, sulfate, phosphate, silicate, fluoride, hydrogen sulfide and ammonia.<sup>8-10</sup> Organic molecules such as humic substances or phytoplankton-derived dissolved organic compounds can also bind  $\text{H}^+$  and thus offer a buffering capacity.<sup>10</sup> A vast number of biogeochemical processes can act to increase or decrease the concentrations

of buffering species in the environment. Aquatic respiration releases CO<sub>2</sub> which will help increase buffer capacity. Conversely aquatic photosynthesis will consume CO<sub>2</sub> which will decrease buffer capacity.<sup>8</sup> Dissolution of minerals is often accompanied by increased buffer capacity. Processes that act to dilute or concentrate salinity, such as precipitation, evaporation and melting or formation of ice also dilute or concentrate buffer capacity.

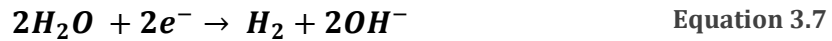
All life forms have an optimum pH range, therefore the ability to resist a pH change in the environment is beneficial. Aquatic life functions optimally between pH 6.0 and 9.0. Anthropogenic wastewater can change the buffer capacity of a water body. Municipal wastewater often contains significant concentrations of calcium and bicarbonate. Acidification of natural water bodies is a pressing global problem.<sup>8</sup> Acidification can affect geochemical cycles and result in the release of toxic heavy metals from complexed forms to solvated forms. Increasing atmospheric CO<sub>2</sub> is resulting in acidification of the oceans, which is in turn causing increased dissolution of calcium carbonate creatures and a rise in the calcite compensation depth by ~ 300 m in some areas.<sup>11-13</sup> Not as much research has been undertaken on the effect of rising atmospheric CO<sub>2</sub> concentrations in freshwater, but the consensus is that acidification is also happening in freshwater systems; the impacts of this are still being investigated.<sup>14,15</sup> There are requirements for a portable or *in-situ* buffer capacity measurement technique to monitor long term trends.

### **3.2.1 Buffer capacity measurements**

Buffer capacity or alkalinity measurements are most often discrete measurements with samples typically analysed by titration. Titrations are effectively a two component measurement, a deliberate perturbation of pH and a measurement of that perturbation. To measure solution pH, the most commonly used technique is the glass potentiometric pH probe.<sup>16</sup> The pH probe consists of an amorphous silicon oxide membrane which can protonate and deprotonate corresponding to the solution composition. Protonation or deprotonation changes the membrane potential, which is measured relative to an internal reference.<sup>16</sup> Glass pH probes work well with traditional titration methods, where the addition of an acid or base titrant perturbs the pH. However



manual addition of a titrant is not feasible for either long term or *in-situ* measurements. For an *in-situ* alkalinity sensor, perturbation of solution pH (by potentiostatic or galvanostatic electrolysis of water) using a secondary electrode is an attractive prospect, Equation 3.6 and Equation 3.7. Both processes result in a pH change:



The polarity of the current/potential determines whether  $\text{H}^+/\text{OH}^-$  are generated, while the magnitude determines the end point of the titration. Under stationary conditions, if the pH sensing element is in the immediate vicinity of the titrant source, diffusion can be relied upon for distribution of the titrant, Figure 3.1. For portable measurement equipment, miniaturisation of the glass probe is often required to enable easy incorporation. However, this results in extremely fragile probes which are unsuitable for the proposed application.

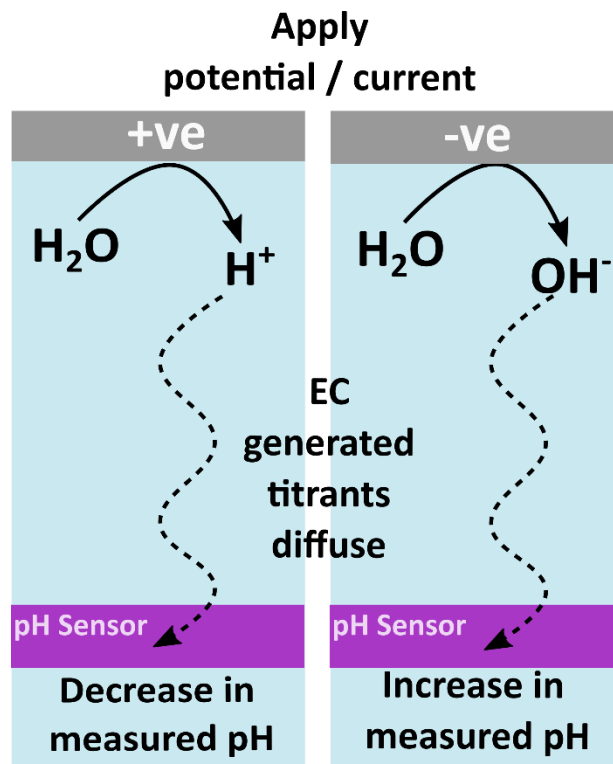


Figure 3.1 Schematic of electrochemical generation of proton or hydroxide ions through the oxidation or reduction of water respectively, diffusion into solution and detection of pH change.

### 3.2.2 Miniaturised pH sensors and alkalinity sensors

A variety of miniaturised pH sensors are currently available. Potentiometric metal oxides,<sup>17</sup> of which iridium oxide ( $\text{IrO}_2$ ) is the most commonly used,<sup>18</sup> are relatively popular. However,  $\text{IrO}_2$  does suffer from slow response times, potential drift and challenges in fabrication. Ion-selective field effect transistors (ISFET),<sup>19,20</sup> whilst being more structurally stable than glass probes and metal oxide sensors, with a fairly good response time, show potential drift over time.<sup>21</sup> Quinone type molecules integrated robustly into discrete micro-spotted regions of the surface of boron doped diamond (BDD-Q) electrodes have recently shown much promise as a drift free, fast responding voltammetric pH sensors in both buffered and unbuffered solutions.<sup>22,23</sup> Non-electrochemical methods are also available for pH sensing such as optical pH sensing and rely on absorbance, luminescence or fluorescence. However, they typically require larger instrumentation for analysis hence reducing their practicality for a portable device.<sup>24</sup>

ISFET pH electrodes have been used as alkalinity sensors due to their small size, rapid response and the ability to integrate a proton generation electrode into the design.<sup>25-31</sup> The pH change as a function of time can be used to infer buffer capacity. A commercial product by Thermo Electron, the Orion FLASH Titrator™, was introduced in the early 2000s. A platinum generating electrode was used which allowed manipulation of polarity and magnitude (to ensure measurement was completed within 10 s), applying either a constant current (3, 20 or 100  $\mu\text{A}$ ) or a current ramp (4, 8 or 12  $\mu\text{A s}^{-1}$ ). The probe was calibrated using two solutions of known buffer capacity. A matrix factor adjustment could be undertaken for more complex samples either by titrating a sample volumetrically and then calibrating to the Orion FLASH Titrator™, or by calibrating with a 50%, 100% and 200% diluted sample. However the technology was not successful due to sensor degradation and the need to tailor the method to the sample media through complex calibration steps and measurement protocols.<sup>31</sup>

A more recent study modified a Honeywell ISFET, by sputtering a thin film of Pt, spaced 100 – 150  $\mu\text{m}$  from the ISFET gate, schematically shown in Figure 3.2. The Pt was used as a generating electrode to oxidise water, the  $\text{H}^+$  then diffuse over

the ISFET which reacts to the changing pH. This device was specifically optimised to monitor the total alkalinity of seawater ( $2200 - 2500 \mu\text{mol kg}^{-1}$ ). A constant current of  $10 - 15 \mu\text{A}$  was found to be optimum in seawater titrations with measurements taking  $25 - 40 \text{ s}$  to complete. Linearity was observed between total alkalinity and  $t_{\text{end}}^{1/2}$  determined by the second inflection of the first derivative of the titration.<sup>31</sup> This technology was modified and integrated into a SeapHOx probe and integrated into a Seabird submersible pump. A series of four check valves were used to control flow through the pump so titration could be undertaken in a quiescent sample. This was successfully used to measure pH and alkalinity of seawater every two minutes for six days.<sup>32</sup> A thin film of Pt is however unstable for long periods of time. The platinum will oxidise and chloride ions which are known to adsorb onto Pt surfaces, can cause corrosion of the Pt surface.<sup>33-35</sup>

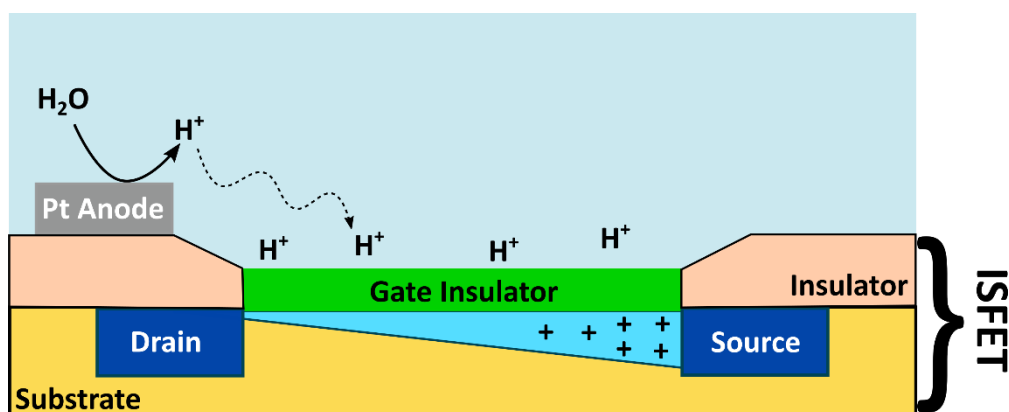


Figure 3.2 Schematic of modified ISFET for alkalinity measurements, modified from Ref 31.

An alternative electrochemical approach, using two ion selective membranes has also been reported using a separate proton source membrane and detector membrane, shown schematically in Figure 3.3.<sup>36</sup> A thin layer of sample solution ( $40 \pm 5 \mu\text{L}$ ) lies between two membranes. A  $300 \text{ mV}$  pulse was applied to the proton source membrane for times from  $30$  to  $120 \text{ s}$ . Stirring the solution between pulses helped equilibrate the solution in the thin channel to bulk concentrations. As the pulse length increased the pH decreased linearly in the absence of base. Expected titration curves were produced with the addition of  $\text{NaOH}$  and  $\text{Na}_2\text{CO}_3$ , with one or two equivalence points observed, respectively.

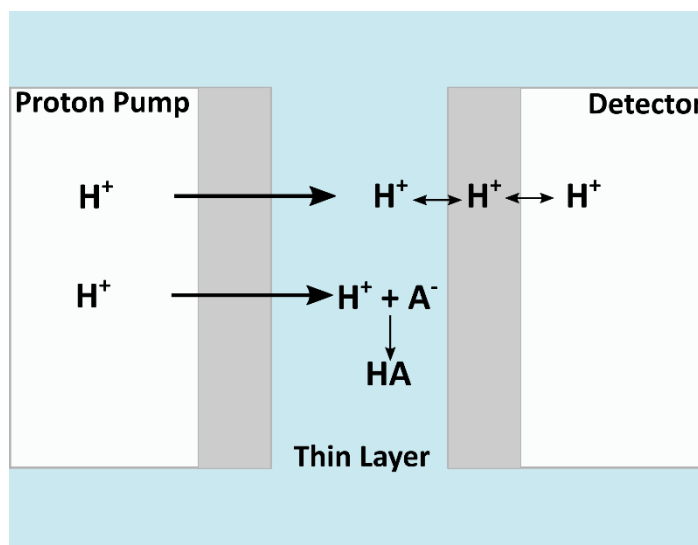


Figure 3.3 Schematic of ion selective membrane alkalinity sensor modified from Ref 36.

The charge released from the proton pump was determined by integrating the output current over the pulse time and plotting against the pH change.<sup>36</sup> This technique was trialled in a river sample. The first derivative was used to determine the equivalence point and the bicarbonate concentration determined to be 23.1 mM. For the same sample a traditional titration provided a concentration of 23.6 mM.<sup>36</sup> This system was used for pH and alkalinity determination of a stratified lake, with measurements undertaken at the shore.<sup>37</sup> It is unclear whether the long term aim would be for this sensor to be on an automated system or remain a user driven device for on-site measurements of manually collected samples. A 0.5 mV h<sup>-1</sup> drift was measured on the pH detection and proton pump membranes calling into question the lifetime of the membranes and the viability of this technique for long term measurements.<sup>38</sup>

A summary of the three technologies is presented in Table 3.1. Although the ISFET technology has advanced from the Orion FLASH Titrator™, issues still remain. The main advantage of the ISFET device is the speed at which the titration could occur. The modification of the Honeywell ISFET with a sputtered platinum generator electrode would not be stable over long term measurements and platinum is not an efficient electrode material for water oxidation, particularly in the presence of chloride. The device utilising membranes is advantageous due to the selectivity to only produce and detect H<sup>+</sup>. Whereas

electrochemical generation of H<sup>+</sup> through water oxidation also produces oxygen, and depending on the applied potential and solution composition could oxidise other species such as chloride reducing the efficiency of the generator. However, in the current form a trained user would still be required and there are issues with drift indicating an issue with the sensor stability over time.

**Table 3.1 Summary table of alkalinity sensor devices.**

Technology	Titrant Generation	pH detection	Advantages	Disadvantages
Thermo Electron Orion FLASH Titrator™	Platinum electrode for water oxidation	ISFET	Fast titration	Side reactions from water splitting Failed commercial product Complex methodologies / calibration
Modified Honeywell ISFET	Platinum electrode for water oxidation	ISFET – Honeywell	<60 s response Nanolitre sample volume Optimised for seawater range Can be made autonomous	Stability of sputtered platinum generation electrode Proton evolution efficiency is not 100% for Pt in presence of Cl <sup>-</sup> Inconsistent manufacture between devices
Proton source and proton selective membrane	Electrochemically driven transport of ions across ion-selective membrane into a thin layer channel	pH sensitive membrane	No production of O <sub>2</sub> Proton selective Absence of fouling affects in natural waters Good agreement with traditional titrations	Unclear as to whether this could be made autonomous Stability of membranes over long term (0.5mV h <sup>-1</sup> drift)

BDD electrodes offer an advantage over the technologies discussed specifically for long term sensing due to the inherent stability of the material.<sup>39</sup> A BDD generator electrode material will remain stable and undamaged. Through ablation of the BDD surface, an extremely robust form of sp<sup>2</sup> bonded carbon is introduced into the surface, which contains surface bound quinones which undergo proton coupled electron transfer.<sup>23</sup> This results in a pH sensitive device (BDD-Q). The three previous technologies discussed all utilise potentiometric pH detection techniques to measure the locally perturbed pH. The quinone response of the BDD-Q is voltammetric, which offers advantages in terms of sensitivity and measurement time. This study utilises a BDD-Q pH sensor in a ring disc configuration as a new method for measuring buffer capacity. Its performance properties are assessed below. The sensor design builds on the development on a BDD ring disc demonstrated by Read *et al.*,<sup>40,41</sup> by incorporating the BDD-Q electrode as the disc electrode.<sup>22,23</sup> H<sup>+</sup> ions are generated through the oxidation of water at a BDD ring, with the resulting decrease in pH measured at the BDD-Q disc. This format of sensor could provide stable, *in-situ*, long term method of buffer capacity measurement.

## 3.3 Experimental

### 3.3.1 Solution preparation.

All solutions were prepared with Milli-Q water (Millipore Corp.), with a resistivity of 18.2 M $\Omega$  cm at 25°C. All reagents were used as received. Potassium nitrate (KNO<sub>3</sub>; 99%, Arcos Organics, UK) was used as a supporting electrolyte. To calibrate the BDD-Q sensor, Carmody buffers were prepared using boric acid (99% Scientific Lab Supplies, UK), citric acid (>99.5%, Fisher Chemical, UK), and tertiary sodium phosphate (extra pure, Arcos Organics, UK).<sup>42</sup> Fresh solutions were prepared for each calibration and the pH was verified using a commercial glass pH probe and meter (SevenEasy, Mettler Toledo). The pH meter was calibrated using Mettler Toledo standard solutions (pH 4, 7 and 10) as per manufacturer guidelines. Dilute solutions of sulfuric acid (H<sub>2</sub>SO<sub>4</sub>;  $\geq$  95%, Fisher Scientific, UK) and potassium hydroxide (KOH; 85%, Fisher Scientific, UK) were used to titrate a 0.1 M KNO<sub>3</sub> solution to evaluate the BDD-Q sensors performance in unbuffered systems. A 0.1 M phosphate buffer stock was prepared using sodium phosphate dibasic heptahydrate (>98%, Sigma-Aldrich, USA) and sodium phosphate monobasic monohydrate (>98%, Calbiochem, Merck, Germany) and diluted to the desired concentrations, 0.1 to 40 mM, by dilution with 0.1 M KNO<sub>3</sub>. A 0.1 M borate buffer solution was also prepared using boric acid powder (>99%, Scientific Laboratory Supplies Ltd., UK) and sodium hydroxide (>99.99%, Sigma-Aldrich, USA) also diluted to the desired concentrations, 0.1 to 40 mM, by dilution with 0.1 M KNO<sub>3</sub>. For solutions containing OH<sup>-</sup> ions, KOH was added to a 0.1 M KNO<sub>3</sub> solution, the pH was measured using the commercial glass pH probe. Experiments were undertaken in a temperature controlled lab at 22-23°C.

### 3.3.2 Fabrication of ring disc electrode.

BDD ring disc electrodes were prepared from a 6 in. freestanding polycrystalline BDD wafer (357  $\mu$ m thick, Electroanalytical Grade, Element Six, Harwell, UK) polished on the growth face to nm roughness and lapped on the nucleation face. The desired electrode geometries were cut using a 355 nm Nd:YAG 34 ns laser micro-machining system (E-355H-ATHI-O system, Oxford Lasers). A support for the ring disc electrode was manufactured from optical grade intrinsic diamond

(Element Six, Harwell, UK). Two recesses were laser cut to house the ring and disc electrodes and to ensure the spacing remained even.

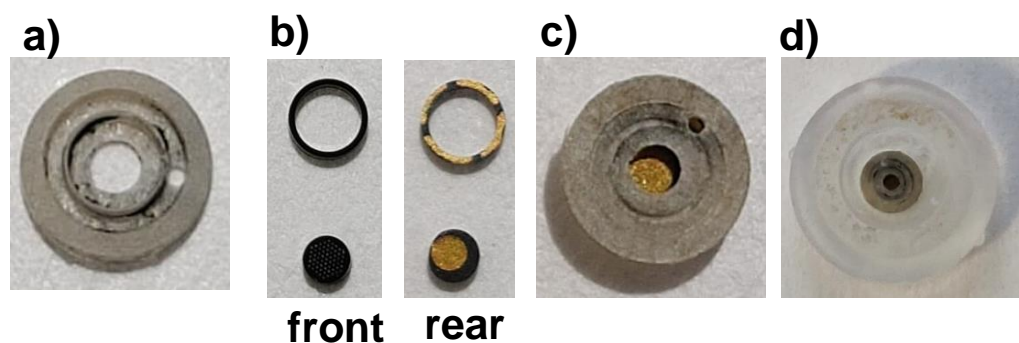


**Figure 3.4** Stages of BDD-Q ring disc electrode fabrication; a) an image of the intrinsic diamond ring disc support (diameter 2.2 mm) with holes for wire contacting. b) Two images of the BDD ring (ID 1.4 mm, OD 1.8 mm) and disc electrodes (1 mm diameter) from the front face and showing the Ti/Au contacts on the rear. c) An image of the BDD ring and disc in position in the support from the rear. d) An image of the BDD ring disc and support in the 3D printed electrode cap.

Two holes were cut in the support located behind both the ring and disc recess in order to place wires onto the back of the electrodes during manufacture. The disc comprised of a 1 mm diameter BDD cylinder and the ring electrode of a BDD tube of 1.4 mm inner diameter and 1.8 mm outer diameter, Figure 3.4b. The BDD electrodes and support were subjected to a hot acid cleaning procedure as outlined in Section 2.3.1.1.

pH sensitive microspots were then added to the disc using laser ablation which converts the  $sp^3$  bonded diamond regions to  $sp^2$  bonded carbon. For most studies, a pattern of 61 pH sensitive spots,  $\sim 10 \mu\text{m}$  deep, were ablated into the BDD surface using the laser micromachining system. The spots were produced by rastering the laser beam in a circular pattern with a nominal pulse density of  $1 \times 10^6$  pulses per  $\text{cm}^2$ . A pulse fluence of  $\sim 14 \text{ J cm}^{-2}$  just above the ablation threshold of diamond was employed. A second pattern consisted of a trench of inner diameter 0.8 mm and outer diameter 0.9 mm, ablated into the BDD, to a depth of  $\sim 12 \mu\text{m}$ . The ablated discs were then hot acid cleaned as described in Section 2.3.1.1, but did not undergo the thermal anneal as it was important to retain the  $sp^2$  bonded carbon areas. To ensure the pH sensitive spots or trench did not become blocked by the insulating epoxy resin used for fabrication the



surface was protected with a layer of polyvinyl alcohol (Wilkinsons, UK) applied to the 1 mm disc using a needle.

To form a reliable ohmic contact Ti (10 nm) / Au (400 nm) was sputtered (Moorfields MiniLab 060 platform sputter/evaporator) onto the rear of the BDD disc and ring and annealed in air at 400°C for 5 h, Figure 3.4b rear. A small amount of superglue was carefully placed onto the intrinsic diamond support to secure the BDD ring and disc to the support, ensuring the Ti/Au contact was not covered by the adhesive, Figure 3.4c. Once secure the intrinsic diamond support and electrodes were placed in an insulating surround 3D printed (Form 3, Formlabs, USA) in clear resin (Formlabs, USA), Figure 3.4d. Silver plated copper wires (450  $\mu\text{m}$ ; RS Components, UK) were contacted to the ring and disc electrodes using conductive epoxy (Chemtronics, CircuitWorks). Once the conductive epoxy resin had set the wires were secured in place with an epoxy resin (Epoxy Resin RX771C/NC, Aradur Hardener HY1300GB, Robnor Resins) and the front face of the electrode also filled with epoxy resin to ensure no gaps were present between the 3D print and the sidewalls of the electrodes.

The surface of the BDD electrodes was exposed by gently polishing on increasingly fine carbide grit paper, ensuring the protective layer of polyvinyl alcohol was removed. The resulting device is shown in Figure 3.5. A final polish on wet alumina-particle coated (0.05  $\mu\text{m}$ , Buehler, Germany) polishing pads was made. Finally, the wires were mechanically protected by sealing borosilicate capillaries (inner diameter 0.6 mm and outer diameter 1.2 mm) to the base of the set resin. To ensure the polyvinyl alcohol and any remaining resin on the electrode surface was fully removed, the disc and ring electrodes were cycled between  $\pm 2$  V in 0.1 M  $\text{H}_2\text{SO}_4$  until the response was stable, typically 20+ cycles.

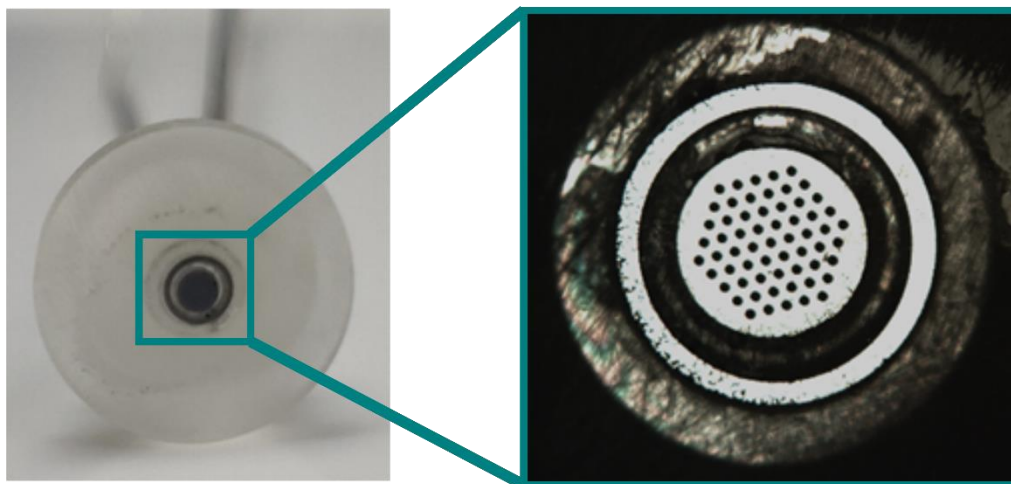


**Figure 3.5** Image of fabricated ring disc electrode and optical microscopy image of BDD ring disc with microspot array. Central disc diameter is 1 mm.

### **3.3.3 Experimental set up**

Electrochemical measurements on the BDD-Q disc were undertaken using a potentiostat (PGSTAT101, Metrohm Autolab), using a three electrode set up. The BDD-Q disc served as the working electrode, a saturated calomel electrode (SCE) as the reference and a platinum coil as the counter electrode. For generation-detection experiments a galvanostat was used (Keithley 6430 Sub-Femtoamp Remote Source Meter) to apply 70  $\mu\text{A}$  between the BDD ring electrode and a second platinum coil counter electrode, Figure 3.6. Voltammetric pH measurements were made on the disc using square wave voltammetry (SWV). Continuous SWV scans were recorded on the BDD-Q disc electrode throughout the experiments at each condition explored. Six scans were taken prior to application of the current to the ring to measure the starting pH of the solution. The SWV scans continued on the disc when turning the current supply on until the SWV peak position stabilised.

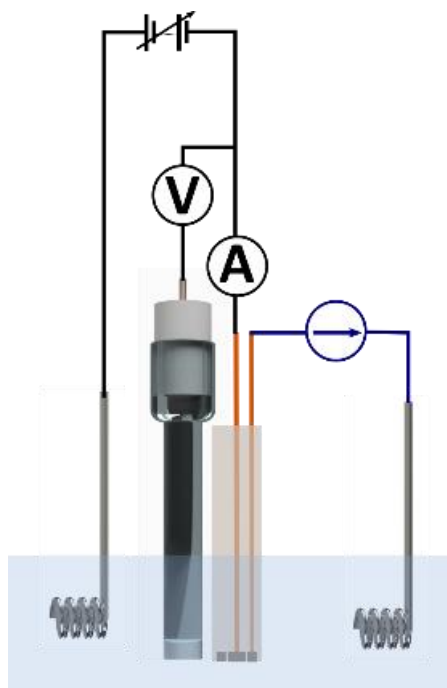


Figure 3.6 Schematic of the electrode set up for buffer capacity measurements. From left to right, Pt coil counter electrode, SCE reference, ring disc electrode, the counter reference and disc are connected to the Autolab potentiostat. A constant current ( $70 \mu\text{A}$ ) is applied between the ring of the ring disc and the second Pt coil counter.

### 3.3.4 Electrochemical characterisation.

Both the ring and the BDD-Q disc were characterised prior to starting proton generator-pH measurement experiments to assess the quality of the electrode material and to confirm the electrode fabrication procedure was successful. Solvent window and capacitance measurements were performed in  $0.1 \text{ M KNO}_3$  solutions, by performing cyclic voltammetry (CV) at a rate of  $0.1 \text{ V s}^{-1}$  between  $\pm 2 \text{ V vs. SCE}$  and  $\pm 0.1 \text{ V vs. SCE}$ , respectively. The solvent window was determined as the potentials between which  $\pm 0.4 \text{ mA cm}^{-2}$  are passed. Capacitance ( $C$ ) was determined, at a fixed scan rate of  $0.1 \text{ V s}^{-1}$  using  $C = i_{\text{average}}/\nu A$  where  $i_{\text{average}}$  is the average current at  $0 \text{ V vs. SCE}$  in the anodic and cathodic sweep (standard digital staircase voltammetry was used,  $1 \text{ mV}$  step),  $\nu$  is the scan rate and  $A$  is the surface area as determined by white light interferometry (Bruker ContourGT, Germany).<sup>39</sup>

Quinone surface coverage (QSC) analysis was undertaken in a pH 2 Carmody buffer using CV between  $0$  and  $0.7 \text{ V vs. SCE}$  at  $0.1 \text{ V s}^{-1}$ .<sup>42</sup> The peak between  $0.25$  and  $0.6 \text{ V}$  is baselined with a straight line and integrated to give the area under

the peak ( $A_p$ ). The quinone surface coverage ( $\Gamma$ ) is calculated by  $\Gamma = \frac{A_p}{nAFv}$  where  $n$  is the number of electrons transferred,  $A$  is the electrode surface area and  $F$  is Faradays Constant and  $v$  is scan rate in  $V s^{-1}$ .

SWV was used for the pH measurements on the BDD-Q disc at a frequency of 150 Hz, a modulation amplitude of 50 mV and a step potential of 4 mV across the range 0.5 to -0.3 V vs. SCE. SWV for bulk pH measurements in Carmody buffers at pH values of 2, 4, 7 and 10 were taken, with six measurements per pH. The average peak position for scans 2-6 were plotted against the pH of the buffer solutions, measured using a glass pH probe, to provide a calibration line, fitted to the equation  $E_p = mpH + c$ , where  $E_p$  is the peak potential and  $m$  and  $c$  are the gradient and intercept determined by the calibration. The same protocol was used to evaluate the pH response in unbuffered solutions, starting at pH 10 and adding acid ( $H_2SO_4$ ) dropwise until pH 2.5. For proton generation-pH measurement experiments, the SWV was recorded continuously along with the measurement time. Each scan takes 1.35 s + approx. 1 s between scans. Peak positions were taken from the SWV data using NOVA 2.4.1 peak picking tool as part of the measurement protocol. The peak positions were converted to pH using the calibration line measured the same day and plotted against time from application of the current to the ring.

### 3.3.5 Reactive-transport Modelling

The pH change at the surface of the ring disc electrode was simulated using the finite element method (FEM) in Comsol Multiphysics 5.6 software (COMSOL, Sweden) by Dr. Ian Mcpherson, Department of Chemistry, University of Warwick. A  $45 \times 45 \text{ mm}^2$  axisymmetric domain was used to represent the system, with the bottom boundary subdivided to form the disc (boundary 1,  $0 < r < 0.5 \text{ mm}$ ), the ring (boundary 3,  $0.7 < r < 0.9 \text{ mm}$ ) and the epoxy sections (boundary 2); the top and right side boundaries (boundary 4,  $r = z = 45 \text{ mm}$ ) represented the bulk conditions and the left boundary coincides with the axis of symmetry, Figure 3.7.

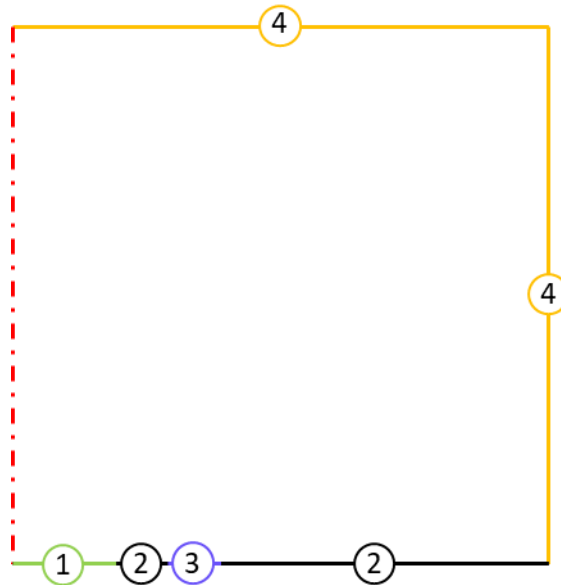


Figure 3.7 Schematic of the boundaries in the COMSOL model; 1 is the disc, 2 the insulating epoxy, 3 the ring, 4 the bulk conditions and the dash dot line the axis of symmetry.

The disc (boundary 1) was assumed to be inert, such that there is no flux at this boundary. The epoxy boundaries (boundary 2) similarly had no flux condition applied. A flux of  $H^+$  proportional to the current density was applied to the ring (boundary 3; Equation 3.8).

$$\mathbf{n} \cdot \mathbf{j}_{H^+} = \frac{i}{AF} \quad \text{Equation 3.8}$$

Where  $A$  is the electrode area and  $F$  is Faraday's constant. The semi-infinite boundaries (boundary 4) were held at the equilibrium concentrations determined from initial modelling of the speciation with the PHREEQC code.<sup>43</sup>

The model assumes speciation based on the PHREEQC database,<sup>43</sup> and considers the transport of the 9 most significant species (Table 3.2). Flux of the  $i$ th species,  $J_i$ , at concentration  $c_i$ , with diffusion coefficient,  $D_i$ , is calculated using Fick's law (Equation 3.9). Equilibria between the species (Table 3.3) are maintained by the continuity equation (Equation 3.10), where  $R_i$  is the reaction flux based on the forward and backward components of the equilibrium reaction with a suitable rate constant (Table 3.3 and Table 3.4). Equilibrium constants were corrected for the local species activity  $a_i$  (Equation 3.11), calculated from the activity

coefficient  $\gamma_i$  based on the local ionic strength,  $I$  (Equation 3.12) using the Davies equation (Equation 3.13) with  $A=1.82 \times 10^6 (\epsilon T)^{-3/2}$ , where  $\epsilon = 78$  and  $T = 298$  K.

For charged species  $b = 0.3$ , for uncharged species  $b = 0.1$ .

$$j_i = -D_i \nabla c_i \quad \text{Equation 3.9}$$

$$\frac{\partial c_i}{\partial t} + \nabla \cdot j_i = R_i \quad \text{Equation 3.10}$$

$$a_i = \gamma_i c_i \quad \text{Equation 3.11}$$

$$I = \frac{1}{2} \sum z_i^2 c_i \quad \text{Equation 3.12}$$

$$\log_{10} \gamma_i = -A z_i^2 \left( \frac{\sqrt{I}}{1 + \sqrt{I}} - bI \right) \quad \text{Equation 3.13}$$

**Table 3.2 Diffusion coefficients applied in the FEM model**

Species	$D$ ( $10^{-5} \text{ cm}^2 \text{ s}^{-1}$ )
H <sup>+</sup>	9.311
OH <sup>-</sup>	5.273
H <sub>3</sub> PO <sub>4</sub>	0.84*
H <sub>2</sub> PO <sub>4</sub> <sup>-</sup>	0.846
HPO <sub>4</sub> <sup>2-</sup>	0.69
PO <sub>4</sub> <sup>3-</sup>	0.612
KHPO <sub>4</sub> <sup>-</sup>	0.581**
K <sup>+</sup>	1.957
NO <sub>3</sub> <sup>-</sup>	1.902

\*H<sub>3</sub>PO<sub>4</sub> value from reference <sup>44</sup> \*\*estimated from  $0.5 \cdot \sqrt{(D_{\text{HPO}_4} \times D_{\text{K}})}$

**Table 3.3 Chemical equilibria considered in FEM model**

Constants	Reaction	pK	$k_b$
$K1 = k_{f1}/k_{b1}$	$H_3PO_4 \rightleftharpoons H^+ + H_2PO_4^-$	2.168	$10^6 \text{ L mol}^{-1} \text{ s}^{-1}$
$K2 = k_{f2}/k_{b2}$	$H_2PO_4^- \rightleftharpoons H^+ + HPO_4^{2-}$	7.207	$10^6 \text{ L mol}^{-1} \text{ s}^{-1}$
$K3 = k_{f3}/k_{b3}$	$HPO_4^{2-} \rightleftharpoons H^+ + PO_4^{3-}$	12.346	$10^6 \text{ L mol}^{-1} \text{ s}^{-1}$
$K4 = k_{f4}/k_{b4}$	$K^+ + HPO_4^{2-} \rightleftharpoons KHPO_4^-$	0.29	$10^6 \text{ s}^{-1}$
$K_w = k_{fw}/k_{bw}$	$H_2O \rightleftharpoons H^+ + OH^-$	13.997	$10^9 \text{ L mol}^{-1} \text{ s}^{-1}$

**Table 3.4 Local flux of species from equilibrium reactions**

Species, $i$	Reaction flux, $R_i$
$H^+$	$k_{bw}*(K_w - c_H*c_{OH}) + k_{b1}*(K1*c_{H3PO4} - c_H*c_{H2PO4}) +$ $k_{b2}*(K2*c_{H2PO4} - c_H*c_{HPO4}) + k_{b3}*(K3*c_{HPO4} -$ $c_H*c_{PO4})$
$OH^-$	$k_{bw}*(K_w - c_H*c_{OH})$
$H_3PO_4$	$k_{b1}(c_H*c_{H2PO4} - K1*c_{H3PO4})$
$H_2PO_4^-$	$k_{b1}(K1*c_{H3PO4} - c_H*c_{H2PO4}) + k_{b2}(c_H*c_{HPO4} -$ $K2*c_{H2PO4})$
$HPO_4^{2-}$	$k_{b2}(K2*c_{H2PO4} - c_H*c_{HPO4}) + k_{b3}(c_H*c_{PO4} - K3*c_{HPO4})$ $+ k_{b4}(c_{KHPO4} - K4*c_K*c_{HPO4})$
$PO_4^{3-}$	$k_{b3}(K3*c_{HPO4} - c_H*c_{PO4})$
$KHPO_4^-$	$k_{b4}(K4*c_K*c_{HPO4} - c_{KHPO4})$
$K^+$	$k_{b4}(c_{KHPO4} - K4*c_K*c_{HPO4})$
$NO_3^-$	0

The following speciation values were used in the simulations for the BDD-Q electrode (Table 3.5) and trench disc electrode (Table 3.6) in the ring disc arrangements for the phosphate buffer solutions as determined from the PHREEQC code.<sup>43</sup>

**Table 3.5 Speciation for simulations of the BDD-Q electrode (concentrations in mM)**

[PO <sub>4</sub> ] <sub>T</sub>	0.5	1	5	10	15	20	25	30	35	40
pH	7.52	7.45	7.52	7.52	7.58	7.52	7.52	7.45	7.52	7.45
[K <sup>+</sup> ]	101	102	109	118	127	136	144	153	162	170
[NO <sub>3</sub> <sup>-</sup> ]	100	100	100	100	100	100	100	100	100	100
[PO <sub>4</sub> <sup>3-</sup> ]	2.30E <sup>-5</sup>	3.82E <sup>-5</sup>	2.44E <sup>-4</sup>	5.17E <sup>-4</sup>	9.63E <sup>-4</sup>	1.15E <sup>-3</sup>	1.51E <sup>-3</sup>	1.56E <sup>-3</sup>	2.30E <sup>-3</sup>	2.25E <sup>-3</sup>
[HPO <sub>4</sub> <sup>2-</sup> ]	0	1	4	8	12	16	19	23	27	30
[KHPO <sub>4</sub> <sup>-</sup> ]	0.03	0.05	0.29	0.60	0.95	1.29	1.67	2.01	2.49	2.85
[H <sub>2</sub> PO <sub>4</sub> <sup>-</sup> ]	0.09	0.20	0.87	1.69	2.21	3.24	3.97	5.35	5.35	6.90
[H <sub>3</sub> PO <sub>4</sub> ]	3.04E <sup>-7</sup>	8.10E <sup>-7</sup>	2.93E <sup>-6</sup>	5.66E <sup>-6</sup>	6.36E <sup>-6</sup>	1.06E <sup>-5</sup>	1.29E <sup>-5</sup>	2.02E <sup>-5</sup>	1.71E <sup>-5</sup>	2.57E <sup>-5</sup>

**Table 3.6 Speciation for simulations of the trench electrode (concentrations in mM)**

[PO <sub>4</sub> ] <sub>T</sub>	0.50	1.00	5.00	10.00	15.00	20.00
pH	7.68	7.62	7.75	7.62	7.68	7.68
[K <sup>+</sup> ]	100.9066	101.7974	109.1442	117.992	127.215	136.293
[NO <sub>3</sub> <sup>-</sup> ]	100	100	100	100	100	100
[PO <sub>4</sub> <sup>3-</sup> ]	3.52E <sup>-05</sup>	6.05E <sup>-05</sup>	0.000447	0.000676	0.00125	0.00176
[HPO <sub>4</sub> <sup>2-</sup> ]	0.405975	0.796775	4.14261	7.99	12.212	16.288
[KHPO <sub>4</sub> <sup>-</sup> ]	0.029002	0.057175	0.307957	0.619	0.983	1.36
[H <sub>2</sub> PO <sub>4</sub> <sup>-</sup> ]	0.064988	0.14599	0.548985	1.391	1.804	2.35
[H <sub>3</sub> PO <sub>4</sub> ]	1.54E <sup>-07</sup>	3.96E <sup>-07</sup>	1.09E <sup>-06</sup>	3.69E <sup>-06</sup>	4.13E <sup>-06</sup>	5.32E <sup>-06</sup>

### 3.3.6 Data analysis for buffer capacity measurement

Data analysis was undertaken using Python. To generate a calibration curve five measurements were taken in each pH buffer, a Savitsky-Golay filter<sup>45</sup> of polynomial degree 4 and window length 15 was used to smooth all data. The potential that corresponded to the minimum current value (termed ‘peak potential’) was chosen for every measurement. For every pH value, the mean average peak potential was then plotted against pH to generate a scatter plot. Data points were fitted linearly to generate a calibration curve, with the coefficient of determination (R<sup>2</sup>) value also calculated.

The aforementioned Savitsky-Golay filter<sup>45</sup> was also used to smooth all generated data considered. Ten SWV datasets were used for every concentration; the first five corresponding to the bulk solution pH and the last five corresponding to the generated pH after a sufficient time period. The mean average peak potential for each dataset was evaluated and mapped onto their corresponding pH value using



the calibration curve. For every concentration, the time taken for the pH to stabilise was also calculated and a scatter plot of rate of pH change against buffer concentration was plotted.

## 3.4 Results and Discussion

### 3.4.1 Electrochemical Characterisation

Electrochemical characterisation of the BDD-Q ring disc electrode was undertaken to assess the electrode performance as described in Section 3.3.4. The resulting current-potential graphs are shown in Figure 3.8 for solvent windows (a), capacitance (b) on both the ring (dashed) and the disc (solid) electrodes and the quinone surface coverage measurement on the disc (c). The bare BDD ring electrode in 0.1 M KNO<sub>3</sub> had a solvent window of 3.15 V and a capacitance of 8.4 μF cm<sup>-2</sup>, the BDD-Q disc electrode had a solvent window of 2.18 V, a capacitance of 15.4 μF cm<sup>-2</sup> and a QSC  $\Gamma = 2.2 \times 10^{-12}$  mol cm<sup>-2</sup>. Bare BDD characteristically has a large solvent window and small capacitance. Introduction of sp<sup>2</sup> carbon acts to reduce the solvent window and increase the capacitance.<sup>39</sup>

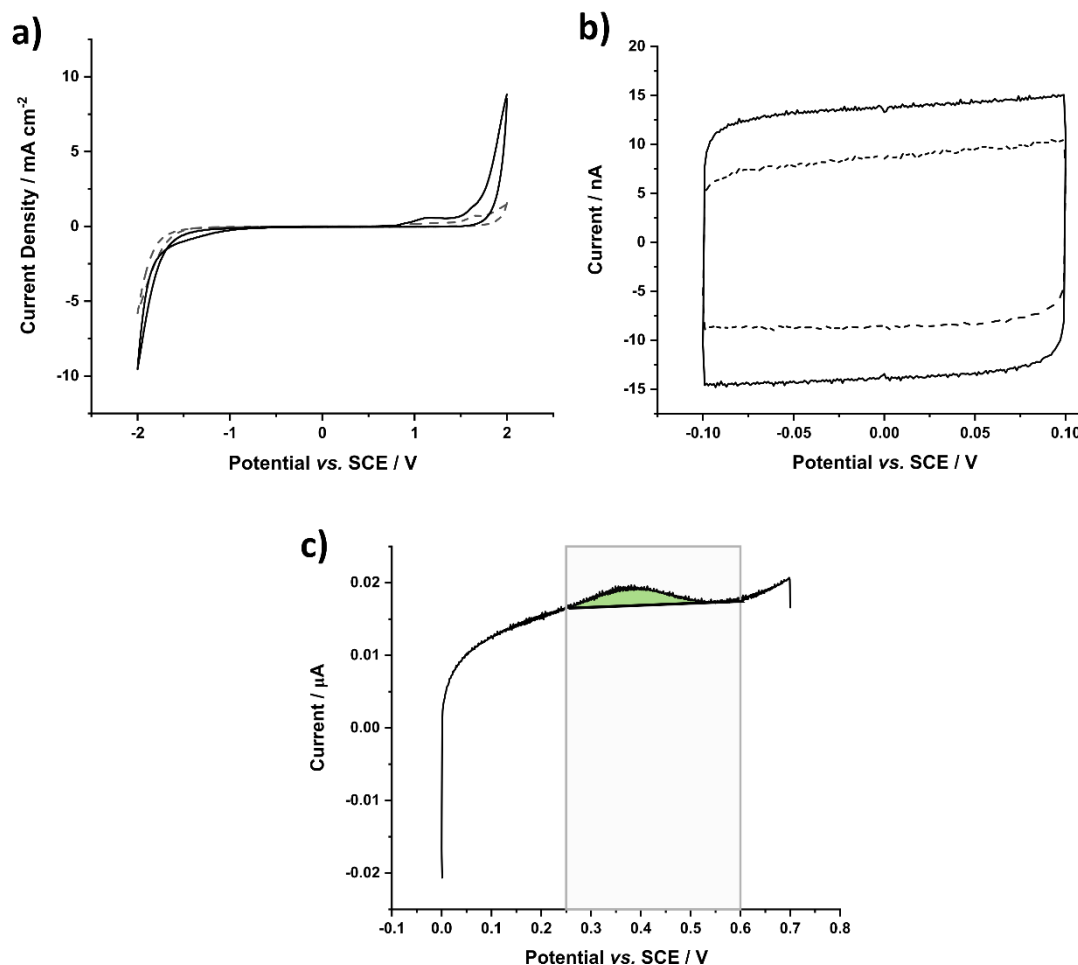


Figure 3.8 Cyclic voltammograms for electrochemical characterisation of blank BDD ring (dashed) and BDD-Q disc electrode (solid) for a) solvent window and b) capacitance and c) quinone surface coverage on the BDD-Q disc all undertaken with a 0.1 V s<sup>-1</sup> scan rate.

In aqueous environments quinone groups show a pH dependence due to the reduction of quinone groups through proton coupled electron transfer (PCET), Equation 3.14.

Under PCET conditions the pH dependent voltammetric shift is 59 mV pH<sup>-1</sup> in



accordance with the Nernst equation (assuming a temperature of 298 K), Equation 3.15.<sup>46</sup>

$$E = E^0 + \frac{0.0592}{2} \log \frac{[Q]}{[QH_2]} - 0.0592 \text{ pH} \quad \text{Equation 3.15}$$

BDD-Q electrodes contain surface integrated quinone groups which show this Nernstian pH dependence.<sup>22</sup> Peak position in the voltammetric scan is pH dependent. By producing a calibration line of peak position versus pH, from known pH buffer solutions, the pH of unknown solutions can be measured. In unbuffered measurements the PCET can cause local proton depletion, SWV is used to minimise this effect.<sup>23</sup>

The SWV response of the BDD-Q disc electrode in the ring-disc geometry, in buffered media at pH 2 (orange), 4 (pink), 7 (green) and 10 (purple), are shown in Figure 3.9a. The calibration response is close to the expected Nernstian response, with a value of 60 mV pH<sup>-1</sup>, Figure 3.9b.<sup>22</sup> The peak position shifts more positive as the solution is made more acidic. The electrode also responds well in unbuffered media over the pH range 2 – 10. The SWV response against pH is shown in Figure 3.9c. The SWV peak positions are plotted against pH and shown in Figure 3.9d, (blue; ■).<sup>23</sup> The use of SWV and careful consideration to the scan range results in a similar response to that observed in the buffered media, suggesting minimal perturbation of the solution pH during the measurement.<sup>23</sup> The pH response of the BDD-Q electrode in unbuffered solutions remained very similar regardless of whether the pH was increased or decreased during adjustment.

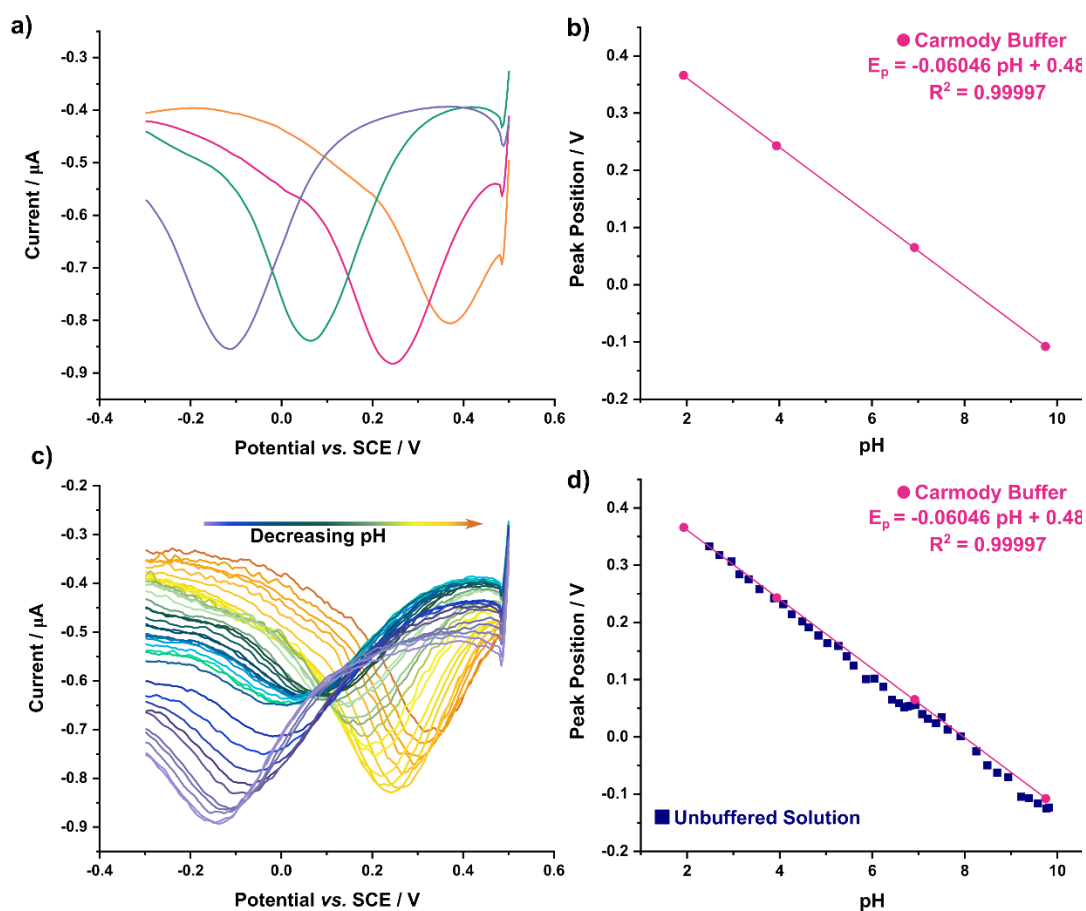


Figure 3.9 pH response of BDD-Q electrode a) SWV response of BDD-Q disc in pH 2 (orange), 4 (pink), 7 (teal) and 10 (purple) Carmody buffers. b) Calibration of SWV peak position against pH measured with glass probe in Carmody buffer solutions (pink; ●). c) SWV response of BDD-Q disc in unbuffered pH adjusted 0.1 M  $\text{KNO}_3$  and d) Calibration of SWV peak against solution pH measure by glass pH probe (blue; ■) solutions and peak positions of buffered data shown in b (pink; ●).

### 3.4.2 Proton Generation in electrolyte solutions

The ability of the BDD ring to generate a controllable proton flux for detection at the BDD-Q disc electrode was assessed first in an unbuffered solution (0.1 M  $\text{KNO}_3$ ). A range of currents (0.1 – 100  $\mu\text{A}$ ) were applied to the ring whilst measuring the SWV pH response on the BDD-Q disc. Figure 3.10a shows SWV time dependent data at the BDD-Q electrode for a ring current of +70  $\mu\text{A}$ . Before the ring current was applied, six SWV scans were recorded, to measure the pH of the 0.1 M  $\text{KNO}_3$  solution (dark blue lines in Figure 3.10a). The current was then applied to the ring prior to the seventh SWV scan. The response was measured over 75 s which corresponds to 30 SWV scans. Each SWV scan takes 1.35 s to complete and there is a delay of approximately 1 s between each scan. Each scan represents a time-dependent snapshot of the pH environment over the disc.

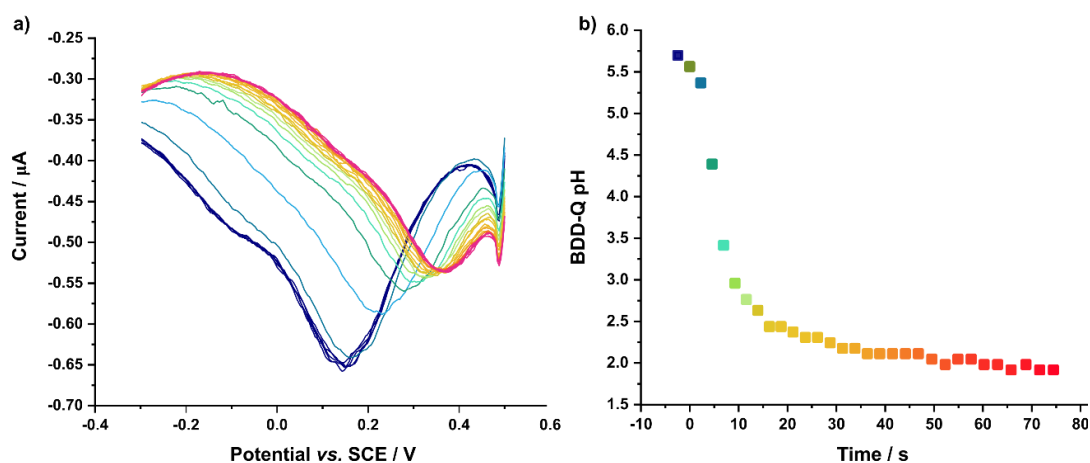


Figure 3.10 a) SWV response on BDD-Q disc in 0.1 M  $\text{KNO}_3$  with 70  $\mu\text{A}$  applied to the ring. b) pH measured by BDD-Q disc over time determined from the data presented in part a. Colours correspond between the two graphs.

Once the current is applied to the ring, the disc peak position shifts to more positive potentials with consecutive scans, *i.e.* time, indicating the measurement environment of the disc electrode is becoming more acidic due to water oxidation on the ring. The BDD-Q disc samples the pH environment at the location of the quinones *i.e.* the microspots where they are in contact with the solution. Note, the SWVs have also been coloured appropriately to denote a shift to more acidic conditions. After an initially rapid shift in peak potential within 16 s (7 scans) the change in peak potential became more gradual indicating a more stable pH environment had been established. The peak potentials were converted to pH, using a calibration line generated prior to these experiments, and are displayed as pH versus time in Figure 3.10b.

Figure 3.11 shows the BDD-Q measured pH data collected at various applied ring currents. At 100  $\mu\text{A}$ , bubble formation was visible and affected the quality of the SWV measurements on the disc. A current of 70  $\mu\text{A}$  was used going forward to provide the maximum pH perturbation free from detrimental bubble formation.

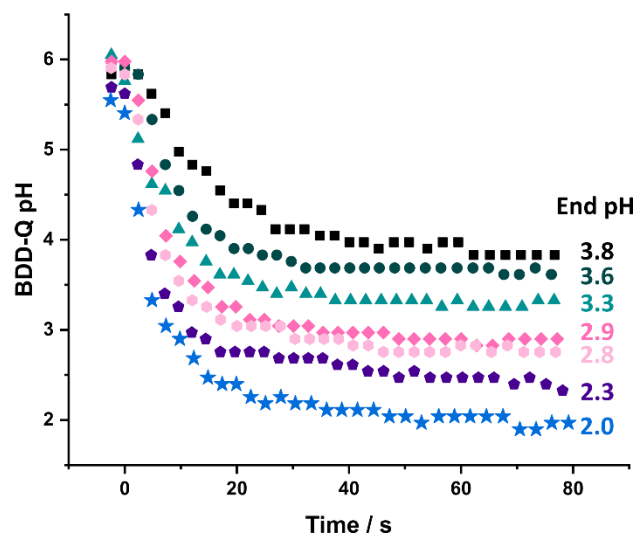


Figure 3.11 Measured BDD-Q response with applied currents of 1.5 (■), 3 (●), 5 (▲), 10 (◆), 15 (◐), 30 (◆) and 50 (★)  $\mu\text{A}$  on BDD ring in 0.1 M  $\text{KNO}_3$ .

### 3.4.3 Proton generation and pH tracking in Phosphate buffer

Experiments were then undertaken in a phosphate buffer, with different buffer concentrations from 0.1 mM to 40 mM, in 0.1 M  $\text{KNO}_3$ , the latter to ensure there was sufficient conductivity to negate ohmic drop effects. Whilst phosphate does not play a significant role in natural water systems, which are mainly buffered by  $\text{CO}_2$ , there are additional impacts to consider with carbonate buffers such as ambient  $\text{CO}_2$  concentration in the lab. For simplicity, phosphate was used as the pH range is comparable to natural waters. The same experimental procedure as for the measurements with water oxidation at the ring in the unbuffered case was used.

Figure 3.12 shows the SWV response on the BDD-Q disc in 1, 10, 15 and 25 mM phosphate buffer solutions (a-d, respectively) with 70  $\mu\text{A}$  applied to the ring. The colour scheme, green to red, is used to indicate the successively acidic pH values. As shown in the unbuffered solutions the peak potential can again be observed to shift to the right hand side indicating an increase in the acidity of the measurement environment of the BDD-Q disc. However, upon closer inspection, the peak shape changes with time. The SWV starts off with a single peak (dark green SWV), which decreases in magnitude while a second peak emerges to the right of it. The second peak grows, whilst the first continues to decrease until only the second peak remains. The peak shapes in this transition period, highlighted

as bold black lines, show either two distinct peaks (Figure 3.12a) or a very broad peak (Figure 3.12b-d).

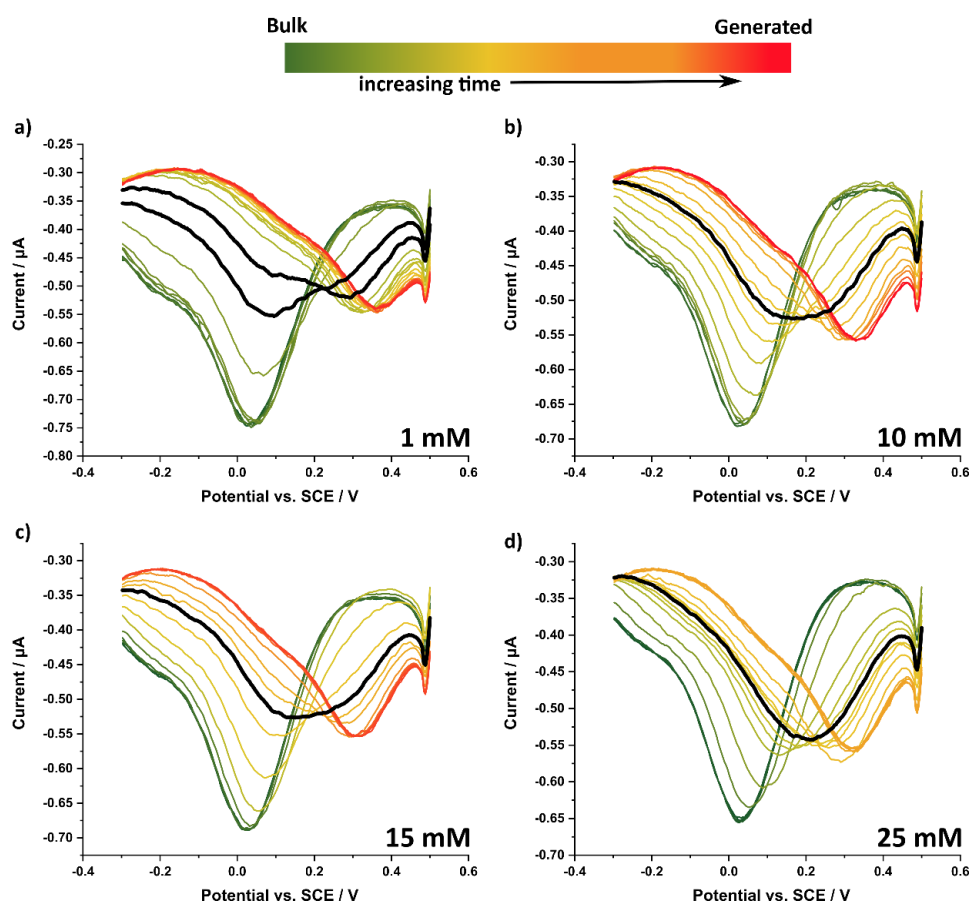


**Figure 3.12** A selection of successive square wave voltammograms from BDD-Q disc with  $70 \mu\text{A}$  applied to the ring in phosphate concentrations of a) 1, b) 10, c) 15 and d) 25 mM, not all SWV included for clarity. Green to red indicates shift from bulk pH to the generated acidic pH. Bold black lines indicate the double peak feature or broadening as discussed in the main text.

Figure 3.13a shows in more detail the 5 mM phosphate buffer solution, where the double peak and peak broadening is also observed in the SWV data. It is challenging to define a single minimum for the double peak or broad peak features. For double peaks and the broad peaks, the NOVA Autolab software picks the position of the dominant pH peak at the most negative current sampled. NOVA peak peaking is displayed in Figure 3.13b with the (■) data points. Due to the close proximity of the ring to the disc there is also an electrochemical noise contribution within the measurement. This could also affect the point sampled by NOVA as the minimum current may not be at the peak minima but rather due to noise, thus making the data look more variable than it is. The data was also

analysed manually by picking the central point of the broad, or clearly dominant peak, Figure 3.13b (●) data points. When the double peak features were at similar currents a central point between the two was taken as at higher buffer concentrations a broader peak is observed. However, it is difficult to determine how representative the peak positions from either method are in terms of the actual pH values being detected.

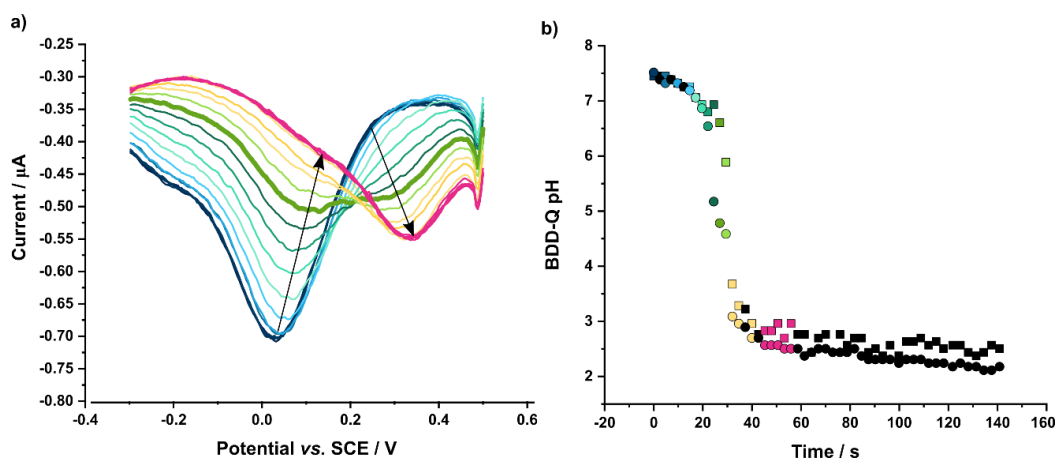


**Figure 3.13 a) SWV response of BDD-Q disc in 5 mM phosphate buffer solution with 70 μA applied to the ring, blue to pink, not all data shown for clarity. b) BDD-Q pH determined from peak position as analysed by NOVA (■) and manually (●), colours correspond between parts a and b.**

Despite these difficulties, the trends observed as buffer concentration increased are as expected. The greater the concentration of buffer the longer was needed for the pH to change and plateau and the smaller the magnitude of the change, Figure 3.14. Measurements made in buffer concentrations above ~ 30 mM became unreliable, as Figure 3.14 shows the data displays variability in the pH readings which fluctuate before finally decreasing. For the higher buffer concentrations longer timescales were required, which appears may be the reason the situation is complicated e.g., density driven convective effects now operate. Due to the longer timescale of the measurement than that required in the unbuffered solutions for the more concentrated buffer solutions small bubbles were observed.



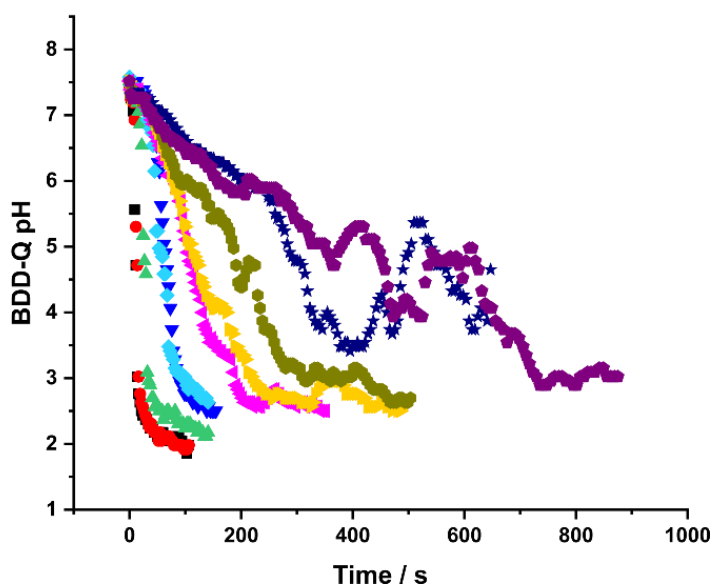


Figure 3.14 Graph showing pH change over time for 0.5 (■), 1 (●), 5 (▲), 10 (▼), 15 (◆), 20 (◀), 25 (▶), 30 (◊), 35 (★), and 40 mM (◆) determined from manual peak picking of SWV data and conversion of peak potential to pH from buffered pH calibration line ( $E_p = -0.06093 \text{ pH} + 0.48977$ ).

#### 3.4.4 Proton generation and pH tracking in hydroxide solutions and borate buffer solutions

To understand whether the double peak feature was unique to the phosphate buffer solution the experiment was repeated in unbuffered 0.1 M  $\text{KNO}_3$  solutions but at higher pH (through addition of  $\text{KOH}$ ). The same current,  $70 \mu\text{A}$ , was applied to the ring. The SWV responses at pH 6.05, 7.02, 9.08 and 11.29 are shown in Figure 3.15, a – d, respectively. At pH 6.05 the SWV peaks shift gradually as the pH changes then remain at a similar peak position similarly to the response seen in the 0.1 M  $\text{KNO}_3$  solution. At pH 7.02 a broadening of the peak is observed during the initial peak position shift, Figure 3.15b. By pH 9.08 and at 11.29 the double peak feature is observed, Figure 3.15c and d, respectively. This confirms the double peak is not a feature of the phosphate buffer. Note the increased scan range at the higher pH values, 0.5 V to -0.3 V increasing to -0.5 V to ensure a clear peak was captured at the higher  $\text{OH}^-$  concentrations.

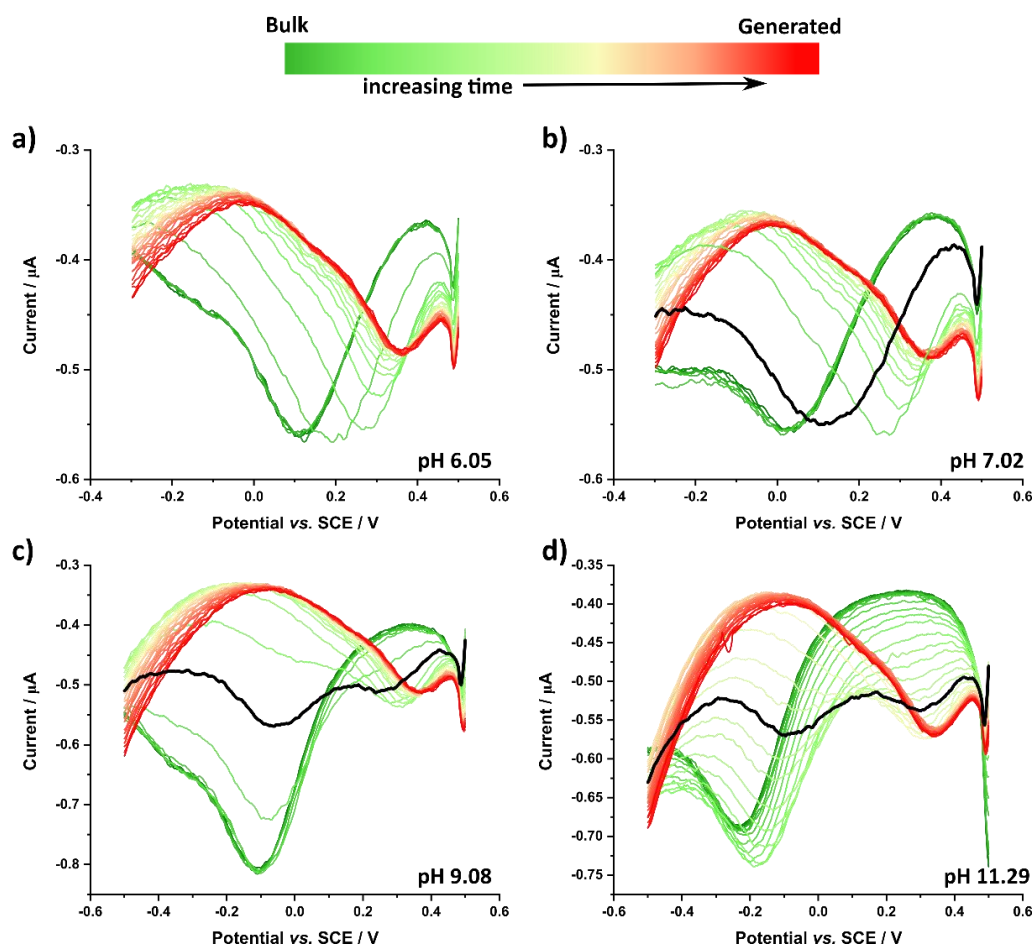


Figure 3.15 SWV response on BDD-Q disc in potassium hydroxide solutions with  $70 \mu\text{A}$  applied to the ring at a) pH 6.05, b) pH 7.02, c) pH 9.08 and d) pH 11.29.

In borate buffer solutions the peak shapes also showed the same trends, Figure 3.16. Initially a broadening was observed in the shifted peak at a concentration of  $0.1 \text{ mM}$  borate, Figure 3.16a. At  $0.5 \text{ mM}$  the appearance of a double peak began to show and was clearly evident by  $5 \text{ mM}$ , Figure 3.16b. As before, as the concentration of proton acceptor species increases so does the time taken for the local pH to become completely acidic, therefore the prevalence of the double peak feature becomes more dominant in the SWV scans, as can be seen in the borate solutions at  $15$  and  $30 \text{ mM}$ , Figure 3.16c and d, respectively.

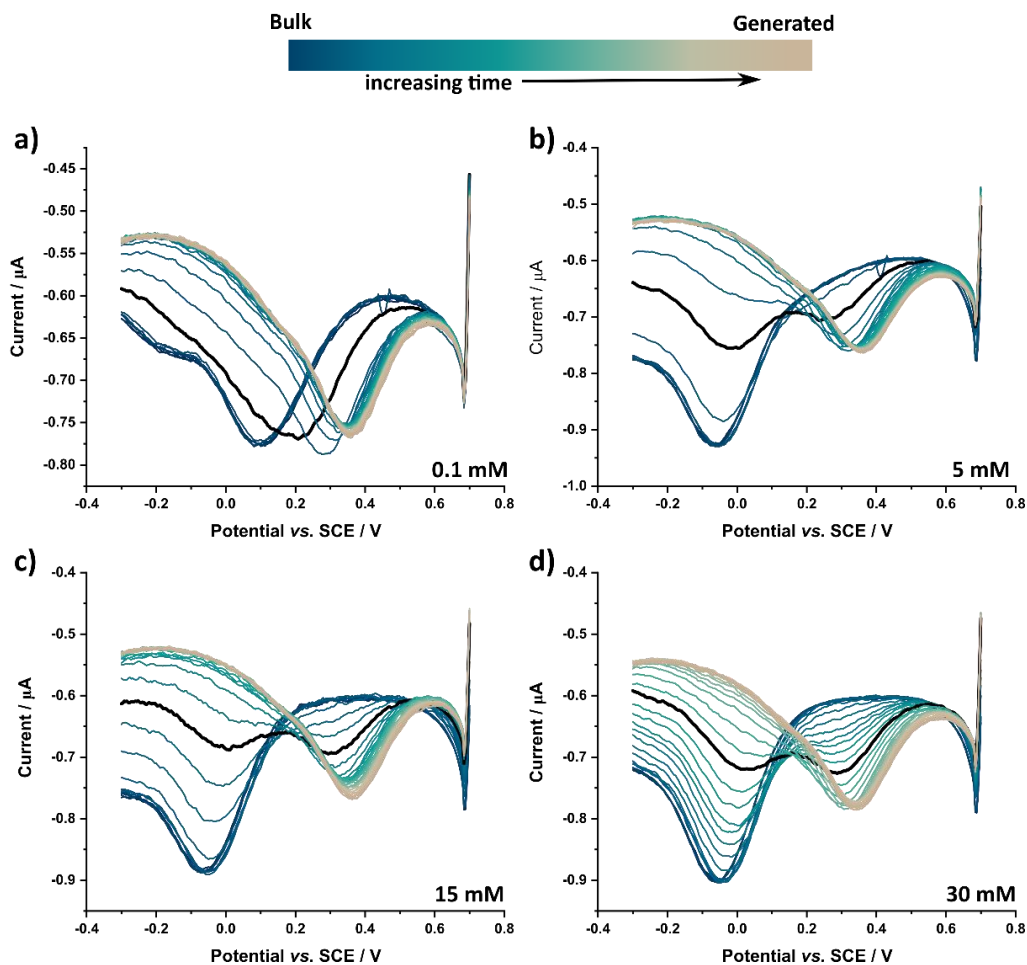


Figure 3.16 SWV response of BDD-Q disc in borate buffer with 70  $\mu\text{A}$  applied to the ring at a) 0.1 mM, b) 5 mM, c) 15 mM and d) 30 mM.

The origin of the double peak in the SWV response on the BDD-Q electrode is very interesting. A previous study using confocal laser scanning microscopy (CLSM) in conjunction with a fluorescent probe (fluorescein) showed a spatial variation when driving water reduction at a ring microelectrode in unbuffered solutions.<sup>47</sup> The study focused more on the bulk pH of the solutions and the applied current or potential than the timescales. At low currents (5 nA) the pH driven fluorescence did not reach the centre of the disc, creating a donut profile, suggesting an uneven proton distribution across the disc. At higher currents (10 nA) a hemispherical profile was observed across the electrode suggesting a more uniform distribution, no timescales were given.<sup>47</sup> In other unpublished work CLSM was used to monitor pH changes on a BDD ring disc electrode, oxidising water at the ring (+16  $\mu\text{A}$ ) in a 0.1, 1 and 10 mM borate buffer solution. At buffer concentrations  $\geq 1$  mM the initial pH decrease and the diffusion of  $\text{H}^+$  across the disc electrode were increasingly inhibited showing an uneven distribution pH

change across the disc.<sup>48</sup> This work suggests that with increased buffer concentration the pH change caused by proton generation is inhibited, due to the protonation of the buffering species. This inhibition slows down the diffusion wave of the increased proton concentration, which produces a spatial variation of pH across the disc profile, during the timescale of the measurement. This is explored further using modelling, *vide infra*.

#### **3.4.5 Response of BDD-Q in multiple pH environments.**

To investigate the hypothesis that the double peak feature is due to the BDD-Q sensor measuring different pH environments over the surface of the disc, a further experiment was undertaken. Two BDD-Q electrodes were connected together (so they experienced the same potential), each placed in their own buffer solution in individual beakers. A calibration of the two electrodes was measured individually (● and ▲) and together (■), for the situation where the buffer solutions were the same. The results are shown in Figure 3.17a, with both electrodes consistently returning a calibration of  $E_p = -0.061 \text{ pH} + 0.49$ .

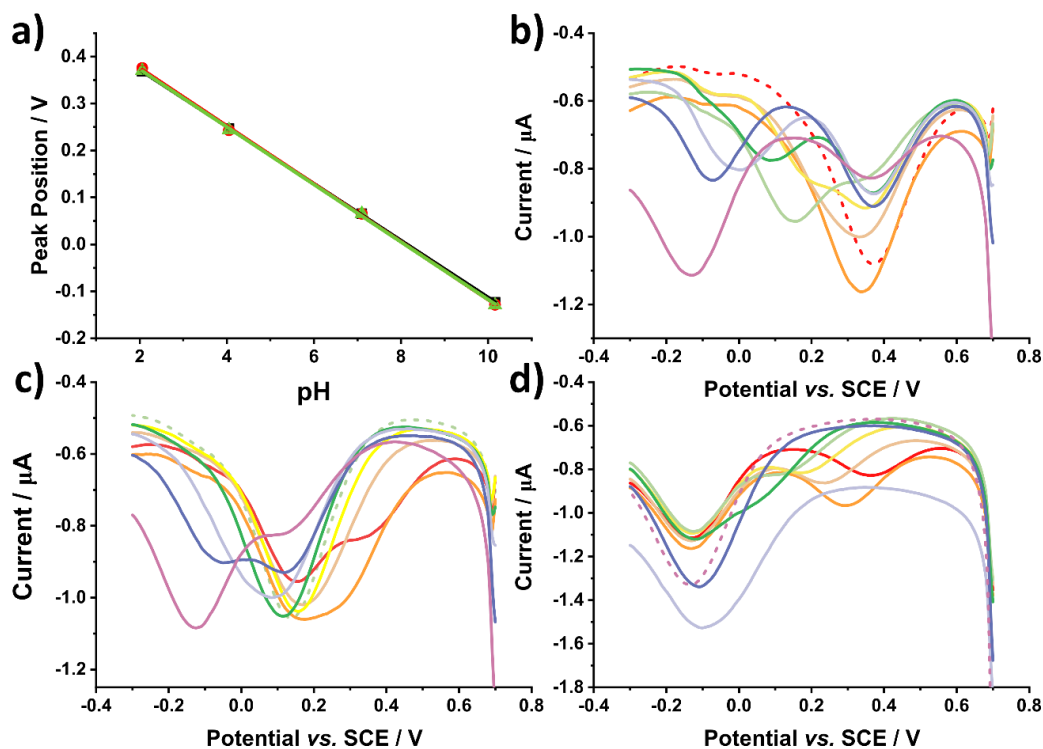


Figure 3.17 a) Calibration of two BDD-Q macroelectrodes together (■) and individually (● and ▲). SWV responses of the two BDD-Q electrodes in buffered solutions between pH 2.06 and 10.16 (solid line colours correspond roughly to pH indicator colours) with one electrode held at b) pH 2.06, c) pH 6.00 and d) pH 10.16, dashed lines are the SWV response with both electrodes in the same solution.

One electrode was then kept at a constant pH (Carmody buffer either pH 2.06, 6.00, or 10.16) whilst the other electrode was placed in a series of different pH buffers across the pH range 2 – 10, Figure 3.17b, c and d, respectively. The SWV obtained is the combined SWV for both electrodes in the two different solutions *i.e.* pH environments, which is in principle similar to the summing of the pH response from the microspots on the BDD-Q disc. The response when both electrodes were in the same pH buffer is presented as a dashed line on each graph, Figure 3.17. In these experiments, single, shifted, double and broadened peaks were observed. In general when the two pH environments were  $\pm 1$  pH unit apart the pH peak was shifted relative to both pH environments. When the pH was at  $\pm 2$  pH units broadened peaks were observed. When the pH environment was  $> \pm 2$  pH units two distinct peaks were seen in the response. The combined response in the different buffered environments supports the uneven pH environment theory but also highlights the difficulty of interpreting these peak position values.

Errors in the pH values returned from the peak position in two pH environments are observed relative to the pH measured by the glass pH probe of the individual Carmody buffer solution pHs, Table 3.7. The buffer solutions were measured with the glass pH probe prior to the electrochemical experiment being undertaken. For analysis manual peak picking was undertaken at the inflection point of the peak. Where two peaks were seen, the peak position corresponding to the solution that was varied was measured, *i.e.* the pH 2 peak in the first column was ignored for the higher pHs from Figure 3.17b. When one electrode remained at pH 2 the values returned were lower than the glass pH probe reading up to ~pH 8. Similarly, when one electrode remained at pH 10 the pH values returned were higher than the glass probe measured across the whole range. When held at pH 6 the values returned for the solutions < pH 6 were higher and solutions > pH 6 were lower than the glass probe measured. In the pH 10.16 solution the peak position returned a value of 10.20 when the second electrode was at pH 6.

**Table 3.7 Peak position and corresponding pH detected by BDD-Q from peaks in Figure 3.17 in two buffer pH environments.**

Glass pH measurement	pH 2.06		pH 6.00		pH 10.16	
	Peak position / V	pH	Peak position / V	pH	Peak position / V	pH
2.06	0.371	2.02	0.351	2.34	0.363	2.15
3.08	0.339	2.54	0.256	3.92	0.295	3.26
4.05	0.331	2.67	0.172	5.29	0.232	4.31
5.03	0.200	4.83	0.156	5.55	0.172	5.29
6.00	0.153	5.62	0.137	5.88	0.117	6.21
7.10	0.093	6.60	0.117	6.21	0.010	7.98
8.15	0.002	8.11	0.077	6.86	-0.089	9.62
9.18	-0.070	9.29	-0.050	8.96	-0.109	9.94
10.16	-0.133	10.34	-0.125	10.20	-0.133	10.34

### 3.4.6 COMSOL modelling of the BDD-Q ring disc in phosphate buffer

To further understand the origin of the SWV peak broadening/splitting, modelling of the generation of  $H^+$  at the ring and diffusion across the disc in the presence of a phosphate buffer as a function of time was carried out. A plot of the average pH over the disc vs. time was outputted for the different phosphate buffer concentrations considered in the experimental data, 0.5, 1, 5, 10, 15, 20, 25, 30, 35 and 40 mM (Figure 3.18). As shown the time taken for the pH change to plateau increases with phosphate concentration and the magnitude of the change decreases at higher concentrations. The final pH values of the model agreed well on the whole with that observed in the experimental data, although deviations were observed at the higher concentrations (>20 mM) with the model output suggesting a lower pH was reached than that observed. The time taken for the pH decrease in the model was consistently less than that seen in the experimental data.

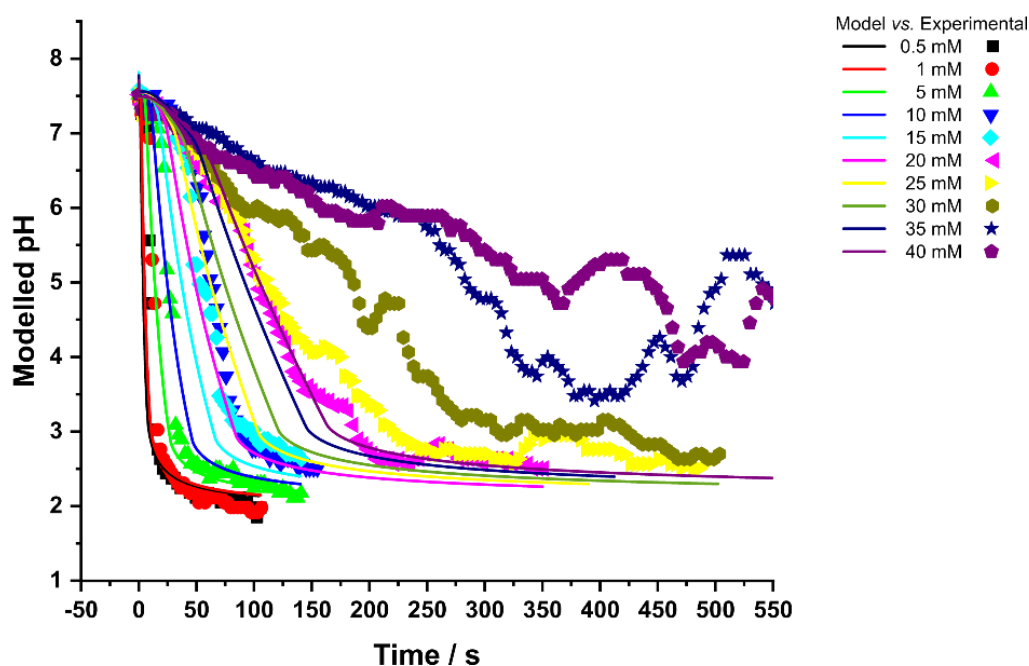


Figure 3.18 COMSOL output (lines) of average pH across the disc with  $70 \mu A$  applied to the ring in phosphate buffer (0.5 mM – 40 mM) and experimental data at the same concentrations (symbols).

It is important to consider the spatial variation in pH over the microspot array. Figure 3.19 shows the simulated electrode surface pH, and sections through the 3D pH isosurface (constructed at unit intervals of pH) from the COMSOL model at 5, 10, 30 and 60 s of  $H^+$  generation at the ring for phosphate buffer

concentrations of 1, 5 and 15 mM. Note that the ring, disc and microspots are also shown as black outlines on the surface. At 5 s, for the concentrations shown, a half torus profile emerging from the electrode surface is observed, with a proton gradient radiating out from the ring surface. The width of the torus decreases, when comparing same time point data, with increasing concentration. For the 1 mM concentration the diameter of the hole in the torus is significantly decreased by 10 s and a hemispherical profile is achieved by 30 s. At 5 mM the diameter of the hole decreases and begins to merge by 30 s and is a hemisphere at 60 s. At 15 mM the profile is still a torus at 60 s.

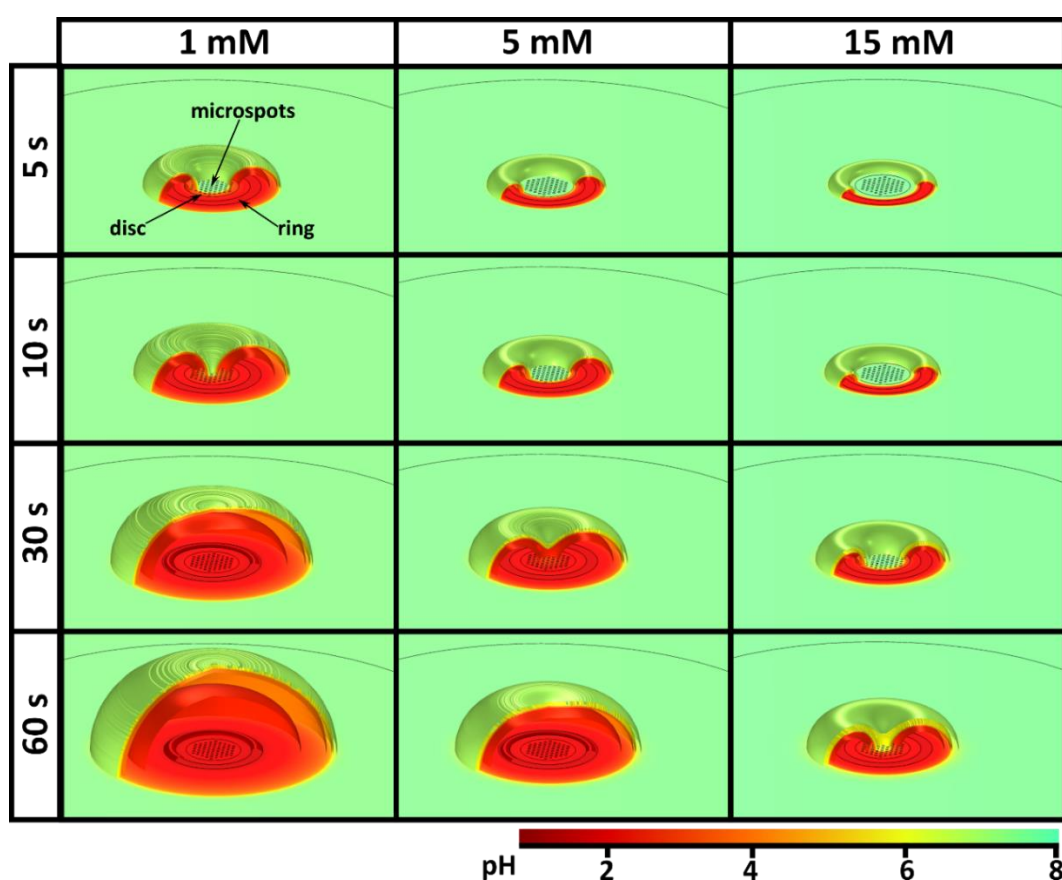
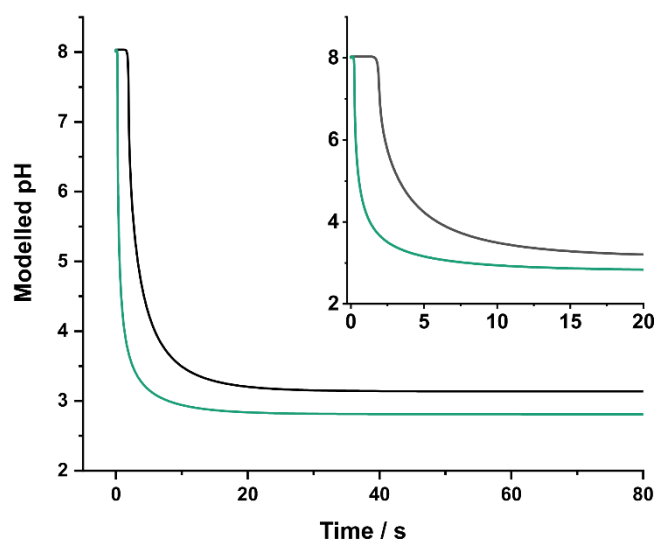


Figure 3.19 COMSOL simulation output of pH generated in phosphate buffer with 70  $\mu$ A applied to the ring at 5, 10, 30 and 60 s for phosphate concentrations at 1, 5 and 15 mM. The outline of the ring electrode and the microspots of the BDD-Q electrodes are also indicated on each image.

This modelling clearly shows the time dependence of the  $H^+$  diffusion front from the ring across the disc, with the higher buffer concentrations taking more time for the generated  $H^+$  concentration to fully cover the disc. The presence of the buffer effectively slows the front of the generated pH across the disc due to the consumption of generated  $H^+$ . In contrast, in unbuffered solutions the movement



of the pH front is not inhibited by buffering and travels rapidly across the disc. **Error! Reference source not found.** shows the profile of the pH at the edge (green) and centre (black) of the disc in unbuffered solution; there is a pH difference of 0.35 pH units at 20 s which then remains fairly constant. The biggest variation is within the first scan (~2s) where a 3.2 pH unit difference is present over the disc.



**Figure 3.20** Modelled pH at edge of disc (green) and centre of disc (black) in 0.1 M  $\text{KNO}_3$  with  $70 \mu\text{A}$  applied to the ring over 80 s. The inset shows the profile over 20 s.

The slowing down of the pH front in buffered solutions means that each ring of microspots experiences a different pH for a relatively long period of time, with respect to the measurement time (2 s). Figure 3.21 shows the simulations in 15 mM phosphate buffer concentration with  $70 \mu\text{A}$  applied to the ring at 30, 40, 50 and 60 s. Experimentally, 3 - 4 complete SWV would be measured between each of these time points.

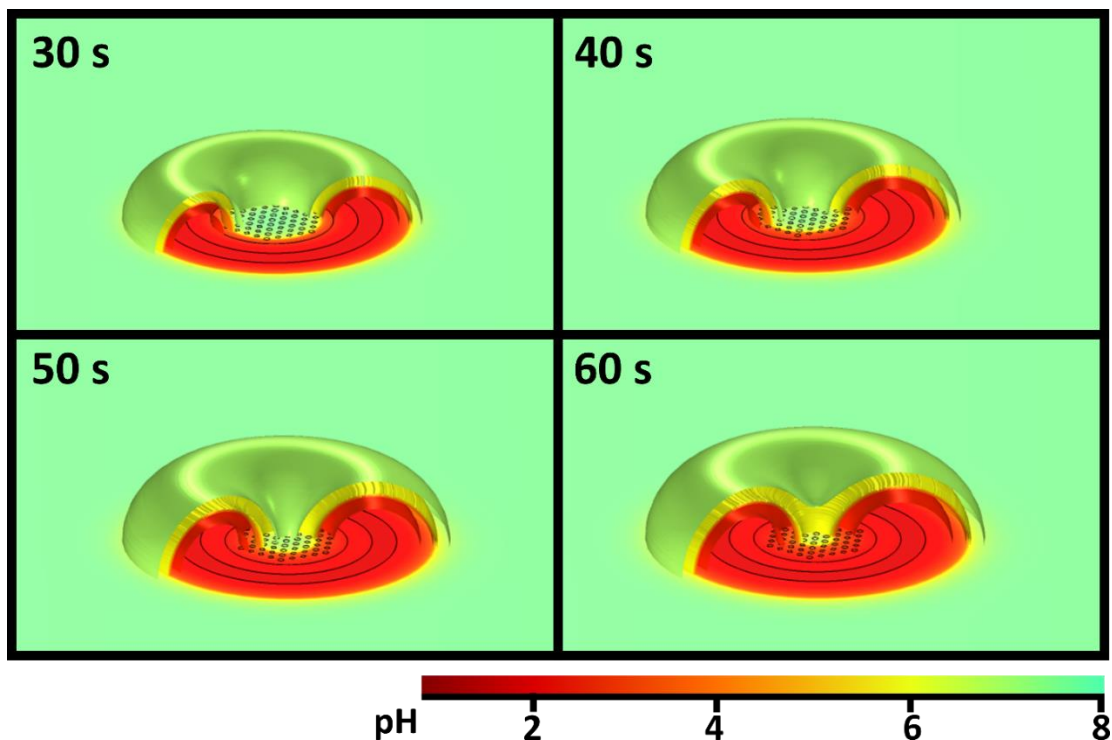


Figure 3.21 COMSOL simulation output of pH generated in 15 mM phosphate buffer with 70  $\mu\text{A}$  applied to the ring at 30, 40, 50 and 60 s. The outline of the ring electrode and the microspots of the BDD-Q electrodes are also indicated on each image.

In the first image of Figure 3.21, at 30 s the generated  $\text{H}^+$  ions are starting to be detected at the 24 outer spots of the hexagonal pattern. The rest of the microspots are still experiencing the bulk pH of the solution, pH 7.5. By 40 s the 24 outer spots are experiencing a pH between 4 and 3 with the next set of 18 spots experiencing a pH between bulk and pH 4. At 50 s the outer 42 spots are between pH 3 and 4, the central spot is at the bulk pH with the remaining spots between bulk and pH 4. By 60 s the torus shape has begun to merge with the six spots around the central spot and the central spot at pH 6, the outer ring of spots are at pH 3 and those in between pH 3 and 4.

Figure 3.22 shows the experimental SWV BDD-Q data in 15 mM phosphate buffer at 31, 42, 53 and 64 s of generation at the ring (each 4 SWV scans apart). The effects shown in the model (Figure 3.21) can also be observed in the data. At 31 s (purple, dash dot line) a well-defined pH response peak is observed. By 42 s (green, dashed line) the peak has shifted more positive and a shoulder has appeared on the right hand side of the more dominant peak, suggesting some of the outer spots are experiencing a more acidic pH environment. The reduction in

current of the more dominant peak could also suggest a reduced number of the quinone groups are measuring the higher pH environment. By 53 s (orange, solid line) a very broad peak with two features is observed suggesting the spots are experiencing two distinct pH environments, the two features are at similar current values. By 64 s the more positive potential peak is dominant, with a shoulder observed on the left hand side. This suggests most of the pH sensitive spots are responding to an acidic environment, but a small number, likely those close to the centre of the disc, are still measuring in a higher pH environment.

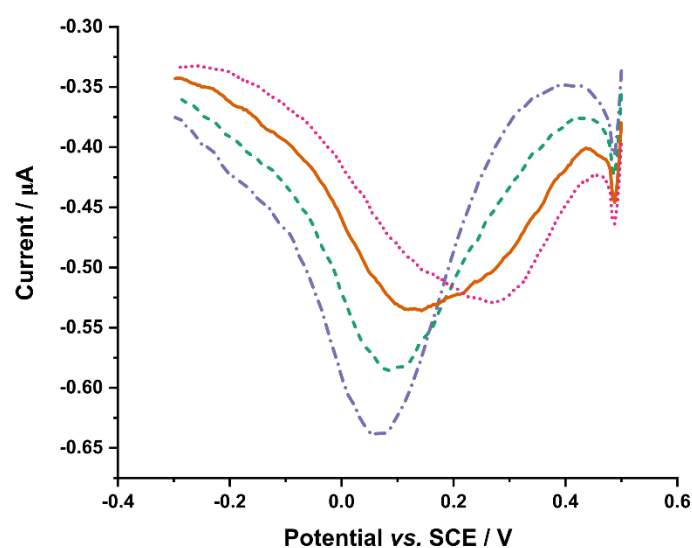


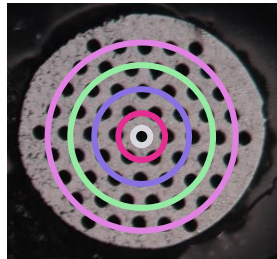
Figure 3.22 SWV response of BDD-Q disc in 15 mM phosphate buffer with 70  $\mu\text{A}$  applied to the ring at 31 (purple; dash dot line), 42 (green; dashed line), 53 (orange; solid line) and 64 (pink; dotted line) s.

The combined contribution of the pH response from all the quinone containing spots controls the peak shape of the voltammetric SWV scan. Therefore after 40 s generating at 70  $\mu\text{A}$  in 15 mM phosphate buffer a higher proportion of the quinone groups in the outer 42 spots of the hexagonal pH pattern will more readily form  $\text{QH}_2$  due to the higher concentration of  $\text{H}^+$ , Equation 3.14. This causes the peak to shift to a more positive peak potential. The quinone groups in the remaining spots are in an environment with a lower concentration of  $\text{H}^+$ , hence a more negative peak potential is measured at these microspots.

The effect of this variation on the measured SWV can be simulated by considering the microspot pattern to consist of 5 groups. The central spot being group 1 and the outer spots group 5, with each group containing an increasing number of spots, as shown in Table 3.8.

**Table 3.8 Groups of microspots and the number of microspots within each group relative to the microspot pattern on the BDD-Q disc.**

Group	Number of microspots
1	1
2	6
3	12
4	18
5	24



The 40 mM simulation, chosen to show the greatest variation in pH, was interpolated into a 3D geometry to allow the time-dependent pH experienced by each spot to be extracted. The outer group of microspots captures the pH change first, followed by groups 4, 3, 2 and then 1 as the H<sup>+</sup> gradient continues across the disc until a hemispherical concentration gradient is formed. The expected SWV response was then estimated by assuming each spot showed a Gaussian SWV peak with a peak position given by  $E_p = -0.06 \text{ pH} + 0.54$ , a full width at half maximum (FWHM) of 75 mV and an amplitude (current) proportional to the number of spots in each ring. The total response was calculated as a linear sum of all the spots.

The contributions of each group and total peak response for several time points can be seen in Figure 3.23. When the pH change is initially detected, the inner rings are equilibrated with the bulk solution but the outer ring (which dominates the response) is changing, *i.e.* 140 and 147 s, which introduces a second peak in the current response. As group 4 experiences the pH change the peaks continue to broaden, *i.e.* 154 s and ultimately lead to the second peak being the more dominant feature, *i.e.* 162 s.

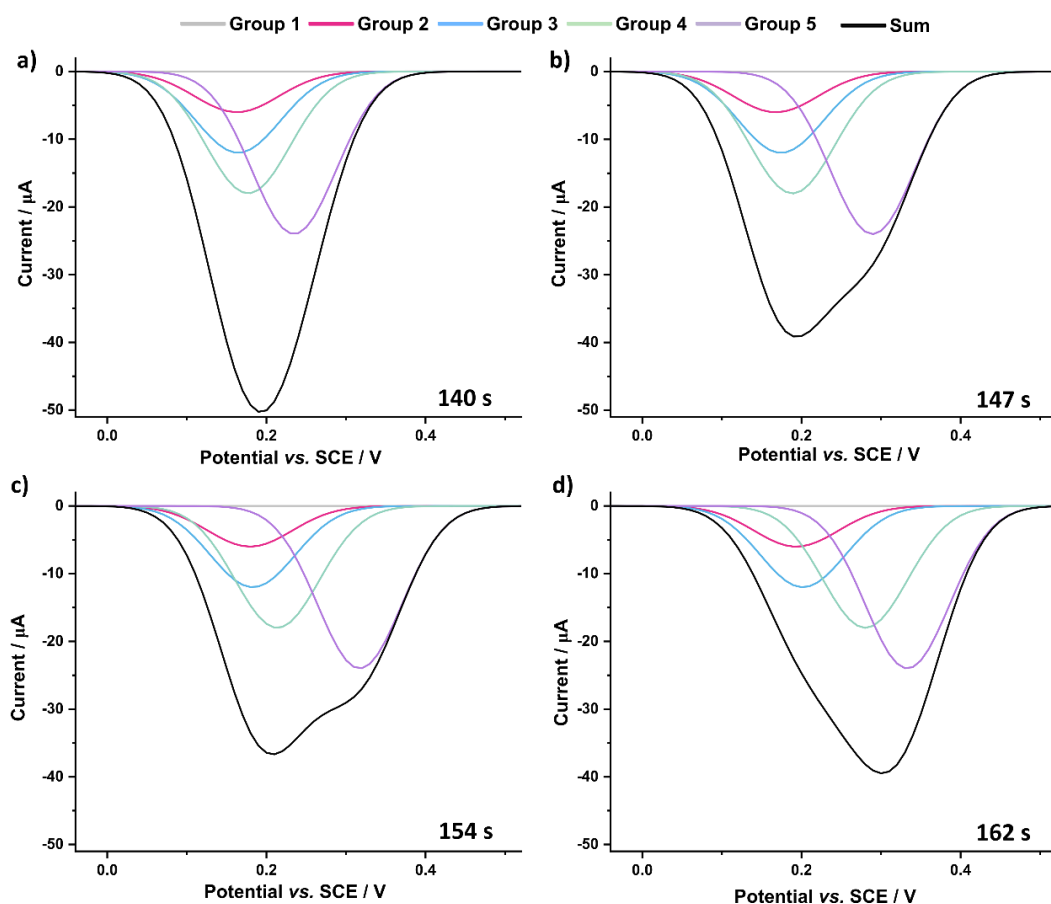


**Figure 3.23** The expected SWV response on the disc in 40 mM phosphate buffer with 70 μA applied to the ring, estimated by assuming each spot showed a Gaussian SWV peak with a peak position given by  $E_p = -0.06 \text{ pH} + 0.54$ , a full width at half maximum (FWHM) of 75 mV and an amplitude (current) proportional to the number of spots in each ring. The response of each microspot group are shown individually, and summed together at 140, 147, 154 and 162 s.

The time dependent pH response of the groups is shown in Figure 3.24a. The combined simulated SWV response for each time point from Figure 3.23, is shown in Figure 3.24b. The SWV peak response is similar in the simulated example as that shown experimentally (Figure 3.22), just at a longer timescale due to the greater buffer concentration.

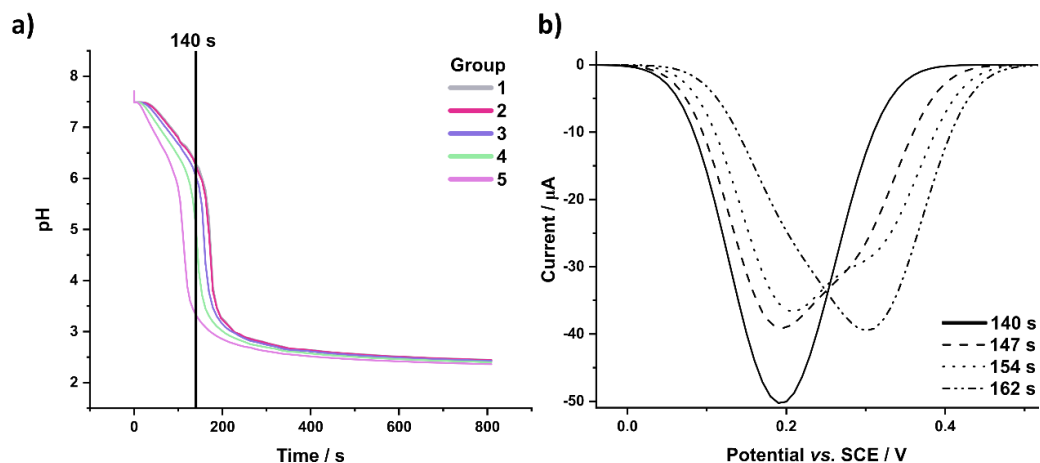


Figure 3.24 a) Modelled pH time graph at distribution of each group of microspots in 40 mM phosphate buffer with  $70 \mu\text{A}$  applied to the ring b) Simulated SWV response summing pH of each group of spots across the disc over time for the same experimental conditions at 140, 147, 154 and 162 s as depicted in Figure 2.23.

Between the model and the experimental data the evidence of the spatial impact of the pH sensitive spots is strong. The voltammetric measurement has provided insight into the mechanism not previously observed with a direct pH measurement. If we replaced the BDD-Q disc electrode with a glass pH probe or metal oxide based potentiometric electrode the output signal is simply a voltage. This varied pH environment would likely manifest as a drift in the potential towards a stabilising value. The voltammetric response of the BDD-Q pH sensor is able to provide far greater insight into the dynamics of the  $\text{H}^+$  generation process for this ring-disc configuration.

### 3.4.7 The Role of Natural Convection

Given the long timescales involved, up to hundreds of seconds, the role of natural convection was also considered. Natural convection is spontaneous motion within a solution driven by thermal fluctuations.<sup>49</sup> This chaotic motion will move solutes around, even in a still solution,<sup>50</sup> and is smallest near the electrode, increasing as the fourth power of distance away from it. Amatore identified this enforced motion as formally equivalent to a diffusion coefficient and included it in models by adding Equation 3.16 as a spatially varying contribution to the regular diffusion coefficient.<sup>50</sup>

$$\left(\frac{x}{\delta}\right)^4 \quad \text{Equation 3.16}$$

$x$  is a spatial dimension, normal to the electrode, and  $\delta$  is the diffusion layer thickness. This correction was applied to the FEM model to probe whether natural convection was playing a role, with two diffusion layer thicknesses considered: 200  $\mu\text{m}$  (close to that used by Amatore *et al.*<sup>50</sup>) and 400  $\mu\text{m}$  (doubled to see the effect). The outputs are shown in Figure 3.25.

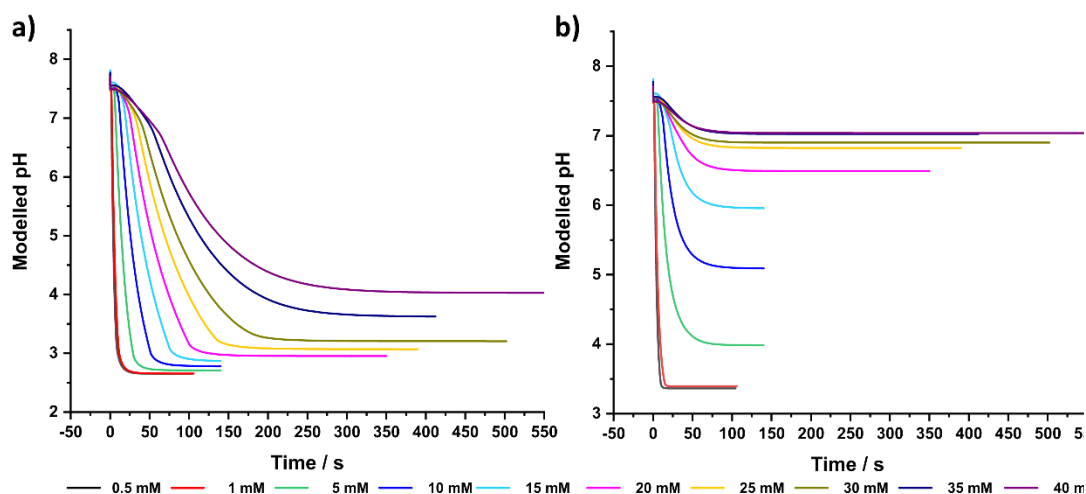
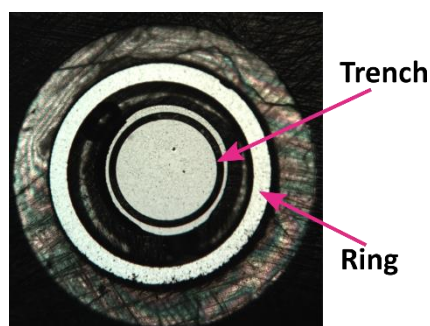


Figure 3.25 COMSOL model output for experimental system measured in Figure 3.14 with the Amatore natural convection factor applied with a) a 400  $\mu\text{m}$  diffusion layer and b) a 200  $\mu\text{m}$  diffusion layer.

With a 200  $\mu\text{m}$  diffusion layer thickness a significant decrease in the magnitude of the final pH change is observed relative to the model without the Amatore correction and the experimental data, Figure 3.25b. At 15 mM, the modelled steady state pH with a 200  $\mu\text{m}$  diffusion layer thickness was pH 6, with a 400  $\mu\text{m}$  diffusion layer thickness the steady state pH was 2.9. Without the Amatore correction it was pH 2.4 whilst the measured experimental pH was 2.8. For concentrations  $< 10$  mM the experimental plateaued pH aligned well with the model without the natural convection correction. For concentrations  $\geq 10$  mM the experimental plateau lies closer to the model with a 400  $\mu\text{m}$  diffusion layer thickness than without convection. Thus, suggesting natural convection may play a role at higher concentrations, which may be due to the longer timescales of the measurement.

#### **3.4.8 Response of trench BDD-Q disc electrode in phosphate buffer with proton generation on ring.**

On the basis that the double peak feature was due to the individual quinone containing spots experiencing different pH environments an alternative  $\text{sp}^2$  carbon pattern was tested. Rather than a series of spots a continuous ring was ablated into the BDD with an inner diameter of 0.8 mm, an outer diameter of 0.9 mm and a depth of 12  $\mu\text{m}$ . This aimed to concentrate the pH sensitive quinones into one area so the variation in pH would be reduced, henceforth referred to as the trench disc, Figure 3.26.



**Figure 3.26** Optical microscopy image of BDD ring with inner diameter of 1.4 mm and outer diameter 1.8 mm and trench disc, trench inner diameter 0.8 mm and outer diameter 0.9 mm.



The standard characterisation of the electrode was performed on the ring and trench disc returning capacitance values of  $21.6 \mu\text{F cm}^{-2}$  and  $19.8 \mu\text{F cm}^{-2}$ , respectively. The pH calibration of the trench disc in Carmody buffer was  $E_p = -0.062 \text{ pH} + 0.50653$ ,  $R^2 = 0.99948$ , the response in unbuffered solution showed an increased slope ( $E_p = 0.065 \text{ pH} + 0.48982$ ) and an  $R^2 = 0.98595$ . The quinone surface coverage of the trench disc was  $7.2 \times 10^{-12} \text{ mol cm}^{-2}$ , substantially higher than  $2.2 \times 10^{-12} \text{ mol cm}^{-2}$ . This could explain the variation in the buffer and unbuffered slopes and calibrations, as it is known that a higher quinone surface coverage can cause more local pH perturbation during the voltammetric pH measurement.<sup>51</sup> The trench disc electrode was used to repeat the experiment in phosphate buffer using the same  $70 \mu\text{A}$  current and SWV parameters. Interestingly, the same double peak feature was still observed, Figure 3.27. Despite condensing the quinone groups into a smaller area there is still a  $50 \mu\text{m}$  distance between the outer and inner edges of the ablated area. Additionally, the disc is not completely central within the ring as can be seen from the optical image, Figure 3.26, which will exacerbate this issue too. Ideally an infinitely thin area of BDD would be ablated but that would come with a loss of sensitivity.

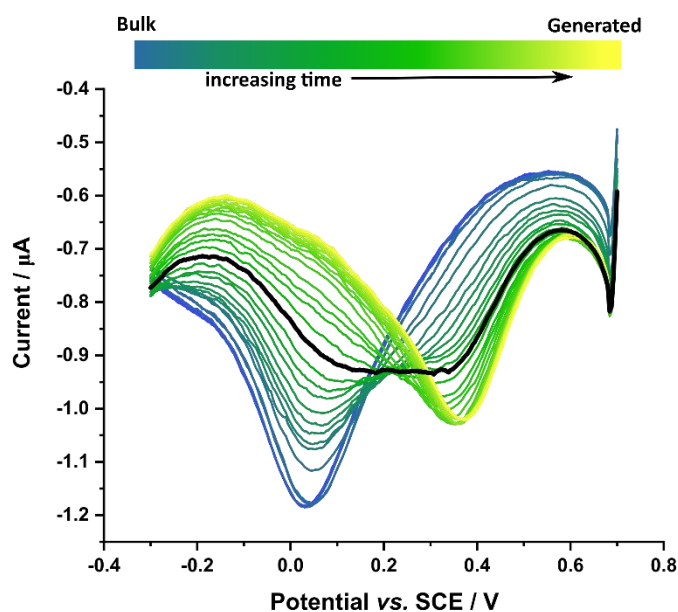


Figure 3.27 SWV response of trench disc in 10 mM phosphate with  $70 \mu\text{A}$  applied to the ring.

However, the change in pattern did result in the pH decrease occurring more quickly on the trench disc (●) than was observed with the microspot pattern (◇), Figure 3.28. This is most clear in the comparison of the two disc electrode patterns in the 10 mM phosphate buffer (blue symbols in Figure 3.28), but is also seen in the 5 mM (green symbols) and 15 mM (purple symbols) solutions. The pH readings from the trench disc also show a lower final pH reading than that recorded on the original BDD-Q microspot disc.

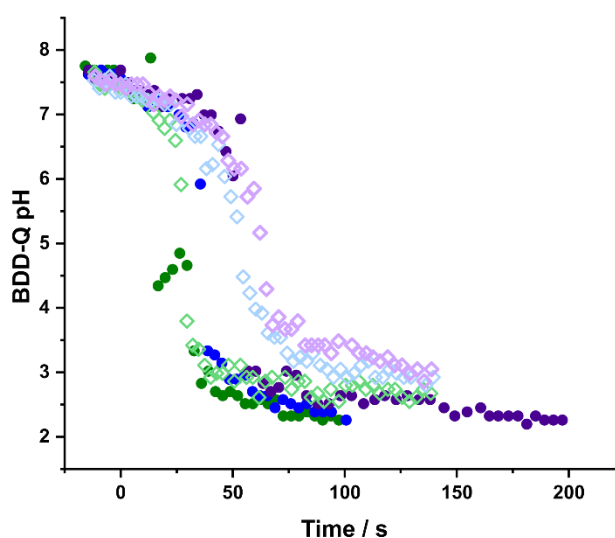


Figure 3.28 Measured pH values on BDD-Q (◇) and trench (●) disc electrodes with 70  $\mu\text{A}$  applied to the ring in 5 mM (green), 10 mM (blue) and 15 mM (purple) phosphate buffer.

When the trench disc geometry is put into the FEM model more rapid pH changes are outputted across the pH sensitive area with a small amount of variation between the maximum and minimum pH values, Figure 3.29a. When the model output for the trench disc (Figure 3.29b; dashed line) is compared to the output for the original BDD-Q disc, which is the average pH across the disc (Figure 3.29b; solid line), it is clear that the spatial distribution of the quinones is an important factor in how quickly the pH change is recorded and the timescales for the buffer capacity to be overcome. Interestingly in the model the final pHs of the two quinone arrangements agree but as already stated a lower final pH value was measured on the trench disc than the BDD-Q. This could however be a variation in the calibration of the discs. The original BDD-Q microspot pattern has been heavily researched and a variety of operational SWV parameters considered for

the best output. In the interest of time the same parameters were used for the trench which may not be the optimum for this arrangement. Alternatively, the BDD-Q spot disc may be under measuring the pH change, or be more affected by natural convection as previously discussed.

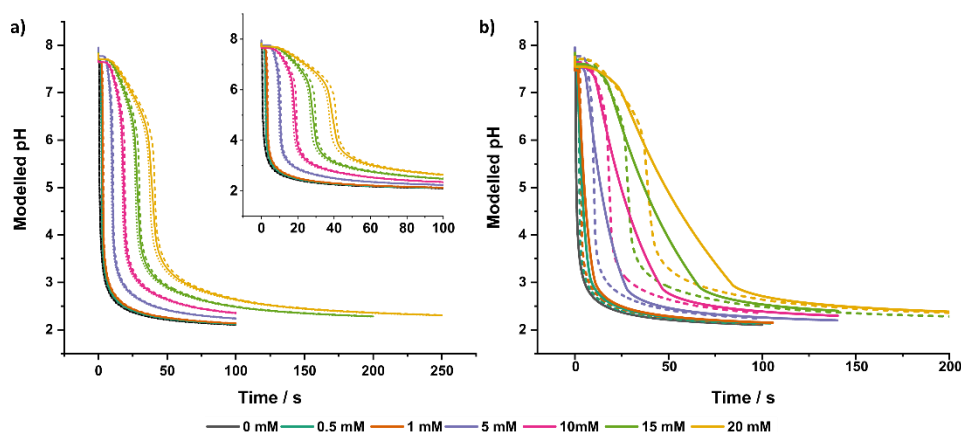


Figure 3.29 a) FEM output for trench disc data with 70  $\mu\text{A}$  applied to the ring in phosphate buffer at 0 (black), 0.5 (teal), 1 (orange), 5 (purple), 10 (pink), 15 (green) and 20 (yellow) mM, the solid lines are the average pH across the trench with the dashed line representing the maximum and the dotted line the minimum pH values. The inset is the same data over the initial 100 s where the majority of the pH change occurs. b) Compares the average pH value for the trench electrode (dashed line) and microspot electrode (solid line) when generating at the ring electrode at 70  $\mu\text{A}$  at the same phosphate buffer concentrations.

### 3.4.9 Analysis of BDD ring disc as a buffer capacity sensor

Given the uncertainties in interpreting the pH values reported by the BDD-Q and trench discs when generating in the presence of buffer, it was decided that this region would not be used to determine any information about buffer capacity. Analysis was undertaken on the bulk pH measurement (prior to the ring generation beginning) and the point the generated pH response showed a single peak at a stable peak potential over five consecutive SWV measurements, as it was assumed the pH gradient over the disc was minimal. Deconvolution of the pH signal response when a pH gradient is present across the disc would require complex fitting analysis and defeats the object of a simple sensor so was not explored further. The pH change observed from the start peak position to the 'stable' single peak and time taken to reach this stable point was used to determine a rate of change, Figure 3.30.

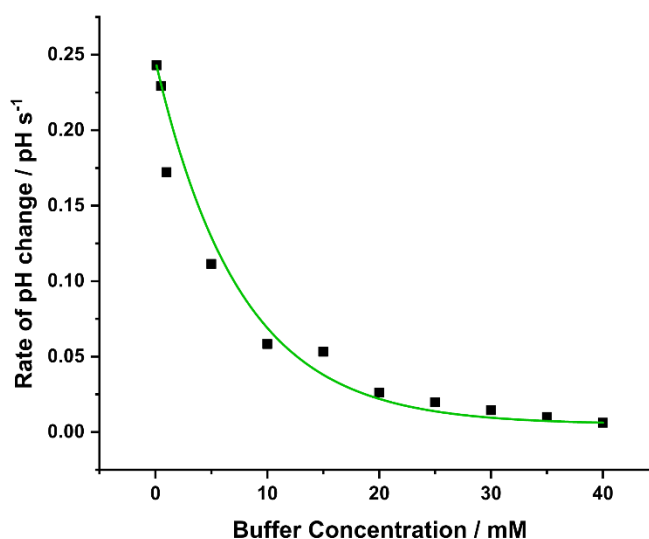


Figure 3.30 Rate of pH change from bulk pH (7.3) to first set of five SWV with a stable single peak position divided by the generation time between plotted against buffer concentration for BDD-Q ring disc in phosphate buffer generating H<sup>+</sup> at 70  $\mu$ A on the BDD ring.

The sensitivity to buffer capacity determined by this method is fairly good, up to  $\sim 10$  mM, after that the sensitivity decreases. We looked at phosphate initially as a buffer as the conditions are in the neutral pH range. However the major buffering species in the environment is carbonate. In seawater carbonate concentrations are 2.2 – 2.5 mM kg<sup>-1</sup> and in rivers 0.957 mM kg<sup>-1</sup>.<sup>52</sup> Therefore this system is likely sensitive enough for environmental systems which are most typically at buffer concentrations < 5 mM. But further investigation would be required, particularly for freshwater systems due to the lower conductivity.

The loss of sensitivity at higher concentrations is logical as a significant concentration of H<sup>+</sup> ions are required to overcome the buffer capacity. The increased timescales required also pose challenges for the analysis as bubble formation and convective processes are more likely to be established. The longer timescales also allow for more diffusion to the area to counteract the local pH change, by introducing additional buffering species to the local area, further increasing the number of H<sup>+</sup> to overcome the buffer capacity. Sensitivity at higher concentrations could be achieved with a smaller disc and ring diameter, however this poses a challenge for manufacture in the current format.

### 3.5 Conclusions and future work

The BDD-Q disc electrode was shown to be able to track dynamic pH changes driven by  $H^+$  generation at a ring electrode in both unbuffered and buffered solutions. In buffered solutions, due to the consumption of  $H^+$  by buffering species, a pH front is formed. This was observed within the voltammetric SWV scans as merged (broad) or double peaks in the presence of buffer. Voltammetric pH measurement on the BDD-Q electrode in a ring disc geometry, supported by FEM modelling, has provided insight into the spatial variation of pH when using a ring disc electrode arrangement for proton detection work in the presence of buffer. Due to the spatial variation of the microspots on the BDD-Q electrode the pH variation across the disc is detected and the response is similar to the case of two pH measurements summed together.

An experimental attempt was made to minimise this effect by concentrating the pH sensitive areas into a narrower region on the disc. However, this still showed a range of pH environments as merged peaks, this could in some part be attributed to the misalignment of the disc within the ring. As a proof of concept study the work in this chapter pushed the limits of the design as observed by the reduction of sensitivity at higher buffer concentrations. However, for an environmental sensor of alkalinity in river or seawater, the sensitivity in this arrangement is already sufficient.

Future work could include verifying the pH gradient during the electrochemical measurement by using a complimentary additional pH sensitive technique such as CLSM. This could further aid understanding of the SWV response under a pH gradient, with further understanding it may be possible to deconvolute the SWV response where double peaks are seen. However, design adjustments either of the BDD-Q disc or the entire sensor may be a more worthwhile avenue to pursue. Here the FEM model would be advantageous as it can guide new designs.

Possible design adaptations for the BDD-Q ring disc electrode for the future include:

- (i) A smaller diameter disc and ring; to reduce the diffusion path over the disc.

- (ii) Variation of the ring thickness; thicker could provide greater area for proton generation but a thinner ring may benefit from a more hemispherical diffusional profile.
- (iii) Variation of the  $sp^2$  carbon region on the disc; how thin would a trench design need to be for the proton gradient to be negligible within the concentration range of interest.

Alternatively, it may be better to reposition the generator electrode such that the BDD-Q disc is subject to a uniform proton gradient. For example,

- (iv) Parallel electrodes with a thin channel between similar, to the membrane device discussed in the introduction, Figure 3.31.<sup>36</sup>

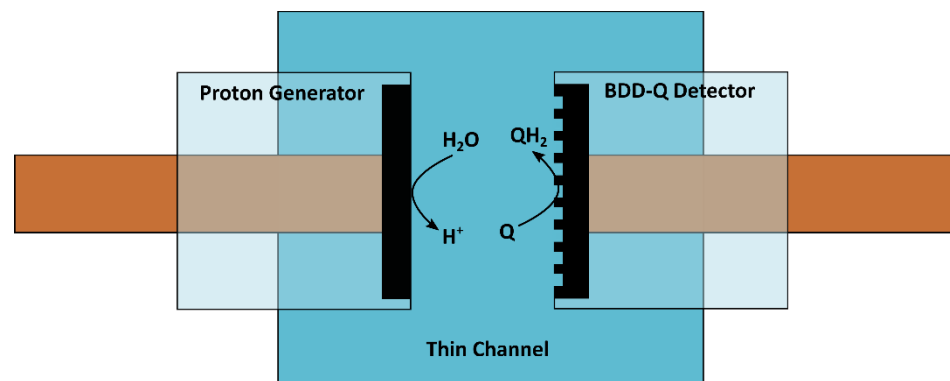


Figure 3.31 Schematic of a suggested thin channel alkalinity sensor using BDD disc electrodes.

Alternatively, it may be possible to have:

- (v) Generator electrodes either side of a detector electrode to introduce  $H^+$  from two directions. This would create a uniform pH more quickly. The design could be in the form of bars in a defined channel or a ring-ring disc type arrangement, Figure 3.32 a and b, respectively. These designs would require optimisation and verification of a BDD-Q electrode in a format other than a disc and consideration to the ablated  $sp^2$  carbon geometry.

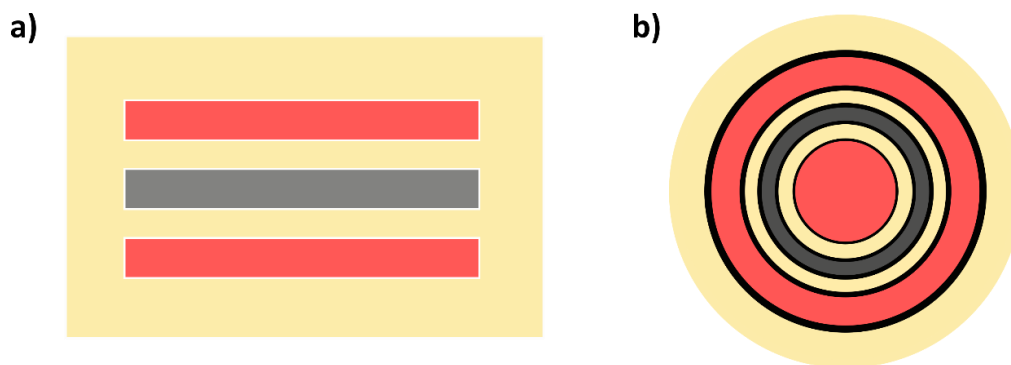


Figure 3.32 Dual proton generation alkalinity sensor designs; red generating electrodes and grey BDD-Q sensing electrodes a) bars that could be placed within a defined channel and b) ring-ring disc electrode configuration.

### 3.6 References

- 1 M. Hillert, *J. Phase Equilibria*, 1995, **16**, 403–410.
- 2 J. W. Mauger, *Dissolution Technol.*, 2017, **24**, 38–51.
- 3 D. D. Van Slyke, *J. Biol. Chem.*, 1922, **52**, 525–570.
- 4 D. R. Lide, Ed., *Handbook of Chemistry and Physics*, CRC Press, Boca Raton, 89th edn., 2008.
- 5 C. Mohan, *A guide for the preparation and use of buffers in biological systems*, EMD Biosciences, Germany, 2003.
- 6 J. Reijenga, A. van Hoof, A. van Loon and B. Teunissen, *Anal. Chem. Insights*, 2013, **8**, 53–71.
- 7 J. Grochowska and R. Brzozowska, *Knowl. Manag. Aquat. Ecosyst.*, 2013, 1–13.
- 8 J. Grochowska, *Water*, 2020, **12**, 1512.
- 9 A. G. Dickson, *Deep Sea Res. Part A, Oceanogr. Res. Pap.*, 1981, **28**, 609–623.
- 10 J. J. Middelburg, K. Soetaert and M. Hagens, *Rev. Geophys.*, 2020, **58**.
- 11 J. C. Orr, V. J. Fabry, O. Aumont, L. Bopp, S. C. Doney, R. A. Feely, A. Gnanadesikan, N. Gruber, A. Ishida, F. Joos, R. M. Key, K. Lindsay, E. Maier-Reimer, R. Matear, P. Monfray, A. Mouchet, R. G. Najjar, G. K. Plattner, K. B. Rodgers, C. L. Sabine, J. L. Sarmiento, R. Schlitzer, R. D. Slater, I. J. Totterdell, M. F. Weirig, Y. Yamanaka and A. Yool, *Nature*, 2005, **437**, 681–686.

- 12 S. C. Doney, V. J. Fabry, R. A. Feely and J. A. Kleypas, *Ann. Rev. Mar. Sci.*, 2009, **1**, 169–192.
- 13 O. Sulpis, B. P. Boudreau, A. Mucci, C. Jenkins, D. S. Trossman, B. K. Arbic and R. M. Key, *Proc. Natl. Acad. Sci. U. S. A.*, 2018, **115**, 11700–11705.
- 14 J. C. Phillips, G. A. McKinley, V. Bennington, H. A. Bootsma, D. J. Pilcher, R. W. Sterner and N. R. Urban, *Oceanography*, 2015, **28**, 136–145.
- 15 L. C. Weiss, L. Pötter, A. Steiger, S. Kruppert, U. Frost and R. Tollrian, *Curr. Biol.*, 2018, **28**, 327–332.e3.
- 16 P. Vanýsek, *Electrochem. Soc. Interface*, 2004, **13**, 19–20.
- 17 L. Manjakkal, D. Szwagierczak and R. Dahiya, *Prog. Mater. Sci.*, 2020, **109**, 100635.
- 18 M. Wang, S. Yao and M. Madou, *Sensors Actuators, B Chem.*, 2002, **81**, 313–315.
- 19 O. Korostynska, K. Arshak, E. Gill and A. Arshak, *Sensors*, 2007, **7**, 3027–3042.
- 20 J. C. Dutta, *Proc. - 2012 2nd Natl. Conf. Comput. Intell. Signal Process. CISP 2012*, 2012, 185–191.
- 21 W. Y. Chung, F. S. He, C. H. Yang and M. C. Wang, *J. Med. Biol. Eng.*, 2006, **26**, 29–34.
- 22 Z. J. Ayres, A. J. Borrill, J. C. Newland, M. E. Newton and J. V. Macpherson, *Anal. Chem.*, 2016, **88**, 974–980.
- 23 S. J. Cobb, Z. J. Ayres, M. E. Newton and J. V. Macpherson, *J. Am. Chem. Soc.*, 2019, **141**, 1035–1044.
- 24 D. Wencel, T. Abel and C. McDonagh, *Anal. Chem.*, 2014, **86**, 15–29.
- 25 B. H. Van Der Schoot and P. Bergveld, *Sensors and Actuators*, 1985, **8**, 11–22.
- 26 B. van der Schoot and P. Bergveld, *Sensors and Actuators*, 1988, **13**, 251–262.
- 27 W. Olthuis, B. H. Van Der Schoot, F. Chavez and P. Bergveld, *Sensors and*



- Actuators*, 1989, **17**, 279–283.
- 28 W. Olthuis, J. Luo, B. H. Van Der Schoot, J. G. Bomer and P. Bergveld, 1990, **2**, 416–420.
- 29 W. Olthuis and P. Bergveld, *Mikrochim. Acta*, 1995, **121**, 191–223.
- 30 B. H. Van Der Schoot, P. Van Der Wal, N. De Rooij and S. West, *Sensors Actuators, B Chem.*, 2005, **105**, 88–95.
- 31 E. M. Briggs, S. Sandoval, A. Erten, Y. Takeshita, A. C. Kummel and T. R. Martz, *ACS Sensors*, 2017, **2**, 1302–1309.
- 32 E. M. Briggs, E. H. De Carlo, C. L. Sabine, N. M. Howins and T. R. Martz, *ACS Earth Sp. Chem.*, 2020, **4**, 355–362.
- 33 J. Llopis and A. Sancho, *J. Electrochem. Soc.*, 1961, **108**, 720.
- 34 R. S. Patil, V. A. Juvekar and V. M. Naik, *Ind. Eng. Chem. Res.*, 2011, **50**, 12946–12959.
- 35 M. W. Breiter, *Electrochim. Acta*, 1963, **8**, 925–935.
- 36 M. G. Afshar, G. A. Crespo and E. Bakker, *Angew. Chemie - Int. Ed.*, 2015, **54**, 8110–8113.
- 37 M. G. Afshar, M. L. Tercier-Waeber, B. Wehrli and E. Bakker, *Geochemical Perspect. Lett.*, 2017, **3**, 85–93.
- 38 M. Ghahraman Afshar, M. L. Tercier-Waeber, B. Wehrli and E. Bakker, *Geochemical Perspect. Lett.*, 2017, **3**, 85–93.
- 39 J. V. Macpherson, *Phys. Chem. Chem. Phys.*, 2015, **17**, 2935–2949.
- 40 T. L. Read, E. Bitziou, M. B. Joseph and J. V. Macpherson, *Anal. Chem.*, 2014, **86**, 367–371.
- 41 T. L. Read, M. B. Joseph and J. V. Macpherson, *Chem. Commun.*, 2016, **52**, 1–4.
- 42 W. R. Carmody, *J. Chem. Educ.*, 2009, **40**, A386.
- 43 D. L. Parkhurst and C. A. J. Appelo, *Description of input and examples for PHREEQC version 3: a computer program for speciation, batch-reaction, one-*

*dimensional transport, and inverse geochemical calculations*, Reston, VA, 2013.

- 44 F. Ruiz-Beviá, J. Fernández-Sempere and N. Boluda-Botella, *AIChE J.*, 1995, **41**, 185–189.
- 45 M. J. E. Savitzky, A.; Golay, *Anal. Chem.*, 1964, **36**, 1627–1639.
- 46 P. S. Guin, S. Das and P. C. Mandal, *Int. J. Electrochem.*, 2011, **2011**, 1–22.
- 47 N. C. Rudd, S. Cannan, E. Bitziou, I. Ciani, A. L. Whitworth and P. R. Unwin, *Anal. Chem.*, 2005, **77**, 6205–6217.
- 48 T. L. Read, University of Warwick, 2016.
- 49 J. K. Novev and R. G. Compton, *Curr. Opin. Electrochem.*, 2018, **7**, 118–129.
- 50 C. Amatore, S. Szunerits, L. Thouin and J. S. Warkocz, *J. Electroanal. Chem.*, 2001, **500**, 62–70.
- 51 S. J. Cobb, Z. J. Ayres, M. E. Newton and J. V Macpherson, *J. Am. Chem. Soc.*, 2019, **141**, 1035–1044.
- 52 S. Lower, *Environ. Chem.*, 1999, 1–26.

## 4 *In-situ* tracking of catalytically driven pH changes on boron doped diamond (BDD) versus copper nanoparticle modified BDD in unbuffered solutions

---

### 4.1 Overview

In this chapter, a boron doped diamond (BDD) ring disc electrode was used to probe local pH changes due to the oxygen reduction reaction (ORR), nitrate reduction reaction (NRR) and water reduction (WR) on both bare BDD electrode and BDD decorated with copper nanoparticles (Cu NPs). Cu NPs were electrochemically deposited onto the ring. Using the same principles as in Chapter 3, the reaction of interest was driven by applying a potential to the BDD ring electrode (either with or without Cu NPs) whilst sequential square wave voltammetry (SWV) measurements were made on the pH sensitised (BDD-Q) disc electrode, capturing the electrocatalysed local pH change over time. To probe NRR, experiments were undertaken in nitrate or sulfate anion based solutions. Using linear sweep voltammetry (LSV) potentials for ORR, NRR and WR in the presence of Cu NPs were identified at -0.4, -1.0 and -2.0 V, respectively. As BDD is electrocatalytically inert to ORR and NRR, small pH changes (<2 pH units) were recorded, at -0.4 and -1.0 V but WR at -2.0 V resulted in a significant pH change in both electrolyte solutions. With Cu NPs present on the ring the pH changes at -0.4, -1.0 and -2.0 V in aerated 0.1 M K<sub>2</sub>SO<sub>4</sub> were larger than those measured on the bare BDD. In the nitrate solution with Cu NPs present, NRR and WR are catalysed with larger pH changes observed than those on bare BDD at -1.0 and -2.0 V, respectively. However, a smaller pH change was observed at -0.4 V with Cu NPs than without suggesting an inhibition of ORR in the presence of Cu NPs. This is attributed to nitrate adsorption acting to block the catalytic activity of the Cu deposits with respect to ORR.

## 4.2 Introduction

Metal electrodeposition is the electrochemically driven deposition of a metal onto an electrode surface typically by the reductive transfer of electrons from electrode to metal cation.<sup>1</sup> Metal deposits can be useful for increasing sensitivity on sensor devices,<sup>2-4</sup> or advancing energy storage and conversion capabilities as electrocatalysts for water splitting, fuel cell technologies and carbon dioxide reduction.<sup>5-7</sup> The electrodeposition of metals can be energy and resource efficient as only small amounts of, often precious, metals are required.<sup>8</sup>

Electrodeposition additionally presents the opportunity to produce micro to nanoparticles (NPs) whose properties can vary from bulk analogues.<sup>9</sup> The properties of NPs can vary wildly depending on NP size and structure.<sup>10-12</sup> To deposit metals on a surface, typically a potential more negative than the thermodynamic standard potential for the metal/metal ion couple, is applied to the working electrode, an overpotential. In some cases electrodeposition can occur at potentials lower than the thermodynamic potential, a process known as underdeposition.<sup>13</sup> This occurs when deposition of the metal onto an electrode surface is more thermodynamically favourable than the metal-metal deposition.

The deposition potential must be carefully chosen as the magnitude of the applied overpotential can influence the morphology of the metal electrodeposits.<sup>14,15</sup> There is often an upper limit to the overpotential that can be applied without competing reactions occurring.<sup>16</sup> For example, the hydrogen evolution reaction (HER), Equation 4.1, and WR, Equation 4.2, result in gaseous bubble formation. In some cases people have used small amounts of gas evolution to their advantage in order to create micro and nanoporous metal deposits.<sup>17-19</sup>



pH is a hugely important factor in metal electrodeposition as the solution pH determines the speciation of metal ions present in solution. In low pH solutions metal ions are generally present in their hydrated metal ion form, Figure 4.1a. As pH increases a decreasing fraction of metal ions will be present in the hydrated

form and are therefore less likely to be electrodeposited in the metallic form, Figure 4.1b.<sup>16,20</sup>

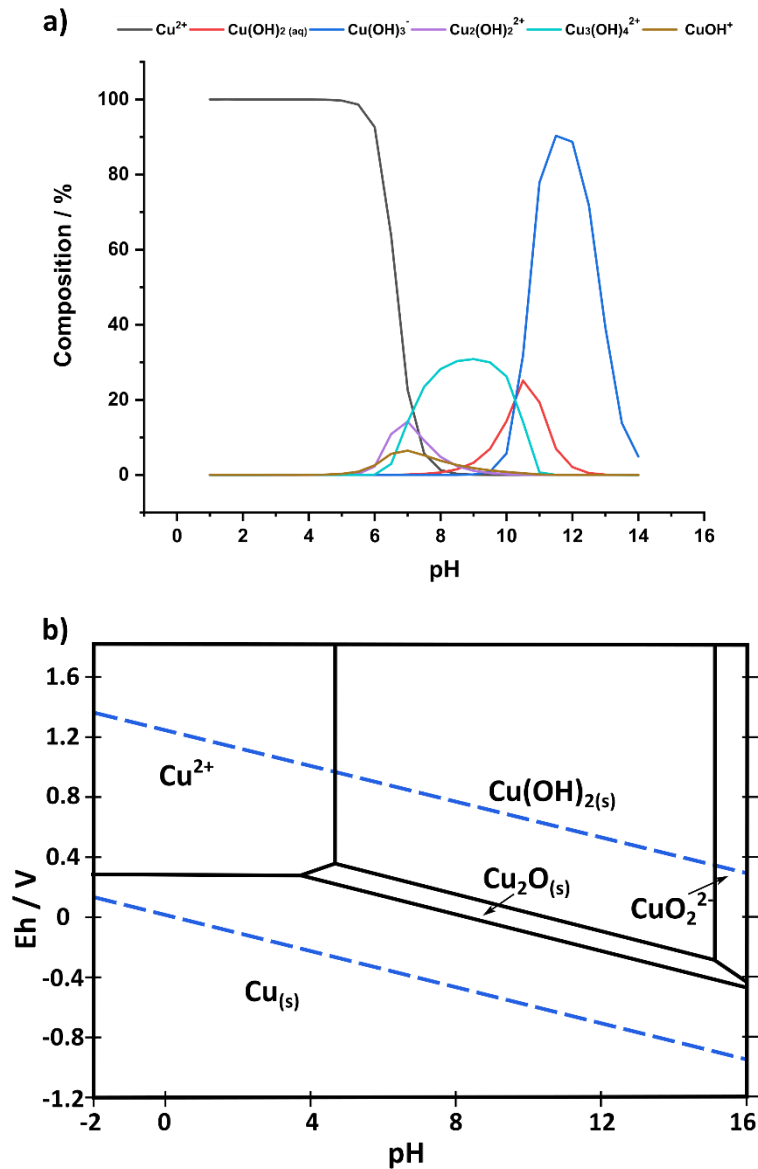


Figure 4.1 a) pH dependent speciation of Cu in water and b) Pourbaix diagram of Cu in water. Both at an ion concentration 0.001 m (mol/kg water). Temperature 25°C.

Electrodeposition of pure metal is often undertaken in acidic media for this reason. Metals are more readily deposited from their hydrated ionic form (Equation 4.3) as the ligated water molecules readily de-solvate during the electrodeposition process.



Electrodeposition parameters are often very carefully controlled to ensure the production of the desired metallic morphology deposit is achieved. Parameters to control include, pH (either as a buffered system or controlled in an unbuffered system), deposition potential (or in some cases deposition current), deposition time, oxygen presence / absence and temperature.<sup>16</sup>

As discussed above if the overpotential is too high Equation 4.1 and Equation 4.2 can occur. Both result in an increase in the local pH, resulting in the formation of metal hydroxides or oxides, Equation 4.4.<sup>21,22</sup> However, for some applications, including supercapacitors, pH sensing and solar cells, metal oxides can be beneficial.<sup>22-25</sup>

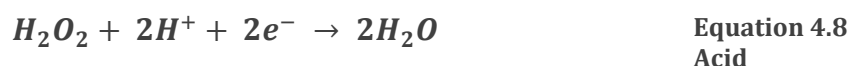


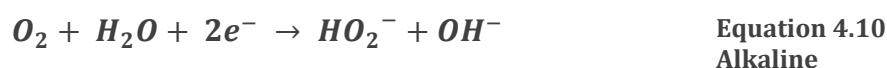
Also of importance is the role of the ORR, in aerated solutions, which can occur via a two or four electron pathway.<sup>26</sup> The mechanisms for either pathway are pH dependent. All mechanisms ultimately result in a pH increase through proton consumption or hydroxide production resulting in an increased likelihood of depositing metal hydroxides/oxides, Equation 4.5 to Equation 4.12.

#### 4 electron pathways

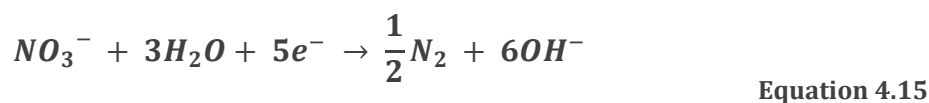
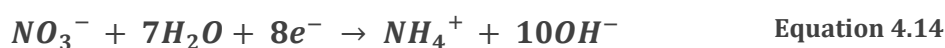


#### 2 electron pathways

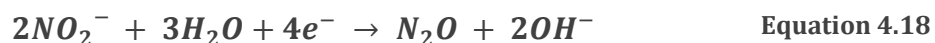
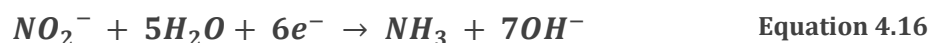




Additionally nitrate anions, which are often used in supporting electrolytes, can undergo the NRR, which again increases the local pH through production of hydroxide ions through one of three postulated mechanisms (Equation 4.13 to Equation 4.15).<sup>27,28</sup>



Nitrite ( $NO_2^-$ ) formed from the reaction in Equation 4.13 can also undergo further reduction to ammonia (Equation 4.16), nitrate gas (Equation 4.17) or nitrous oxide (Equation 4.18) producing additional hydroxide ions.<sup>29,30</sup>



Sulfate, another common supporting electrolyte anion, can be electrochemically oxidised resulting in the formation of sulfate radical ions and persulfate ions, however there is no corresponding pH change as the mechanism involves radical chemistry.<sup>31</sup>

As shown in Equation 4.1, Equation 4.2 and Equation 4.5 to 4.18, there are various possible electrochemical reactions that result in an increase in solution pH. Even if the solution is buffered, the magnitude of the buffer capacity is important as it may be locally overcome depending on the concentration of OH<sup>-</sup> produced and the buffer capacity of the electrolyte (see Chapter 3). Once metals are electrodeposited on the electrode surface, the hybrid electrode is typically dominated by the properties of the deposited metal, especially in the case of carbon electrodes.<sup>16</sup> This is due to the metals having a greater electrocatalytic effect on reactions such as HER, WR, ORR and NRR, than the support substrate.

As a metal, Cu is widely used for consumer electronics, photovoltaics and is increasingly gaining traction as a catalyst for CO<sub>2</sub> reduction applications.<sup>32-35</sup> Cu is very reactive and easily transitions between oxidation states. Cu is most commonly found in the 0, +1 or +2 oxidation states. Cu readily reacts to its two major oxide forms, copper (I) oxide (Cu<sub>2</sub>O) and copper (II) oxide (CuO).<sup>36</sup> Cu has been reported to have an electrocatalytic effect on ORR,<sup>37</sup> oxygen evolution from water oxidation,<sup>38</sup> H<sub>2</sub>O<sub>2</sub> reduction,<sup>39</sup> NRR<sup>27</sup> and CO<sub>2</sub>RR.<sup>40</sup> However it is not always explicitly stated which form the Cu is in for these reactions. As shown above, ORR, H<sub>2</sub>O<sub>2</sub> reduction and NRR actively change the local pH environment, if the solution is unbuffered or the local buffer capacity is overcome by the experimental conditions.

Due to the highly reactive nature of Cu it is possible that chemical and morphological transformations may occur during the electrochemical process of interest, decreasing the efficiency and lifetime of the catalyst. This has been shown for the use of Cu and Cu related oxide structures in carbon dioxide electrocatalysis.<sup>41-44</sup> pH is potentially a major driver of these transformations, which is often overlooked.

The aim of this chapter is to measure the pH changes associated with ORR, NRR and WR on both blank BDD (carbon) electrodes<sup>45</sup> and in the presence of electrodeposited Cu NPs. This work utilises a similar ring disc design to that used in Chapter 3 but with a thicker ring to ensure sufficient Cu was electrodeposited to detect a pH change from the processes of interest. The ring was held at appropriate potentials to drive ORR, NRR and WR with and without the presence



of Cu deposits. The integrated BDD-Q disc was utilised to measure the resulting pH change over a time period of approximately 30 s (20 SWV scans) in both nitrate and sulfate electrolytes.

## 4.3 Experimental

### 4.3.1 Chemicals & solutions

All solutions were prepared using ultra-pure deionised water with a resistivity of  $\geq 18.2 \text{ M}\Omega \text{ cm}$  at  $25^\circ\text{C}$  (Millipore, Watford, UK). Electrodes were characterised as described in Chapter 2 using 0.1 M potassium nitrate ( $\text{KNO}_3$ ; 99 %, Acros Organics) for capacitance and solvent window measurements. Carmody buffers were prepared as previously described<sup>46</sup> with boric acid ( $\text{H}_3\text{BO}_3$ ; > 99 %, Scientific Lab Supplies), citric acid ( $\text{C}_6\text{H}_8\text{O}_7$ ;  $\geq 99.5$  %, Fisher Chemicals) and tertiary sodium phosphate ( $\text{Na}_3\text{PO}_4$ ;  $\geq 99$  %, Acros Organics), pH 2 was used for quinone surface coverage (QSC) measurements, pH 4, 7 and 10 were used to calibrate the BDD-Q sensor. For unbuffered measurements 0.1 M  $\text{KNO}_3$  was adjusted with potassium hydroxide (KOH; 85 % Fisher Scientific) and sulphuric acid ( $\text{H}_2\text{SO}_4$ ;  $\geq 95$  %, Fisher Scientific). Acetate buffer was prepared with sodium acetate ( $\text{C}_2\text{H}_3\text{NaO}_2$ ; 99 %, Fisher Chemicals) and glacial acetic acid ( $\text{C}_2\text{H}_4\text{O}_2$ ; 99 %, Sigma Aldrich). Cu was electrodeposited from a deoxygenated acetate buffer solution containing 100  $\mu\text{M}$  copper(II) sulphate pentahydrate ( $\text{CuSO}_4$ ; 99 – 102 %, Merck, Germany). Solutions of 0.1 M  $\text{KNO}_3$  and 0.1 M potassium sulphate ( $\text{K}_2\text{SO}_4$ ;  $\geq 99$  %, Sigma Aldrich) were used during ring disc experiments. Solutions were deoxygenated by bubbling Ar gas (BOC Ltd., UK) through the solution until saturated (minimum  $1 \text{ ml min}^{-1}$ ). Solutions were also oxygenated to aid identification of oxygen based reactions by bubbling  $\text{O}_2$  gas through the solution for a minimum time period corresponding to  $1 \text{ ml min}^{-1}$ . Experiments were undertaken in a temperature controlled lab at  $22\text{-}23^\circ\text{C}$ .

### 4.3.2 Electrode Fabrication

The electrodes were fabricated from freestanding electroanalytical grade polycrystalline BDD cut to the desired geometries using a 355 nm Nd:YAG 34 ns laser micro-machining system (E-355H-ATHI-O system, Oxford Lasers). In this case 1 mm diameter cylinders for the BDD-Q disc and BDD tubes with inner diameter 1.4 mm and outer diameter 2.5 mm were employed. Both were

subjected to a hot acid cleaning procedure as described in Section 2.3.1.1. The cylinders for BDD-Q sensing were subjected to a 600°C thermal anneal in air for 5 hours to remove any remaining sp<sup>2</sup> carbon. They then underwent further ablation from the laser to form the sp<sup>2</sup> carbon containing microspots. A second hot acid treatment was undertaken to remove any loose material and oxygen terminate the remaining material. To provide an electrical contact on all the BDD electrodes, Ti (10 nm) / Au (400 nm) was sputtered (Moorfields MiniLab 060 platform sputter/evaporator) onto the back (lapped) face. To form an ohmic contact these were annealed at 400°C for 5 hours in air, forming a titanium carbide contact between the carbon and titanium layers.

For initial deposition work 1 mm cylinders were sealed in pulled glass capillaries (O.D. 2 mm; I.D. 1.16 mm, Harvard Apparatus Ltd., Kent, UK) with the sputtered contact facing the open end of the capillary. A vacuum was then applied and the edges of the BDD cylinders were heat sealed (Narishige PB-7) within the capillaries. Once sealed the BDD surface was exposed by polishing away the excess glass on CarbiMet grit paper with increasingly fine grains and finally alumina (0.05 µm) paste (Buehler, Germany) until the BDD face was exposed, verified with optical microscopy (Olympus BH-2-HLSH). The back of the capillary was filled with conductive epoxy (Chemtronics, CircuitWorks, UK) and a 0.8 mm diameter copper wire, polished flat (R.S. Components, UK) inserted in contact with the back side of the BDD cylinder. Finally, epoxy resin was added at the top of the capillary to seal the conductive epoxy and stabilise the copper wire, (Araldite, RS, UK).

For the ring disc electrode fabrication followed a similar process to that described in Chapter 3, the biggest difference being a 3D printed mount (Form3, Formlabs) was used to house the ring and disc electrode rather than the intrinsic diamond support to fit the cut geometries and provide a guide for the wires to be contacted. The front face of the BDD-Q disc was coated with polyvinyl acetate (Wilkinsons, UK) to temporarily block the microspots. The coated BDD-Q disc and ring were mounted into the print, ensuring the contacts aligned with the wire guides, and sealed in place with UV cured clear resin (Formlabs). The front face was polished back using increasingly fine carbide paper to expose the BDD faces

and a multimeter was used to ensure the contacts had not been covered. Silver coated copper wires (RS Components, UK) with a 0.45 mm diameter were polished flat on carbide paper and used to contact to the back of the BDD disc and ring using conductive epoxy and left to dry for a minimum of 1 hour. Clear resin was added and UV cured to seal the wires in place. Successful contact was checked with a multimeter. A 3D printed electrode body was then superglued to the cap and backfilled with more clear resin and UV cured, Figure 4.2.

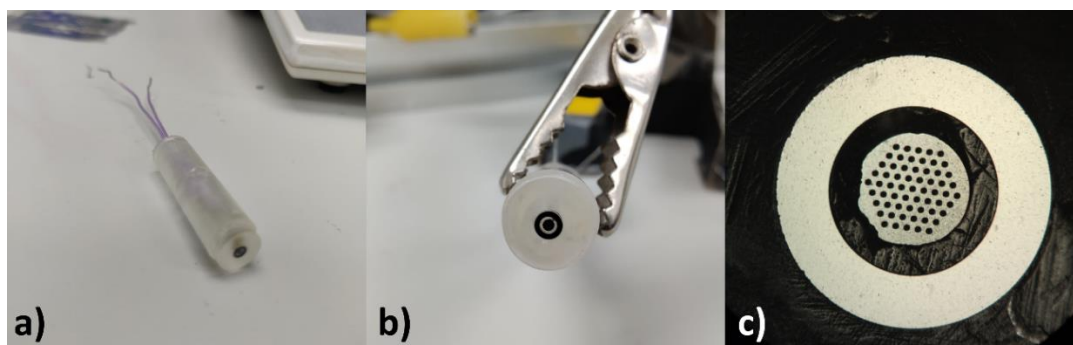


**Figure 4.2** Images of ring disc electrode a) electrode body in final form, b) electrode face and c) optical microscopy image of BDD ring and BDD-Q disc (diameter 1 mm). Note the non-circular appearance of the disc electrode is due to a small amount of resin remaining on the surface of the disc.

### 4.3.3 Electrochemical Measurements

Two potentiostats were used to complete this work. A CH Instruments (CHI)750A was used for initial characterisation and preliminary Cu deposition work. A CHI 760E was used for dual ring disc measurements, operated as a bipotentiostat. The ring, disc and glass sealed electrodes were characterised independently for capacitance and solvent window as described in Sections 2.5.1 and 2.5.2, respectively. The BDD-Q disc was also characterised for QSC as described in Section 2.5.4.

Square wave voltammetry (SWV) was used for pH measurements on the BDD-Q disc (frequency = 150 Hz, amplitude = 0.1 V and step = 4 mV). A cathodic scan range of 0.4 V to -0.3 V was used for calibration and the majority of experiments.<sup>47</sup> The range was increased to -0.6 V for experiments that showed the greatest pH change to ensure the peak was captured. For pH measurement of the bulk solution of interest, six sequential SWV measurements were performed, the first discarded and the remaining five averaged, hence referred to as bulk pH measurements. When recording sequential pH measurements, once the

potentiostat completes a SWV, and prior to recording the next SWV, the potentiostat needs to reset. This involves holding the BDD-Q electrode at open circuit potential (OCP) for a period of  $\sim 100$ 's ms, before the SWV starts again.

Prior to all experiments the BDD-Q electrode was calibrated in pH 4, 7 and 10 Carmody buffers at room temperature as bulk pH measurements. The peak position at the known pH values was used to create a calibration line in the  $E_p = mpH + c$  form. The performance was assessed in an unbuffered solution of 0.1 M  $KNO_3$  acidified to  $\sim$  pH 4 using dilute  $H_2SO_4$ , sequential addition of dilute KOH was used to increase the pH of the solution up to pH 10. A glass pH probe and meter (SevenEasy, Mettler Toledo) was used to measure the pH across the range prior to each BDD-Q measurement.

When performing dual electrode local pH measurements and operating the potentiostat in bipotentiostatic mode, a potential was applied continuously to the ring electrode whilst sequential SWVs were recorded at the BDD-Q disc. In contrast to single electrode measurement, the bipotentiostat instead of letting the disc electrode sit at OCP in between SWVs, requires a potential to be defined. This is due to keeping the cell on between sweeps to maintain the applied potential at the ring. The impact on the pH measurement, of holding the BDD-Q disc electrode at either the start or end potential of the SWV, in between scans, was explored (*vide infra*).

For dual electrode measurements, prior to starting the measurement, the pH of the solution was first measured using the BDD-Q disc electrode as a bulk pH measurement (6 sequential SWV), no potential applied to the ring. For experiments with Cu deposits on the ring, the electrode was removed from the electrolyte solution, Cu was electrodeposited on the ring and the electrodes were rinsed in DI water before being returned to the electrolyte solution. A constant potential of either -0.2, -0.4, -1.0 or -2.0 V vs. SCE was applied to the ring (either bare BDD or Cu NP-BDD) whilst the disc simultaneously performed 20 SWV scans to monitor the local pH change, returning to the start potential of the SWV scan whilst the potentiostat reset between the scans.

Electrochemical deposition of Cu on the ring electrode was performed using current-time (i-t) amperometry in a deoxygenated 100  $\mu$ M  $CuSO_4$  acetate buffer

solution (pH 3.1) holding at -0.6 V for 20 s. Verification of the chemical identity of the electrodeposited species was undertaken by performing a linear sweep voltammetry (LSV) in an acetate buffer, scanning from -0.1 V to 0.6 V to identify a Cu stripping peak and supported by scanning electron microscope (SEM) imaging. After the measurement the Cu electrodeposit was removed by holding the ring at +1.5 V for 20 s in 0.1 M H<sub>2</sub>SO<sub>4</sub>, verified by the absence of a Cu stripping peak in an LSV.

## 4.4 Results and Discussion

### 4.4.1 Electrochemical Characterisation

The BDD ring and BDD-Q disc electrodes had a solvent window of 4.1 V and 2.3 V respectively, and a capacitance of 17.3  $\mu\text{F cm}^{-1}$  and 21.8  $\mu\text{F cm}^{-1}$ , respectively, based on surface areas determined from the 3D profile using white light interferometry (Bruker Controur GTX, Germany). As expected the BDD-Q disc shows a reduced solvent window and higher capacitance than the bare BDD ring due to the deliberate incorporation of sp<sup>2</sup> carbon material.<sup>45</sup> The BDD-Q disc electrode has a QSC of  $3.23 \times 10^{-12} \text{ mol cm}^{-2}$ , calculated again using the surface area from interferometry. The disc showed a pH calibration slope of 60 mV pH<sup>-1</sup> ( $R^2 = 0.997$ ) in buffered solutions (blue; ■) close to the expected Nernstian response, Figure 4.3a.<sup>48</sup> In an unbuffered solution the slope increased slightly to 66 mV pH<sup>-1</sup> ( $R^2 = 0.992$ ) Figure 4.3a (pink; ▲). Ideally the buffered and the ideal response would align, as was seen in Chapter 3 when using an Autolab PGSTAT101 potentiostat.

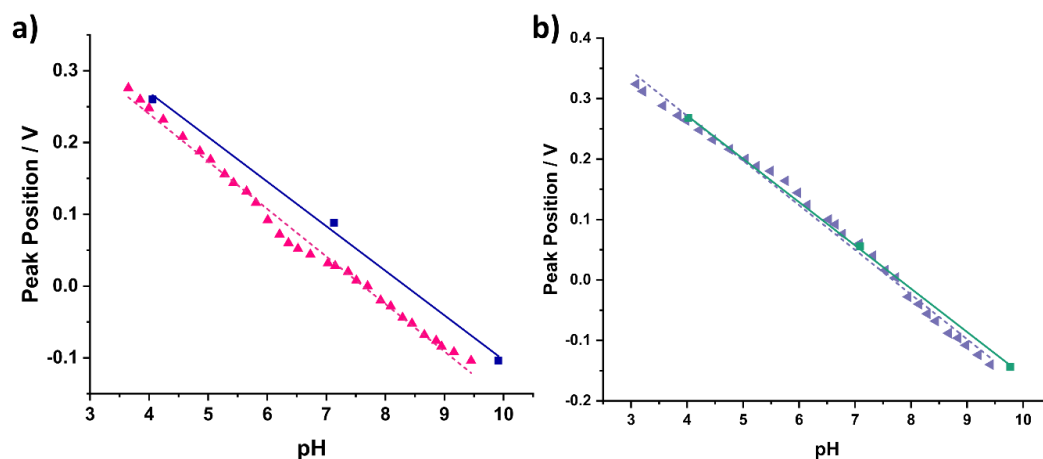


Figure 4.3 Calibration graph for BDD-Q disc electrode at a)  $10 \mu\text{A V}^{-1}$  sensitivity in Carmody buffer solutions (solid line; ■; blue) and pH response in unbuffered solution (dashed line; ▲; pink) and b)  $1 \mu\text{A V}^{-1}$  sensitivities. Carmody buffer solutions (solid line; ■; green) and pH response in unbuffered solution (dashed line; ▲; purple).

Interestingly, we observed that when changing the current sensitivity setting from  $10 \mu\text{A V}^{-1}$  (as for data shown in Figure 4.3a) to  $1 \mu\text{A V}^{-1}$  with the potentiostat used for these experiments (CHI760E) then alignment between buffered and unbuffered data was observed (Figure 4.3b). However, the slope of the calibration had increased to  $72 \text{ mV pH}^{-1}$  in the buffered case (green; ■) and  $74 \text{ mV pH}^{-1}$  in the unbuffered case at a current sensitivity of  $1 \mu\text{A V}^{-1}$ . To explore this further raw *i-t* decay curves using the multipotential step (STEP) techniques were programmed into the CHI. 12 potential steps (6 SWV steps) were input with the smallest sample interval of 10 kHz (0.1 ms) matching as closely as possible the SWV parameters used across the potential range 0.246 to 0.230 V in pH 4 Carmody buffer. Note, the SWV was recorded at a frequency of 150 kHz, the STEP techniques cannot sample this quickly, however, this is still a representative example of the *i-t* decay.

The first forward and reverse step, under the grey panel in Figure 4.4b, are discounted as this step effectively conditions the electrode solution interface for the measurement. At  $0.1 \mu\text{A V}^{-1}$  the potentiostat software reported a current overflow. This did not occur at sensitivities of  $10 \mu\text{A V}^{-1}$  and  $1 \mu\text{A V}^{-1}$ . When looking at the *i-t* decays the  $1 \mu\text{A V}^{-1}$  current decays recorded are outside the range the potentiostat can measure, hence the flatline response (dashed blue

line). This is likely due to an overload of the i/V converter which takes time to recover and distorts the results, seen as an increase in the calibration slope. As SWV records the measurements as a current average over the last 50 – 100% of the i-t decay (region in dashed box, Figure 4.4b) in the forward and reverse step, the current is not overloading in this region, hence the potentiostat does not report an overflow current.

From the outputted current in the normal SWV scan (Figure 4.4a) the sensitivity should be set at  $1 \mu\text{A V}^{-1}$ , however this is evidently not appropriate. This variation in calibration slope with sensitivity has not previously been noticed when using glass sealed BDD-Q macroelectrodes. It is possible this effect has been exacerbated by increased resistance in the BDD-Q ring disc electrode. This behaviour is still not fully understood but highlights issues associated with using commercial potentiostats in that the user rarely gets access to the raw data and only sees data which has been processed by the potentiostat.<sup>49</sup> For the purpose of the experiment this is not problematic, a buffered calibration line as seen in Figure 4.3a was used for all peak position to pH conversions but recalibrated prior to each experimental run and the calibration was verified by recalibrating after each set of experiments. All SWV measurements were made at a sensitivity of  $10 \mu\text{A V}^{-1}$ .

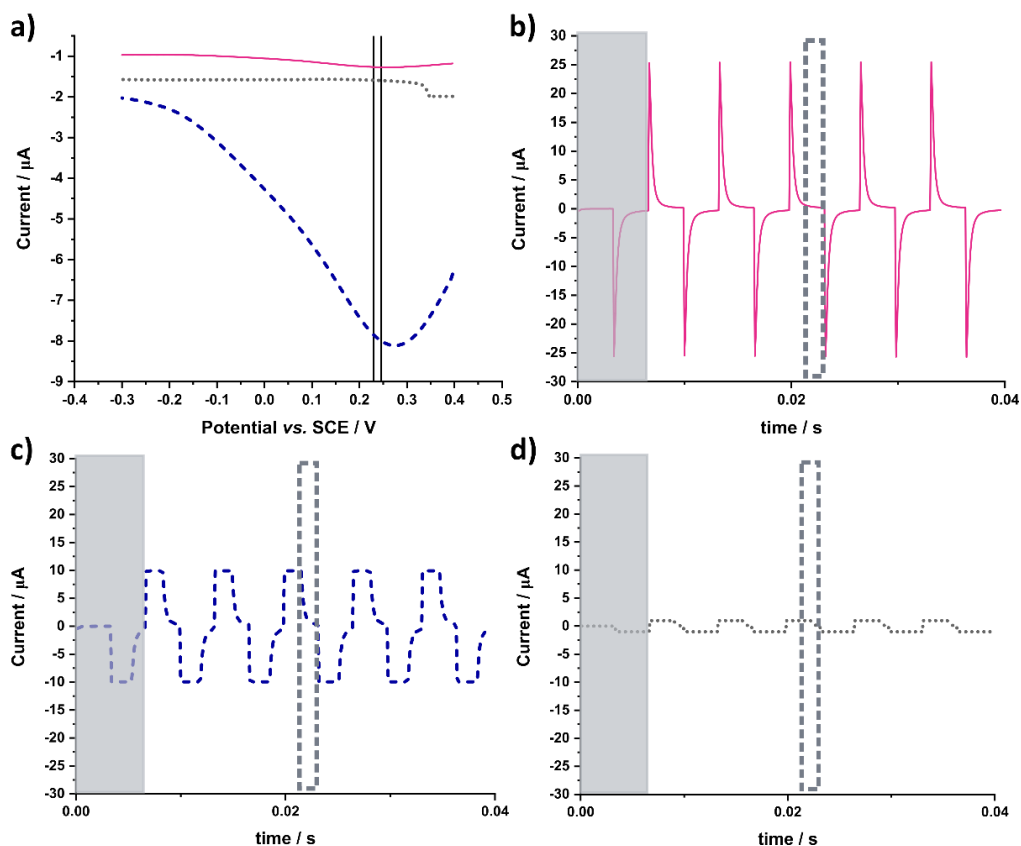


Figure 4.4 a) SWV responses of BDD-Q disc in ring disc arrangement at  $0.1 \mu\text{A V}^{-1}$  (black dotted line)  $1 \mu\text{A V}^{-1}$  (blue dashed line)  $10 \mu\text{A V}^{-1}$  (pink solid line) and *i-t* decay response over 0.246 to 0.230 V using STEP measurement to simulate SWV response at at b)  $10 \mu\text{A V}^{-1}$  (pink solid line), c)  $1 \mu\text{A V}^{-1}$  (blue dashed line) and d)  $0.1 \mu\text{A V}^{-1}$  (black dotted line). Grey box covers first 'step' response is not representative in the first measurement. Dashed grey box shows 50 -100% region of one *i-t* decay, the region sampled by the potentiostat during a SWV measurement.

To verify whether the holding potential at the BDD-Q disc electrode between SWV measurements impacted the pH measurement on the disc, SWV measurements in pH 4, 7 and 10 buffered solutions were made with the electrode held at either (i) OCP ( $\blacktriangle$ ); (ii) at the final potential of the scan, typically -0.3 V, ( $\blacksquare$ ); or (iii) returning to the start potential, 0.4 V, ( $\bullet$ ), Figure 4.5. As can be seen, in Figure 4.5b, the calibration gradient and  $R^2$  values were the same for all three conditions;  $-57.1 \text{ mV pH}^{-1}$  and 0.993, respectively. The intercept value was 0.474 V for OCP and holding at the final potential whilst for returning to the start potential, was 0.470 V. Given that all three conditions result in very similar responses, any could have been used. Returning to the start potential in between sequential SWV scans was used for all subsequent bipotentiostatic experiments



as for the experiments with Cu present holding at 0.4 V would additionally prevent any Cu deposition on the disc.

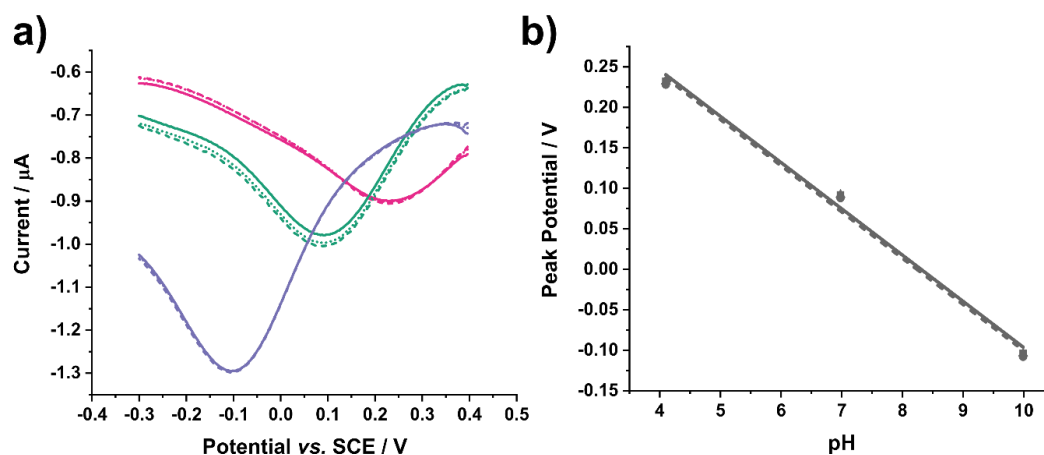


Figure 4.5 (a) pH calibration SWV measurements in pH 4 (pink), 7 (green) and 10 (purple) Carmody buffers and (b) corresponding pH calibration lines under OCP (solid line;  $\blacktriangle$ ), Cell On returning to start potential (dashed line;  $\bullet$ ) and Cell on holding at final potential (dotted line;  $\blacksquare$ )

#### 4.4.2 Electrochemical response of bare BDD

To provide a baseline for the electrocatalytic activity of Cu, the response of the bare BDD ring was investigated in both nitrate ( $\text{KNO}_3$ ) and sulfate ( $\text{K}_2\text{SO}_4$ ) electrolytes at 0.1 M concentration, typically pH 5.5 and 6.0 respectively. Initially, LSVs were taken scanning cathodically from 0.0 V to -2.0 V vs. SCE in both electrolyte solutions, Figure 4.6. The scans were virtually featureless until the solvent window due to the electrocatalytically inert qualities of BDD.<sup>45</sup> Processes such as ORR which are present in aerated solutions are often convoluted with WR and other solvent window features on BDD, due to the very slow electron transfer kinetics for ORR.<sup>45</sup> The solvent window is slightly reduced in the nitrate electrolyte than the sulfate, this is most likely due to the pH differences between the two solutions, the slightly more acidic pH of the nitrate (pH 5.5) contains more protons than the sulfate (pH 6.0) solution which shifts the water reduction to a less negative potential. Any  $\text{sp}^2$  carbon exposed on the edges of the ring could catalyse ORR and WR, but the contributions appear to be minimal in this data, as the current is featureless at low potentials.<sup>45</sup>

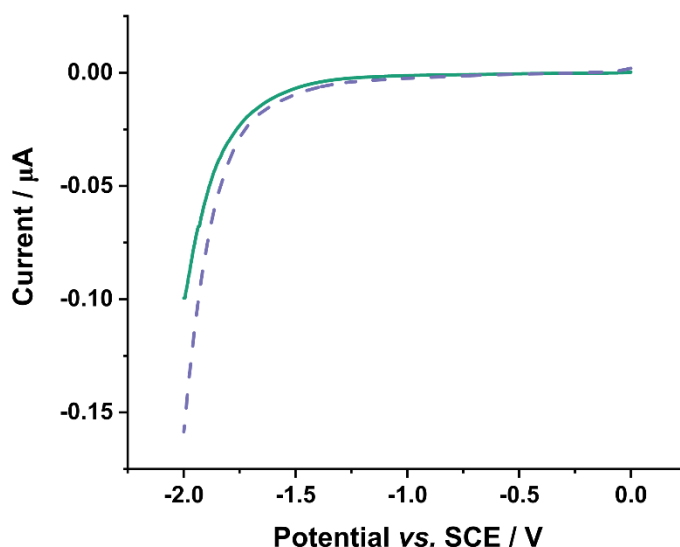


Figure 4.6 LSV on bare BDD ring electrode in aerated 0.1 M  $\text{KNO}_3$  (purple; dotted line) and 0.1 M  $\text{K}_2\text{SO}_4$  (green) solutions. Undertaken with a  $0.1 \text{ V s}^{-1}$  scan rate.

#### 4.4.3 Electrochemical response of Cu NP-BDD electrode

As previously stated in Section 4.2, Cu is stable in many different forms. Therefore investigation was first required to ensure the correct electrodeposition conditions for formation of pure  $\text{Cu}^0$  metal deposits. Exclusion of oxygen and working in acidic conditions are known to aid the deposition of Cu metal. Previous work from the group<sup>20</sup> had considered the effect of different electrolyte solutions on the deposition of Cu and concluded that a deoxygenated acetate buffer solution at pH 3.1 consistently produced  $\text{Cu}^0$  deposits. Therefore a  $100 \mu\text{M}$   $\text{CuSO}_4$  deoxygenated acetate buffer solution was used for deposition of Cu. Anodic Stripping Voltammetry (ASV) in acetate buffer was used to confirm the deposits were Cu metal. A CV was performed on the ring of the ring disc electrode in the deposition solution, as shown in Figure 4.7. A clear deposition peak was seen at  $-0.17 \text{ V vs. SCE}$ , followed by a stripping peak in the oxidative scan at  $0.11 \text{ V}$  which can be associated with the removal of  $\text{Cu}^0$  in the  $\text{Cu}^{2+}$  form.

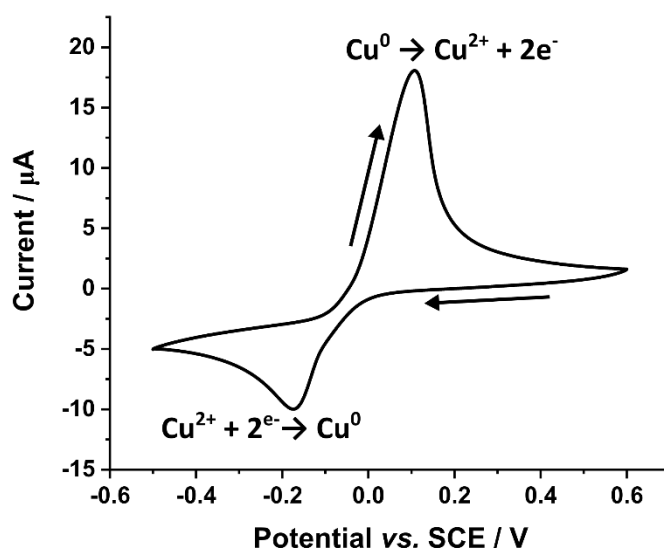


Figure 4.7 A cyclic voltammogram performed on the ring of the BDD ring disc electrode in  $100 \mu\text{M}$   $\text{CuSO}_4$  deoxygenated acetate buffer, pH 3.1. Scan rate =  $0.1 \text{ V s}^{-1}$ .

A series of deposition potentials and times were investigated and the resulting deposits characterised using ASV. Stripping was performed as quickly as possible after deposition to limit possible oxidation or transformation. The electrode was moved to an acetate buffer solution that did not contain Cu for stripping. Initially  $-0.80 \text{ V}$  was chosen as a deposition potential, which is well past the reduction peak seen in Figure 4.7. This high overpotential was chosen to encourage deposition of a high density of smaller particles across the ring. Deposition times of 10 s, 20 s and 30 s were considered, Figure 4.8a. All three stripping peaks showed an initial peak  $\sim 0.10 - 0.15 \text{ V}$  but exhibited a broad shoulder suggesting the presence of a heterogeneous morphologies and possible copper (I or II) oxide presence resulting in stripping over a broader potential range. A deposition time of 20 s was chosen to investigate alternative deposition potentials. The additional potentials considered were  $-0.50$ ,  $-0.60$  and  $-0.70 \text{ V}$ , Figure 4.8b.

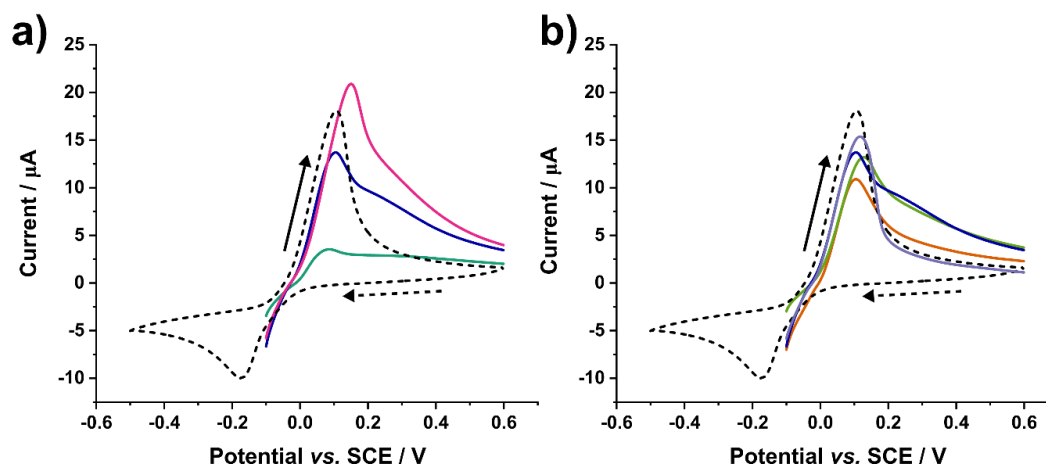


Figure 4.8 Dashed line is Cu CV performed on the ring of the BDD ring disc electrode in 100  $\mu\text{M}$   $\text{CuSO}_4$  deoxygenated acetate buffer over laid by; a) ASV data from Cu deposition in deoxygenated 100  $\mu\text{M}$   $\text{CuSO}_4$  in acetate buffer at -0.8 V for 10 s (green), 20 s (blue) and 30 s (pink) stripped in acetate buffer solution, b) ASV data from Cu deposition in deoxygenated 100  $\mu\text{M}$   $\text{CuSO}_4$  in acetate buffer for 20 s at -0.5 V (orange), -0.6 V (purple), -0.7 V (green) and -0.8 V (blue). All undertaken at a scan rate of 0.1  $\text{V s}^{-1}$ .

The most well-defined stripping peak was from the deposition at -0.60 V for 20 s (Figure 4.8b; purple line), aligning well with the stripping peak of Cu recorded in the CV. No significant shoulder was observed, suggesting the morphology of deposits was uniform and homogeneous. The more negative peak potentials showed reduced peak heights and broader shoulders in comparison suggesting again a range of deposited morphologies. At -0.5 V the peak height was reduced compared to -0.6 V and showed a higher baseline after the peak. Therefore a 20 s deposition time at -0.6 V was used for experiments with Cu present as these ASV peaks suggest that produces the most uniform deposit on the ring electrode.

Scanning electron microscopy (SEM) was used to further probe the Cu deposits, Figure 4.9. The electrodeposited Cu particles are on the nanometre scale and the morphology is consistent with deposits of  $\text{Cu}^0$ , previously verified by Energy Dispersive X-Ray Analysis (EDX) by the absence of oxygen in the locations of Cu deposits.<sup>20</sup> It was challenging to capture clear SEM images of the deposits on the ring electrode due to the large amount of polymer the electrodes are set in. Therefore, EDX on these deposits was not possible, and image quality is limited due to the build-up of charge on the electrode during the image capture.

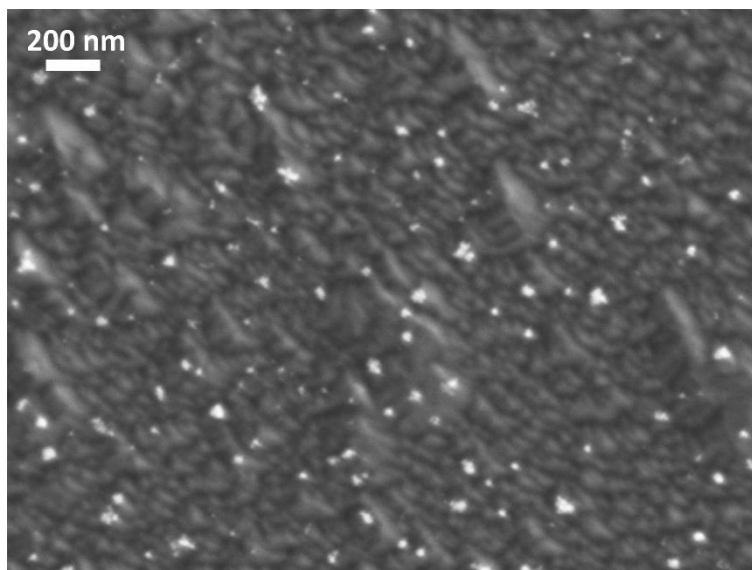


Figure 4.9 SEM image of Cu deposits (white spots) on ring of BDD-Q ring disc electrode, deposited from a deoxygenated 100  $\mu\text{M}$   $\text{CuSO}_2$  acetate buffer solution by holding at -0.6 V vs. SCE for 20 s.

#### 4.4.4 Electrocatalytic effect of Cu

LSVs were repeated with Cu electrodeposited on the ring using the procedure determined in Section 4.4.3, Figure 4.10. It is immediately evident that Cu shows electrocatalytic activity when compared against the response for the bare BDD ring electrode (dotted lines). Starting with deoxygenated conditions (Figure 4.10 a and b; dashed line), the current starts to rapidly increase in nitrate media at a potential of -1.2 V vs. SCE, compared with -1.6 V vs. SCE for sulfate solutions. This decreased solvent window in nitrate media is likely associated with Cu NP catalysed NRR and WR,<sup>27</sup> whilst in sulfate solutions it is likely to be due only to Cu catalysed WR. In ambient conditions (Figure 4.10 a and b; solid line) a pre wave at -1.0 V in the nitrate solution and a smaller response is evident in sulfate media at -1.2 V likely to be ORR.

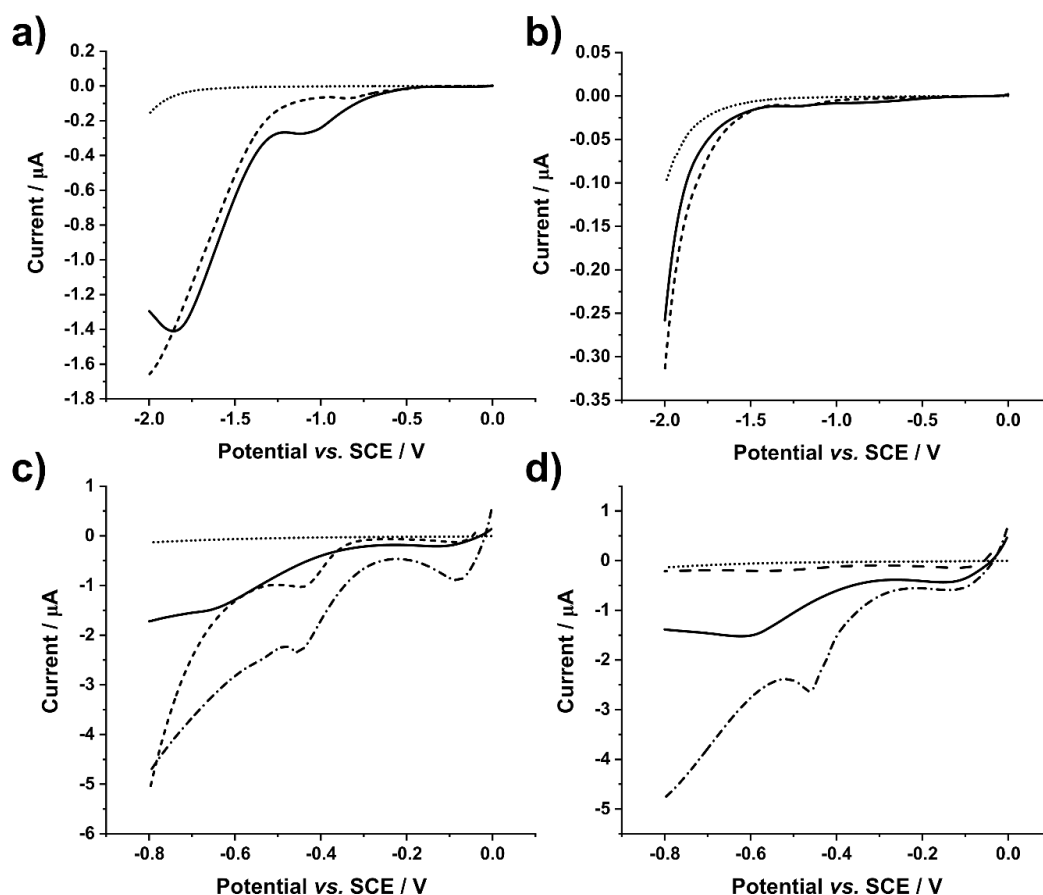


Figure 4.10 LSV responses in 0.1 M  $\text{KNO}_3$  (a & c) and 0.1 M  $\text{K}_2\text{SO}_4$  (b & d) on ring electrode of ring disc (a & b) and a 1 mm macro electrode (c & d) without Cu NPs (dotted line), and with Cu NPs in; aerated solutions (solid line), deoxygenated solutions (dashed line) and oxygenated solutions (dot dash line). Undertaken with a  $0.1 \text{ V s}^{-1}$  scan rate.

To investigate further the role of oxygen in solution, LSVs were repeated with a reduced scan range 0 to -0.8 V, on a 1 mm Cu NP-BDD macroelectrode in aerated, deoxygenated and oxygen saturated solutions Figure 4.10 c and d. The initial peak seen in all LSVs around -0.1 V is likely a Cu electrodeposition peak due to the small amount of dissolution of the Cu deposits prior to and at the start of the LSV, as these potentials are close to the Cu stripping peak. A clear peak is seen in the oxygen saturated solutions (dash dot line) with a peak at -0.45 V and -0.46 V in the  $\text{KNO}_3$  (Figure 4.10c) and  $\text{K}_2\text{SO}_4$  (Figure 4.10d) solutions, respectively. This is likely to be Cu catalysed ORR. This peak is also observed in the deoxygenated  $\text{KNO}_3$  solution, this is likely due to an incomplete removal of all  $\text{O}_2$  or regassing of  $\text{O}_2$  whilst setting up the electrodes.<sup>50</sup> Without a glove box it is challenging to remove all  $\text{O}_2$  despite using an argon blanket and reducing set up times as much as possible during the measurement. The deoxygenated sulfate

solution shows much lower currents than the aerated and oxygen saturated solutions. In the ambient LSVs (solid lines) the ORR peak is shifted to  $\sim -0.65$  V. There appear to be some differences in the potentials between the data on the macroelectrode and the ring electrode. However, this is not surprising as the geometry, area, Cu NP density and fabrication of the two electrodes are likely to impact the electrochemistry and account for these variations.

The catalytic effect of Cu NPs compared to the blank BDD electrode surface is evident from this data. ORR, NRR and WR all result in a pH increase. The BDD-Q ring disc provides an opportunity to measure the pH changes over a time period whilst driving an electrochemical reaction on the Cu NP-BDD electrode. This was achieved by applying four ring electrode potentials (i)  $-0.2$  V; (ii)  $-0.4$  V; (iii)  $-1.0$  V and (iv)  $-2.0$  V corresponding to potentials where (i) no reaction should occur, (ii) ORR and (iii) NRR has commenced and (iv) WR is dominating. All potentials considered were applied in both aerated nitrate and sulfate solutions. Deoxygenated solutions were also used to probe the role of ORR at an applied ring potential of  $-0.4$  V. The concentration of dissolved oxygen in ambient solutions is ca.  $0.25$  mM,  $20\%$   $O_2$  at  $25^\circ\text{C}$ ,<sup>51</sup> which is significantly lower than the concentrations of nitrate and water, at potentials where NRR and WR occur the contribution of ORR to the overall pH change was expected to be minimal. Therefore, deoxygenating the solution for applied potentials of  $-1.0$  and  $-2.0$  V was deemed unnecessary. Note, prior to switching on the ring electrode potential, a bulk pH measurement was made on the BDD-Q disc electrode which reflects the bulk pH of the solution to be used for the experiment. A continuous potential was then applied to the ring electrode whilst simultaneously performing 20 sequential SWV measurements on the disc electrode,  $\sim 30$  s scanning time in total. Experiments were first carried out using the bare BDD ring electrode.

#### 4.4.4.1 pH Tracking in Nitrate Electrolyte

The starting pH in the  $0.1$  M  $\text{KNO}_3$  solution was typically measured to be pH  $5.5$  using the glass pH probe, although fluctuations between pH  $5.0$  and  $6.0$  were observed. This is likely due to age of the solution and the dissolved  $\text{CO}_2$  present

which can fluctuate within the lab. When no potential was applied to the ring electrode the SWV peak position remained fixed for the 20 sequential SWV scans. Figure 4.11 shows the BDD-Q SWV peaks recorded continuously upon application of a potential of -2.0 V vs. SCE to the BDD ring in an aerated 0.1 M  $\text{KNO}_3$  solution over a timescale of  $\sim 33$  s. The SWV peak potential shifted by 404 mV, which corresponds to a pH increase of 6.9 pH units, from pH 5.1 to 14.4. At this potential on the BDD ring, current will flow due to the WR. This was the largest shift in peak potential observed in the nitrate electrolyte. Note, the scan range was extended to -0.6 V for these measurements to capture the change in peak potential position due to the large change in the local pH. The scan range is typically kept as narrow as possible, to avoid encountering any faradaic process which could alter the local pH.<sup>47</sup> However, as shown in Figure 4.11, there appeared to be no obvious competing reactions. Extending the potential window, increases the total scan time by approximately 3 s.

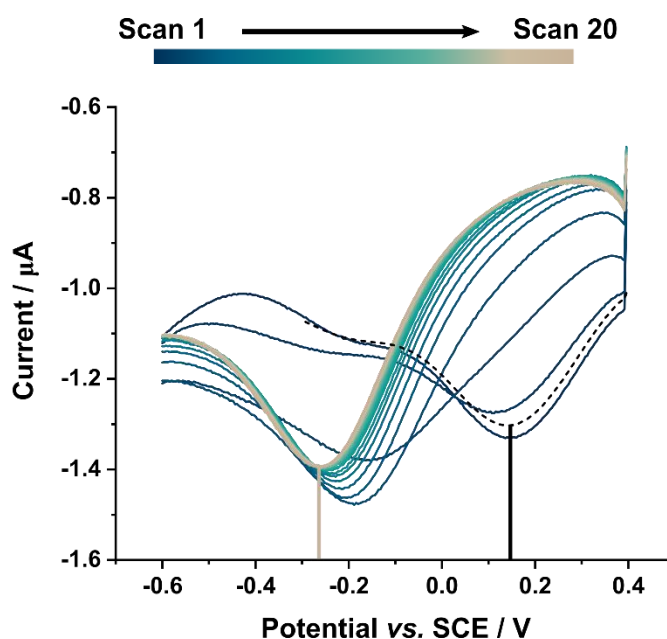


**Figure 4.11** Background response of BDD ring disc electrode in aerated 0.1 M  $\text{KNO}_3$ . Dashed line is the bulk measurement on disc prior to applying a potential to the ring. 20 sequential SWV scans on disc electrode with -2.0 V applied to the ring.



The peak potentials were converted to pH values using the calibration curve  $E_p = -0.05879 \text{ pH} + 0.49571$  and the pH change (from the bulk pH measurement) plotted as a function of SWV scan number (which equates to time, approximately 2 s per scan). This was performed for all ring potentials applied (-0.2, -0.4 aerated and deoxygenated, -1.0 and -2.0 V) and is displayed in Figure 4.12.

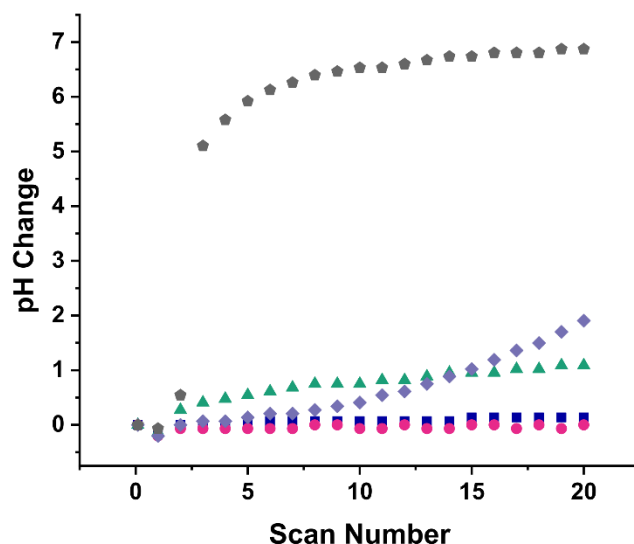


Figure 4.12 The measured pH change in an aerated 0.1 M  $\text{KNO}_3$  on the disc electrode, unless otherwise stated, at ring potentials of -0.2 V (■), -0.4 V in deoxygenated solution (●), -0.4 V (▲), -1.0 V (◆) and -2.0 V (◆) normalised to measured bulk concentration.

SWV data for an applied ring potential of -0.4 V in a deoxygenated 0.1 M  $\text{KNO}_3$  solution is shown in Figure 4.13. When oxygen was removed, by bubbling argon at a minimum rate of  $1 \text{ ml min}^{-1}$  through the solution, no overall peak shift was observed between the bulk measurement and the final pH peak of the scan, as expected due to their being no faradaic process occurring at this potential to result in a pH change. Note, the deoxygenation process results in an increase in the pH of the starting solution, due to the removal of dissolved  $\text{CO}_2$ . When measured with a glass pH probe the starting pH of the deoxygenated  $\text{KNO}_3$  solution was 7.70.

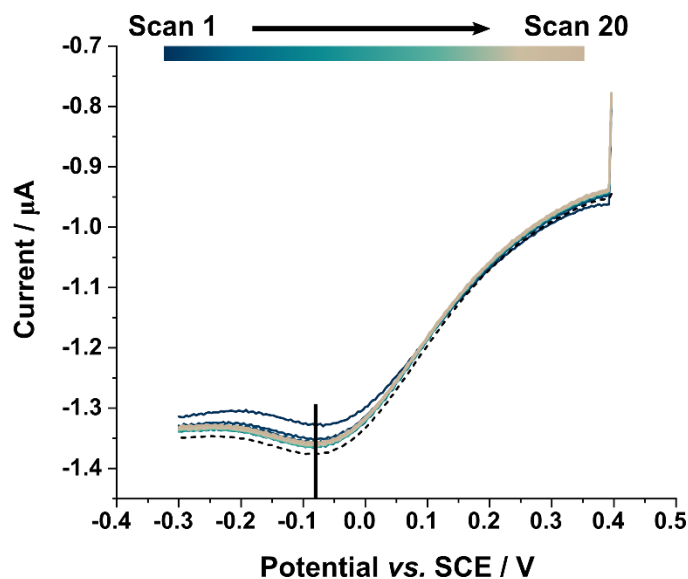


Figure 4.13 Background response of ring disc electrode in deoxygenated 0.1 M  $\text{KNO}_3$ . Dashed line is the bulk measurement on disc prior to applying a potential to the ring. 20 sequential SWV scans on disc electrode with -0.4 V applied to the ring.

In Figure 4.13, the first scan in this SWV sequence is shifted slightly more positive than the bulk pH measurement (dashed line) and the other SWV peaks. A slightly different response for the first SWV, is nearly always seen with SWV BDD-Q measurements. This is attributed to the electrode surface dissipating any surface charge from interfacial interactions between the solution and electrode that occur at OCP prior to the commencement of the experiment. This is why the first scan is discarded in bulk SWV pH measurements. However, for these measurements, where sequential SWVs were used to monitor the time evolving local pH gradient, the first SWV data point was included, but based on our understanding of SWV measurements should be treated with caution. This accounts for the apparent negative pH change observed in the second data point of Figure 4.12. The first data point at scan number 0, corresponds to the bulk pH measurement. In order to visualise the pH changes more clearly, we report pH changes on the y axis normalised to the bulk pH for each measurement.

The SWV for pH tracking in aerated  $\text{KNO}_3$  solutions at applied BDD ring potentials of -0.2, -0.4 and -1.0 V over a  $\sim 30$  s time period are shown in Figure 4.14. At -0.2 V a peak potential shift of 8 mV is recorded, Figure 4.14a, corresponding to a pH increase of 0.14 pH units. The shift could be due to either a small amount of ORR

or slight instability in the pH measurement. Any exposed edge on the ring will contain small amounts of  $sp^2$  carbon which can catalyse ORR,<sup>45</sup> however given the small applied potential this is more likely to be a small instability of the BDD-Q sensor in the unbuffered solution. However, ORR clearly plays a small role as at -0.4 V there is a peak position shift of 64 mV in the aerated solution, Figure 4.14b, compared to no shift in the deoxygenated solution, Figure 4.13. This is a 0.75 pH unit increase under aerated conditions. At -1.0 V a 112 mV shift in peak potential was observed, corresponding to an increase of 1.9 pH units from the starting pH 6.53, Figure 4.14c.

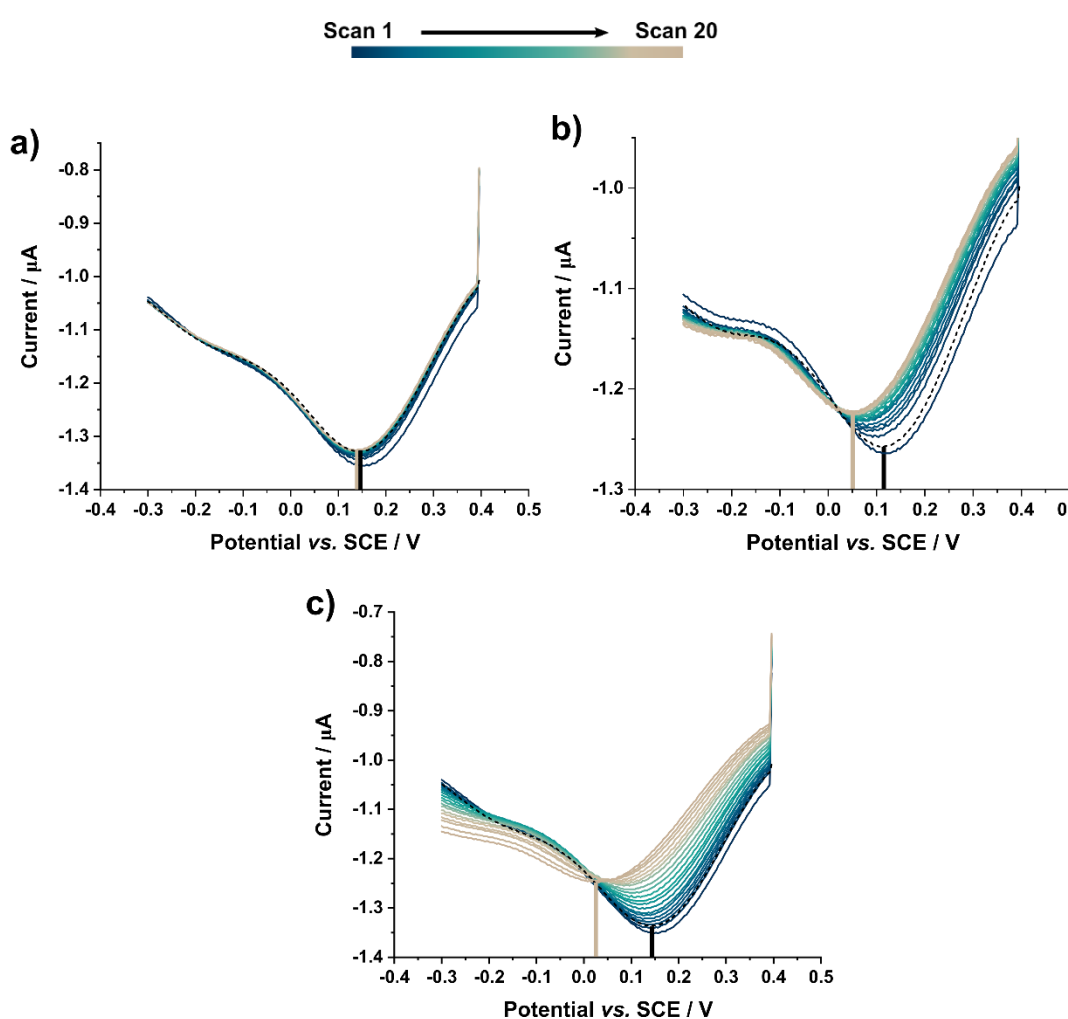


Figure 4.14 Background response of ring disc electrode in aerated 0.1 M  $KNO_3$ . Dashed line is the bulk measurement on disc prior to applying a potential to the ring. a) 20 sequential SWV scans on disc electrode with -0.2 V applied to the ring b) 20 sequential SWV scans on disc electrode with -0.4 V applied to the ring and c) 20 sequential SWV scans on disc electrode with -1.0 V applied to the ring.

#### 4.4.4.2 pH Tracking in Sulfate Electrolyte

The aerated 0.1 M  $K_2SO_4$  solution has a slightly higher starting pH than the aerated nitrate solution, of around 6.0, likely due to the formation of  $HSO_4^-$  ions, consuming a small amount of protons in the solution. Again variations between pH 5.9 and 6.5 were measured in each solution on the glass pH probe throughout the day. No shift in the BDD-Q SWV peak position was seen as a function of time, compared to the bulk solution, when -0.2 V was applied to the ring in an aerated solution, Figure 4.15a. An 84 mV shift was observed when the ring was held at -1.0 V corresponding to a 1.4 pH unit increase, Figure 4.15b. Similar currents were passed at the BDD ring in both electrolyte solutions when -1.0 V was applied suggesting a small contribution of WR is occurring at this potential.

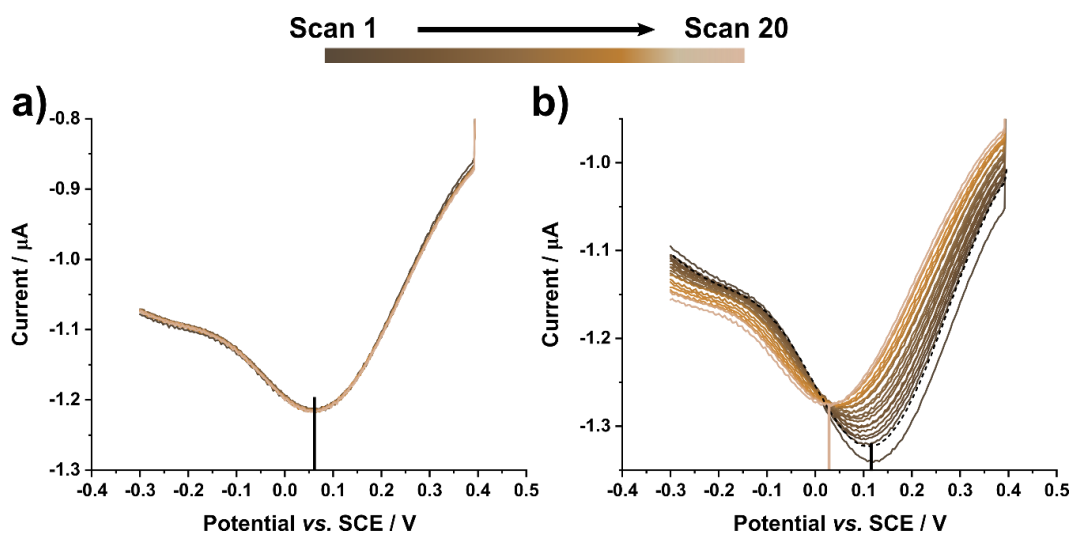
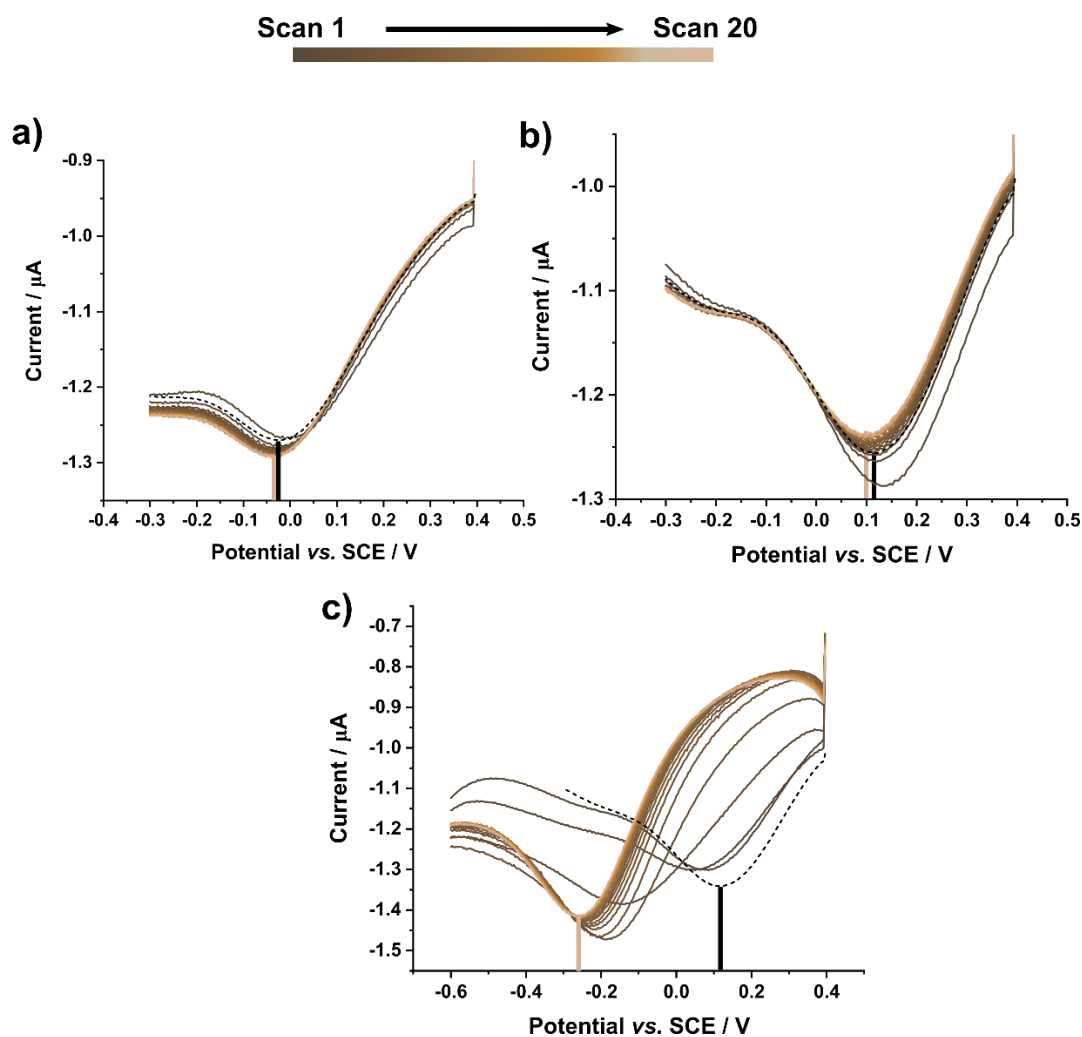


Figure 4.15 Background response of ring disc electrode in aerated 0.1 M  $K_2SO_4$ . Dashed line is the bulk measurement on disc prior to applying a potential to the ring. a) 20 sequential SWV scans on disc electrode with -0.2 V applied to the ring b) 20 sequential SWV scans on disc electrode with -1.0 V applied to the ring.

A small shift in the SWV peak potential was measured at -0.4 V in both the deoxygenated and aerated 0.1 M  $K_2SO_4$  solutions of 12 mV and 16 mV, Figure 4.16 a and b, respectively. In the aerated 0.1 M  $K_2SO_4$  solution the 16 mV shift equates to a 0.27 pH unit increase, much less than the 1.09 pH unit increase in the  $KNO_3$  solution. This possibly suggests a reduced contribution of ORR (at the  $sp^2$  carbon features) in the presence of sulfate ions at this potential. The similar shift observed in the deoxygenated solution, corresponds to 0.20 pH unit increase, this

is most likely due to a small amount of ORR from incomplete oxygen removal. Again the most significant SWV peak potential shift was observed at -2.0 V with a 376 mV shift corresponding to a 6.4 pH unit increase from 6.5 to 12.9 (Figure 4.16c), attributable to WR and requiring a larger potential scan range to capture the changing SWVs. The overall pH changes normalised to the bulk concentration measurement, calculated in the same way as for the nitrate, are shown in Figure 4.17.



**Figure 4.16** Background response of ring disc electrode in 0.1 M  $K_2SO_4$ . Dashed line is the bulk measurement on disc prior to applying a potential to the ring. a) 20 sequential SWV scans on disc electrode with -0.4 V applied to the ring in a deoxygenated solution b) 20 sequential SWV scans on disc electrode with -0.4 V applied to the ring in an aerated solution and c) 20 sequential SWV scans on disc electrode with -2.0 V applied to the ring in an aerated solution.

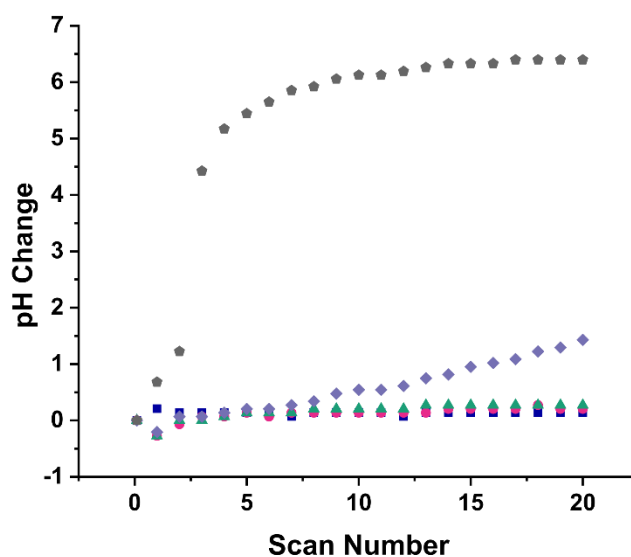


Figure 4.17 The measured pH change in 0.1 M K<sub>2</sub>SO<sub>4</sub> on the disc electrode at ring potentials of -0.2 V (■), -0.4 V in deoxygenated solution (●), -0.4 V (▲), -1.0 V (◆) and -2.0 V (●) normalised to measured bulk concentration. Unless stated all solutions are aerated.

The data above has shown that the ring disc BDD-Q pH sensor arrangement in the two different electrolyte solutions is capable of detecting electrochemically induced changes in the local pH. A summary of the results is shown in Table 4.1.

Table 4.1 Summary table of pH change measured on BDD-Q disc over ~ 30s in 0.1 M KNO<sub>3</sub> and K<sub>2</sub>SO<sub>4</sub> solutions when a range of potentials are applied to the bare BDD ring electrode.

Applied Ring E / V	Nitrate pH change	Sulfate pH change
-0.2	0.14	0
-0.4 Deoxygenated	0	0.20
-0.4	1.09	0.27
-1	1.91	1.43
-2	6.87	6.40

#### 4.4.5 pH Tracking with a Cu-NP BDD Ring Electrode

To consider how the electrocatalytic activity of the Cu NPs on the BDD influenced local pH changes, the same potentials were applied to the ring electrode after electrodeposition of Cu NPs. As before a bulk pH measurement was made on the

BDD-Q disc in the electrolyte solution. An electrodeposition was then performed on the ring with the conditions determined in Section 4.4.3, before being replaced into the electrolyte solution for the experiment. In initial experiments, a significant second peak was observed on the BDD-Q disc. The main pH peak was also shifted by 64 mV in the positive direction, *i.e.* indicating a more acidic solution, Figure 4.18a. These two factors suggested transfer of the deposition solution into the test solution. The acetate buffer at pH 3.1 was responsible for causing a slight acidic pH shift, whilst it was postulated that the second peak was due to Cu deposition from transferred  $\text{Cu}^{2+}$  ions locally accumulated on the disc electrode.<sup>47</sup> An attempt was made to minimise this second peak via the inclusion of a more vigorous rinsing step. Two procedures were investigated, gentle rinsing in static DI water and stirring in DI water or the test electrolyte solution.

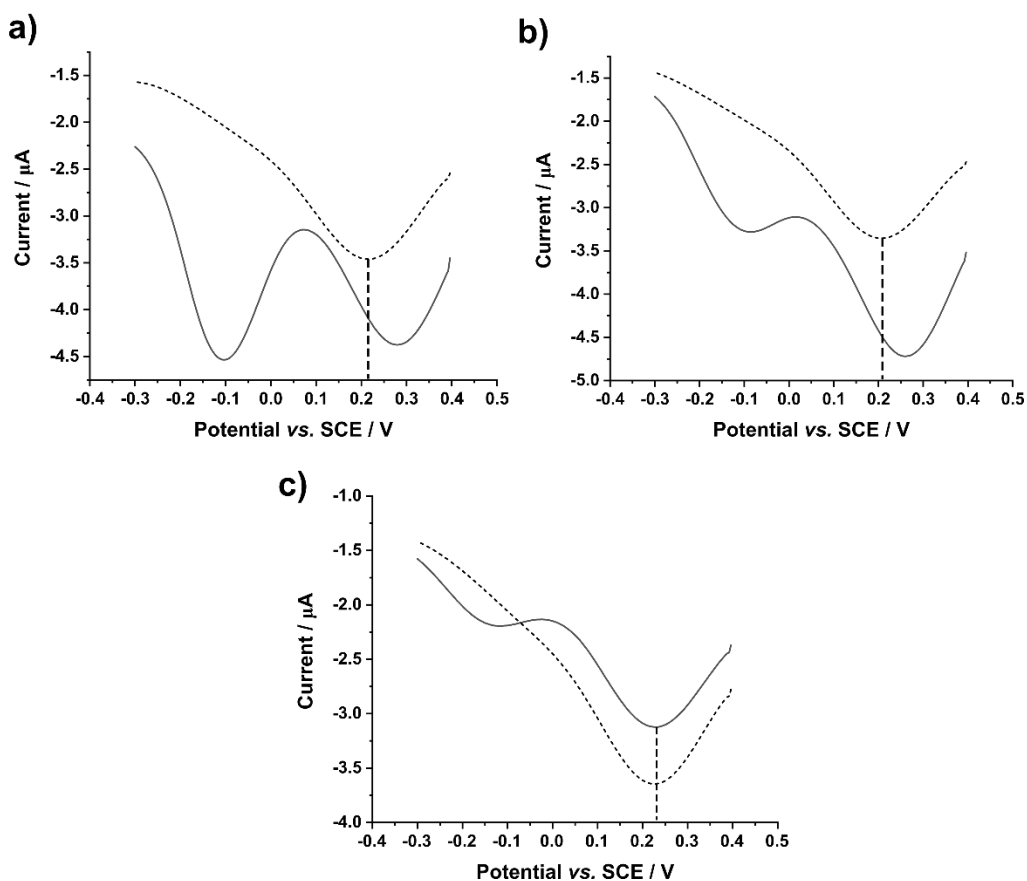


Figure 4.18 Bulk pH measurements in 0.1 M  $\text{KNO}_3$  on BDD-Q disc before Cu deposition (dashed line) and after Cu deposition returned to the original 0.1 M  $\text{KNO}_3$  solution (solid line) a) without rinsing, b) rinsed gently in static DI and c) rinsed in DI stirred with a magnetic flea.

Gentle rinsing in DI water reduced the magnitude of the second potential peak at -0.1 V but an acidic shift in the pH peak still occurred, Figure 4.18b. When the electrode was placed into an electrolyte solution stirred with a magnetic flea the pH peak aligned well with the bulk pH measurement and the second peak was significantly reduced, Figure 4.18c. Therefore, this mode of rinsing was used for all further experiments with Cu electrodeposited electrodes. Note, the reference and counter electrodes were also rinsed with DI water before being placed into the measurement solution to further reduce carry over. The data was discarded if the bulk pH was significantly different to the starting pH recorded by the BDD-Q disc electrode.

Fresh Cu NPs were deposited for each experiment to ensure that  $\text{Cu}^0$  was the deposited form and in the same morphology at the start of each experiment. Given the applied potentials it is possible that the Cu species would have changed through the duration of the experiment. Whilst the rinsing technique chosen could potentially oxidise the surface layers of the Cu deposits,<sup>52</sup> ensuring no carry-over of the deposition solution was a more significant barrier to the experiment. Once the pH tracking measurement was complete, the electrode was transferred to a 0.1 M  $\text{H}_2\text{SO}_4$  solution where an oxidative potential of 1.5 V was applied to the ring for 20 s to electrochemically remove the Cu deposits via Cu oxidation. An LSV was then performed in a fresh 0.1 M  $\text{H}_2\text{SO}_4$  solution to ensure no Cu stripping features were observed. Manual polishing with alumina particles was conducted prior to the calibration of the BDD-Q disc, the very first experiment, for each run of experiments. However, alumina polishing was avoided during individual experiments of the run to ensure the original calibration held and to ensure the condition of the ring and disc were not changed due to exposure of the BDD edges, as the insulating resin can be removed by over polishing. The calibration was also verified by repeating the calibration measurements at the end of each set of experiments.

#### 4.4.5.1 pH Tracking with Cu nanoparticles in Nitrate electrolyte

The same applied ring potentials were considered as on the blank BDD ring (-0.2, -0.4, -1.0 and -2.0 V vs. SCE), with Cu NPs decorating the ring. As before 20 SWVs, corresponding to approximately 30 s, were captured in aerated 0.1 M  $\text{KNO}_3$  (and



a deoxygenated 0.1 M  $\text{KNO}_3$  solution at -0.4 V) to monitor any variation in the local pH environment. The SWV response in aerated  $\text{KNO}_3$  at -1.0 and -2.0 V are shown in Figure 4.19 a and b, respectively. When the larger potentials were applied to the ring electrode, significant pH shifts were seen. The 6.66 pH unit increase, a SWV peak position shift of 392 mV, at -1.0 V is a significant increase compared to the 1.91 pH increase at this potential at the bare BDD ring electrode. During a time period of 30 s the local pH environment rose to a pH of 11.71 with Cu NPs present, Figure 4.19a. The pH peak shifts to more negative potentials with this pH increase, however there is no visual evidence of interference from the second peak, believed to be associated with Cu. At the increased local pH, Cu would not be present in the  $\text{Cu}^{2+}$  form so it is also possible that deposition to the pure metal does not occur. The peak position of this second peak varies across the experiments (*vide infra*). The large increase measured at -1.0 V can be attributed to significant ORR, NRR and possibly small amounts of WR. At this potential, with the Cu NPs the ring passed 10's  $\mu\text{A}$  of current.

The pH increase at -2.0 V was even more extreme than without the Cu present shifting by 544 mV, an increase of 9.24 pH units calculated from the buffered calibration over  $\sim 33$  s. The measured peak position shift is so large it is outside the calibration range, so it is difficult to fully quantify this shift. A large decrease in potential is observed in between the bulk SWV peak position (dashed line) and the first SWV measurement when -2.0 V applied to the ring, showing a variation in the local pH almost instantly, Figure 4.19b.

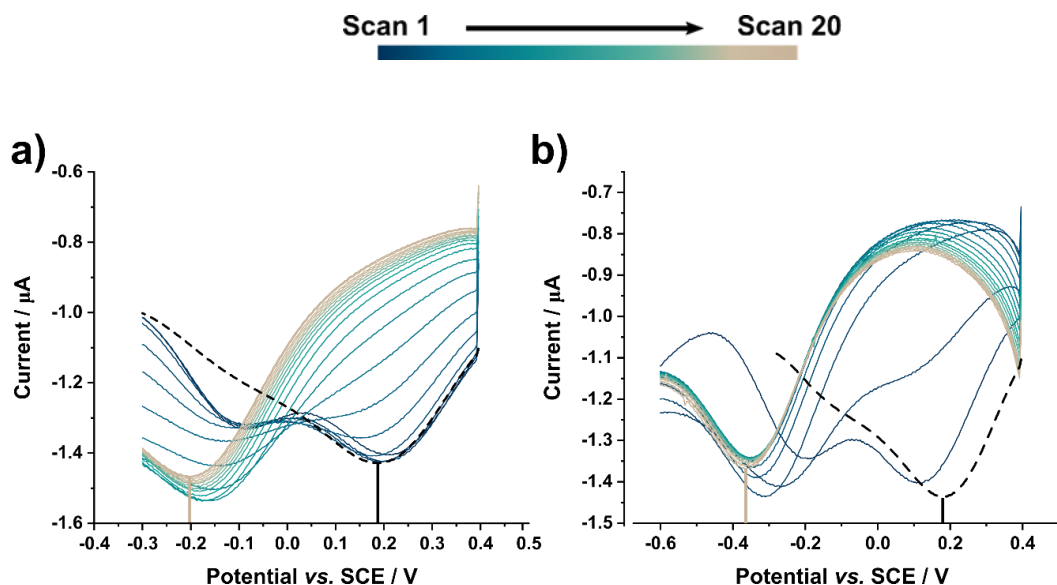


**Figure 4.19** Response of ring disc electrode in aerated 0.1 M  $\text{KNO}_3$  with Cu NPs electrodeposited on the ring subsequently held at a) -1 V and b) -2 V. Dashed line is the bulk measurement on disc prior to deposition of Cu from a deoxygenated 100  $\mu\text{M}$   $\text{Cu}_2\text{SO}_4$  solution onto the ring. 20 sequential SWV scans on disc electrode at each potential are shown. Vertical solid lines indicate the shift of the pH peak from scan one (blue) to scan twenty (beige).

In contrast, the SWV show very little change in peak position when -0.2 V is applied to the Cu NP decorated ring in an aerated 0.1 M  $\text{KNO}_3$  solution, Figure 4.20. An offset in peak potential is seen between the bulk pH SWV measurement (dashed line) and the sequential SWV recorded with -0.2 V applied to the ring.

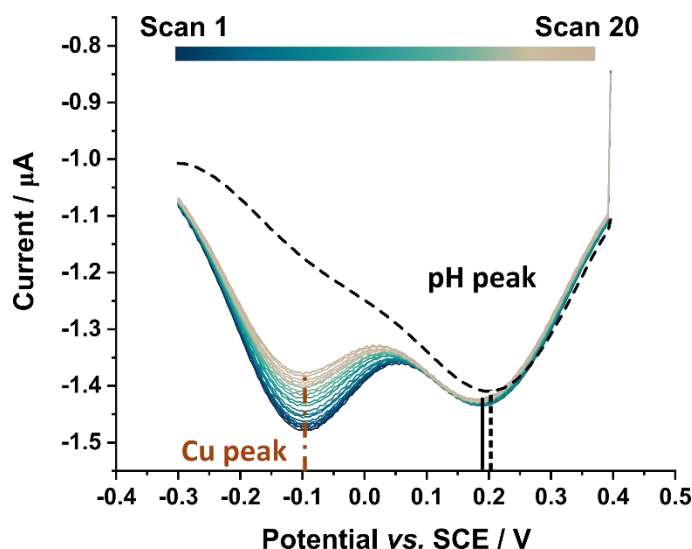


Figure 4.20 Response of ring disc electrode in aerated 0.1 M  $\text{KNO}_3$  with Cu NPs electrodeposited on the ring. Dashed line is the bulk measurement on disc prior to deposition of Cu from a deoxygenated 100  $\mu\text{M}$   $\text{Cu}_2\text{SO}_4$  solution onto the ring. 20 sequential SWV scans on disc electrode with -0.2 V applied to the ring. Dashed vertical line indicates the peak position of the bulk pH measurement, solid vertical line indicates the stability of the pH peak potential during the measurement and the orange, dash dot vertical line indicates the stability of the second peak throughout the scans thought to be associated with some form of Cu deposition.

The shift in peak position within the sequential SWV corresponds to a 0.14 pH unit shift, whereas the shift compared to the bulk measurement 0.34 pH units. The potential in the main experiment (with -0.2 V applied to the ring) is more negative than the bulk pH peak which excludes the transfer of deposition solution as a cause of the shift. The shift could be the result of interference from the Cu peak causing the pH associated peak to broaden in comparison to the bulk measurement where there is no Cu interference. The Cu associated peak remains at the same potential throughout the 20 SWV scans but decreases in magnitude. Given the stability of both peaks in the 20 SWVs, and the decrease in potential compared to the bulk measurement, the 0.14 pH unit increase within the 20 SWVs most likely reflects the actual change in the local environment driven by small amounts of Cu NP electrocatalysed ORR.

The results when -0.4 V was applied to the Cu NP decorated ring in both the deoxygenated and aerated 0.1 M  $\text{KNO}_3$  solution were not as expected, Figure 4.21. In the deoxygenated solution, Figure 4.21a, a 28 mV shift is observed in the peak position of the pH peak between the bulk and 20<sup>th</sup> SWV measurement. This

corresponds to a 0.48 pH unit increase. This is a greater shift than observed on the blank BDD ring under the same conditions. In the aerated solution at -0.4 V a 44 mV shift is seen in the pH associated SWV peak. This corresponds to a 0.75 pH unit increase, less than the 1.09 pH unit increase observed on the blank BDD ring. This is an unexpected result as Cu is expected to be catalytic towards ORR so a larger pH shift was expected with the Cu NPs present.

NRR is a complex process on Cu, reduction to ammonia occurs through a nitrite intermediate in acidic media.<sup>28,53</sup> In acidic conditions, nitrate co-adsorbs to Cu surfaces with water or hydronium molecules which form hydrogen bridge bonds through the lone electron pairs of oxygen atoms. When reduced to nitrite the hydronium ions are no longer present.<sup>53</sup> There is also evidence of nitrate and nitrite adsorption on Cu in alkaline solutions (0.1 and 1 M NaOH).<sup>27,29</sup> In these extreme alkaline conditions, ~ pH 13, nitrate was adsorbed to Cu at -0.7 V vs. SCE but wasn't reduced until -1.0 V vs. SCE.<sup>29</sup> Our system is at a significantly more neutral pH range than these studies which will affect the potential at which these reactions occur as protons are involved. There is little literature on the adsorption of nitrate ions in near neutral pH environments. The minimal pH change measured in the deoxygenated solution at -0.4 V suggests the potential is not extreme enough to be reducing the nitrate ion, but the nitrate ions could be adsorbed to the Cu, reducing the number of catalytic sites for ORR, hence the smaller pH shift than expected in the aerated solution. The pH change observed in the deoxygenated solution, compared to the blank BDD ring electrode data, either suggests deoxygenation of the solution was not complete or an additional process with a small pH effect is occurring at -0.4 V.

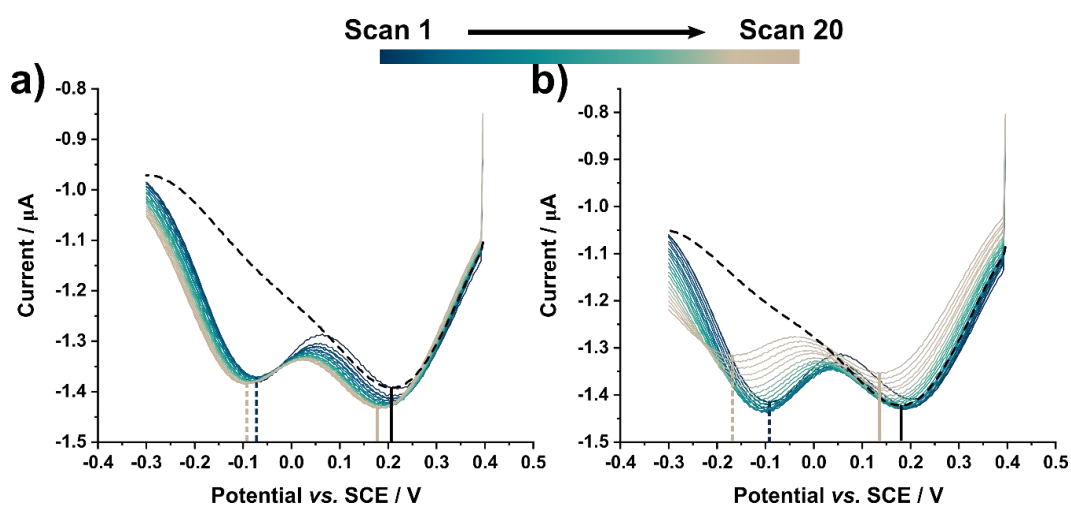


**Figure 4.21** Response of ring disc electrode in 0.1 M  $\text{KNO}_3$  with Cu NPs electrodeposited on the ring at -0.4 V. Dashed line is the bulk measurement on disc prior to deposition of Cu from a deoxygenated 100  $\mu\text{M}$   $\text{Cu}_2\text{SO}_4$  solution onto the ring. 20 sequential SWV scans on disc electrode with -0.4 V applied to the ring in a) deoxygenated 0.1 M  $\text{KNO}_3$  and b) in aerated 0.1 M  $\text{KNO}_3$ . Vertical solid lines indicate the shift of the pH peak from scan one (blue) to scan twenty (beige). Vertical dashed lines indicate the shift in potential of the Cu associated peak from scan one (blue) to scan twenty (beige).

The Cu deposition associated peak is evident in all of these experiments, Figure 4.19 to 4.21, despite implementation of the rinsing technique described at the start of this section. As noted, at -0.2 V the peak remains stable throughout the 20 SWV scans at -0.096 V, Figure 4.20. In Figure 4.19, as the main pH peak shifts more negative with applied ring potentials of -1.0 V and -2.0 V, the Cu peak is masked after the first 7 and 2 SWV scans, respectively.

The overall Cu NP electrocatalysed pH changes over the 30 s timescale (33 s for -2.0 V data) are shown in Figure 4.22 (gold) alongside the pH changes recorded from the bare BDD ring (purple) at the same potentials and conditions. Cu is significantly more reactive than the bare BDD at -1.0 V (◆) and -2.0 V (◆) resulting in an extremely alkaline local environment being formed. A small increase in local pH environment was measured when -0.2 V (■) was applied to the Cu NP decorated ring, where no increase was observed on the bare BDD. The pH change at -0.4 V in the aerated solution (▲) was less than expected with the presence of Cu NPs, which may be due to adsorption of nitrate ions blocking the catalytic activity of the Cu NPs towards ORR. A very similar pH change was observed in the deaerated solution. An increase was seen with the presence of Cu

NPs in the deoxygenated solution at -0.4 V (●), possibly suggesting a reaction other than ORR occurs at this potential.

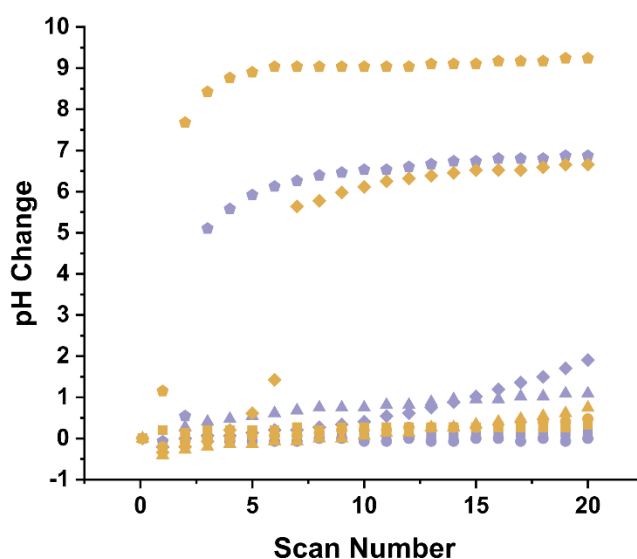
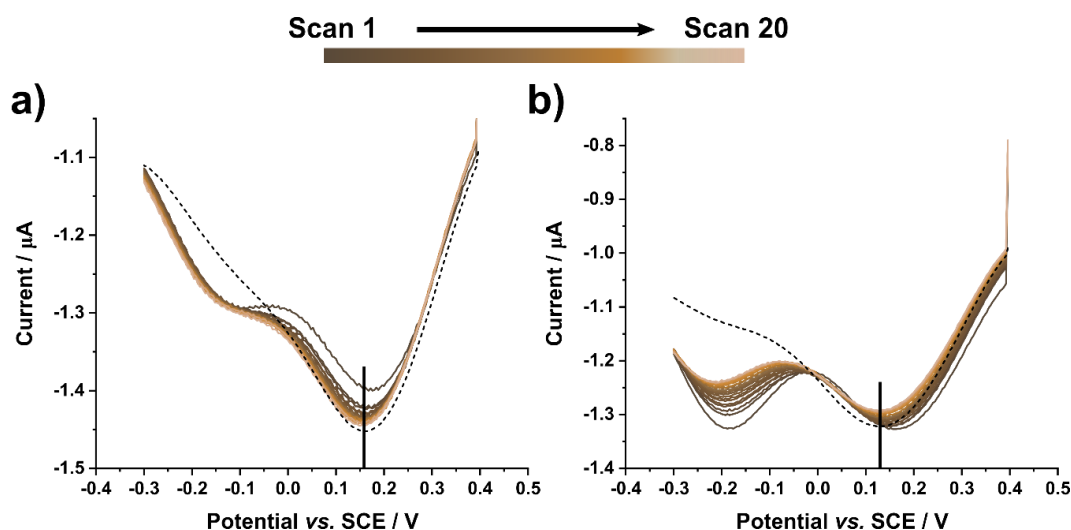


Figure 4.22 The measured pH change in 0.1 M  $\text{KNO}_3$  on the disc electrode at ring potentials of -0.2 V (■), -0.4 V in deoxygenated solution (●), -0.4 V in an aerated solution (▲), -1.0 V (◆) and -2.0 V (●) normalised to measured bulk concentration for bare BDD ring (purple) and with Cu NPs (gold).

#### 4.4.5.2 pH Tracking with Cu NPs in Sulfate electrolyte

Again, the same applied ring potentials were considered (-0.2, -0.4, -1.0 and -2.0 V vs. SCE) in a 0.1 M sulfate electrolyte solution with the presence of Cu NPs. As before, 20 SWV, corresponding to approximately 30 s, were captured in aerated 0.1 M  $\text{K}_2\text{SO}_4$  (and a deoxygenated 0.1 M  $\text{K}_2\text{SO}_4$  solution at -0.4 V) to monitor any variation in the local pH environment. Figure 4.23 shows the SWV response in aerated 0.1 M  $\text{K}_2\text{SO}_4$  with -0.2 V applied to the Cu nanoparticle decorated ring (a) and in deoxygenated 0.1 M  $\text{K}_2\text{SO}_4$  with -0.4 V applied to the Cu nanoparticle decorated ring (b). No overall shift was observed in the pH associated peaks in either of these conditions. The bulk SWV measurement in Figure 4.23b aligns well with the 20<sup>th</sup> SWV scan of the experiment. There is a slight shift in the peak positions between the 1<sup>st</sup> and 20<sup>th</sup> scan, which could be due to small amounts of ORR. Alternatively, a small amount of the acidic Cu deposition solution could have been carried over and the pH naturally settled back to the bulk during the measurement.



**Figure 4.23** Response of ring disc electrode in aerated 0.1 M  $\text{K}_2\text{SO}_4$  with Cu NPs electrodeposited on the ring subsequently held at a)  $-0.2$  V and b)  $-0.4$  V in a deoxygenated solution. Dashed line is the bulk measurement on disc prior to deposition of Cu from a deoxygenated  $100 \mu\text{M}$   $\text{Cu}_2\text{SO}_4$  solution onto the ring. 20 sequential SWV scans on disc electrode at each potential are shown. Vertical solid lines indicate pH peak position.

Unlike in the nitrate solution a significant pH change of 3.5 pH units, with a peak shift of 204 mV, was observed at  $-0.4$  V in the aerated sulfate solution, Figure 4.24a. Given that the sulfate anions are more inert than the nitrate anions a bigger pH shift suggests the catalytic activity of the Cu NPs is uninhibited for ORR in sulfate compared to the nitrate system. The pH SWV peak shift at  $-1.0$  V on the ring with Cu deposits was 304 mV, a 1.66 pH unit further increase than that measured at  $-0.4$  V in the aerated  $\text{K}_2\text{SO}_4$  solution with an overall shift of 5.16 pH units, Figure 4.24b. This is a smaller shift than seen at  $-1.0$  V in the nitrate solution by around 1.50 pH units further supporting the increased rate of NRR at this higher potential in the  $\text{KNO}_3$  solution.

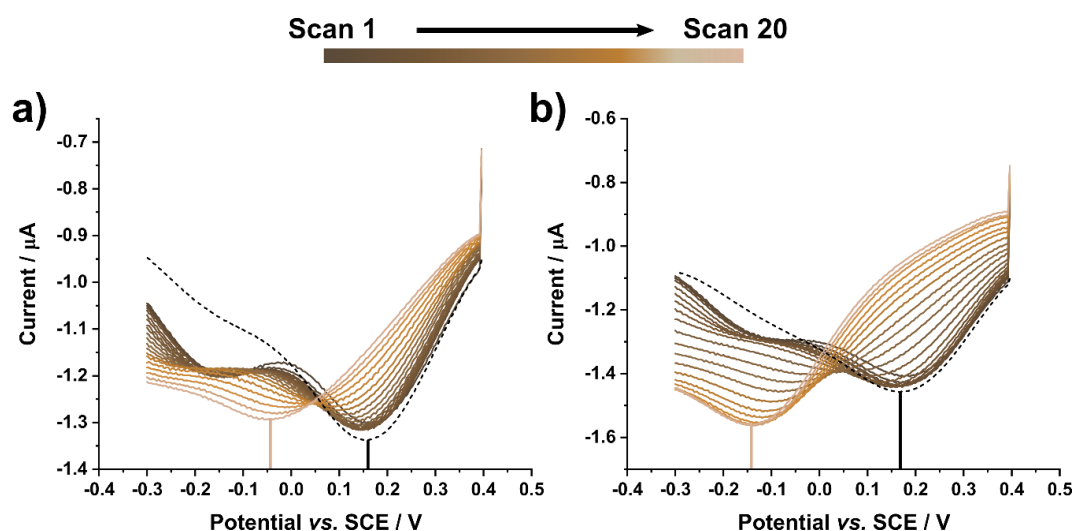


Figure 4.24 Response of ring disc electrode in aerated 0.1 M  $K_2SO_4$  with Cu NPs electrodeposited on the ring subsequently held at a)  $-0.4$  V and b)  $-1$  V. Dashed line is the bulk measurement on disc prior to deposition of Cu from a deoxygenated  $100 \mu M$   $Cu_2SO_4$  solution onto the ring. 20 sequential SWV scans on disc electrode at each potential are shown. Vertical solid lines indicate the shift of the pH peak from scan one (dark brown) to scan twenty (beige).

A 600 mV shift was measured in the SWV pH peak position over 33 s when  $-2.0$  V was applied to the ring decorated with Cu NPs, Figure 4.25. This corresponds to a pH change of 10.19 units, an additional pH change of almost 3.8 for the same applied potential to bare BDD in 0.1 M  $K_2SO_4$ . This extreme pH change is beyond the calibration of the BDD-Q probe so values should be interpreted carefully. This pH increase is due to WR catalysed on the Cu NPs.



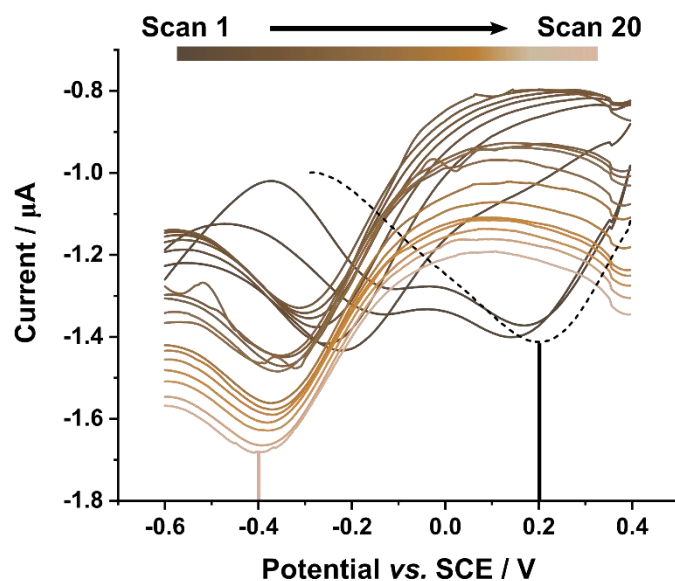


Figure 4.25 Response of ring disc electrode in aerated 0.1 M  $K_2SO_4$  with Cu NPs electrodeposited on the ring subsequently held at  $-2.0$  V. Dashed line is the bulk measurement on disc prior to deposition of Cu from a deoxygenated  $100 \mu M$   $Cu_2SO_4$  solution onto the ring. 20 sequential SWV scans on disc electrode at each potential are shown. Vertical solid lines indicate the shift of the pH peak from scan one (dark brown) to scan twenty (beige).

The overall pH changes over 30 - 33 s are shown in Figure 4.26 alongside the pH changes recorded from the bare BDD ring at the same potentials and conditions in 0.1 M  $K_2SO_4$ . Cu NPs are significantly more reactive than the bare BDD at  $-0.4$  ( $\blacktriangle$ ),  $-1.0$  ( $\blacklozenge$ ) and  $-2.0$  V ( $\blacklozenge$ ) in the aerated sulfate solution resulting in a highly alkaline local environment being formed. The local pH change was minimal in the deoxygenated sulfate solution at  $-0.4$  V ( $\bullet$ ) and in the aerated solution at  $-0.2$  V applied potentials ( $\blacksquare$ ).

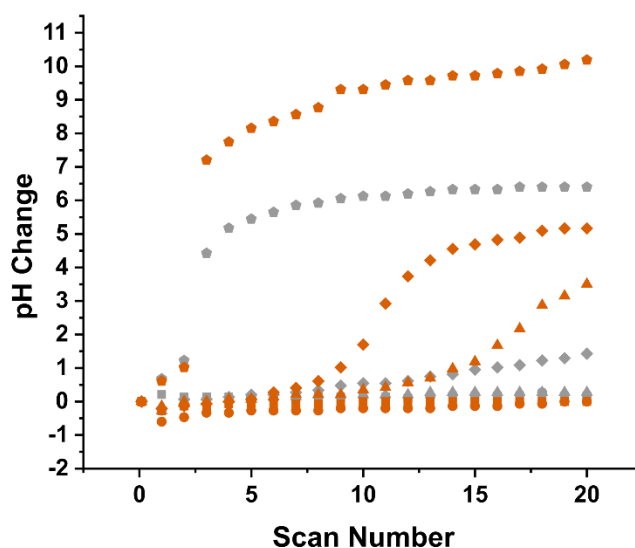


Figure 4.26 The measured pH change in 0.1 M  $K_2SO_4$  on the disc electrode at ring potentials of -0.2 V (■), -0.4 V in deoxygenated solution (●), -0.4 V in an aerated solution (▲), -1 V (◆) and -2 V (◆) normalised to measured bulk concentration for bare BDD ring (grey) and with Cu NPs (orange).

#### 4.4.5.3 Comparison of electrocatalysed pH changes in nitrate and sulfate solutions on bare BDD and BDD decorated with copper nanoparticles

Table 4.2 shows a summary of the measured local pH changes in both the  $KNO_3$  and  $K_2SO_4$  solutions on the BDD-Q ring disc electrode with the applied ring potentials (-0.2, -0.4, -1.0 and -2.0 V) on both the blank BDD ring and the BDD ring decorated with Cu NPs.

Table 4.2 Summary table of pH change measured on BDD-Q disc over ~ 30s in 0.1 M  $KNO_3$  and  $K_2SO_4$  solutions when a range of potentials are applied to the bare BDD ring electrode and when Cu NPs are present on the BDD ring electrode.

Applied Ring E / V	Nitrate		Sulfate	
	pH change BDD	pH change Cu	pH change BDD	pH change Cu
-0.2	0.14	0.34	0.00	0.00
-0.4 Deoxygenated	0.00	0.48	0.20	0.00
-0.4	1.09	0.75	0.27	3.50
-1.0	1.91	6.66	1.43	5.16
-2.0	6.87	9.24	6.40	10.19

Cu NPs significantly increased the local pH change with applied ring potentials of -1.0 and -2.0 V in both electrolyte solutions compared to the pH changes induced using only BDD. With Cu NPs present, at -0.4 and -0.2 V in the sulfate solution the pH changes were minimal with the exception of -0.4 V in the aerated solution. The pH changes in the nitrate solution at -0.4 and -0.2 V were more variable than those in the sulfate solution but showed larger pH increases, except for at -0.4 V with Cu NPs on the ring in the aerated nitrate solution. The Cu NP electrocatalysed local pH increases measured, particularly at -1.0 and -2.0 V in both solutions and at -0.4 V in the aerated sulfate solution, would almost certainly have an impact on the stability of the metallic Cu NPs and potentially affect further reactions on these NPs.

#### 4.5 Conclusions and future work

This work has proven the local pH changes caused by the electrocatalytic activity of metal (Cu) deposits can be tracked using the BDD ring BDD-Q disc morphology using sequential 2 s length voltammetric scans. This technique also introduces the possibility of tracking time dependent pH influencing reactions *in-situ*. This experimental set up could be used to probe the local pH changes associated with other electrocatalytic reactions, in different electrolytes or with different metal or metal oxide deposits.

This work also highlighted some potential issues with commercial potentiostats which caused variation in the electrochemical response observed on the BDD-Q electrode. An understanding of the behaviour of the commercial instrument when making these types of measurement is extremely important. For sequential scan measurements, such as that employed here it is necessary to establish whether a potential is applied between the scans or not and thought should be made as to the impacts of the potential on the experiment.

An interesting result recorded with Cu NPs deposited on the ring is the apparent inhibition of ORR in nitrate solutions at -0.4 V, in contrast to that seen in the sulfate electrolyte, attributed to nitrate adsorption. Little literature is available on the adsorption of nitrate at near neutral pHs. Further work to explore if nitrate adsorption was blocking the catalytic Cu NP sites and therefore reducing the catalytic behaviour would be interesting and would be a useful addition to the

literature. This could be achieved by utilising surface sensitive spectroscopic techniques such as electrochemical scanning tunnelling microscopy or surface enhanced Raman spectroscopy alongside electrochemical techniques.<sup>53</sup>

As expected, Cu was catalytic to ORR, NRR and WR. These electrocatalytic reactions resulted in significant local pH changes at the BDD-Q disc electrode. Consideration should be made to the effect of such rapid pH increases on the original NP deposit. The metal is unlikely to remain in the metallic form after such large pH increases. For these experiments, an unbuffered system was used, where the pH changes will be at their greatest. Similar experiments could be carried out in buffered or acidified solutions, in order to understand whether the buffer and proton concentration is adequate to negate these local pH changes. Due to the challenges of measuring pH changes on a ring disc electrode in the presence of buffer, as discussed in Chapter 3, the aid of an optical pH tracking technique *i.e.* confocal laser scanning microscopy could be used to help verify and interpret the measured pH changes.

This study only looked at one copper morphology, there was intent to also look at the electrocatalytic effect of copper oxide nanostructures and determine whether the oxide deposits showed the same catalytic behaviour as the Cu metal, but time was lacking. The intention was also to consider any morphological changes to the deposits before and after driving ORR, NRR and WR. This would have initially been done by scanning electron microscopy and energy-dispersive X-ray spectroscopy. Further interrogation could be undertaken using identical location transmission electron microscopy.<sup>54,55</sup> Some design adjustments would be required if the deposits on the ring electrode were to be considered in the SEM, reducing the size of the electrode body and radius of the cap would introduce less polymer material and may improve the image quality.

## 4.6 References

- 1 A. M. Tarditi, M. L. Bosko and L. M. Cornaglia, *Compr. Mater. Finish.*, 2017, **3-3**, 1-24.
- 2 K. Pungjunun, S. Chaiyo, I. Jantrahong, S. Nantaphol, W. Siangproh and O. Chailapakul, *Microchim. Acta*, 2018, **185**, 324.
- 3 L. Cui, J. Wu and H. Ju, *Chem. - A Eur. J.*, 2015, **21**, 11525-11530.
- 4 L. A. Hutton, M. E. Newton, P. R. Unwin and J. V. Macpherson, *Anal. Chem.*, 2009, **81**, 1023-1032.
- 5 C. Wang, M. Waje, X. Wang, J. M. Tang, R. C. Haddon and Y. Yan, *Nano Lett.*, 2004, **4**, 345-348.
- 6 B. You and Y. Sun, *Acc. Chem. Res.*, 2018, **51**, 1571-1580.
- 7 W. Yang, K. Dastafkan, C. Jia and C. Zhao, *Adv. Mater. Technol.*, 2018, **3**, 1-20.
- 8 S. Ghosh and R. N. Basu, *Nanoscale*, 2018, **10**, 11241-11280.
- 9 K. Brainina, N. Stozhko, M. Bukharinova and E. Vikulova, *Phys. Sci. Rev.*, 2019, **3**:9.
- 10 I. Gurrappa and L. Binder, *Sci. Technol. Adv. Mater.*, 2008, **9**:4.
- 11 L. P. Bicelli, B. Bozzini, C. Mele and L. D'Urzo, *Int. J. Electrochem. Sci.*, 2008, **3**, 356-408.
- 12 S. C. S. Lai, R. A. Lazenby, P. M. Kirkman and P. R. Unwin, *Chem. Sci.*, 2015, **6**, 1126-1138.
- 13 S. Szabó, *Int. Rev. Phys. Chem.*, 1991, **10**, 207-248.
- 14 L. M. Plyasova, I. Y. Molina, A. N. Gavrilov, S. V. Cherepanova, O. V. Cherstiouk, N. A. Rudina, E. R. Savinova and G. A. Tsirlina, *Electrochim. Acta*, 2006, **51**, 4477-4488.
- 15 D. Grujicic and B. Pesic, *Electrochim. Acta*, 2002, **47**, 2901-2912.
- 16 A. J. Borrill, N. E. Reily and J. V. Macpherson, *Analyst*, 2019, **144**, 6834-6849.

- 17 S. E. Stanca, O. Vogt, G. Zieger, A. Ihring, J. Dellith, A. Undisz, M. Rettenmayr and H. Schmidt, *Commun. Chem.*, 2021, **4**, 1–13.
- 18 Y. Li, Y. Y. Song, C. Yang and X. H. Xia, *Electrochem. commun.*, 2007, **9**, 981–988.
- 19 H. C. Shin, J. Dong and M. Liu, *Adv. Mater.*, 2003, **15**, 1610–1614.
- 20 A. J. Borrill, University of Warwick, 2020.
- 21 P. Veluchamy and H. Minoura, *J. Mater. Sci. Lett.*, 1996, **15**, 1705–1707.
- 22 G. H. A. Therese and P. V. Kamath, *Chem. Mater.*, 2000, **12**, 1195–1204.
- 23 L. Manjakkal, D. Szwagierczak and R. Dahiya, *Prog. Mater. Sci.*, 2020, **109**, 100635.
- 24 V. D. Patake, S. S. Joshi, C. D. Lokhande and O. S. Joo, *Mater. Chem. Phys.*, 2009, **114**, 6–9.
- 25 V. Georgieva and M. Ristov, *Sol. Energy Mater. Sol. Cells*, 2002, **73**, 67–73.
- 26 E. Yeager, *Electrochim. Acta*, 1984, **29**, 1527–1537.
- 27 E. Pérez-Gallent, M. C. Figueiredo, I. Katsounaros and M. T. M. Koper, *Electrochim. Acta*, 2017, **227**, 77–84.
- 28 K. Bouzek, M. Paidar, A. Sadílková and H. Bergmann, *J. Appl. Electrochem.*, 2001, **31**, 1185–1193.
- 29 D. Reyter, D. Bélanger and L. Roué, *Electrochim. Acta*, 2008, **53**, 5977–5984.
- 30 T. Öznülüer, B. Özdurak and H. Öztürk Doğan, *J. Electroanal. Chem.*, 2013, **699**, 1–5.
- 31 J. Davis, J. C. Baygents and J. Farrell, *Electrochim. Acta*, 2014, **150**, 68–74.
- 32 V. B. Nam and D. Lee, *Nanomaterials*, 2016, **6**, 47.
- 33 J. Kwon, H. Cho, Y. D. Suh, J. Lee, H. Lee, J. Jung, D. Kim, D. Lee, S. Hong and S. H. Ko, *Adv. Mater. Technol.*, 2017, **2**, 1600222.
- 34 V. Reddy, M. Reddy, M. Reddy, P. Reddy, S. Gedi, K. Kumar, Y. Bathal, B. Pejjai, W. Kyoung, T. Ramakrishna, R. Kotte and C. Park, *J. Ind. Eng. Chem.*, 2019, **76**, 39–74.

- 35 J. Zhao, S. Xue, J. Barber, Y. Zhou, J. Meng and X. Ke, *J. Mater. Chem. A*, 2020, **8**, 4700–4734.
- 36 C. Kartal, Y. Hanedar, T. Öznülüer and Ü. Demir, *Langmuir*, 2017, **33**, 3960–3967.
- 37 M. V. Vazquez, S. R. de Sanchez, E. J. Calvo and D. J. Schiffrin, *J. Electroanal. Chem.*, 1994, **374**, 189–197.
- 38 Y. Deng, A. D. Handoko, Y. Du, S. Xi and B. S. Yeo, *ACS Catal.*, 2016, **6**, 2473–2481.
- 39 M. V. Vazquez, S. R. de Sanchez, E. J. Calvo and D. J. Schiffrin, *J. Electroanal. Chem.*, 1994, **374**, 179–187.
- 40 D. Ren, J. Fong and B. S. Yeo, *Nat. Commun.*, 2018, **9**.
- 41 A. J. Garza, A. T. Bell and M. Head-Gordon, *ACS Catal.*, 2018, **8**, 1490–1499.
- 42 P. Sebastián-Pascual, S. Mezzavilla, I. E. L. Stephens and M. Escudero-Escribano, *ChemCatChem*, 2019, **11**, 3626–3645.
- 43 P. Grosse, D. Gao, F. Scholten, I. Sinev, H. Mistry and B. Roldan Cuenya, *Angew. Chemie - Int. Ed.*, 2018, **57**, 6192–6197.
- 44 F. S. Roberts, K. P. Kuhl and A. Nilsson, *Angew. Chemie*, 2015, **127**, 5268–5271.
- 45 J. V. Macpherson, *Phys. Chem. Chem. Phys.*, 2015, **17**, 2935–2949.
- 46 W. R. Carmody, *J. Chem. Educ.*, 2009, **40**, A386.
- 47 S. J. Cobb, Z. J. Ayres, M. E. Newton and J. V. Macpherson, *J. Am. Chem. Soc.*, 2019, **141**, 1035–1044.
- 48 Z. J. Ayres, A. J. Borrill, J. C. Newland, M. E. Newton and J. V. Macpherson, *Anal. Chem.*, 2016, **88**, 974–980.
- 49 A. W. Colburn, K. J. Levey, D. O’Hare and J. V. Macpherson, *Phys. Chem. Chem. Phys.*, 2021, **23**, 8100–8117.
- 50 T. L. Read, S. J. Cobb and J. V. Macpherson, *ACS Sensors*, 2019, **4**, 756–763.
- 51 E. S. Smotkin, F. T. Moy and W. Z. Plachy, *BBA - Biomembr.*, 1991, **1061**, 33–

38.

- 52 D. J. G. Ives and A. E. Rawson, *J. Electrochem. Soc.*, 1962, **109**, 458–462.
- 53 S. E. Bae, K. L. Stewart and A. A. Gewirth, *J. Am. Chem. Soc.*, 2007, **129**, 10171–10180.
- 54 R. M. Arán-Ais, Y. Yu, R. Hovden, J. Solla-Gullón, E. Herrero, J. M. Feliu and H. D. Abruña, *J. Am. Chem. Soc.*, 2015, **137**, 14992–14998.
- 55 N. Hodnik and S. Cherevko, *Curr. Opin. Electrochem.*, 2019, **15**, 73–82.



## 5 Electrochemical Copper Detection

---

### 5.1 Overview

Electrochemical detection of heavy metals on solid electrodes using anodic stripping voltammetry (ASV) from real solutions can be a challenge due to the non-ideal pH of the solution resulting in the formation of metal oxide and hydroxide deposits. Heavy metals in the environment are often at concentrations in the ppb range requiring low detection limits from sensors. Two techniques are explored in this chapter that act to mitigate the issues associated with metal deposition and analysis on solid electrodes. Both techniques could be modified to allow for on-site analysis of heavy metals from natural waters *i.e.* lakes or rivers.

X-ray fluorescence (XRF) was used to quantify metals on an electrode surface after an electrochemical (EC) preconcentration step, EC-XRF. The EC preconcentration step was undertaken using a rotating disc electrode to increase, in a controllable way, the mass transport of analyte to the surface of the electrode. A user friendly design of electrode is considered in this chapter and compared to the results from previous studies using this technique. The second technique uses a ring disc electrode configuration to locally acidify the environment over the disc by oxidising water at the ring. An acidic environment encourages the deposition of the metal in its metallic form aiding subsequent stripping voltammetry. This chapter considers the feasibility of using this technique at environmentally relevant concentrations.

Both techniques go some way to solving the analysis problems associated with ASV on solid electrodes. The XRF analysis detected the presence of the metal on the surface regardless of the deposited form of the metal. However, the form of the metal greatly impacted the stability of the deposit on the electrode surface during deposition and XRF analysis. The locally acidified environment generated on the ring disc electrode aided deposition of copper (Cu) in the metallic form, but at lower concentrations the oxygen species generated during water oxidation oxidised the deposit impacting the stripping voltammetry.

## 5.2 Introduction

### 5.2.1 Heavy metals, the environment, and health

Heavy metals and associated non-metals and metalloids are toxic, and most are believed to have a carcinogenic effect.<sup>1,2</sup> Cu is an essential nutrient required for infant growth, immune response, bone strength, iron transport, cholesterol and glucose metabolism and brain development. However in high concentrations Cu is toxic.<sup>3</sup> Cu transitions between Cu<sup>II</sup> to Cu<sup>I</sup> during metabolic reactions, if present in excess in cells Cu ions can react and form of superoxide and hydroxide radicals which can cause cellular damage.<sup>1</sup> Diseases such as Wilsons disease, Menkes disease, some cancers, hepatitis and diabetes can reduce the livers ability to remove excess copper and result in copper deficiency or toxicity.<sup>4,5</sup> Cu as well as a number of other heavy metals (As, Cd, Cr, Fe, Pb, Hg, Ni and Zn) appear on the Environmental Quality Standards Directive list for the Water Framework Directive assessments as priority substances for water quality.<sup>6</sup>

Concentrations of heavy metals such as Cu can be naturally elevated due to the local geology of an area. Metal rich rocks erode to produce metal rich soils which can leach into water ways. Human activities, such as mining and smelting, can lead to a further increase in heavy metals. Some of the most contaminated sites in the UK are a result of the mining legacy *i.e.* Parys Mountain, Wales, once the largest Cu mine in the world.<sup>7</sup> Acid mine drainage, commonly associated with coal and metal mines, is an anthropogenically derived pathway to increased metal concentrations in waterways.<sup>8</sup>

Currently heavy metal analysis from solution is typically undertaken using inductively coupled plasma mass spectrometry (ICP-MS), although inductively coupled plasma optical emission spectrometry or atomic absorption spectrometry are also used.<sup>9-11</sup> All of these techniques require point samples from the site which are then returned to the laboratory for analysis. For ICP-MS the sample is filtered and acidified in the laboratory before analysis.<sup>12</sup> ICP-MS is a very sensitive technique (down to ppt); however, the instrument is large, expensive and requires a trained operative so is not adaptable to at source or *in-situ* measurements.<sup>13</sup>

### 5.2.2 Electrochemical Detection of Metals

Electrochemical sensing provides the opportunity for low cost, sensitive and potentially portable technologies that provide the opportunity for at the source measurement, unlike ICP-MS. Electrochemical detection of metals is most often associated with ASV. Historically the use of mercury electrodes for ASV was very reliable and produced very sensitive analyses for heavy metal detection in aqueous samples.<sup>14,15</sup> However since the move to solid electrodes, due to the toxicity of mercury, and despite extensive academic literature, very few commercial products using ASV exist.<sup>16</sup> There are various reasons for this.

Uniform metal electrodeposition on solid electrodes is challenging. To begin with the electrode surface itself is heterogeneous, which can result in heterogeneous deposition morphologies on the same electrode. Unlike mercury electrodes, which retain the properties of the Hg when a metal amalgam forms, metal deposition on a solid electrode changes the surface properties of the electrode, as explored in Chapter 4. In unbuffered solutions, the increase in local pH from the hydrogen evolution reaction (HER), oxygen reduction reaction (ORR) or nitrate reduction reaction (NRR) results in a mix of oxide and hydroxide deposits. Local pH increases are often counteracted by performing deposition in strongly acidic solutions or in the presence of buffers. For ASV it is important that the deposition parameters and preparation of the electrode surface are optimised to try and move towards a homogeneous, monodisperse distribution of deposited structures on the electrode surface to aid the quantification of the stripping peak. Heterogeneous metal deposits result in broader stripping peaks. If the metal is not in the metallic form, stripping may not occur resulting in underrepresentation of the concentration in the sample.

Two heavy metal detection techniques developed on boron doped diamond (BDD) by the Macpherson research group have been proposed to mitigate some of the issues observed on solid electrodes for metal detection. The first utilises metal deposition to preconcentrate metals on the electrode surface but quantitatively analyses the deposits using XRF, presented as EC-XRF.<sup>17-19</sup> The second technique used a ring disc electrode to locally generate an acidic pH to aid the deposition of metal for stripping analysis.<sup>20,21</sup>

The ring disc morphology utilises the ring electrode to oxidise water and decrease the pH of the local environment, as in Chapter 3, to increase the likelihood of deposition in a metallic form. This concept was demonstrated in a 1 mM mercury solution and in 100  $\mu\text{M}$   $\text{Cu}^{2+}$  with 100  $\mu\text{M}$  of a triethylenetetramine (TETA) ligand also present.<sup>20,21</sup> For the mercury experiments, locally decreasing the pH to 2, from neutral solutions, produced a comparable mercury deposition and stripping response to a bulk pH 2 solution. This showed promise for electrochemical detection in non-acidic solutions, such as environmental water samples.<sup>20</sup> For the Cu experiment, it was demonstrated that locally changing the pH altered the speciation of the Cu-TETA system, with higher current densities promoting increasing quantities of Cu in the free  $\text{Cu}^{2+}$  form. Neither study considered the quantifiable response of the stripping voltammetry under the local decreased pH conditions for stripping voltammetry. The concept of *in-situ* local pH control has recently been reported using interdigitated gold electrodes,<sup>22</sup> and used for free chlorine, monochloramine and silver ion detection.<sup>23-25</sup>

The concept of EC-XRF utilises a BDD substrate, which is effectively 'invisible' to the X-rays, as carbon and boron are non-interfering elements, and provides a low background for measurements. The interrogation area of the XRF is  $\sim 12$  mm in diameter at the widest part of the ellipse thus a larger than standard electrode was required, 25 mm in diameter. BDD of 250  $\mu\text{m}$  thickness, polished to nm roughness on the growth face was used. A 50  $\mu\text{m}$  disc was considered but was extremely fragile to handle, although provided slightly lower backgrounds than the 250  $\mu\text{m}$  disc ultimately used.<sup>17</sup> Forced convection was introduced via a rotating disc electrode to increase the rate of mass transport during the deposition step. The set-up was such that the BDD could be removed from the Teflon capped holder and placed in the XRF for analysis. The Teflon cap contained a 14 mm diameter hole in order to reduce the electrode area so that it was closer to the interrogation area of the XRF. An O-ring was used to create a watertight seal when a metal rod was screwed into the cap, compressing the O-ring against the BDD and forming an electrical connection with the BDD, Figure 5.1.

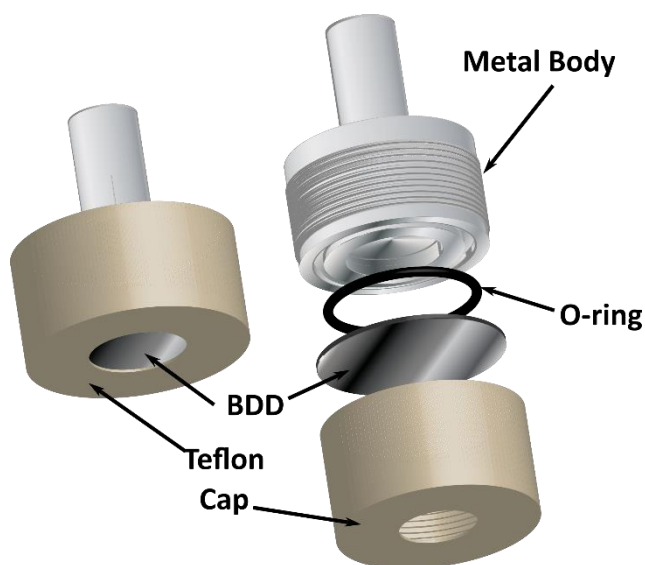


**Figure 5.1** Rotating disc electrode design for EC-XRF studies in References 11 and 12. Left hand side shows the assembled of the electrode the right shows the components within the electrode. Schematic not to scale, BDD disc has a diameter of 25 mm.

An experimental design approach was used to consider the effect of deposition potential, deposition time and metal concentration of both Cu and Pb individually, and the metal ratio of Cu and Pb when co-deposited. Excellent correlation ( $R^2 > 0.998$ ) was reported for both Cu and Pb with increasing deposition time at the reported potentials (-0.55, -1 and -1.75 V) in 100 nM solutions. The more negative the deposition potential the higher signal intensity from the XRF, thus -1.75 V for 4000 s was used to investigate the signal intensity over the metal concentration range 1 nM to 1000 nM (0.06 ppb – 60 ppb Cu, 0.2 ppb – 200 ppb Pb). Limits of detection of 0.75 nM (0.05 ppb) for Cu and 1.8 nM (0.04 ppb) for Pb are quoted with  $R^2$  value of 0.995 and 0.999, respectively.

Despite promising results, the EC-XRF electrode set-up was difficult to use and could result in the BDD cracking, if not handled extremely carefully. Therefore, a more user friendly electrode was designed. The effectiveness of the new electrode design is evaluated in this chapter with considerations towards optimisation of the technique. Quantification of Cu at low concentrations using ASV under locally acidified conditions on a BDD ring disc electrode is also explored.

## 5.3 Experimental

### 5.3.1 Solution Preparation

All solutions were prepared using Milli-Q water (Millipore Corp.) resistivity 18.2 M $\Omega$  cm at 25°C and, unless otherwise stated, all reagents were used as received. The supporting electrolytes used were 0.1 M potassium nitrate (KNO<sub>3</sub>;  $\geq$  99.0 %, Acros Organics, UK), 0.2 M nitric acid (HNO<sub>3</sub>; ACS Reagent, Honeywell Fluka, Seelze, Germany) or acetate buffer made from sodium acetate (C<sub>2</sub>H<sub>3</sub>NaO<sub>2</sub>; 99 %, Fisher Chemicals) and glacial acetic acid (C<sub>2</sub>H<sub>4</sub>O<sub>2</sub>; 99 %, Sigma Aldrich). The solutions used for electrochemical characterisation were 0.1 M KNO<sub>3</sub> and 1 mM rutheniumhexamine(III) chloride (Cl<sub>3</sub>Ru(NH<sub>3</sub>)<sub>6</sub><sup>3+</sup>; 99 %, Strem chemicals, Newbury Port, MA) supported with 0.1 M KNO<sub>3</sub>. Cu solutions were made up from Cu(NO<sub>3</sub>)<sub>2</sub> ( $\geq$ 99.9999 %, Aldrich). Buffer solutions were prepared according to the Carmody method to obtain the desired pH using boric acid (99% Scientific Lab Supplies, UK), citric acid (>99.5 %, Fisher Chemical, UK), and tertiary sodium phosphate (extra pure, Arcos Organics, UK).<sup>26</sup> The iridium oxide (IrOx) solution used was prepared as previously described;<sup>27,28</sup> 4.45 mM iridium tetrachloride (Alfa Aesar, USA), 1 mL of hydrogen peroxide (H<sub>2</sub>O<sub>2</sub>; 30 % w/w), and 39mM oxalic acid dehydrate (Aldrich, USA) were added sequentially to 100 mL of water and stirred for 30 min, 10 min, and 10 min intervals, respectively. Anhydrous potassium carbonate (Fisher Scientific, USA) was added until a pH of 10.5 was achieved resulting in a pale yellow-green solution. This was stirred for 48 h until the solution had stabilized and appeared purple in colour. The iridium oxide solution was refrigerated between uses. Experiments were undertaken in a laboratory with no temperature control where temperatures could be between 15 and 30°C.

### 5.3.2 Electrochemical Characterisation

Both electrode systems were characterised using cyclic voltammetry or relevant measurements of the electrode capacitance, solvent window, quinone surface coverage and peak separation ( $\Delta E_p$ ) as described in Section 2.5. The electrode surface areas (cm<sup>2</sup>) were determined by white light interferometry (Bruker ContourGT, Germany). Cyclic voltammograms for Randles-Sevcik and Levich calculations were conducted in 1 mM Ru(NH<sub>3</sub>)<sub>6</sub><sup>3+</sup> with 0.1 M KNO<sub>3</sub> supporting

electrolyte scanning in the range 0.2 V to -0.5 V.  $\Delta E_p$  at a 0.1 V s<sup>-1</sup> scan rate was used to identify any resistivity in the contact or electrode material where the expected theoretical value is  $\Delta E_p = 57/n$  mV.<sup>29</sup> Scan rates of 0.05 to 0.25 V s<sup>-1</sup> were used for Randles-Sevcik assessments and rotation rates between 250 and 2500 rpm were used for Levich assessments. The Randles-Sevcik equation;<sup>30</sup>

$$i_p = 0.4463nFAC \left( \frac{nFvD}{RT} \right)^{\frac{1}{2}} \quad \text{Equation 5.1}$$

where  $i_p$  is peak current in A,  $n$  is the number of electrons transferred in the redox event,  $F$  is Faradays constant,  $A$  is the electrode area in cm<sup>2</sup>,  $D$  is the diffusion coefficient,  $C$  is the concentration in mol cm<sup>-3</sup>,  $v$  is scan rate in V s<sup>-1</sup>,  $R$  is the gas constant and  $T$  is temperature in K.<sup>30</sup> The Levich equation<sup>30</sup> was used to infer about they hydrodynamic behaviour of the EC-XRF electrode. The Levich equation is;

$$i_l = (0.620)nFAD^{\frac{2}{3}}\omega^{\frac{1}{2}}\nu^{-\frac{1}{6}}C \quad \text{Equation 5.2}$$

where  $i_l$  is the limiting current in A,  $\omega$  is the angular rotation rate of the electrode in rpm and  $\nu$  is kinematic viscosity (cm<sup>2</sup> s<sup>-1</sup>).

### 5.3.3 EC-XRF Rotating Disc Electrode Design and Measurements

#### 5.3.3.1 EC-XRF Rotating Disc Electrode

The redesigned BDD rotating disc electrode used for EC-XRF comprised of a 21 mm diameter polycrystalline BDD disc (Electrochemical Processing Grade, Element Six, Harwell, UK) 250  $\mu$ m thick, inset and sealed into a Polyether ether ketone (PEEK) surround using epoxy overcoat (Chemtronics, RS Components, UK). This made up the electrode cap which contained a screw thread to attach to the electrode body, Figure 5.2. The BDD had four points of contact with a sputter coated Ti (10 nm) /Pt (400 nm) and thermally annealed (400°C, 5 h in air) which aligned with four gold coated pins (RS Components, UK) on the electrode body, manufactured from brass held within a PEEK surround. The cap containing the BDD electrode screwed onto the brass of the electrode body, Figure 5.2. An O-

ring was held within the electrode body to form a watertight seal with the electrode cap, which was sometimes reinforced using Kapton tape around the seal. The electrode body contained a screw thread to attach to a Gamry rotator (Gamry RDE710 Rotating Electrode, USA). This formed the working electrode of a typical three electrode system with a saturated calomel reference (SCE) electrode, and a coiled platinum wire as a counter electrode. All potentials reported are *versus* SCE unless otherwise stated.

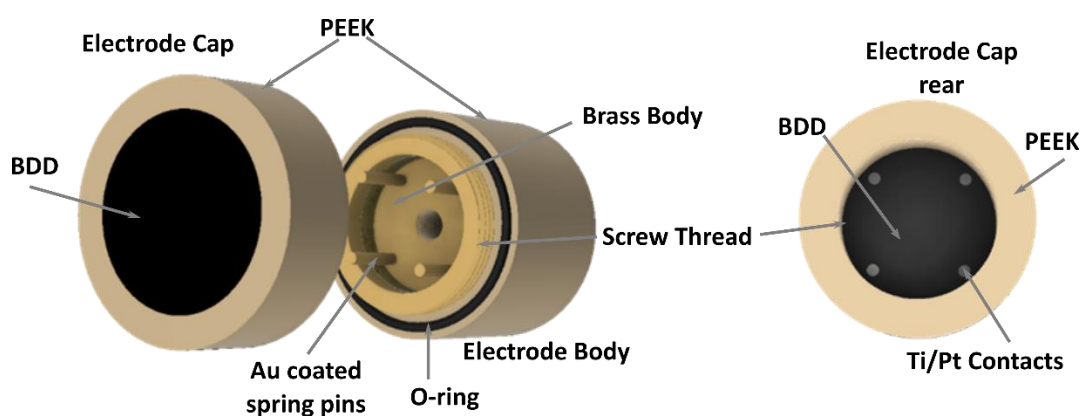


**Figure 5.2** New rotating disc electrode design. Left hand side shows the assembly of the electrode cap and body, the figure on the right shows the rear of the electrode cap to highlight the ohmic contacts. Schematic not to scale, BDD diameter 21 mm.

### 5.3.3.2 EC-XRF Electrochemical Measurements

Prior to use the surface of the BDD was cleaned using alumina polish (0.05  $\mu\text{m}$  Micropolish, Buehler, Germany) on a water saturated polishing pad (Microcloth, Buehler, Germany), followed by polishing on a clean water saturated polishing pad and rinsing with deionised water. This process has previously been shown to be an effective cleaning mechanism.<sup>17</sup> Once cleaned and assembled the electrode was mounted onto a Gamry commercial rotator face down into 50 ml of solution and rotated at 1200 rpm whilst a deposition was performed. A potentiostat (CHI760C, CH Instruments Inc., USA) was used to hold a constant potential for a defined period. After deposition the electrode was carefully removed from solution. The cap of the electrode was removed, gently rinsed with DI water and dried in a vacuum desiccator before analysis by XRF.



### 5.3.3.3 ED-XRF

A Rigaku NEX-CG: 50 kV Pd X-ray tube secondary carousel system with Cu, Mo, Al and RX9 (polarising target) was used with a Zr collimator, an irradiated 24 x 22 mm (oval) spot size was interrogated. All XRF analysis was undertaken with the following parameters: vacuum, Mo target, 300 s live time, automatic current, 1.6  $\mu$ s shaping time. Cu excitation was most efficient on the molybdenum secondary target, providing the best signal to noise ratio.

## 5.3.4 Ring Disc Electrode Fabrication and Measurements

### 5.3.4.1 Blank Ring Disc electrodes

The ring disc electrodes are comprised of electroanalytical grade BDD, a 1 mm diameter cylinder and a tube of inner diameter 1.4 mm and outer diameter of 1.8 mm. The desired geometries were cut from a 357  $\mu$ m thick freestanding BDD wafer using a 355 nm Nd:YAG 34 ns laser micromachining system (E-355H-ATHI-O system, Oxford Lasers). The BDD underwent the hot acid cleaning procedure, thermal anneal and ohmic contacting procedures as outlined in Sections 2.3.1.1 and 2.3.1.3. The BDD disc was sealed as centrally as possible inside the ring using epoxy resin (Epoxy Resin RX771C/NC, Aradur Hardener HY1300GB, Robnor Resins: Figure 5.3a). Once dried any epoxy covering the back surface was removed using acetone and a scalpel blade taking care not to damage the contacts. Cu or silver coated Cu wires were dipped in conductive epoxy (Chemtronics, CircuitWorks) and firmly placed against the Ti/Au contact for each component to form an electrical connection (Figure 5.3b). A wider Teflon ring was placed around the electrode and filled with epoxy resin. Once set the epoxy resin was removed from the Teflon ring and polished using carbide paper with successively fine grains until the BDD disc and ring were exposed (Figure 5.3c, d and e). Finally, a polish with alumina particles (0.05  $\mu$ m Micropolish, Buehler) on a water saturated polishing pad (Microcloth, Bueheler) was employed.

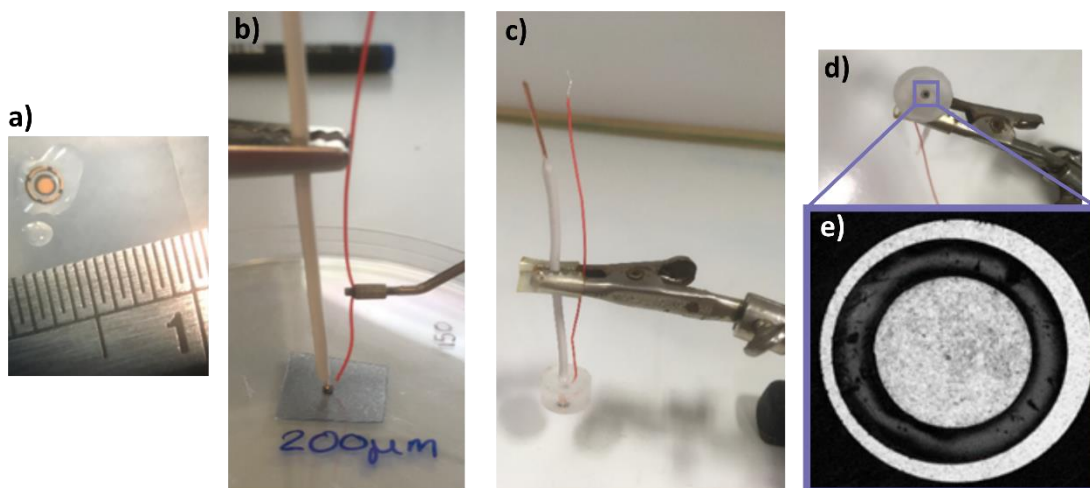
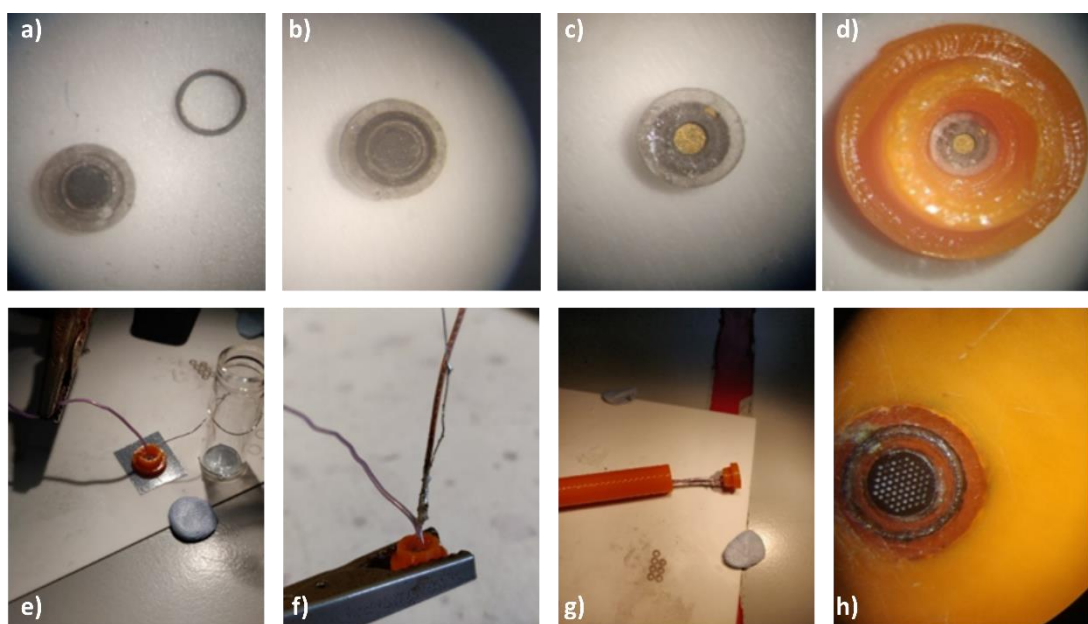


Figure 5.3 Stages of the fabrication process for a BDD ring disc electrode. a) Ti/Au sputtered ring and disc, sealed in epoxy resin as centrally as possible. b) Placement of copper wire (thick white) on disc and silver plated copper wire (red) on ring contacted with silver epoxy. c) and d) reverse and front of completed electrode, respectively. e) Image of ring disc taken by optical microscope, disc = 1 mm diameter ( $\varnothing$ ).

#### 5.3.4.2 BDD-Q ring disc electrode fabrication

The BDD-Q ring disc electrodes were fabricated in a similar way to that described in Section 3.3.2. However, prior to assembly the microspots were infilled with melted high impact polystyrene (HIPS) (dissolvable in D-Limonene) to ensure the microspots were not blocked permanently during fabrication, rather than polyvinyl alcohol as used in Section 3.3.2. The thermal grade diamond support was again used, the ring and disc were superglued into the thermal grade diamond support (Figure 5.4 a - c) before being placed into a 3D printed Polyethylene terephthalate (PET) cap (Figure 5.4d; Lulzbot TAZ 6). Wires were attached as described in section 5.3.4.1 (Figure 5.4e) and the back of the electrode cap was infilled with epoxy resin. Once set a thicker Cu wire (0.8 mm) was soldered onto the thin wire (0.254 mm) of the ring (Figure 5.4f). The cap and wires were placed into a 3D printed tube to form an electrode body and infilled with epoxy resin (Figure 5.4g). Once set the electrode face was exposed from the cap by polishing with successively fine carbide paper and finally an alumina polish. Once exposed the HIPS was dissolved from the lasered microspots by alternating immersion in D-limonene and mechanical polishing on alumina covered polishing pads.



**Figure 5.4** Stages of the fabrication process for BDD-Q ring disc fabrication (disc  $\varnothing$  1 mm) using thermal grade diamond ( $\varnothing$  2.2 mm) support and 3D printed components. The microspots were infilled with HIPS during fabrication which can be seen in the final image.

#### 5.3.4.3 Ring Disc Electrochemical Measurements

All electrochemical measurements on the ring disc electrodes were made using a three electrode system with the disc of the ring disc electrodes forming the working electrode, an SCE (IJ Cambria Scientific Ltd., UK) as the reference and a coiled platinum wire as the counter electrode. A PGSTAT101 potentiostat (Metrohm Autolab, Netherlands) was used to conduct the electrochemical measurements. For experiments where generation of protons on the ring was employed a galvanostat was used (Keithley 6430 Sub-Femtoamp Remote Source Meter) along with a secondary coiled platinum wire to complete the circuit. Solution pH measurements were compared to a glass pH probe (SevenEasy; Mettler Toledo; UK).

#### 5.3.4.4 Iridium Oxide Film deposition

A pH sensitive iridium oxide film was employed on the BDD disc to determine the local pH.<sup>31</sup> The film was electrodeposited using chronoamperometry pulsing between 0 and 0.85 V vs. SCE for a pulse length of 0.2 s for a total of 7 minutes. The iridium oxide solution used was prepared as previously described.<sup>27,28</sup> Deposition was carried out using a CH Instrument 760E potentiostat. The film

was imaged on an optical microscope to ensure a uniform film was deposited and left to hydrate in pH 7 phosphate buffer for 48 hours. The films' response to pH was characterised by calibrating the open circuit potential (OCP) of the film in Carmody buffers, pausing the measurement when changing the solution and allowing the response to stabilise in each solution.

## 5.4 Results and Discussion

### 5.4.1 EC-XRF Design and Experimental Variation

There are several differences between the rotating disc electrode and set up used for this chapter and that used for the original EC-XRF research.<sup>17</sup> The original design, where the BDD was removed from the entire set up to place into the XRF, often resulted in breakages of the thin BDD. Therefore, integration of the BDD into the electrode design to increase the stability was an essential component of the redesign. Once integrated into the electrode, there was no requirement for a cap over the BDD which left an increased electrochemically active area but allowed for more consistent hydrodynamic flow across the electrode during rotation, aiding mass transport. Additionally, this allowed for an O-ring to be integrated into the electrode body to provide a watertight seal rather than placing it onto the BDD face itself.

As the BDD substrate itself is thin and has a minimal background in the XRF, consideration had to be made to the ohmic contact on the BDD. The original design had a ring contact around the edge of the BDD. This was reduced in this design to four point contacts that aligned with spring pins on the electrode body. The positioning of the pins onto the point contacts was essential so care had to be taken to ensure the contacts and pins were aligned during assembly. The smaller metal contact area on the back of the BDD reduced the XRF background compared to the original ring contact.

### 5.4.2 EC-XRF Electrode characterisation

The electrochemical properties of the new electrode design were assessed through a number of characterisation experiments as described in Section 2.5. BDD is known to have low capacitance and a large solvent window,<sup>32</sup> these properties were confirmed on each electrode cap with values  $< 6 \mu\text{F cm}^{-2}$  and

solvent windows > 3 V. For example, the electrode data shown in Figure 5.5 returned values of  $4.38 \mu\text{F cm}^{-2}$  (a) and 3.61 V (b), respectively.

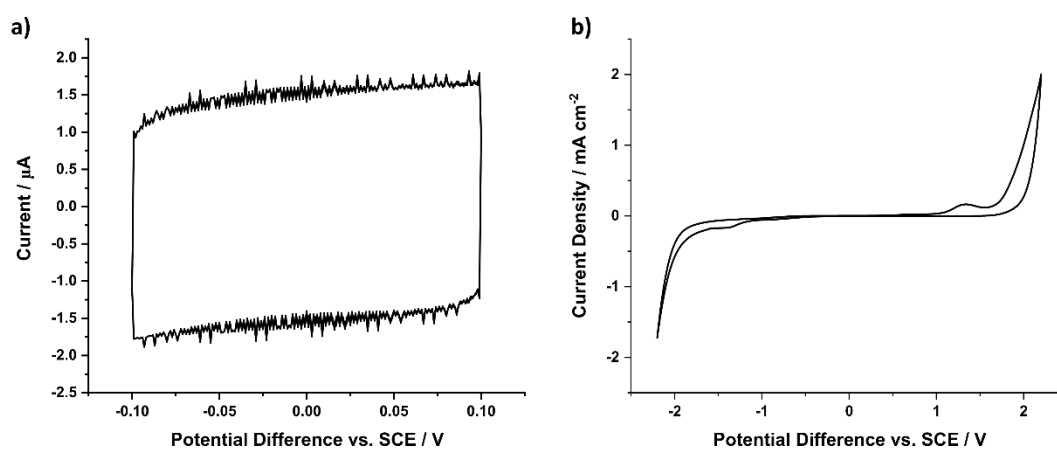


**Figure 5.5** Cyclic voltammograms in 0.1 M  $\text{KNO}_3$  run at  $0.1 \text{ V s}^{-1}$  for capacitance (a) and solvent window (b) measurements of EC-XRF electrode ( $\phi$  21 mm) in stationary solution. Measurements were undertaken under stationary conditions with a  $0.1 \text{ V s}^{-1}$  scan rate.

Cyclic voltammograms were conducted at scan rates of 0.05, 0.1, 0.15, 0.2 and  $0.25 \text{ V s}^{-1}$  and at rotation rates of 0, 500, 1000, 1200 and 1500 rpm. The  $\Delta E_p$  for  $\text{Ru}(\text{NH}_3)_6^{3+}$  reduction / oxidation, at  $0.1 \text{ V s}^{-1}$  in stationary solution was 79 mV, Figure 5.6a. This slightly larger than expected value (based on an ohmically contacted 1 mm disc)<sup>33</sup> suggests there is additional resistance in the set-up. This may be material resistance, due to the large area of the disc.

By rearranging the Randles-Sevcik equation (Equation 5.1) and the Levich equation (Equation 5.2) a diffusion coefficient,  $D$ , can be calculated for  $\text{Ru}(\text{NH}_3)_6^{3+}$  from the gradient of the line in Figure 5.6 aii and bii, respectively. From the Randles-Sevcik equation  $D = 5.6 \times 10^{-6} \text{ cm}^2 \text{ s}^{-1}$  and from the Levich equation  $D = 9.7 \times 10^{-6} \text{ cm}^2 \text{ s}^{-1}$ . Literature values of  $D$  for  $\text{Ru}(\text{NH}_3)_6^{3+}$  range from  $6.0 \times 10^{-6} \text{ cm}^2 \text{ s}^{-1}$  -  $8.7 \times 10^{-6} \text{ cm}^2 \text{ s}^{-1}$ .<sup>34-37</sup> Whilst electrolyte identity and concentration will impact the measured  $D$  value,<sup>38</sup> for a fixed solution the same  $D$  would be expected to be measured for the two techniques. However, the Levich equation assumes an infinite insulator around the rotating electrode.<sup>30</sup> Here there is only a small insulating area present around the disc which can allow for solution flow up the side of the electrode body, changing the hydrodynamics. The Randles-Sevcik equation assumes diffusion limited planar diffusion which should be achieved on the 21 mm EC-XRF disc, but the  $\Delta E_p$  values suggest small kinetic

or resistive contributions in the CV which may also contribute to the deviation observed.

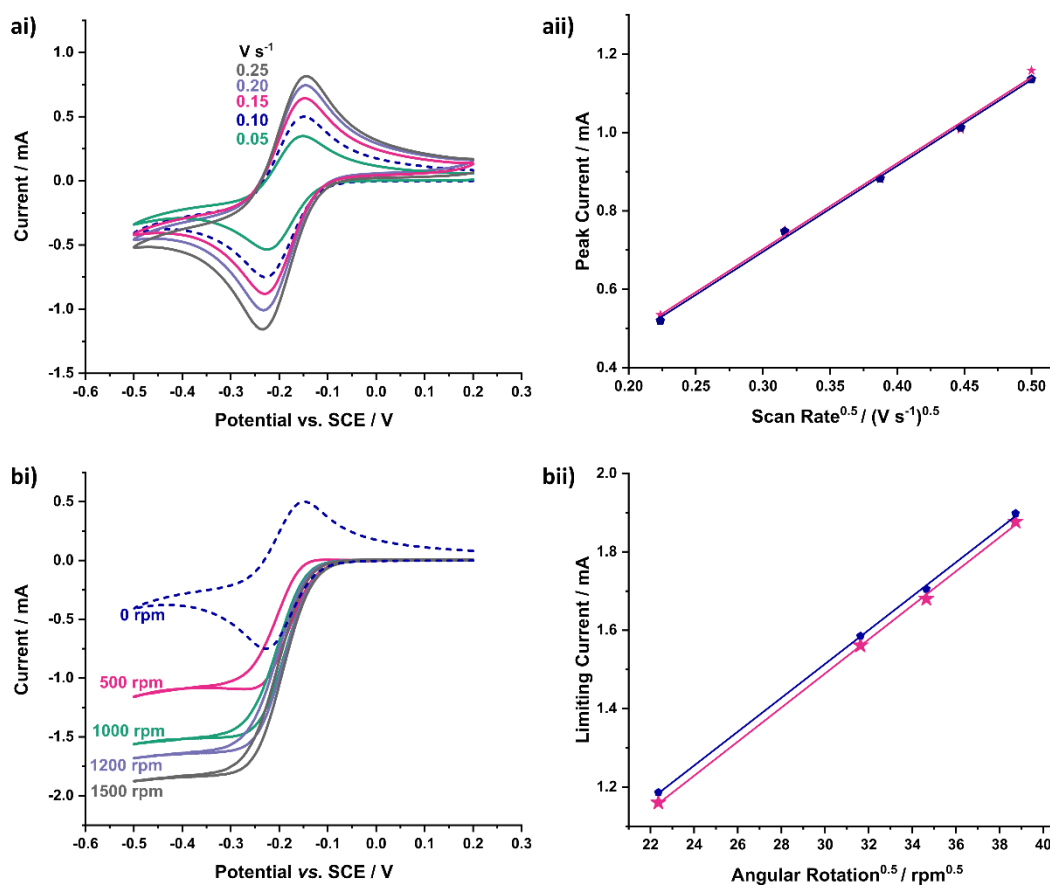


Figure 5.6 a) Randle-Sevcik analysis of EC-XRF electrode ai) CVs at various scan rates, the CV at  $0.1 \text{ V s}^{-1}$  is highlighted by the dashed line. aii) shows the experimental peak current data from ai. and a second rotating disc electrode cap. b) Levich analysis of E-XRF electrode bi) Cyclic voltammograms at various rotation rates with the stationary CV at  $0.1 \text{ V s}^{-1}$  for comparison (dashed line). bii) shows the experimental limiting current data from bi.

A background XRF signal for the BDD discs was determined by placing the clean RDE cap in the XRF chamber and running an analysis. A spectrum of the area of interest from two BDD electrode caps is shown in Figure 5.7. Small peaks are observed for Fe, Cu and Zn which can be attributed to the brass and steel components inside the XRF chamber. The lighter carbon and boron atoms in the diamond structure allow the photons to pass through and interact with the chamber behind the substrate. Pt peaks are also observed from the sputtered contacts on the rear of the disc.

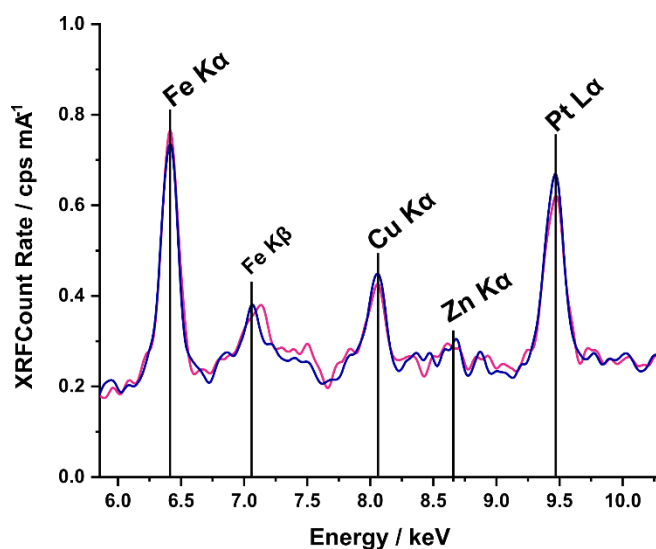


Figure 5.7 XRF background spectra of two EC-XRF electrode caps in the region of interest using the Mo target.

### 5.4.3 Copper EC-XRF

To consider the electrochemical response of Cu on the large (21 mm diameter) EC-XRF electrodes, CVs of 100 ppm (1.6 mM) Cu (as  $\text{Cu}(\text{NO}_3)_2$ ) were undertaken in a variety of background electrolytes; (a) 0.1 M  $\text{KNO}_3$ , (b) 0.2 M  $\text{HNO}_3$  and (c) 0.1 M acetate buffer at pH 4.5, Figure 5.8. 0.1 M  $\text{KNO}_3$  was considered as this is a common background electrolyte used in electrochemical experiments. ICP-MS analysis is typically undertaken in heavily acidified solutions (1-5%  $\text{HNO}_3$ ) so a high concentration  $\text{HNO}_3$  solution was used for comparison.<sup>12</sup> Finally, acetate buffers are most commonly used for ASV.<sup>39-41</sup>

All CVs were undertaken in aerated solutions as for real life experiments it is impractical to maintain a deoxygenated solution. In 0.1 M  $\text{KNO}_3$ , Figure 5.8 (top) a broad deposition peak is seen in the first cycle and then a sharper deposition peak in the second cycle at a slightly lower potential, this indicates that the initial nucleation of Cu on the BDD surface is challenging but once Cu deposits have formed Cu can deposit more readily onto the Cu deposits. In the oxidative part of both cycles a stripping peak is observed at 0.25 V vs. SCE. In contrast, in the 0.2 M  $\text{HNO}_3$  and acetate buffer solutions, a broad stripping peak is observed at around 0.1 V vs. SCE, a lower potential than observed in the  $\text{KNO}_3$  solution and closer to the  $E^0$  value of Cu. This suggests Cu is deposited in its metallic form from these solutions and the deposits in 0.1 M  $\text{KNO}_3$  may not be pure Cu metal.

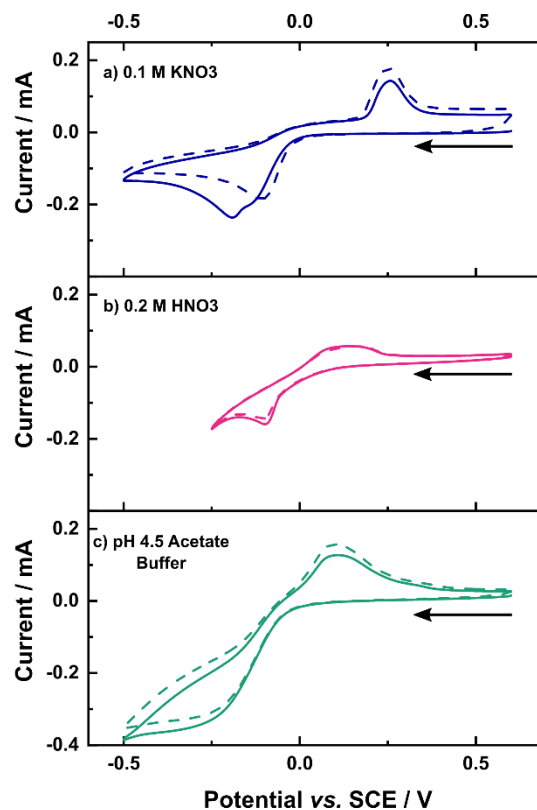


Figure 5.8 CVs of 100 ppm  $\text{Cu}(\text{NO}_3)_2$  in a) 0.1 M  $\text{KNO}_3$  b) 0.2 M  $\text{HNO}_3$  and c) pH 4.5 acetate buffer on the EC-XRF rotating disc electrode at  $0.1 \text{ V s}^{-1}$ . Solid line is the first cycle and dashed line indicates the second cycle.

#### 5.4.3.1 Effect of deposition potential

The effect of deposition potential on the  $\text{Cu K}\alpha$  XRF peak intensity was considered in both 0.1 M  $\text{KNO}_3$  (navy squares) and 0.2 M  $\text{HNO}_3$  (pink circles) solutions as shown in Figure 5.9a. For all experiments a concentration of 1 ppm  $\text{Cu}(\text{NO}_3)_2$ , a deposition time of 3600 s and a rotation speed of 1200 rpm was used. The two solutions showed different  $\text{Cu K}\alpha$  XRF peak intensity responses to increased deposition potential as shown in Figure 5.9. This relationship is also different from that reported in the original EC-XRF paper which used a different experimental set-up.<sup>17</sup>



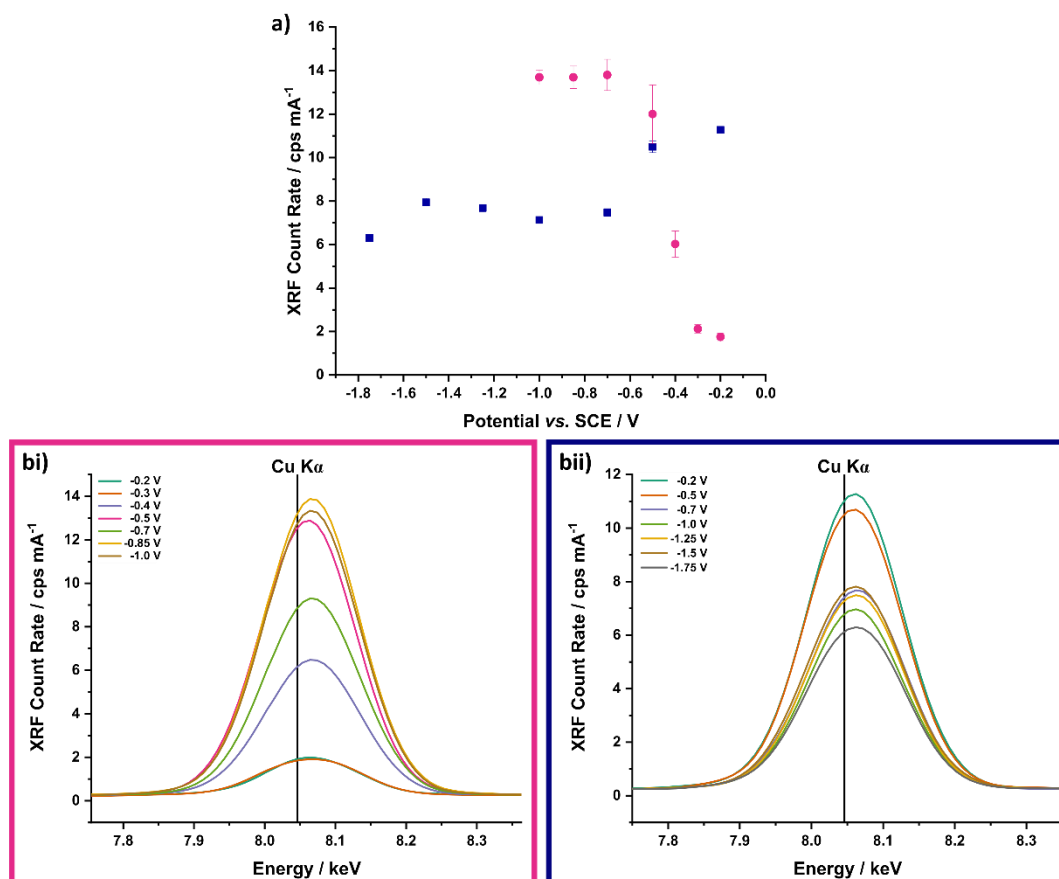


Figure 5.9 a) Average XRF count rate ( $n=3$ ) of Cu  $K\alpha$  after electrodeposition of 1 ppm Cu at different potentials for 3600 s at 1200 rpm in 0.2 M  $\text{HNO}_3$  (pink; circles; bi) and 0.1 M  $\text{KNO}_3$  (navy; squares; bii). bi and bii are raw XRF spectra of one run in each condition at the deposition potentials tested.

In 0.1 M  $\text{KNO}_3$  the highest intensity observed was at -0.2 V (11.2 cps  $\text{mA}^{-1}$ ), the lowest potential considered, dropping slightly to 7.1 cps  $\text{mA}^{-1}$  at -1.0 V. The decrease at -1.75 V we attribute to hydrogen gas formation from water reduction removing deposits from the BDD surface. Note this is the potential used by Hutton et al. in the original EC-XRF paper.<sup>42</sup> Contrastingly in  $\text{HNO}_3$  the signal intensity increased with increasingly negative deposition potentials before plateauing above -0.7 V. The potential was not increased beyond -1.0 V vs SCE, due to formation of hydrogen gas bubbles from HER in the acidic solution. It was also noted that the error bars were larger under the acidic conditions than neutral. However, the highest intensity in 0.2 M  $\text{HNO}_3$  is greater than the highest intensity of the 0.1 M  $\text{KNO}_3$  solution.

To explore further the observed behaviour a comparative study applying -0.2 V and -0.7 V vs. SCE in both solutions was undertaken, with the surfaces analysed using SEM post deposition, Figure 5.10, in addition to XRF analysis, Figure 5.11. A higher  $\text{Cu}^{2+}$  concentration (10 ppm) was used to aid visualisation of the deposits, the deposition time was reduced to 1800 s but rotation remained at 1200 rpm. The resulting deposits were very varied as seen in Figure 5.10.

At -0.2 V in 0.1 M  $\text{KNO}_3$  a significant amount of Cu was deposited hence the Cu coloured appearance of the electrode Figure 5.10 ai. In contrast the black appearance of the electrode in Figure 5.10 bi is the BDD surface showing minimal Cu deposition, in agreement with the XRF data, green lines in Figure 5.11. At -0.7 V in the 0.2 M  $\text{HNO}_3$  solution, deposition of Cu species occurs producing micron sized deposits, Figure 5.10 dii, the 'maple leaf' like deposition observed in di was consistently seen for these deposition parameters. These deposits resulted in the most intense Cu  $\text{K}\alpha$  peaks in the XRF spectra, Figure 5.11. The deposits formed at -0.7 V in the 0.1 M  $\text{KNO}_3$  show mostly two morphologies in the SEM Figure 5.10 cii. Small discrete deposits are seen on the left and a dense porous deposit right of the SEM image, which is at the centre of the disc, Figure 5.10 ci. Due to the blueish hue of the deposit, it is believed to be a Cu hydroxide deposit<sup>43</sup> rather than a Cu metal or oxide deposit. This species proved to be extremely unstable on the BDD surface and was easily washed off when rinsing the electrode or removing the electrode from solution, resulting in variability in the XRF spectra, purple lines in Figure 5.11b. The image in Figure 5.10ci also nicely displays the hydrodynamic flow pattern the electrode experiences during rotation.

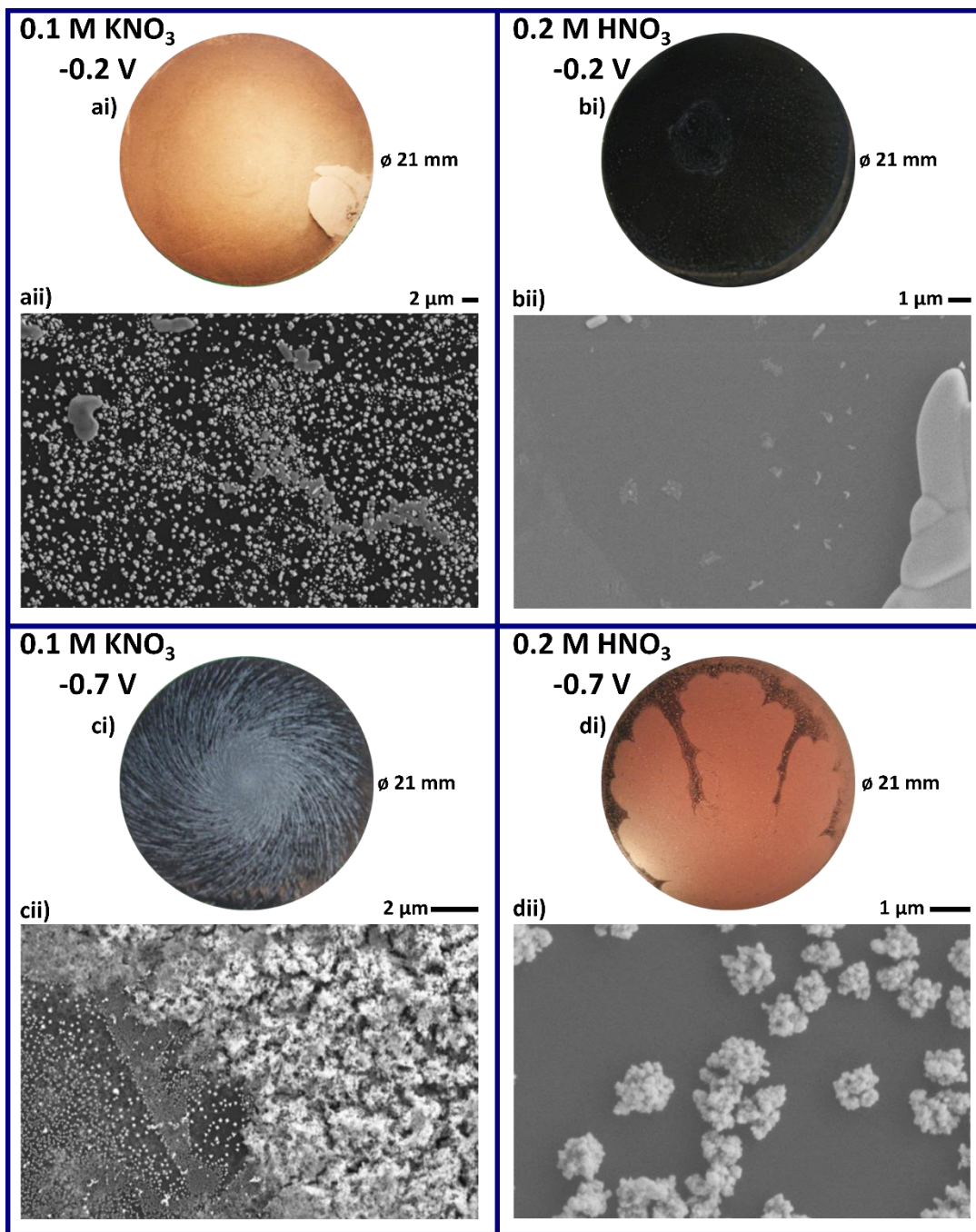


Figure 5.10 Optical images (i) and SEM images (ii) of Cu deposits from solutions containing 10 ppm  $\text{Cu}(\text{NO}_3)_2$  deposited for 1800 s at 1200 rpm at -0.2 V (a and b) and -0.7 V (c and d) in 0.1 M  $\text{KNO}_3$  (a and c) and 0.2 M  $\text{HNO}_3$  (b and d).

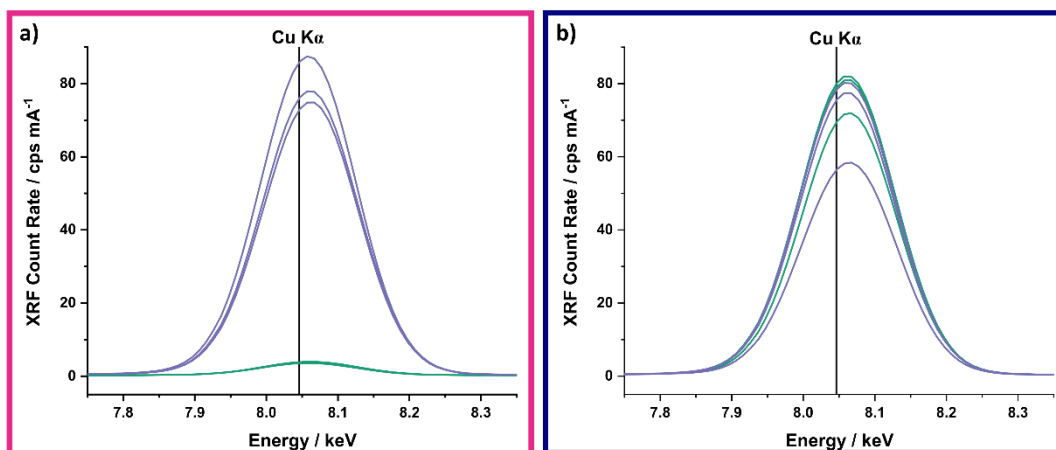


Figure 5.11 XRF spectra from Cu deposition in a 10 ppm  $\text{Cu}^{2+}$  solution for 1800 s at 1200 rpm at -0.2 V (green lines) and -0.7 V (purple lines) in a) 0.2 M  $\text{HNO}_3$  and b) 0.1 M  $\text{KNO}_3$ .

#### 5.4.3.2 Copper Calibration curve

To quantify the Cu detection capabilities of EC-XRF a series of  $\text{Cu}(\text{NO}_3)_2$  concentrations between 1 ppb to 5 ppm were analysed by XRF after deposition for 3600 s at 1200 rpm in both the 0.1 M  $\text{KNO}_3$  and 0.2 M  $\text{HNO}_3$  solutions. In the 0.1 M  $\text{KNO}_3$  solution a deposition potential of -0.2 V was insufficient to deposit Cu at concentrations at  $\leq 10$  ppb. Therefore -0.5 V was used as a deposition potential for the concentration experiments in 0.1 M  $\text{KNO}_3$ , as this potential only shows a slightly lower XRF intensity than -0.2 V, Figure 5.9. In the acid solution a deposition potential of -0.7 V was used. Both solutions were considered to determine if one was better across the concentration range of interest. Figure 5.12 shows the average XRF intensity ( $n = 3$ ) across four orders of magnitude for both solutions. The response in both solutions is relatively linear when plotted as  $\text{Log}_{10}$  XRF count rate vs.  $\text{Log}_{10}$  Cu concentration. The XRF count rate is consistently higher in the 0.2 M  $\text{HNO}_3$  solution than 0.1 M  $\text{KNO}_3$  following the trend observed in the deposition potential experiments, Figure 5.9. For example, at 5000 ppb the acidic solution showed an average intensity of  $64.8 \text{ cps mA}^{-1}$  significantly higher than the  $22.0 \text{ cps mA}^{-1}$  in 0.1 M  $\text{KNO}_3$ . Depositions in 0.1 M  $\text{KNO}_3$  show improved linearity to the 0.2 M  $\text{HNO}_3$  solution, with  $R^2$  values of 0.963 and 0.744 respectively. In both conditions 10 ppb was highly variable, however generally the  $\text{KNO}_3$  solution was better suited to the low ppb concentrations than the acid. Using twenty XRF measurements of the blank BDD discs the variation in the measurement was determined and the standard deviation (SD) of the

backgrounds determined. The limit of quantification is typically quoted as 10 x SD and the limit of detection as 3 x SD.<sup>44,45</sup> Here, the limit of quantification of Cu was determined as 7.6 ppb (10 x SD = 0.62 cps mA<sup>-1</sup>) in 0.1 M KNO<sub>3</sub> and 0.9 ppb in 0.2 M HNO<sub>3</sub> (using non weighted linear fitting) and the limit of detection was 0.76 ppb in 0.1 M KNO<sub>3</sub> and a negative concentration in 0.2 M HNO<sub>3</sub> (3x SD = 0.186 cps mA<sup>-1</sup>) indicating an issue with low concentrations and backgrounds in the acid solution.

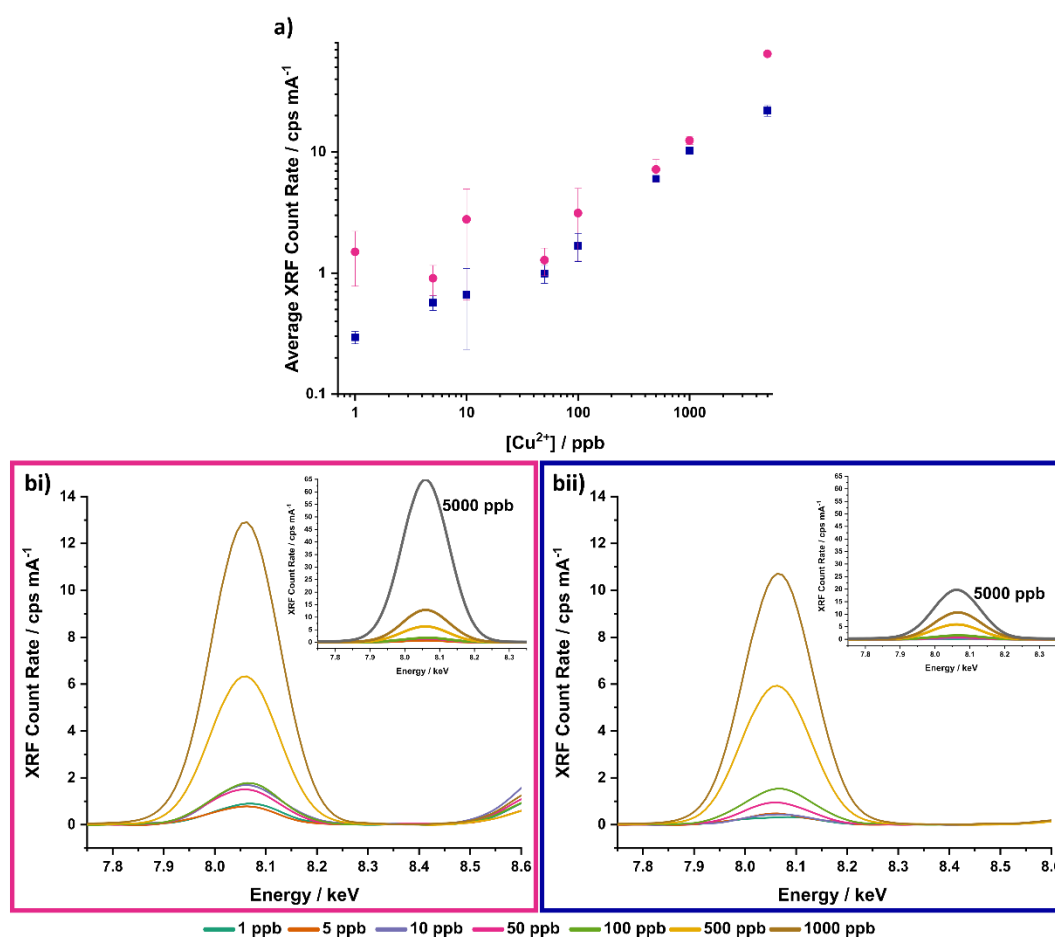


Figure 5.12 a) Average XRF count rate (n=3) of Cu K $\alpha$  after electrodeposition of Cu at different concentrations for 3600 s at 1200 rpm in at -0.7 V in 0.2 M KNO<sub>3</sub> (pink; circles; bi) and at -0.5 V in 0.1 M KNO<sub>3</sub> (navy; squares; bii). bi and bii are raw XRF spectra of one run for each concentration range, insets show the spectra for 5000 ppb.

### 5.4.3.3 Supporting Electrolyte/reducing variability

In an attempt to decrease the variability, several different experimental conditions were trialled at a Cu concentration of 500 ppb, Figure 5.13. A concern was raised that the variability observed at 0.2 M HNO<sub>3</sub> was due to dissolution of the deposits in the strong acid reducing the overall signal. Therefore a 0.01 M HNO<sub>3</sub> solution (purple) was considered as an alternative using the same -0.7 V deposition potential (◆) as for the 0.2 M HNO<sub>3</sub> solution (pink). This showed some improvement in variability but the intensity was lower than the results obtained in 0.1 M KNO<sub>3</sub> (navy).

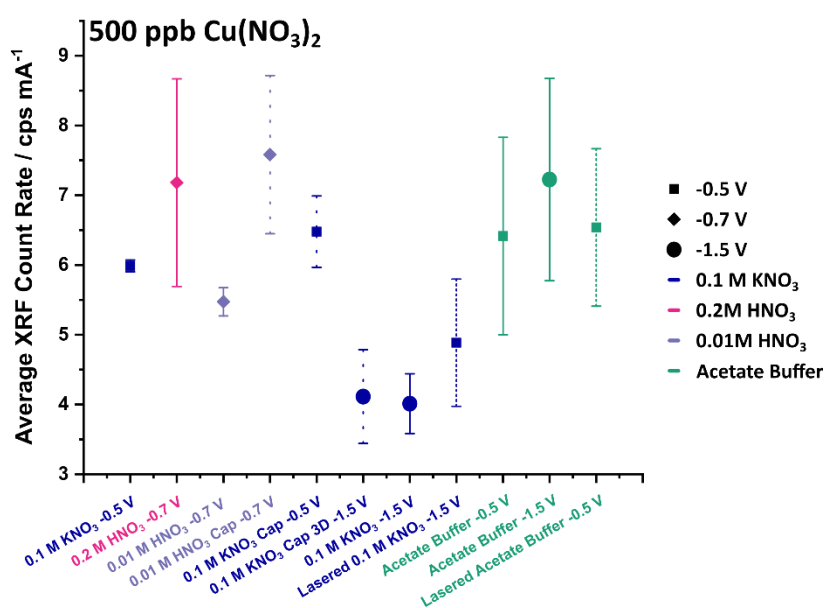


Figure 5.13 Average XRF count rate (n=3) from depositions for 3600 s at 1200 rpm with 500 ppb Cu using a variety of supporting electrolytes, deposition potentials and other conditions to understand the variability observed.

An observation was made that when the electrode was removed from solution the surface tension resulted in a droplet of solution on the electrode surface. As this droplet fell it is possible that some of the deposit on the electrode surface could be removed. The original EC-XRF electrode design used by Hutton *et al.* included a cap over the BDD with a recessed area exposed to solution. Given stability of deposits on the surface had been identified as an issue it was decided to try depositions with a cap and see how this affected the response in XRF intensity. The cap also reduces the active area of the electrode and protects the electrode surface from some of the hydrodynamic flow as the BDD is recessed within the cap, Figure 5.13 dotted lines.

At -0.7 V in 0.01 M HNO<sub>3</sub> the XRF signal was greater when the cap was used, but more variable across the three runs, Figure 5.13. In the KNO<sub>3</sub> solution with a deposition potential of -0.5 V (■) the XRF count rate was again greater when a cap was used but was again more variable between runs. At a higher deposition potential, -1.5 V (●) closer to that used by Hutton *et al.*, the intensity was lower and more variable than the new design with optimised parameters, Figure 5.13. It is thus possible that the electrochemical deposition is not causing the variability observed but rather the process of removing the electrode from solution and drying the surface prior to the XRF analysis.

As Figure 5.8c shows, deposition in acetate buffer also results in deposition of Cu metal (as for acidic solutions). A 500 ppb Cu acetate solution (pH 4.5) was trialled at -0.5 and -1.5 V, comparable to the 0.1 M KNO<sub>3</sub> solutions and the Hutton *et al.* conditions. In the acetate buffer the XRF signal was greater than in KNO<sub>3</sub>, and greater at the more negative deposition potential, but again more variable. This further supports the suspicion that the transfer of the electrode from the solution into the air for XRF analysis may play a large role in the variability. The BDD electrode used is very smooth (polished to ~ nm roughness) which could impact particle adhesion to the surface. A solution to this problem was to laser micromachine the BDD surface to introduce rougher channels where the deposits may stick better, dashed lines in Figure 5.13. Unfortunately, this approach was too effective, and it was then difficult to remove all of the deposited Cu. This meant the disc was not fully clean between runs, accounting for some of the variability observed in these experiments.

#### 5.4.3.4 Analysis of EC-XRF Redesign and Functionality

Despite the redesign and optimisation of conditions for EC-XRF multiple challenges were presented during testing. The XRF count rates reported in this study were nearly two orders of magnitude lower than that reported by Hutton *et al.*<sup>42</sup> Although we note that the XRF system had been impaired after the Hutton *et al.* study due to solution leaking into the XRF chamber. Whilst the system was fixed, we never obtained the same XRF intensities as previously. Follow-up work by Ayres *et al.* on palladium detection in pharmaceuticals showed intensities more similar to those reported here.<sup>18</sup>

Whilst the redesign was significantly more user friendly it presented its own challenges. Manual polishing of the electrode was standard practice during the cleaning procedure, however, this resulted in edge effects on the electrode becoming more pronounced with time due to the removal of the adhesive. Additionally, there was concern surrounding the epoxy, used to seal the BDD in the PEEK cap, retaining some metal deposits. Due to the hardness of BDD, the Au coating on the electrical contact springs was also eroded with continued use, exposing the brass which then transferred onto the rear face of the BDD and resulted in increasing background signals during XRF analysis. This was combated by running a background measurement on the electrode prior to each measurement, this did however add steps to the measurement and the analysis stages. This also made ensuring the BDD was clean challenging as the background spectra could vary.

The stability of the deposits, either during electrodeposition or during preparation for XRF analysis seemed the most significant challenge. As with all metal deposition the form of the deposit depended on the electrolyte, buffer capacity of the solution and deposition potential. The long deposition times, requirement for rotation, smooth BDD surface and the processing steps between deposition and analysis, increased the variability in these experiments making it a challenge for quantification of the deposits.

However, this technique could be useful as a semi-quantitative or informative technique where a heavy metal contamination is suspected in a water body. For example, a water sample from the Hayle estuary (Cornwall) was analysed using both ICP-MS and the EC-XRF technique. The area around Hayle has a mining legacy and the estuary sediments are known to contain elevated concentrations of Cu, Sn, As, Pb and Zn.<sup>46,47</sup> ICP-MS returned concentrations of 40 ppb Cu and 400 ppb Zn from an acidified sample. EC-XRF was undertaken either in the sample as received (green solid line), with 0.1 M KNO<sub>3</sub> added (navy dashed line) or in 0.2 M HNO<sub>3</sub> (pink dotted line) using a deposition potential of -1.0 V, a rotation of 1200 rpm and a deposition time of 3600 s, Figure 5.14. Both Cu and Zn peaks were observed in the XRF spectra. The supporting electrolyte (as acid or KNO<sub>3</sub>) increased the Cu intensity but decreased the Zn intensity relative to just



the water sample. Multi metal samples are more challenging to analyse as a range of interferences during metal deposition and the XRF analysis can occur *i.e.* formation of intermetallic deposits,<sup>15,48,49</sup> one metal coating another deposit which, depending on the thickness, could shield the first metal from detection by XRF.<sup>50</sup> Cu and Zn are known to form an intermetallic compound during metal deposition.<sup>41,48,51</sup> However this indicates that this technique could be used to identify contaminants from water samples but further consideration on the effects of intermetallic formation for both metal deposition and XRF analysis would be required.

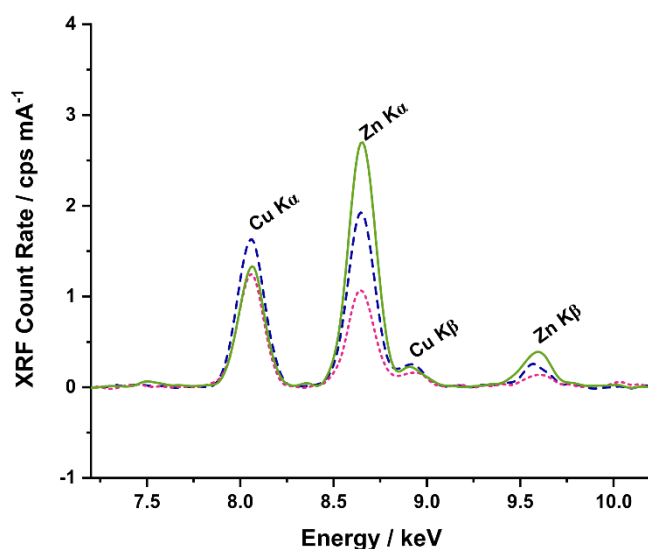


Figure 5.14 XRF spectra of deposited metals from a sample of water from Hayle estuary (green; solid line), with 0.1 M  $\text{KNO}_3$  (navy; dashed line) and 0.2 M  $\text{HNO}_3$  (pink; dotted line) after deposition from 50 ml of solution at -1.0 V for 3600 s at 1200 rpm.

#### 5.4.4 Anodic Stripping Voltammetry under locally controlled pH environments

As shown above, solution pH and composition can affect the chemical identity of the deposited metal e.g. pure metal versus metal oxide/hydroxide. Previous work in the Macpherson group had shown success in depositing mercury and Cu under locally acidified environments using a ring disc electrode configuration.<sup>20,21</sup> However, these studies were undertaken at relatively high concentrations. The second section of this chapter considers this method at significantly lower, and more environmentally relevant, concentrations of Cu.

## 5.4.5 Ring Disc Electrode Characterisation

### 5.4.5.1 BDD and BDD-Q Macroelectrodes

To initially investigate the impact of  $sp^2$  carbon features on Cu detection, 1 mm diameter discs of BDD and BDD-Q were sealed in glass capillaries, polished to expose the diamond and contacted using a conductive epoxy and a Cu wire as described in Section 2.3.2.

The BDD (navy) and BDD-Q (pink) electrodes were characterised for capacitance, Figure 5.15, returning values of  $6.68 \mu\text{F cm}^{-2}$  and  $19.67 \mu\text{F cm}^{-2}$ , respectively. The respective solvent windows were 3.38 V and 3.61 V, Figure 5.15b. Measurements and values were made as described in Section 2.5.1 and Section 2.5.2. The quinone surface coverage ( $\Gamma$ ) of the BDD-Q electrode was determined as described in Section 2.5.4 and for this electrode returned a value of  $\Gamma = 3.4 \times 10^{-12} \text{ mol cm}^{-2}$ .

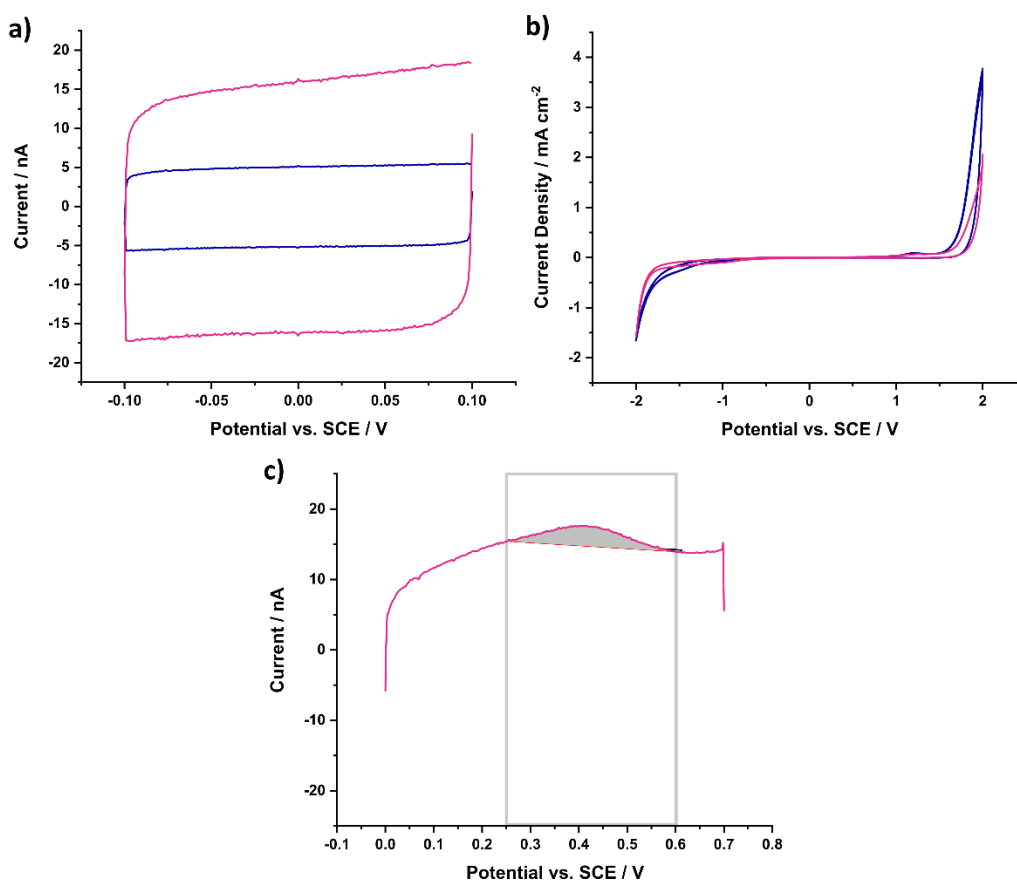


Figure 5.15 Characterisation data of BDD (navy) and BDD-Q (pink) glass sealed macroelectrodes for capacitance (a) and solvent window (b) in 0.1 M KNO<sub>3</sub> and QSC (c; BDD-Q only) in pH 2 Carmody Buffer. All undertaken with a  $0.1 \text{ V s}^{-1}$  scan rate.

### 5.4.5.2 BDD Ring Disc Electrode Characterisation

Blank BDD ring disc electrodes were fabricated as described in Section 5.3.4.1. For the data shown in Figure 5.16 the capacitance, solvent window and  $\Delta E_p$  values for 1 mM  $\text{Ru}(\text{NH}_3)_6^{3+}$  are shown in Table 5.1. The latter measurement was not used for characterisation of BDD-Q electrodes as the  $\text{Ru}(\text{NH}_3)_6^{3+}$  is difficult to remove from the  $\text{sp}^2$  bonded carbon in the microspots, due to adsorption, which can impact future experiments.

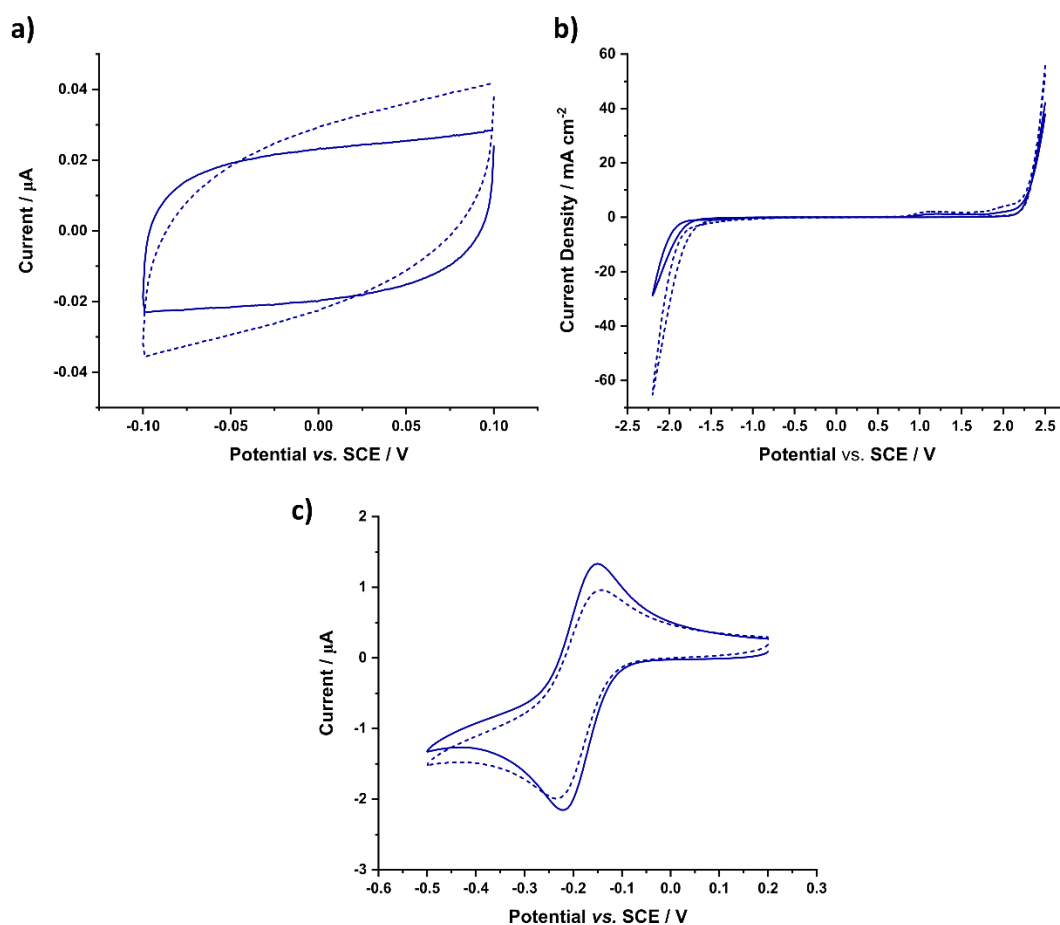


Figure 5.16 Characterisation data of BDD ring (dashed line) disc (solid line) electrode for capacitance (a), solvent window (b) in 0.1 M  $\text{KNO}_3$  and  $\Delta E_p$  (c) in 1 mM  $\text{Ru}(\text{NH}_3)_6^{3+}$  in 0.1 M  $\text{KNO}_3$ . All undertaken with a  $0.1 \text{ V s}^{-1}$  scan rate.

Table 5.1 Electrochemical Characterisation Values for BDD Ring Disc Electrode

	BDD Disc	BDD Ring
Capacitance / $\mu\text{F cm}^{-2}$	18.3	42.7
Solvent Window / V	2.04	1.64
$\Delta E_p$ / mV	69	88

Whilst these values are indicative of exposed  $sp^2$  carbon on the sidewalls of the BDD cylinders,<sup>52</sup> the complexity of the fabrication procedure means it is very difficult to make a perfect coplanar sealed ring disc electrode. Refinement of the fabrication procedure, as described in Section 5.3.4.2, was undertaken to aid in making sure the electrodes were coplanar and the spacing between the ring and disc was uniform.

#### 5.4.5.3 BDD-Q Ring Disc Electrode Characterisation

Ring disc electrodes incorporating the BDD-Q disc electrode were fabricated as described in Section 5.3.4.2. The use of the diamond support aided positioning and attachment of wires to the contacts, making fabrication easier. Again, electrochemical characterisation was undertaken on the ring disc electrodes. The responses are shown in Figure 5.17 with corresponding values in Table 5.2. The electrochemical response of the ring electrodes still indicates the presence of  $sp^2$  carbon. However, as the rings of these electrodes were extremely thin (Figure 5.18 Optical Image of BDD-Q ring disc electrode. Pink rings denote the boundary of the ring electrode. Disc is 1 mm in diameter.), it is likely there was a considerable amount of exposed  $sp^2$  carbon 'edge' which likely contributed to the high capacitance and small solvent window.

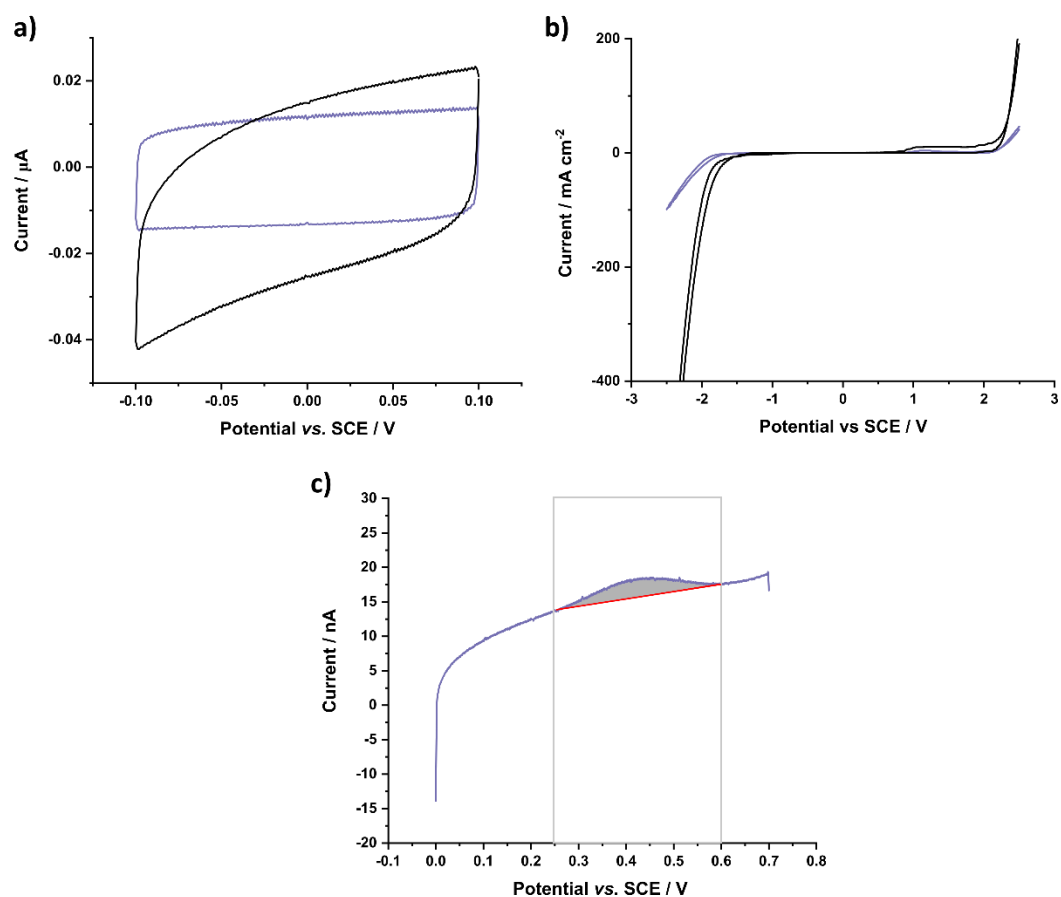


Figure 5.17 Characterisation data of BDD-Q Disc (purple) and BDD ring (Black) electrode for capacitance (a) and solvent window (b) in 0.1 M  $\text{KNO}_3$  and QSC (c; BDD-Q Disc only) in pH 2 Carmody Buffer. All undertaken with a  $0.1 \text{ V s}^{-1}$  scan rate.

Table 5.2 Electrochemical Characterisation Values for BDD-Q Ring Disc Electrode

	BDD-Q Disc	BDD Ring
Capacitance / $\mu\text{F cm}^{-2}$	13.8	139
Solvent Window / V	1.7	0.8
QSC / $\text{mol cm}^{-2}$	$2.88 \times 10^{-12}$	n/a

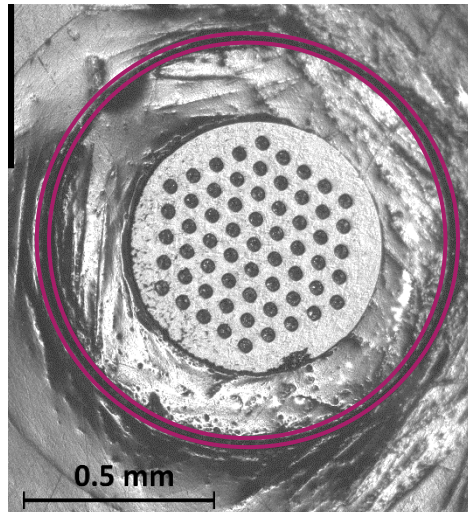


Figure 5.18 Optical Image of BDD-Q ring disc electrode. Pink rings denote the boundary of the ring electrode. Disc is 1 mm in diameter.

#### 5.4.6 Exploring BDD and BDD-Q electrodes for Cu detection and the effect of pH

As previously discussed metallic deposition occurs most readily from acidic solutions where the majority of metal ions are in the hydrated state. For this reason, initial CVs were run at pH 2 (Figure 5.19). The large negative current flowing at -0.5 V on both electrodes can be associated with HER. Both electrodes show only one Cu stripping peak, at 0.13 V.

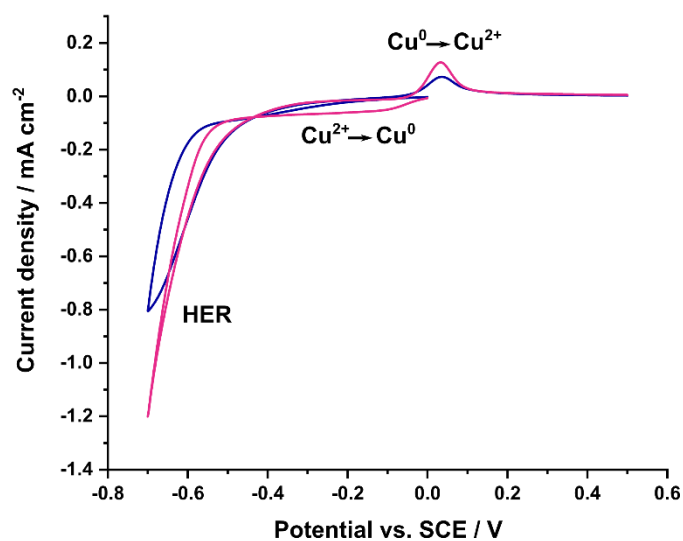


Figure 5.19 CV of 10 ppm Cu in an aerated solution on BDD (Blue) and BDD-Q (Pink) glass sealed macroelectrodes, at pH 2. Scan rate of 0.1 Vs

To explore the effect of pH, additional CVs were run at two additional bulk pH values, pH 4.4 and 5.2 adjusted by HNO<sub>3</sub>, in 0.1 M KNO<sub>3</sub>. In both solutions much lower current densities were passed indicating a reduction in the available Cu<sup>2+</sup> and there was an absence of significant HER, within the potential range investigated, Figure 5.20. At pH 4.4 two stripping peaks were observed (Figure 5.20a). The first peak is at a similar potential to that seen in the pH 2 solution but at a reduced current. This peak is likely still a Cu metal stripping peak. On the BDD electrode the second peak occurs at a more positive potential than the second peak on the BDD-Q electrode at 0.30 and 0.19 V, respectively. This feature is again observed at pH 5.2 (Figure 5.20b) with the second peak being the dominant peak in the CV. The second peak is likely to be associated with an oxide form of the Cu, given the higher pH solutions used under non-buffered conditions.

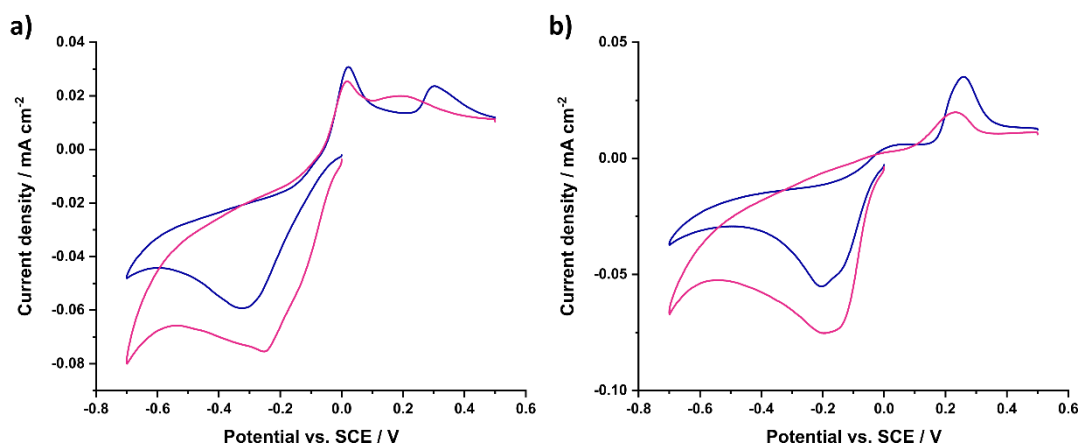


Figure 5.20 CV of 10 ppm Cu on BDD (Blue) and BDD-Q (Pink) electrodes, at pH 4.4 (a) and 5.2 (b). Scan rate of 0.1 Vs<sup>-1</sup>.

#### 5.4.7 Anodic Stripping Voltammetry of copper in acidic bulk solutions on BDD and BDD-Q electrodes

ASV was employed to determine the deposition and stripping behaviour of Cu on both the BDD and BDD-Q surfaces. Both electrodes were held at -0.5 V for 5 minutes in a pH 2 solution containing 10, 50 or 100 ppb Cu<sup>2+</sup>. Once deposition was completed linear sweep voltammetry (LSV) was used to strip the deposited metal off the electrode by scanning in a positive direction, Figure 5.21. In general, the BDD-Q electrode showed higher currents in the stripping step (Figure 5.21). However, both electrodes showed a similar pattern with 100 ppb passing the

highest stripping current, then 50 ppb with a very small peak at 10 ppb but, interestingly, a larger second peak for 10 ppb is also observed. From the data above we speculate that this shifted peak corresponds to an oxide form of Cu. Reasons for its formation are discussed later.

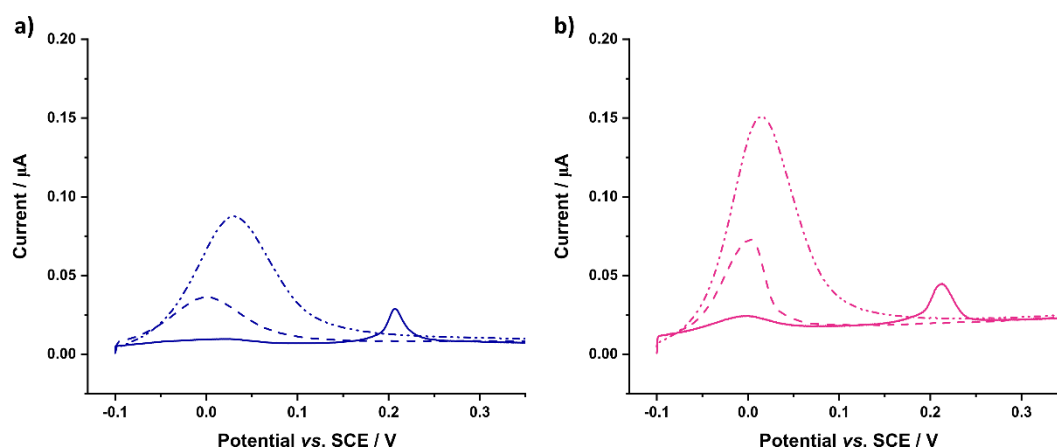


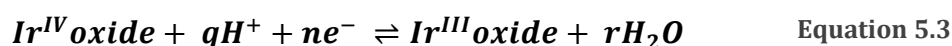
Figure 5.21 Stripping step of ppb Cu in pH 2 solution on bare BDD (Blue) and BDD-Q (Pink) electrodes. Concentrations tested; 10 ppb (solid), 50 ppb (--) and 100 ppb (---). Deposition parameters; -0.5 V, 5 mins. Undertaken with a 0.1 V s<sup>-1</sup> scan rate.

Due to the reliable stripping characteristics under acidic conditions a methodology to locally change the pH over an electrode, rather than changing the bulk pH, was employed. This is a more feasible technique for on-site analysis than carrying concentrated acids to a location.

## 5.4.8 Local pH change measurement

### 5.4.8.1 Iridium oxide thin film

A pH sensitive iridium oxide (IrOx) thin film was electrochemically deposited onto the BDD disc electrode<sup>20,27,28,31</sup> in the ring disc electrode geometry, in order to validate the pH decrease when oxidising water on the ring. IrOx shows a potentiometric response to pH as a function of transition between the two oxidation states;<sup>31</sup>



Once deposited the IrOx film was left to hydrate in pH 7 phosphate buffer for two days. The pH response was calibrated in Carmody buffers across the pH range of



interest (2 – 8: Figure 5.22a).<sup>26</sup> The film showed a super nernstian response at 64 mV pH<sup>-1</sup>, Figure 5.22b, in keeping with previous literature.<sup>31</sup>

A current of +50  $\mu\text{A}$  was applied to the ring electrode, after an initial stabilisation period of 5 minutes in the 0.1 M  $\text{KNO}_3$  solution, to create a local acidic environment, Figure 5.22a.<sup>21</sup> Prior to application of the ring current, the potential of the IrOx film on the disc electrode, which indicates the bulk pH of the solution, corresponded to a pH 5.1 - 5.3. Once 50  $\mu\text{A}$  was applied to the ring the local pH in the vicinity of the disc decreased and stabilised around pH 2.0 – 2.1.

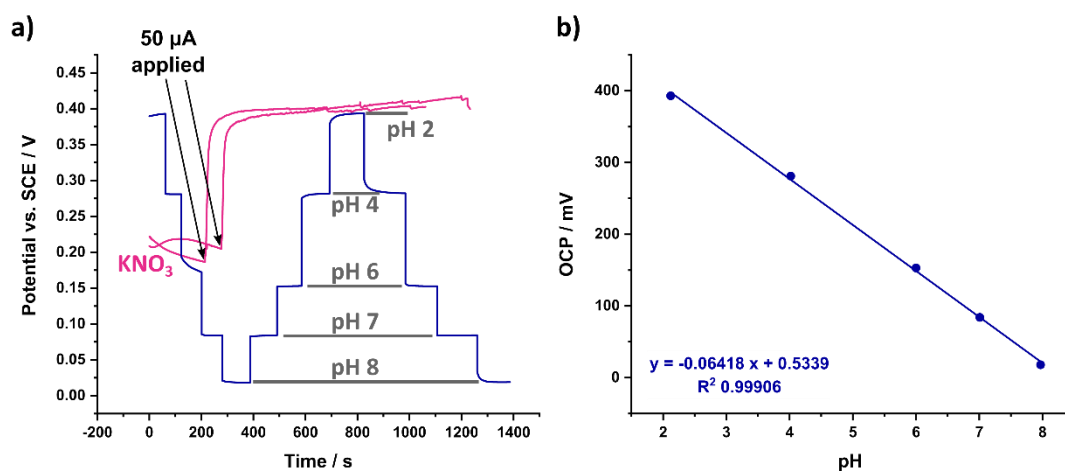


**Figure 5.22 Iridium oxide calibration (navy) collected by running an OCP measurement (a) and changing the buffer solution approximately every 3-5 minutes once the response had stabilised. Overlaid is the response of the iridium oxide electrode on the disc in  $\text{KNO}_3$  for approximately 5 minutes and whilst 50  $\mu\text{A}$  is applied to the ring (pink). B) is the calibration line of the iridium oxide taken at the stable potentials in (a) and plotted against the pH measured by a glass probe.**

However, when trying to use the IrOx film repeatedly, to look at the effect of different currents applied to the ring, the calibration of the IrOx calibration was observed to shift, Figure 5.23. Variation in the  $\text{Ir}^{3+}/\text{Ir}^{4+}$  ratio, electrode preparation, age of the film and exposure to redox agents has been shown to affect the pH calibration.<sup>31</sup> The process of water oxidation not only produces protons but also oxygen which potentially could oxidise the IrOx film disrupting the potentiostatic pH response baseline. It was therefore difficult to quantify the pH changes using an IrOx thin film for this experiment.

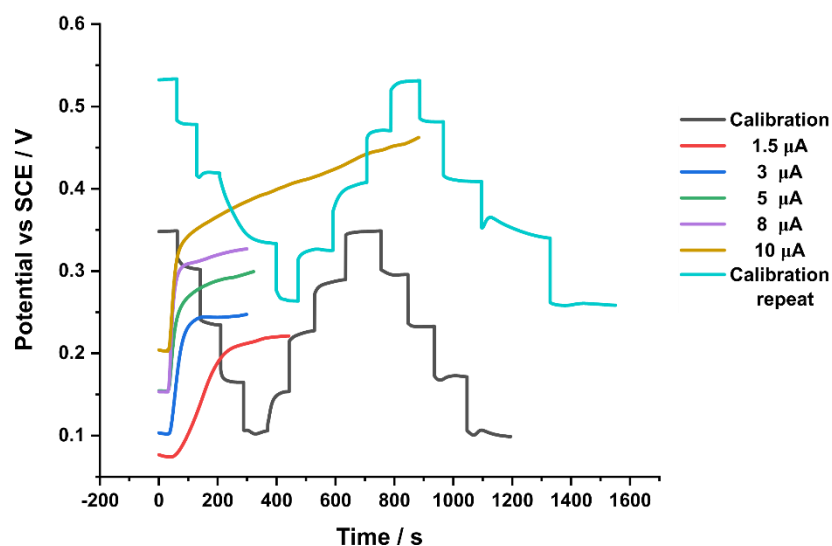
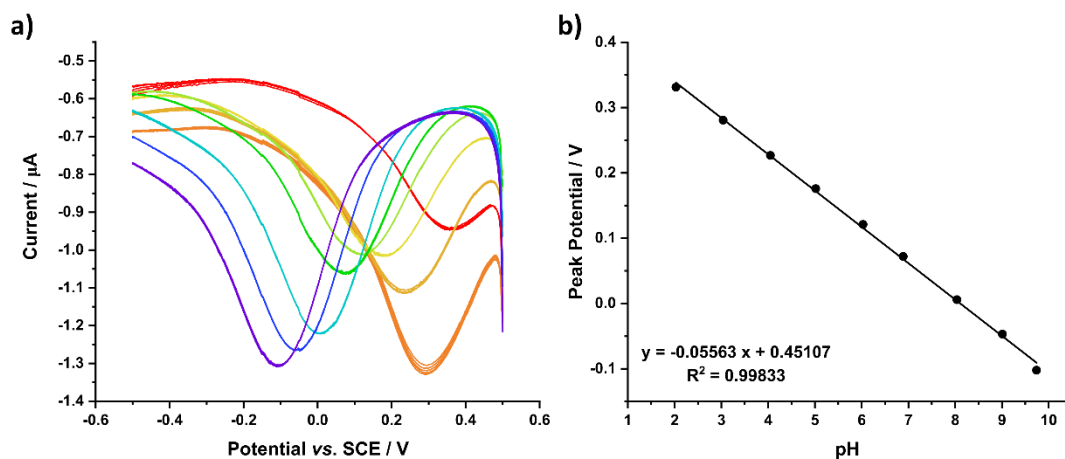


Figure 5.23 Calibration of iridium oxide film before (black) and after (blue) generating on the ring to measure local pH shift at ring currents of 1.5, 3, 5, 8 and 10  $\mu\text{A}$ . The calibration steps of of iridium oxide film was collected by running an OCP measurement and changing the buffer solution approximately every 3-5 minutes once the response had stabilised, as in figure 5.22.

#### 5.4.8.2 BDD-Q Ring Disc Electrodes

As shown in Chapters 3 and 4, the BDD-Q disc has proved a stable pH sensor in the ring disc geometry. The pH response of the BDD-Q ring disc electrode fabricated for these experiments was verified in known pH solutions of Carmody buffers across the pH range 2 - 10, Figure 5.24. Using the peak position potential a calibration line of  $E_p = -0.056 \text{ pH} + 0.451$  ( $R^2 = 0.99833$ ) was measured, with a slope of  $56 \text{ mV pH}^{-1}$ , which is slightly lower than the expected  $59 \text{ mV pH}^{-1}$  for a truly Nernstian response.



**Figure 5.24** pH response BDD-Q disc in ring disc electrode configuration in carmody buffers pH 2 – 10. Square wave voltammetry at 150 Hz, 0.1 V amplitude, 1 mV step between 0.5 and -0.5 V (a). Peak potential plotted vs. pH (b).

As discussed in previous chapters the pH response in unbuffered solutions is more challenging to measure due to local proton depletion effects, and  $sp^2$  catalysed ORR, most evident around neutral pHs.<sup>53</sup> Such a deviation was observed on this electrode, Figure 5.25.<sup>53</sup>

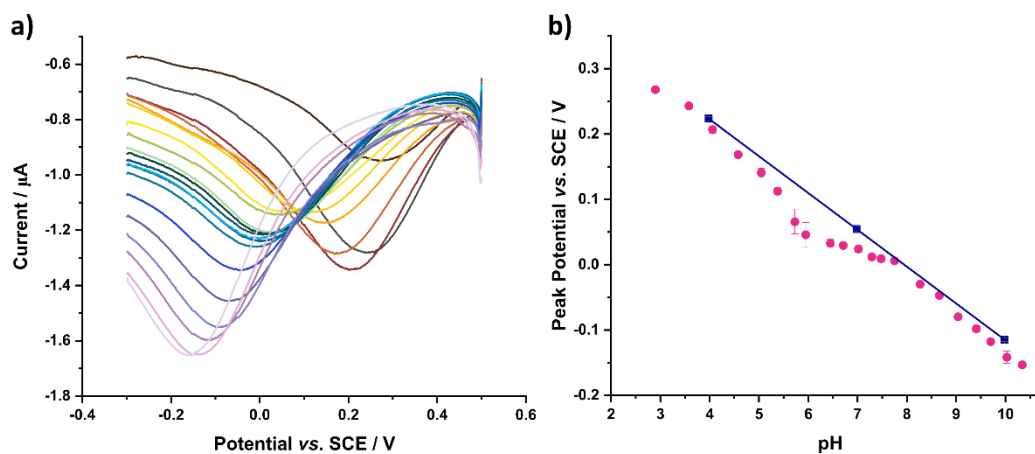


**Figure 5.25** pH response of BDD-Q disc in ring disc electrode configuration in pH adjusted 0.1 M  $KNO_3$  between pH 2 and 10. Square wave voltammetry at 150 Hz, 0.1 V amplitude, 1 mV step between 0.5 and -0.3 V (a) pH adjusted with KOH and  $H_2SO_4$ . Peak potential plotted vs. pH (b) with calibration line from measurement in pH 4, 7 and 10 Carmody buffers.

However, the pH values of interest for the experiments are < pH 7. Further measurements were made in the pH range 2-7, by altering the scan range of the SWV measurement from 0.5 V - -0.3 V to 0.7 V - -0.15 to capture the more acidic peaks and limit quinone catalysed ORR at the more reductive potential. As can be

seen, a better agreement between the buffered calibration and unbuffered measurements was obtained, Figure 5.26.

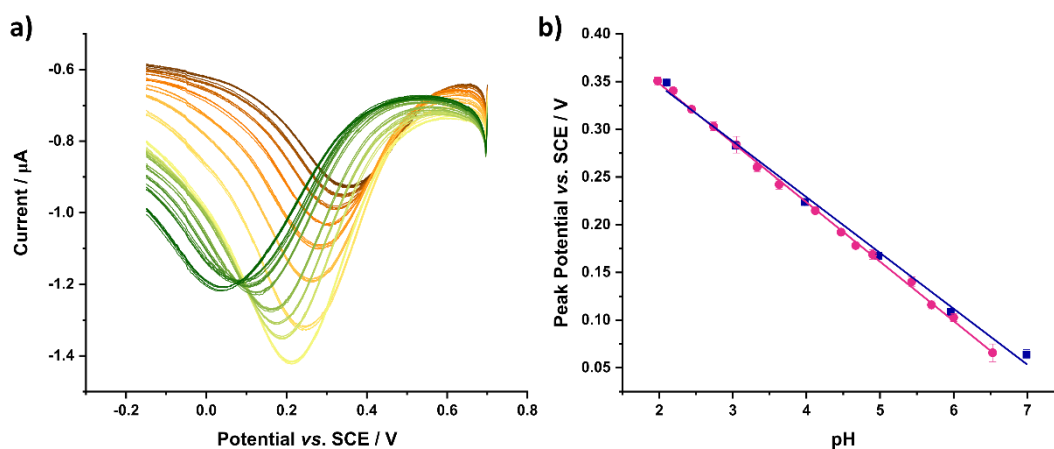


Figure 5.26 pH response of BDD-Q disc in ring disc electrode configuration in pH adjusted 0.1 M  $\text{KNO}_3$  between pH 2 and 7. Square wave voltammetry at 150 Hz, 0.1 V amplitude, 1 mV step between 0.7 and -0.15 V (a) pH adjusted with KOH and  $\text{H}_2\text{SO}_4$ . Peak potential plotted vs. pH (b) with calibration line from measurement in pH 2, 3, 4, 5, 6 and 7 Carmody buffers.

The same concept as that utilised in Chapter 3 was used for these pH detection studies. A range of positive currents were applied to the ring in 0.1 M  $\text{KNO}_3$  to assess the local pH shift due to proton generation from water oxidation, Figure 5.27. A shift in peak position to increasingly positive potentials is observed as the environment becomes more acidic with time. As observed in the unbuffered solutions in Chapter 3 the larger the current applied the lower the local pH environment over the disc, Figure 5.28. The minimum pH reached was pH 1.5 with +70  $\mu\text{A}$  applied to the ring.

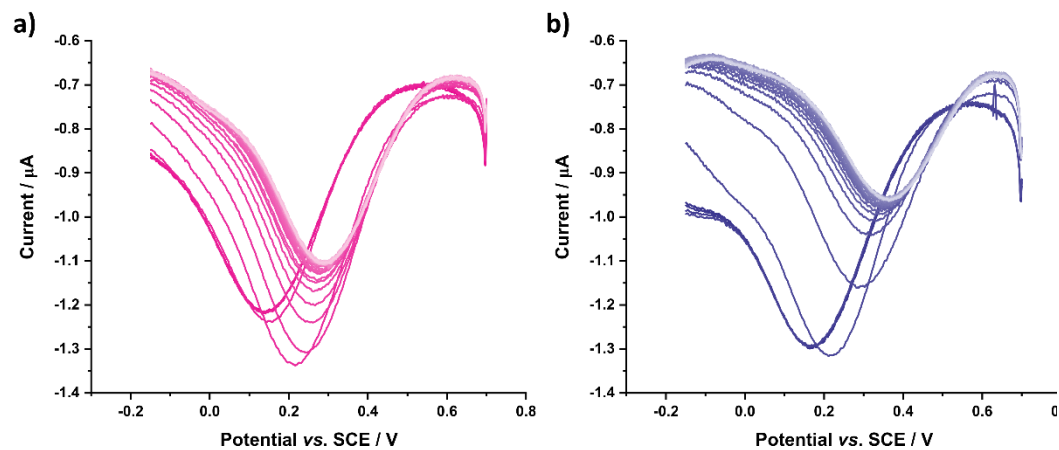


Figure 5.27 pH response of BDD-Q Disc in ring disc electrode configuration in 0.1 M  $\text{KNO}_3$  generating at 8  $\mu\text{A}$  (a) and 70  $\mu\text{A}$  (b) on the ring after 5 sweeps. Square wave voltammetry at 150 Hz, 0.1 V amplitude, 1 mV step between 0.7 and -0.15 V

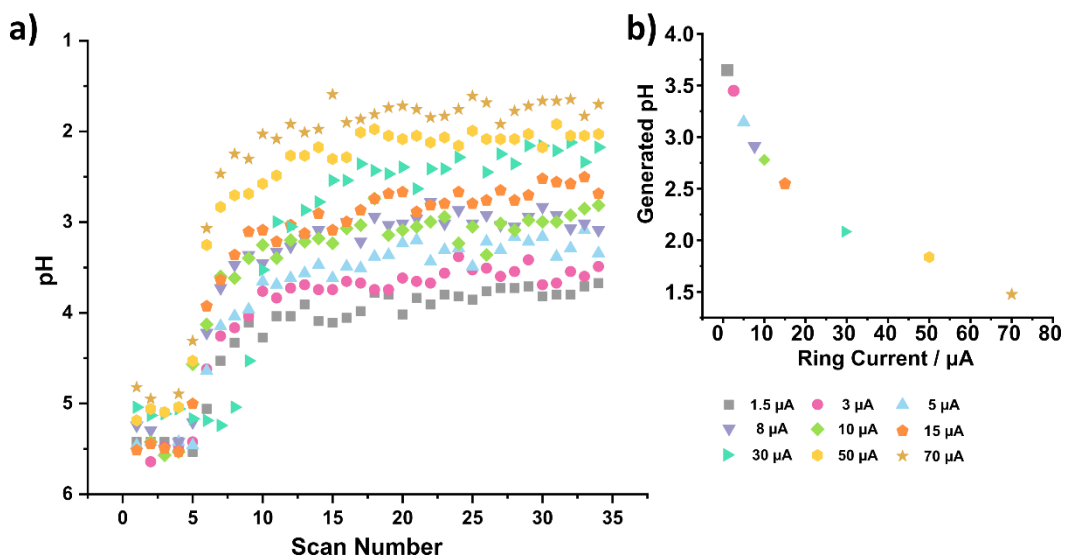


Figure 5.28 Shift in peak position on BDD-Q disc with scan number whilst generating on the ring at different currents (a) (starting at scan 5) and associated pH value from calibration line once plateaued (b).

## 5.4.9 Cu detection in locally acidic environment on BDD ring disc electrode

### 5.4.9.1 Effect of local pH decrease

Deposition was undertaken in 0.1 M  $\text{KNO}_3$  (pH 5.5) containing  $\text{Cu}^{2+}$  at different concentrations in the range 10 – 0.1 ppm. Deposition was undertaken on the BDD disc electrode in the ring disc configuration with no current applied to the ring (green) and +50  $\mu\text{A}$  applied to the ring (pink) to generate a local pH change to pH 1.8 (as measured using the BDD-Q ring disc electrode). The Cu deposition parameters employed were, -0.7 V (for 5 mins) due to the ring disc being slightly more resistive than the glass sealed electrodes employed for the original deposition investigations. To ensure all the Cu was removed from the surface, five stripping LSVs were run for each experiment, the first two are shown in Figure 5.29. No Cu stripping peaks were observed from deposition in the bulk solution (green lines, Figure 5.29). With an applied ring current, at 10 ppm  $\text{Cu}^{2+}$  a large peak at the expected potential for Cu metal stripping was observed.<sup>21</sup> However, at 1 ppm  $\text{Cu}^{2+}$ , despite using the same generating current, two peaks were observed, similar to the CV at pH 4.4, Figure 5.29b. A very small peak was observed in 0.1 ppm at the potential of the second peak at 1 ppm, Figure 5.29b. These two features again suggest the formation of Cu oxides despite the pH environment favouring deposition of Cu metal. However, as stated in section 5.4.8.1, water oxidation also results in local  $\text{O}_2$  production in addition to protons. Therefore, it is possible that a high flux of  $\text{O}_2$  accelerates conversion of Cu to Cu oxide materials, which is more pronounced the lower the concentration of Cu on the surface. Additionally, ORR electrocatalysed on the Cu deposits (to produce hydroxide ions) could also result in the formation of Cu oxide species.

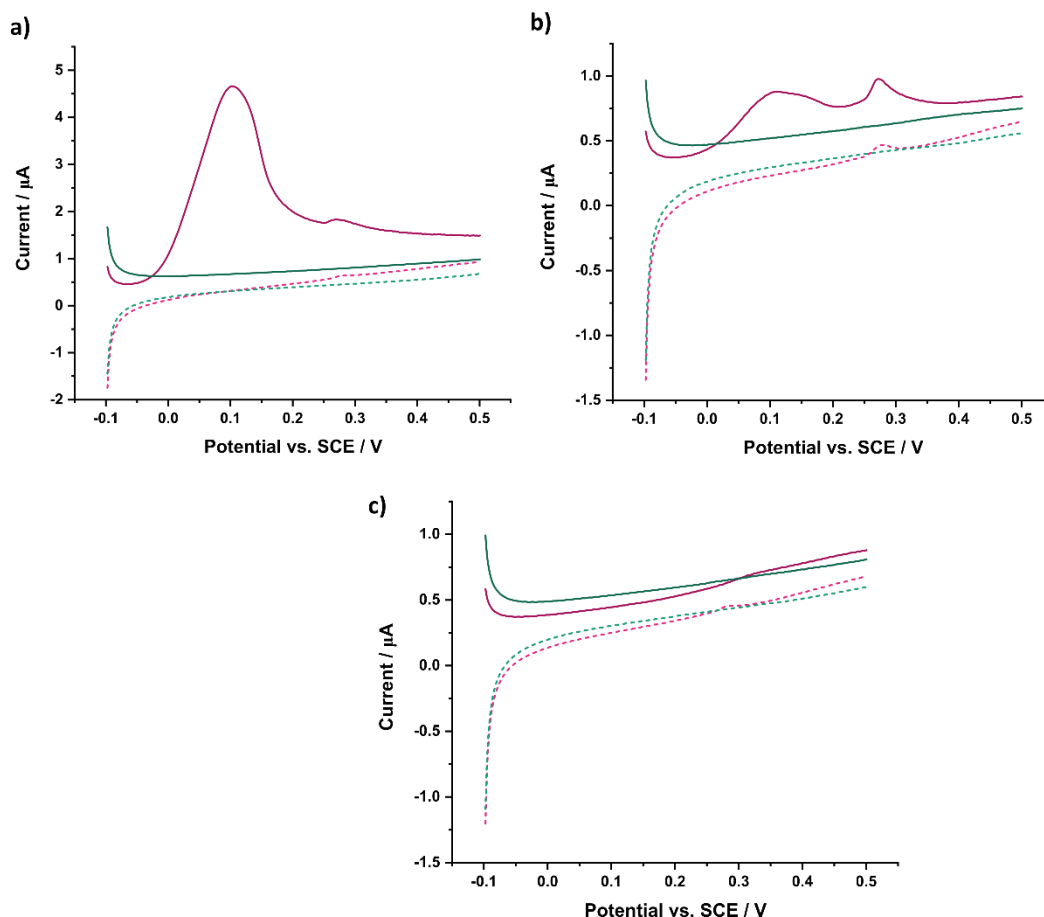


Figure 5.29 LSV of Cu in 0.1 M  $\text{KNO}_3$  (green) and when applying 50  $\mu\text{A}$  on ring (pink). At a) 10 ppm, b) 1 ppm and c) 0.1 ppm Sequential LSVs to ensure all deposits are removed, the first of which is shown for each condition (dashed line). Deposition -0.7 V for 5 mins, if generating, allowed to generate for 1 minute prior to deposition. All undertaken with a 0.1  $\text{V s}^{-1}$  scan rate.

#### 5.4.9.2 Effect of water oxidation on the local environment

To explore further whether the Cu related peak observed at around 0.3 V vs. SCE (e.g. Figure 5.29b) was a result of  $\text{O}_2$  generated on the ring, ASV was repeated in Cu solutions at 100, 500 and 1000 ppb concentrations under three conditions, Figure 5.30. The first was using an aerated acidic pH 2 solution (navy) and the other two conditions were aerated (green) and deoxygenated (pink) 0.1 M  $\text{KNO}_3$  solutions. For all three solutions 50  $\mu\text{A}$  was applied to the ring. For deoxygenation Ar was bubbled through the solution.

The bulk pH 2 solutions show a dominant peak in the region between 0.0 V and 0.1 V as expected for Cu stripping, Figure 5.30. At 100 ppb a shoulder is observed on this peak and a small peak is present at 0.3 V. In the 0.1 M  $\text{KNO}_3$  solutions with 50  $\mu\text{A}$  applied to the ring, regardless of whether the solution was aerated or

degassed the peak at  $\sim 0.3$  V is present, supporting the theory that water oxidation is producing an oxygen species that causes Cu oxide formation. Deoxygenating the solution does result in this peak being less dominant, especially in the 500 ppb case, Figure 5.30b, but it is still present. At higher concentrations the oxide peak is less dominant.

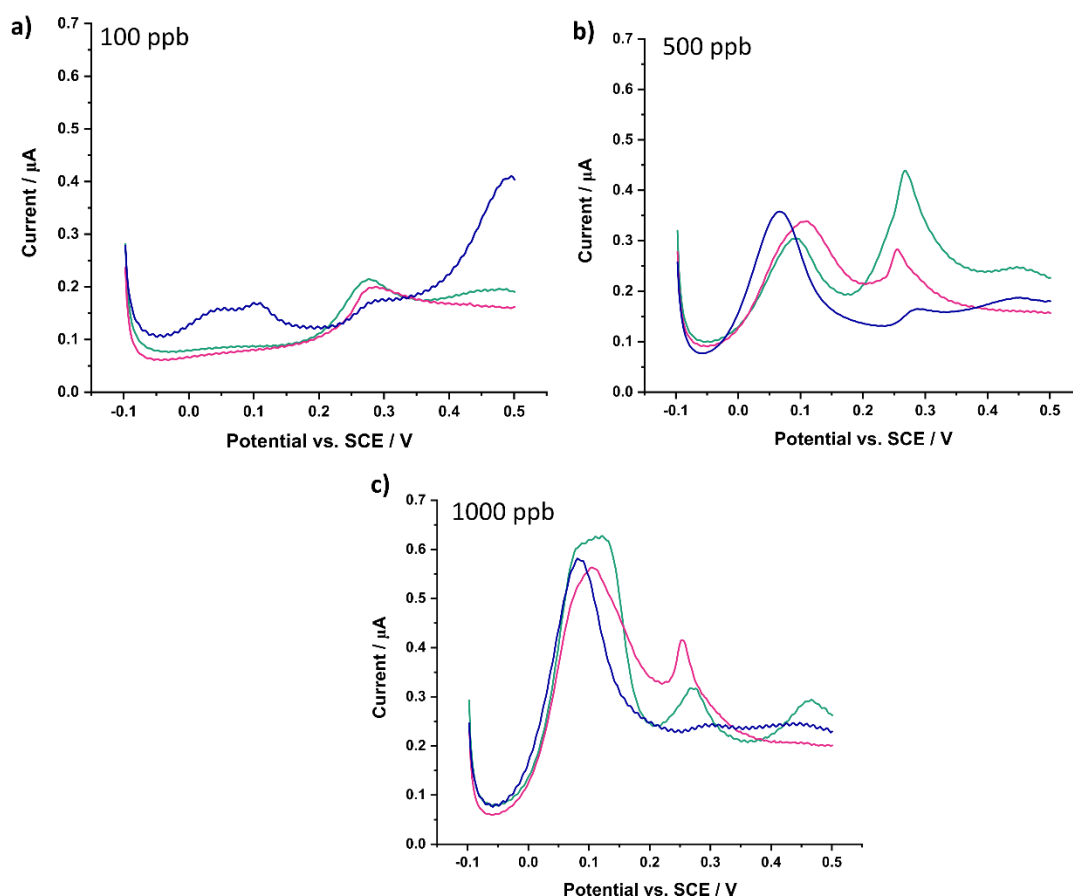


**Figure 5.30** LSV of 500 ppb Cu at bulk pH 2 (blue), and in 0.1 M  $\text{KNO}_3$  with 50  $\mu\text{A}$  applied to the ring in an aerated solution (green) and a deoxygenated solution (pink). Deposition -0.7 V for 5 mins, ring allowed to generate for 1 minute prior to deposition. All undertaken with a 0.1  $\text{V s}^{-1}$  scan rate.

The BDD-Q disc also presents the possibility of detecting the presence of oxygen voltammetrically as  $\text{sp}^2$  bonded carbon catalyses oxygen reduction compared to BDD.<sup>54</sup> Sequential LSVs on the BDD-Q electrode were recorded in aerated 0.1 M  $\text{KNO}_3$  sampling every 15 s for a period of 5 minutes whilst generating on the ring (50  $\mu\text{A}$ ), Figure 5.31. The dominant peak is that associated with HER. Using the Randles-Sevcik equation (Equation 5.1) as an approximation, and the measured pH value for  $\text{H}^+$  concentration = 0.01 M, the peak current of HER can be estimated, assuming  $A = 8.36 \times 10^{-3} \text{ cm}^2$ ,  $D = 9.3 \times 10^{-5} \text{ cm}^2 \text{ s}^{-1}$ ,<sup>55,56</sup>  $n = 1$  and at a scan rate of



$0.2 \text{ V s}^{-1}$ .  $i_p$  is estimated as  $97 \text{ } \mu\text{A}$  (at  $25^\circ\text{C}$ ), which is slightly lower than that seen experimentally,  $136 \text{ } \mu\text{A}$ . The aerated concentration of dissolved oxygen is approximately  $0.25 \text{ mM}$ ,<sup>57</sup> assuming  $n = 4$  and  $D = 2.1 \times 10^{-5} \text{ cm}^2 \text{ s}^{-1}$ ,<sup>58</sup> an approximate current for ORR is  $9 \text{ } \mu\text{A}$  (at  $25^\circ\text{C}$ ). Although in reality this value will be higher due to oxygen production at the ring. However, given the position of the HER peak, it is highly likely the ORR peak is enveloped by the HER peak.

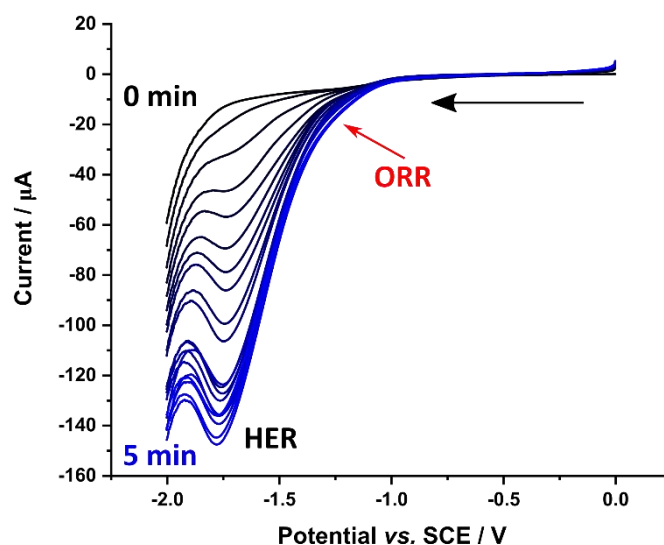


Figure 5.31 Sequential LSVs on BDD-Q disc (scan rate of  $0.2 \text{ V s}^{-1}$ ) in  $0.1 \text{ M KNO}_3$  with  $50 \text{ } \mu\text{A}$  applied to the ring for 5 minutes with an LSV recorded every 15 s. Undertaken at a  $0.1 \text{ V s}^{-1}$  scan rate.

This experiment was repeated for a range of ring currents,  $1.5, 3, 5, 8, 10, 15, 30, 50$  and  $70 \text{ } \mu\text{A}$ , Figure 5.32. As shown previously, the higher the applied current the lower the pH value produced. Also interesting for the highest current ( $70 \text{ } \mu\text{A}$ ), where the largest concentration of dissolved oxygen is expected the appearance of the ORR wave becomes more apparent.

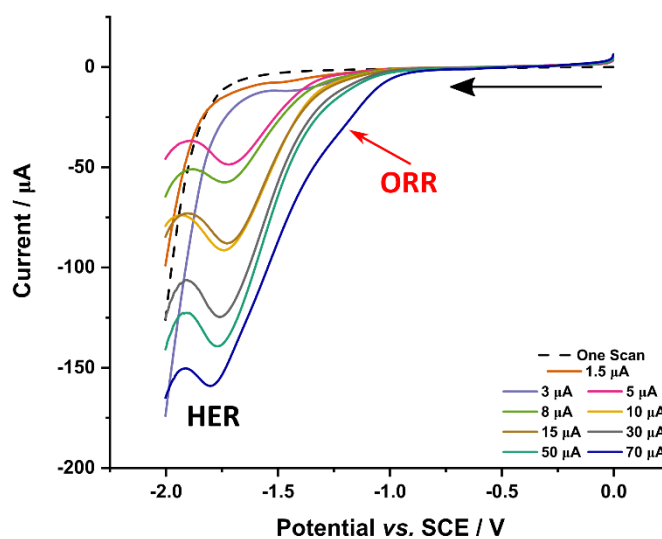


Figure 5.32 LSVs on BDD-Q disc (scan rate of  $0.2 \text{ V s}^{-1}$ ) in  $0.1 \text{ M KNO}_3$  with a number of currents applied to the ring electrode after 5 minutes. All undertaken with a  $0.1 \text{ V s}^{-1}$  scan rate.

However, as the ORR peak was difficult to resolve using LSV, due to the prevalence of the HER peak, the response was also investigated using SWV, Figure 5.33. The scan range was reduced to focus on the ORR region. ORR peak on BDD-Q has also previously been reported at a peak potential of  $-1.0 \text{ V}$ .<sup>54</sup> A clear ORR peak is observed at  $10 \mu\text{A}$ , Figure 5.33a, which increases in current with time. At  $30 \mu\text{A}$ , Figure 5.33b, an increase in the ORR peak is still seen and dominates the response at the end of the sampling time.

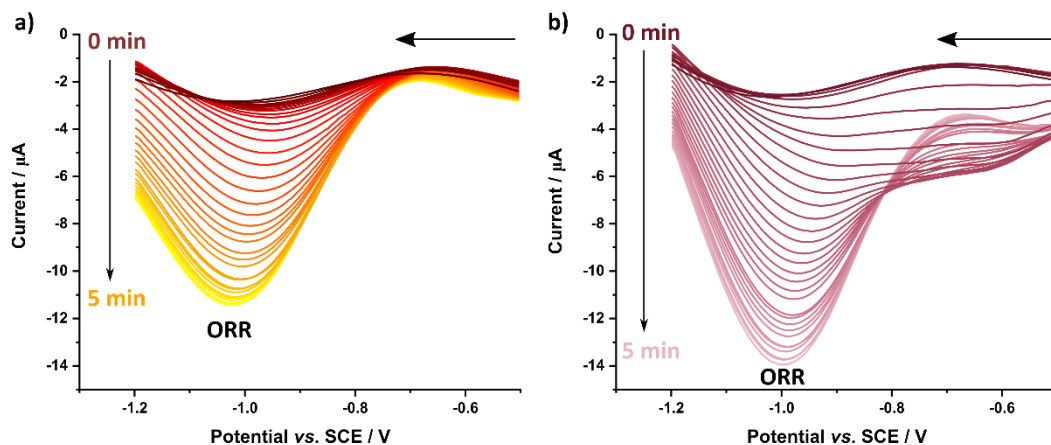


Figure 5.33 SWV on BDD-Q disc whilst generating at a) 10  $\mu\text{A}$  and b) 30  $\mu\text{A}$  for 70 seconds, sampling every 2 seconds. 150 Hz, 4 mV step, 1 mV amplitude.

#### 5.4.10 Effect of ring current on Cu ASV

Finally, it was considered whether a lower ring current than 50  $\mu\text{A}$  could minimise the concentration of dissolved oxygen in solution but still be acidic enough to encourage Cu deposition in the metallic form. Changing the current applied to the ring (70, 50, 30, 15, 5, 3  $\mu\text{A}$ ) changes the stripping response observed, Figure 5.34a. Two peaks were again observed at 50 and 70  $\mu\text{A}$  ring currents, the first associated with pure Cu stripping and the second with Cu oxides. The intensity of the second peak can be seen to decrease as the ring current is lowered (from 50  $\mu\text{A}$  to 30  $\mu\text{A}$ ), at currents below 30  $\mu\text{A}$  no second peak is observed but a higher background current is seen, Figure 5.34a.

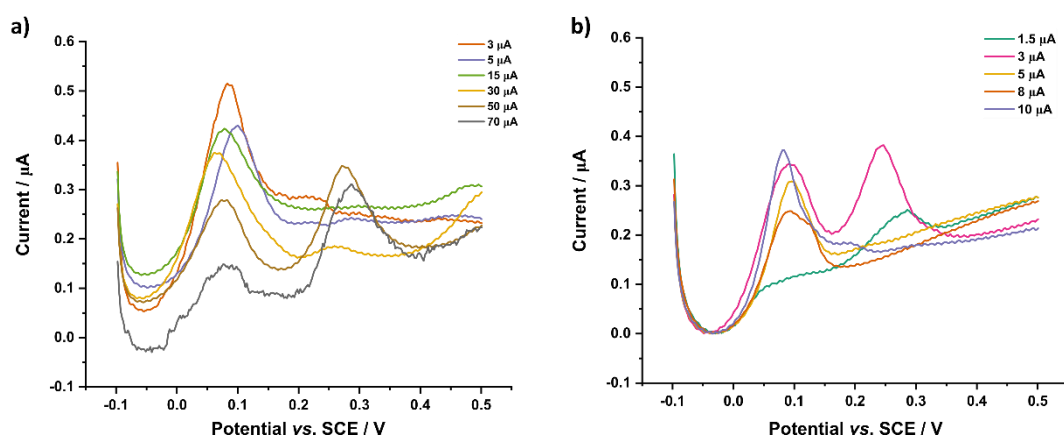


Figure 5.34 LSV of 500 ppb Cu deposited under different ring currents in aerated 0.1 M  $\text{KNO}_3$  solutions. Deposition at -0.7 V for 5 mins, ring allowed to generate for 1 minute prior to deposition. All undertaken with a 0.1  $\text{V s}^{-1}$  scan rate.

When 10, 8 and 5  $\mu\text{A}$  are considered, Figure 5.34b, Cu stripping peaks with minimal observance of the Cu oxide peak are produced. With a ring current of 3  $\mu\text{A}$ , producing a measured local pH of 3.6, two peaks are again observed, and at 1.5  $\mu\text{A}$  (local pH = 3.8) only the Cu oxide peak is present. As less oxygen should be present in the local environment at these currents than at the higher ring currents where no oxide peak is observed, the pH environment must not be acidic enough to promote Cu metal deposition at these ring currents.

Although varying the ring current shows some promise, as seen in Figure 5.21 the lower the concentration of Cu the more of an impact ORR has on the deposit. Therefore, although there is potential for this technique at higher concentrations the introduction of oxygen species through splitting water is still problematic at low concentrations.

## 5.5 Conclusions

Two different approaches were considered to solve some of the challenges of metal detection on solid electrodes. EC-XRF aimed to remove the challenge of electrodepositing the metal in the metallic form as XRF will detect Cu regardless of oxidation state. The new EC-XRF rotating disc electrode design was much more user friendly in terms of set up and removal of the BDD for subsequent XRF analysis. However, the limit of detection reported by Hutton et al., was not reached. The morphology of the deposit impacted the stability of the deposit on the surface during electrodeposition and transfer of the electrode for XRF analysis. This resulted in variability in the quantification at defined concentrations. A number of experimental conditions were tried with the aim of improving sensitivity and repeatability however none significantly improved the results. However, trialling the technique in natural waters showed the successful detection of Cu and Zn. EC-XRF could be a useful semi-quantitative technique to identify heavy metal contaminants relatively quickly in polluted waters.

Development of an at source ASV sensor for heavy metal detection was also considered. Detection of metals under locally acidified environments aims at encouraging deposition of metals into the metallic form. A locally acidic environment was successfully generated on a ring electrode through water oxidation with the pH change detected by a BDD-Q disc electrode which could be

used to acidify samples on site. Although this technique worked well at high concentrations (ppm) of  $\text{Cu}^{2+}$ , when the concentration was reduced to ppb concentrations, oxides were formed, which renders ASV ineffective. Water oxidation also produces oxygen species as well as protons which can also exacerbate metal oxide formation. An effort was made to voltammetrically detect the generated oxygen but the ORR peak became engulfed by the HER peak in LSV. SWV helped isolate the ORR response. The ring current was found to control both the acidity of the local environment and the oxygen concentration. Reducing the ring current aided deposition in the metallic form but oxides were still formed at ring currents  $> 10 \mu\text{A}$  due to the generated oxygen. At ring currents of  $1.5 \mu\text{A}$  and  $3 \mu\text{A}$  the pH environment was not acidic enough to promote Cu metal deposition. In future reducing the deposition time could aid the formation of metallic deposits but may impact the sensitivity of the technique.

## 5.6 References

- 1 P. B. Tchounwou, C. G. Yedjou, A. K. Patlolla and D. J. Sutton, 2012, **101**, 1–30.
- 2 H. S. Kim, Y. J. Kim and Y. R. Seo, *J. Cancer Prev.*, 2015, **20**, 232–240.
- 3 M. Olivares and R. Uauy, *Am. J. Clin. Nutr.*, 1996, **63**, 791S–796S.
- 4 J. Bertinato and M. R. L'Abbé, *J. Nutr. Biochem.*, 2004, **15**, 316–322.
- 5 A. Hordyjewska, Ł. Popiołek and J. Kocot, *BioMetals*, 2014, **27**, 611–621.
- 6 Council Directive 2008/105/EC on environmental quality standards in the field of water policy, *Off. J. Eur. Union*, 2008, **L348/84**, 84–97.
- 7 B. Wilson and F. B. Pyatt, *Ecotoxicol. Environ. Saf.*, 2007, **66**, 224–231.
- 8 A. Akcil and S. Koldas, *J. Clean. Prod.*, 2006, **14**, 1139–1145.
- 9 G. K. Kinuthia, V. Ngure, D. Beti, R. Lugalia, A. Wangila and L. Kamau, *Sci. Rep.*, 2020, **10**, 1–13.
- 10 M. Ghaderpoori, B. kamarehie, A. Jafari, A. Ghaderpoury and M. Karami, *Data Br.*, 2018, **16**, 685–692.
- 11 M. K. Tiwari, S. Bajpai, U. K. Dewangan and R. K. Tamrakar, *Karbala Int. J.*

- Mod. Sci.*, 2015, **1**, 9–14.
- 12 R. S. Pappas, *Spectroscopy*, 2012, **27**, 20–31.
- 13 E. Perkin, 2001, 1–8.
- 14 T. M. Florence, *Analyst*, 1986, **111**, 489-505 ST-Electrochemical Approaches to Trace-.
- 15 W. D. Ellis, *J. Chem. Educ.*, 1973, **50**, A131.
- 16 A. J. Borrill, N. E. Reily and J. V. Macpherson, *Analyst*, 2019, **144**, 6834–6849.
- 17 L. A. Hutton, G. D. O. Neil, T. L. Read, Z. J. Ayres, M. E. Newton, J. V. Macpherson, G. D. O’Neil, T. L. Read, G. D. O’Neil, Z. J. Ayres, M. E. Newton and J. V. Macpherson, *Anal. Chem.*, 2014, **86**, 4566–4572.
- 18 Z. J. Ayres, M. E. Newton and J. V. Macpherson, *Analyst*, 2016, **141**, 3349–3357.
- 19 G. D. O’Neil, M. E. Newton and J. V. Macpherson, *Anal. Chem.*, 2015, **87**, 4933–4940.
- 20 T. L. Read, E. Bitziou, M. B. Joseph and J. V. Macpherson, *Anal. Chem.*, 2014, **86**, 367–371.
- 21 T. L. Read, M. B. Joseph and J. V. Macpherson, *Chem. Commun.*, 2016, **52**, 1–4.
- 22 B. O’Sullivan, B. Patella, R. Daly, I. Seymour, C. Robinson, P. Lovera, J. Rohan, R. Inguanta and A. O’Riordan, *Electrochim. Acta*, 2021, **395**, 139113.
- 23 I. Seymour, B. O’Sullivan, P. Lovera, J. F. Rohan and A. O’Riordan, *Sensors Actuators, B Chem.*, 2020, **325**, 128774.
- 24 I. Seymour, B. O’Sullivan, P. Lovera, J. F. Rohan and A. O’Riordan, *ACS Sensors*, 2021, **6**, 1030–1038.
- 25 L. A. Wasiewska, I. Seymour, B. Patella, R. Inguanta, C. M. Burgess, G. Duffy and A. O’Riordan, *Sensors Actuators, B Chem.*, 2021, **333**, 129531.
- 26 W. R. Carmody, *J. Chem. Educ.*, 2009, **40**, A386.

- 27 K. Yamanaka, *Jpn. J. Appl. Phys.*, 1989, **28**, 632–637.
- 28 K. Yamanaka, *Jpn. J. Appl. Phys.*, 1991, **30**, 1285–1289.
- 29 R. S. Nicholson and I. Shain, *Anal. Chem.*, 1964, **36**, 706–723.
- 30 A. J. Bard and L. R. Faulkner, *Electrochemical Methods: Fundamentals and Applications*, Wiley, New York, 2nd Editio., 2001.
- 31 S. Kakooei, M. C. Ismail and B. Ari-wahjoedi, *Int. J. Mater. Sci. Innov.*, 2013, **1**, 62–72.
- 32 J. V. Macpherson, *Phys. Chem. Chem. Phys.*, 2015, **17**, 2935–2949.
- 33 L. A. Hutton, M. E. Newton, P. R. Unwin and J. V. Macpherson, *Anal. Chem.*, 2009, **81**, 1023–1032.
- 34 J. Mauzeroll, E. A. Hueske and A. J. Bard, *Anal. Chem.*, 2003, **75**, 3880–3889.
- 35 J. V. Macpherson, D. O’Hare, P. R. Unwin and C. P. Winlove, *Biophys. J.*, 1997, **73**, 2771–2781.
- 36 C. E. Banks, R. G. Compton, A. C. Fisher and I. E. Henley, *Phys. Chem. Chem. Phys.*, 2004, **6**, 3147–3152.
- 37 H. Olivia, B. V. Sarada, D. Shin, T. N. Rao and A. Fujishima, *Analyst*, 2002, **127**, 1572–1575.
- 38 Y. Wang, J. G. Limon-Petersen and R. G. Compton, *J. Electroanal. Chem.*, 2011, **652**, 13–17.
- 39 Y. Lu, X. Liang, C. Niyungeko, J. Zhou, J. Xu and G. Tian, *Talanta*, 2018, **178**, 324–338.
- 40 G. E. Batley and T. M. Florence, *Anal. Lett.*, 1976, **9**, 379–388.
- 41 J. Wang, *Electroanalysis*, 2005, **17**, 1341–1346.
- 42 L. A. Hutton, G. D. O’Neil, T. L. Read, Z. J. Ayres, M. E. Newton and J. V. Macpherson, *Anal. Chem.*, 2014, **86**, 4566–4572.
- 43 N. Fredj and T. D. Burleigh, *J. Electrochem. Soc.*, 2011, **158**, C104.
- 44 E. Prats-Alfonso, L. Abad, N. Casañ-Pastor, J. Gonzalo-Ruiz and E. Baldrich, *Biosens. Bioelectron.*, 2013, **39**, 163–169.

- 45 O. A. Farghaly and M. A. Ghandour, *Environ. Res.*, 2005, **97**, 229–235.
- 46 G. K. Rollinson, D. Pirrie, M. R. Power, A. Cundy and G. S. Camm, *Geosci. South-West Engl.*, 2007, **11**, 326–337.
- 47 D. Pirrie, G. K. Rollinson and M. R. Power, *Geosci. South-West Engl.*, 2009, **12**, 162–170.
- 48 L. Pinto and S. G. Lemos, *Electroanalysis*, 2014, **26**, 299–305.
- 49 M. B. Gumpu, S. Sethuraman, U. M. Krishnan and J. B. B. Rayappan, *Sensors Actuators, B Chem.*, 2015, **213**, 515–533.
- 50 E. Marguá, B. Zawisza and R. Sitko, *TrAC - Trends Anal. Chem.*, 2014, **53**, 73–83.
- 51 C. J. M. Kramer, Y. Guo-hui and J. C. Duinker, *Fresenius' Zeitschrift für Anal. Chemie*, 1984, **317**, 383–384.
- 52 J. Li, C. L. Bentley, S. Y. Tan, V. S. S. Mosali, M. A. Rahman, S. J. Cobb, S. X. Guo, J. V. Macpherson, P. R. Unwin, A. M. Bond and J. Zhang, *J. Phys. Chem. C*, 2019, **123**, 17397–17406.
- 53 S. J. Cobb, Z. J. Ayres, M. E. Newton and J. V. Macpherson, *J. Am. Chem. Soc.*, 2019, **141**, 1035–1044.
- 54 T. L. Read, S. J. Cobb and J. V. Macpherson, *ACS Sensors*, 2019, **4**, 756–763.
- 55 N. Agmon, *Chem. Phys. Lett.*, 1995, **50**, 456–462.
- 56 N. Amdursky, Y. Lin, N. Aho and G. Groenhof, *Proc. Natl. Acad. Sci. U. S. A.*, 2019, **116**, 2443–2451.
- 57 E. S. Smotkin, F. T. Moy and W. Z. Plachy, *BBA - Biomembr.*, 1991, **1061**, 33–38.
- 58 E. L. Cussler, *Diffusion: Mass Transfer in Fluid Systems*, Cambridge University Press, Third Edit., 2009.



## 6 Low Potential Biofilm Control

---

### 6.1 Overview

Biofouling in water environments is a significant problem for a number of industries, from fish and shellfish farms to shipping and healthcare. The impacts of biofouling can result in significant financial losses for businesses and potentially serious health implications for individuals with infections. Biofilms are a beneficial life form for bacteria due to the protection provided by the extracellular polymeric substance (EPS) and symbiotic behaviours with other cells. For electrochemical sensors, biofilm formation on the sensor surface will impact sensor performance, as the detector signal is dependent on the electrode cleanliness, resulting in decreased sensitivity and calibration shifts. This is one of the biggest barriers to long term *in-situ* electrochemical sensing.

An early stage of the biofilm formation process is adhesion of individual bacterial cells to the electrode surface. The majority of bacterial cells have a net negative surface charge on their cell membrane. Although bacteria can overcome forces to interact with surfaces, electrostatic repulsion can make the initial attachment step more challenging. Boron doped diamond (BDD) has been shown to be a low biofouling electrode material. This chapter considers whether the lifetime of a BDD electrochemical sensor placed in an aqueous system could be extended through the application of small voltages to repel bacterial cells, in this case *Pseudomonas aeruginosa*, from the surface. *P. aeruginosa* was used as a monospecies biofilm culture as it is a moderate to strong biofilm former and has previously been extensively characterised. A novel experimental set-up was designed and fabricated to investigate the role electrode potential can play in slowing down biofilm formation on BDD electrodes.

## 6.2 Introduction

### 6.2.1 Biofouling

Biofouling is a huge challenge in medical, environmental and industrial fields. Contamination on medical devices can cause infection from pathogenic microorganisms and ultimately rejection or malfunction of a medical device.<sup>1,2</sup> Biofilm induced infections are significantly harder for the host immune system to attack, and to treat medically, so often result in chronic infections.<sup>3-5</sup> Biofouling in water systems can aid the transmission of bacterial pathogens, leading to persistent and life-threatening infections.<sup>6-8</sup> Biofouling induced problems are also widespread in the shipping industry leading to increased fuel consumption, engine stress, reduced speed, corrosion and environmental concerns through introduction of alien species.<sup>9-11</sup> Industrial biofouling can affect a wide range of industries from food production and water utilities to nuclear power plants and membrane systems.<sup>11-20</sup>

Hence there has been significant investment in research to mitigate the formation and effects of biofouling. The use of biocides, although common, is not always effective as biofilms are typically more resistant to biocides and antimicrobials than planktonic cells.<sup>21,22</sup> For some applications merely inactivating the microorganisms is not sufficient as 'dead' biofilms can act as a source of endotoxins, encourage recolonization, provide shelter for pathogens and impact surface sensitive reactions.<sup>23</sup> Surface modifications have been suggested to combat biofouling. These range from surface coatings and antibacterial adhesion agents, to incorporation of silver or copper nanoparticles, engineered nanostructures and antimicrobial agents including quorum quenchers.<sup>24-33</sup> However, for some applications, such as sensors, where the surface has already been tailored to optimise detection sensitivity, surface modification is not a viable option.

### 6.2.2 Electrochemical control of bacteria and biofilms

For electrochemical based sensors it is useful to consider how electrochemical conditions (e.g. applied voltage/current) can be used to manipulate and ultimately retard biofilm growth. There are two main mechanisms of electrochemical biofilm control (1) delaying adhesion of cells and (2) removal of

mature biofilms.<sup>34</sup> This chapter considers the delaying of adhesion, however, a brief mention of some techniques used to remove mature biofilms is also given.

At near neutral pH, as expected in the majority of environmental and physiological settings, bacterial cells generally have a net negative surface.<sup>35</sup> Cell structures are grouped in two main groups, Gram negative and Gram positive corresponding to the response from a Gram staining procedure.<sup>36</sup> During a Gram stain cells are stained using crystal violet dye where the interactions described in Section 1.6.3.3 occur. After staining an iodine solution is added which forms a complex with the crystal violet dye resulting in a larger molecule which is insoluble in water. Ethanol or acetone is added which interacts with the membrane lipids of both Gram negative and Gram positive bacteria. Gram positive cells have no outer membrane but several layers of peptidoglycan external to a plasma membrane.<sup>37</sup> When ethanol or acetone is added the thick, cross-linked peptidoglycan dehydrates and constricts trapping the large crystal violet-iodine complexed stain, hence these are known as gram positive cells.<sup>36</sup> Teichoic acids link the peptidoglycan layers to the plasma membrane. The teichoic acids contain negatively charged phosphoryl groups resulting in a negative surface charge.<sup>38,39</sup>

Gram negative bacteria contain a single layer of the peptidoglycan cell wall between an outer and inner membrane, during the dehydration process the outer membrane is degraded and becomes 'leaky' allowing the crystal violet-iodine complex to be removed from the cell during subsequent washing steps.<sup>36,37</sup> The outer membrane is composed of phospholipids with lipopolysaccharide groups on the outer membrane surface. These are in contact with the aqueous environment, the phosphate groups in the lipopolysaccharides cause a negative electrostatic surface charge.<sup>38,40</sup> Cell surface charge is often determined using zeta-potential measurements, calculated from cell mobility under the influence of an electrical field.<sup>38</sup> The zeta potential of bacteria is typically in the range of 1's-10's of mV but is species variable and influenced by media conditions *e.g.* salt concentration and pH.<sup>38,41</sup> All surfaces in solutions have a charge associated due to ion adsorption. Therefore, electrostatic attraction or repulsion between cells and surfaces can occur.

#### 6.2.2.1 Previous electrochemical studies on prevention of cell attachment

One significant experiment investigated *Pseudomonas fluorescens* bacteria attachment in an electrochemical flow cell on a gold coated glass slide over 15 minutes. The open circuit potential (OCP) was  $\sim 0.2$  V vs. Ag|AgCl in aerated 0.01 M NaCl, which is more positive than the point of zero charge (PZC) on gold in the same solution (0.00 – 0.07 V vs. Ag|AgCl-KCl-sat). Under these conditions, spontaneous irreversible attachment of cells was observed by image capture from phase-contrast microscopy at 30 s intervals. Attached cells were identifiable as black dots, out of focus cells were not counted as these were not adhered to the surface. When potentials of -0.2 V and -0.5 V vs. Ag|AgCl were applied, inhibition of bacterial adhesion by  $\sim 80\%$  and  $\sim 90\%$  was observed, respectively compared to that observed at OCP. The inhibition of attachment at negative potentials was attributed to electrostatic repulsion between the electrode surface, which was more negative than the PZC, and the negatively charged bacterial cells.<sup>42</sup>

A comparison was made in a solution with increased ionic strength, 0.1 M NaCl. At the OCP fewer cells adhered than were observed in the 0.01 M solution. However, at -0.2 V vs. Ag|AgCl, cell adhesion was higher than in the 0.01 M NaCl solution, whilst at -0.5 V vs. Ag|AgCl, adhesion was still minimal. Both effects were attributed to the more effective screening of surface charge by the higher ionic strength solution. Screening of the positive potential OCP ( $\sim 0.2$  V) in the 0.1 M solution led to a reduction in the electrostatic attraction between the positive surface and the negatively charged cells. Whilst more effective screening of the negative electrode potential led to greater cell adhesion at -0.2 V vs. Ag|AgCl in 0.1 M NaCl than in 0.01 M NaCl. The negative charge at the surface at -0.5 V vs. Ag|AgCl was assumed to be great enough that double layer effects were negligible and repulsion between the surface and cells dominated irrespective of the ionic strength.<sup>42</sup>

The response of fluorescence tagged *Pseudomonas aeruginosa* on indium tin oxide electrodes to negative, positive and alternating currents has also been investigated.<sup>43</sup> The electrodes were exposed to the bacterial culture for 90 mins at a flow rate of  $1.3 \text{ ml min}^{-1}$ . The density of adhered bacterial cells was

determined by counting adhered cells on five micrographs for each condition and expressed as a percentage compared to the number of adhered bacteria with no current applied *i.e.* where 100 % is for the no current applied surface. Adhesion was lowest (at 19%) when negative currents in the range -7.5 to -15  $\mu\text{A cm}^{-2}$  were applied. This reduced adhesion was attributed to the repulsion of negatively charged cells from the surface.

At the positive applied currents, +7.5 to +15  $\mu\text{A cm}^{-2}$  cellular adhesion was 70 – 80 % compared to the number of cells adhered when no current was applied. Time lapse recordings of the positively charged electrode showed adhesion of bacteria to the surface but the bacteria were later removed and swept away by the current flow. When the positive current was switched off an influx of cells was observed to adhere to the surface which may have skewed the results. Alternating the current at  $\pm 15 \mu\text{A cm}^{-2}$  over one minute cycles throughout the 90 minutes resulted in low adhesion at 27%, only slightly higher than the values obtained at the negative applied currents. This was attributed to the prevention of adhesion from the negative charge. Live/dead staining was used to determine the condition of the adhered cells. With no applied current, nearly all the cells were live. Under the alternating current ~58% of the adhered cells were dead, whereas at positive or negative currents  $\leq 4\%$  of the adhered cells were dead. The positive current during the alternating current scenario is thought to inactivate the adhered bacteria.<sup>43,44</sup>

An alternative method proposed to prevent cell adhesion is to create superhydrophobic/hydrophobic surfaces by entrapment of gases in pores on a surface. The dry environment of the bubble prevents attachment and retards bacterial growth.<sup>45</sup> Hydrogen gas was formed through the hydrogen evolution reaction on stainless steel at -3 V. *Escherichia coli* adhesion was reduced by 99.5% over 16 hours growth time compared to a control with no bubble formation.<sup>45</sup> When hydrogen was generated post cellular adhesion, live dead staining showed the adhered bacteria were now dead, in contrast to the no potential applied control sample, where the majority were still alive.<sup>45</sup> The authors attribute this to the hydrogen bubbles engulfing the adhered cells and producing dry voids between the electrode surface and the solution due to the

low solubility of water in hydrogen.<sup>45</sup> Bacterial cells require a liquid for metabolic activities across the membrane. However, for this to be a practical solution to biofouling on electrodes the gas bubbles would need to be removed prior to sensing experiments as they would also hinder electrochemical reactions.

#### 6.2.2.2 Previous electrochemical studies on prevention of biofilm formation

The effect of potential on biofilm formation with *P. fluorescens* was considered on gold coated glass slides in an electrochemical flow cell for 8 hours by the same group mentioned first in Section 6.2.2.1.<sup>46</sup> When positive potentials were applied (+0.5 V vs. Ag|AgCl) a 30 - 40 minute lag prior to exponential growth was observed compared to growth at +0.1 and -0.2 V vs. Ag|AgCl. No growth was observed at +0.8 V vs. Ag|AgCl. The cells at +0.5 V vs. Ag|AgCl were consistently smaller and showed an increased doubling time (time taken for the number of cells to double) than those at -0.2 V suggesting inhibition of metabolic pathways at a positive potential.<sup>46</sup> Analysis of the biofilm structure at -0.2 and +0.5 V vs. Ag|AgCl at 3 and 8 hours was also undertaken by taking sequential micrographs, increasing the focal plane by 4.5  $\mu\text{m}$  for each image starting at the electrode surface. Patchy biofilms of 13  $\mu\text{m}$  thickness were observed at both potentials after 3 hours. At -0.2 V vs. Ag|AgCl there was an irregular distribution of diffuse microcolonies comprised of long cells, whilst at +0.5 V vs. Ag|AgCl small microcolonies containing small cells were observed. By 8 hours the diffuse microcolonies observed at -0.2 V vs. Ag|AgCl were  $24 \pm 2 \mu\text{m}$  thick in mushroom shaped biofilm. This was thought to occur due to the electrostatic repulsion between the surface and the cells forming open colonies with weak surface associations.

At +0.5 V vs. Ag|AgCl the highest cell density was at the surface with a pyramidal microcolony formation reaching a maximum thickness of 18  $\mu\text{m}$ . The electrostatic attraction between the positive surface and the negative cells retain daughter cells at the surface, hence the highest cell density is at the surface. Although these two studies present useful results, due to the nature of the microscopy analysis, no biological repeats are present, and no mention is made on repeatability. The analysis is entirely dependent on image analysis. The second study, although running for longer timescales still only probes the

microcolony stage of biofilm formation and doesn't achieve mature biofilm formation so only considers the start of the biofouling process.

Pulsed potential techniques have also been used to control biofilm formation. Parallel, interdigitated titanium electrodes were used to consider the effect of localised high strength electric fields on prevention of *P. aeruginosa* biofilm formation.<sup>47</sup> Electrodes were exposed to a stirred solution of bacteria containing media for 6 days and analysed using fluorescent live-dead stains. The images were analysed to determine coverage and compared to electrodes with no applied potentials. High voltage pulses ( $\pm 2.5$  V) were shown to prevent biofilm formation at both a 200 Hz and 10 000 Hz frequency with short pulses at a 1% duty ratio (percentage of pulsing time over one cycle). At a 50% duty ratio at  $\pm 5$  V, with longer pulses, biofilm formation was not prevented for either frequency. When low voltage pulses ( $\pm 250$  mV) were applied frequencies of 200 Hz resulted in reduced biofilm production but at 10 000 Hz, biofilm formation was enhanced.<sup>47</sup> In general a greater coverage of cells across the surface of the electrode contained fewer live cells indicating that the pulsed conditions not only affected the total number of cells but also the viability of the cells that were adhered.<sup>47</sup> No discussion was made on the effect of using interdigitated electrodes. The change in the biofilm response was attributed to electrostatic interactions, electric currents and ionic displacements, with very little explanation beyond this.<sup>47</sup>

Electrochemical generation of biocides has also shown to be effective at retarding biofilm growth, termed the bactericidal effect. For example, with the right electrode material, reactive oxygen species (ROS) such as hydrogen peroxide ( $H_2O_2$ ) can be generated when oxygen is present, which can delay bacterial attachment and inhibit growth on the electrode.<sup>48</sup> A study applying -600 mV vs. Ag|AgCl to a stainless steel electrode for 40 hours in the presence of *P. aeruginosa* in a continuously air saturated medium showed minimal biofilm growth compared to significant biofilm growth on the same material without a potential applied. This was attributed to the electrochemical production of  $H_2O_2$  at the electrode surface.<sup>48</sup> Scanning electron microscopy images of the surface showed cell debris on the polarised electrode indicating the potential and/or the

presence of H<sub>2</sub>O<sub>2</sub> caused damage to the cells.<sup>48</sup> At sufficiently high overpotentials in chlorine containing media, Cl<sub>2</sub> or reactive chlorine compounds such as hypochlorous acid can also be formed; hypochlorous acid is a strong disinfectant and therefore kills the cells present, even in a mature biofilm.<sup>34,49</sup>

#### 6.2.2.3 The bioelectric effect

The final electrochemical technique worthy of mentioning is the bioelectric effect which combines the application of external antimicrobials (*i.e.* aminoglycosides, quinolones, tetracycline, erythromycin, daptomycin, moxifloxacin or polymyxin B) with an electric current or field to aid in the prevention or removal of biofilms. Combination with a current (or field) means antimicrobial concentrations more similar to those used for planktonic bacteria can be used, rather than excessive doses typically used on biofilms.<sup>50</sup> Several mechanisms have been proposed to explain the increased efficacy of antimicrobials in the presence of an electric current including: (i) disruption of the EPS matrix to allow antimicrobials to penetrate into the biofilm, (ii) increased membrane permeability, (iii) increased bacterial growth due to electrolytic generation of oxygen (and subsequently enhanced susceptibility to antimicrobials *i.e.* aminoglycosides that attack growth mechanisms of cells), (iv) electrochemical generation of potentiating oxidants.<sup>51</sup> However, it is important to note the bioelectric effect has only been found to occur with certain antimicrobials.<sup>52</sup>

#### 6.2.2.4 Project Aims and Objectives

The above studies employed gold, indium oxide, titanium and stainless steel electrode materials. Boron doped diamond (BDD), not only has interesting electrical properties but has been shown to be a low biofouling material compared to other common electrode and packaging materials.<sup>53-55</sup> For example, attachment of *P. aeruginosa* was found to be reduced on polished, oxygen terminated, hydrophilic BDD surfaces compared to hydrophobic or roughened BDD surfaces.<sup>54</sup> BDD, as discussed in Chapter 1, is finding considerable use as an electrochemical sensor material,<sup>56-61</sup> also evidenced by the data in Chapters 3, 4 and 5. The material properties lend BDD to use as a long term *in-situ* sensor in aqueous environments.



Whilst degradation of the material properties of the BDD during long term use in water systems is not a concern, the main issue is build-up of biofilm on the electrode surface. The aim of this chapter is thus to investigate extending the functional lifetime of BDD electrochemical based sensors by exploring the effect of electrode potential on cellular attachment and biofilm formation on the electrode surface. BDD provides an interesting material for these studies as compared to the electrodes mentioned in the studies discussed, BDD has a wide non-faradaic potential window providing the opportunity to probe larger windows without the complication of faradic products (e.g.  $H^+/OH^-$ ) potentially affecting cellular adhesion. *P. aeruginosa* is used for the study as it is prevalent in locations with human influence, it is a strong biofilm producer and has been commonly utilised for biofilm studies.<sup>62-64</sup>

## 6.3 Experimental

### 6.3.1 3D printing

Several 3D printed materials were considered for the project. Test wells were designed in blocks of 10.0 mm x 42.5 mm x 13.0 mm, containing five wells of 6.5 mm diameter and 11.0 mm depth using computer aided design (CAD; Fusion 360, Autodesk, USA), Figure 6.1. The wells were printed with 2.85 mm diameter filaments of at layer heights of 0.10, 0.18 and 0.25 mm in polyethylene terephthalate (PET; EPR InnoPET, Innofil3D, Netherlands), polylactic acid (PLA; rPLA, Filamentive, UK) and high impact polystyrene (HIPS; Filamentive, UK) on a fused deposition modelling (FDM) 3D printer (Taz6, Lulzbot, USA) and in a clear polymethylmethacrylate (PMMA) resin (FormLabs Standard Clear, FormLabs, USA) and a high temp PMMA resin (FormLabs High Temp Resin, FormLabs, USA) on a Form 3 stereolithography (SLA) printer at 50  $\mu$ m layer resolution (Formlabs, USA). These prints were used to test the response of the materials to sterilisation by autoclaving and verification of the materials using a crystal violet assay (CVA), *vide infra*.

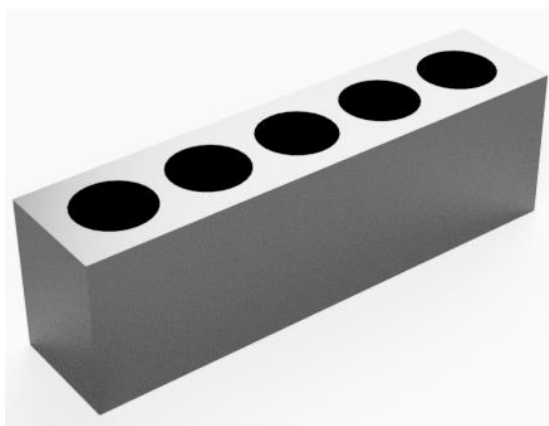


Figure 6.1 CAD model of 3D printed test wells

The final set-up was printed using the high temp resin on the Form 3 SLA printer with a 50  $\mu\text{m}$  layer height. After printing, the parts were washed in isopropanol (IPA; Analytical Grade, Fisher Chemicals, UK) for 6 minutes to remove excess resin (Form Wash, FormLabs, USA), an additional UV cure was undertaken at 80°C for 120 mins (Form Cure, FormLabs, USA). The support material was then removed manually, and polished to ensure a smooth finish. To enhance further the thermal stability of the 3D print a thermal cure was also undertaken in a lab oven at 160°C for 3 h. An ethylene polypropylene rubber sheet (1.5 mm thick, RS Components, Corby, UK) was used as a gasket material, gaskets were cut with a 10.0 mm outer diameter and a 5.0 mm inner diameter (Cricut Maker, Utah, USA).

### 6.3.2 BDD electrode fabrication

The BDD electrode was manufactured from electrochemical processing grade BDD from Element Six Ltd (polycrystalline and freestanding; Harwell, UK), polished on both the nucleation face and the growth face to nm roughness. Two geometries were used, *vide infra*, 4 mm rounds and rectangular pieces 5 mm x 10 mm. The desired geometries were cut using a laser micromachining system (E-355H-3-ATHI-O, Oxford Lasers, Didcot, UK), the top 1 mm of both geometries was laser roughened using a 532 nm Nd:YAG laser micromachining system (A-Series, Oxford Lasers Ltd. UK) with a nominal pulse length of 15 ns and a fluence of  $\sim 20$  J  $\text{cm}^{-2}$ . The BDD samples were subjected to the hot acid cleaning procedure as outlined in Section 2.3.1.1. The BDD samples did not undergo a 600°C thermal anneal step as this results in increased surface roughness due to etching at the grain boundaries.<sup>65</sup> A Ti/Au ohmic contact was sputtered (Moorfields MiniLab

060 platform sputter/evaporator) onto the electrodes as outlined in Section 2.3.1.3. A Hirshmann measurement crocodile clip (RS Components, UK) was soldered to a length of copper wire (0.8 mm diameter, RS Components, UK). The spring on the clip was sealed using nail varnish to prevent rusting. For measurements the edge of the clip was aligned with the edge of the sputtered contact on the BDD.

### **6.3.3 3D printed experimental set-up**

Prior to each experimental set up the 3D printed cell and clips were sterilised by autoclave (121°C for 15 mins; VARIO 2228, Dixons, UK) with each component wrapped in aluminium foil (Lakeland, UK). The BDD samples, Pt gauze, and gaskets were sterilised by soaking in 70% ethanol (Fisher Chemicals, UK) for a minimum of 3 hours. A Nafion-212 membrane (Alfa Aersar, USA) was cut to size using sterile scissors and sterilised under ultraviolet light for 10 minutes. The membrane was removed from the support material and soaked in sterile water for 1 hour. Using aseptic techniques in a microbiology safety cabinet (MSC) the set-up was assembled. Initially the wells and lids were prepared. The gaskets were rinsed in sterile water to dilute excess ethanol, then placed into the indents of the outer and central wells. The soaked Nafion membrane was placed onto the gaskets on the central well, the outer wells were aligned and then clamped together using a jubilee clip (JCS HI-GRIP 60 -80 mm, RS Components, UK). The wire of the clip was placed through the hole into the lids. The sterile BDD samples were clipped in place. The BDD was aligned parallel to the gaskets and membrane and secured in place with silicon tubing (0.8 mm, RS components, UK). Luria-Bertani (LB) broth (10 g/L tryptone, 5 g/L yeast extract, 10 g/L NaCl) was added to the wells, 14 ml in the central well and 1 ml in each of the outer wells. The set-up was placed into a sealed container, removed from the MSC and incubated overnight at 37°C. The optical density of LB in each well was measured the next day using a Jenway spectrophotometer (Cole-Palmer, Staffordshire, UK) to ensure sterility.

### **6.3.4 Bacterial strain, media and growth conditions**

*P. aeruginosa* was used in the biofilm studies. The PA01 strain was used as a monospecies biofilm producer. PA01 originated from Australia, isolated from a

clinical; non-respiratory infection.<sup>64</sup> PA01 has been widely used for biofilm formation studies and is well characterised both by phenotype and genotype.<sup>66-68</sup> PA01 was stored as a frozen stock (-20°C freezer) in LB broth with 20% glycerol until use.

Prior to each experiment PA01 was transferred from the frozen glycerol stock to LB agar plates and incubated aerobically at 37°C for 18 – 24 h. The strain was subcultured to LB broth and incubated at 37°C at 120 rpm for 5 h. The optical density was monitored at 600 nm ( $OD_{600}$ ) using a Jenway spectrophotometer to ensure the culture had reached the mid-exponential growth phase ( $OD > 0.2$ , corresponding to approximately  $10^8$  cells  $ml^{-1}$ ). From the culture a bacterial inoculum corresponding to approximately  $2 \times 10^7$  cells  $ml^{-1}$  was prepared, of which 1 ml was added to each of the outer wells of the 3D printed experimental set-up.

### **6.3.5 Experimental set up with potential applied.**

Once sterility of the set-up had been confirmed, and the inoculum prepared, the 3D printed set-up was placed into the MSC, a reference electrode (SCE; CHI150, CH Instruments Inc, USA) and Pt gauze counter electrode were added to the central well containing LB broth. A RTD thermometer (Omega, UK) was also placed into the central well to monitor the solution temperature throughout the experiment. The PA01 inoculum (approximately  $2 \times 10^7$  cells in 1 ml) was added to each outer well and the BDD electrodes dipped into it as the lids were replaced. The Ivium WE32 (Alvatek, USA) cables were connected to the wire soldered to the clip and a potential was applied to the BDD samples using the connected Ivium Compactstat (Alvatek, USA). A laptop was used to record electrochemical data every 2 minutes through Iviumsoft and temperature data every 5 minutes for 70-72 h. The set up remained in the MSC for the duration of the experiment.

Once complete the potential was stopped on the BDD electrodes which were removed from the set-up and placed into individual wells of a 96-well plate (Corning, Durham, USA). The BDD was rinsed twice by pipetting and aspirating 330  $\mu l$  sterile water to remove any planktonic cells. The biofilm was fixed by incubation at 70°C for 1 hr for analysis with a CVA. The culture of each well was also removed and the  $OD_{600}$  measured using a Jenway spectrophotometer.

### 6.3.6 Crystal violet assay

Once the biofilm was fixed to the BDD substrate 200  $\mu\text{l}$  of 0.1 % crystal violet aqueous solution (1% in  $\text{H}_2\text{O}$ ; Sigma Aldrich, St Louis, USA) was added to the wells for 15 minutes. The stain was then removed from the wells and rinsed with sterile water three times to remove excess stain. The stained biofilm was solubilised in 200  $\mu\text{l}$  of 30% acetic acid ( $\geq 97\%$ ; Fisher Scientific, Loughborough, UK) for 15 minutes. The solubilised stain was then transferred to a new 96-well plate and the absorbance was measured at 595 nm using a Multiskan FC Microplate Photometer (Fisher Scientific, Loughborough, UK).

## 6.4 Results and Discussion

### 6.4.1 Material Testing and Experimental design

One of the major challenges for this work was finding the right material to produce a watertight experimental cell that could be repeatedly sterilised in an autoclave. The first experimental cell was fabricated in glass. Borosilicate glass can be reused for microbiological experiments provided it is effectively cleaned between experiments, the advantage of borosilicate glass is that it can withstand repeated sterilisation.<sup>69</sup> Due to design requirements, *vide infra*, the cell comprised two separate compartments that would be separated by a membrane for each experiment. To place the membrane between the two compartments, the cell needed to be modular. However, ensuring a watertight seal when constructing the cell without the use of vacuum grease was difficult. Vacuum grease is not ideal for electrochemical studies, or indeed for microbiological studies. The composition of vacuum grease is not always stated and there is a risk of low volatiles entering the solution which could cause contamination, surface fouling and compromise bacterial growth. Therefore, an alternative design and material was sought.

3D printing in laboratory environments is an increasingly popular technique as the cost of instrumentation has decreased in recent years.<sup>70-72</sup> A FDM printer was used for all initial studies investigating the performance properties of the thermoplastics PET, PLA and HIPS. Replicas of the polystyrene 96 well plates, commonly used in cell biology, were designed and printed in each of the three

materials and then autoclaved at 121°C for 15 minutes to test the materials. PET printed wells were produced using different layer thicknesses (0.1, 0.18 and 0.25 mm) to determine whether the thickness of the print (a smaller layer thickness increases the print time as more 'layers' are printed) had an effect, all showed significant deformation after autoclaving, with the worst for the 0.1 mm layer height print, Figure 6.2.

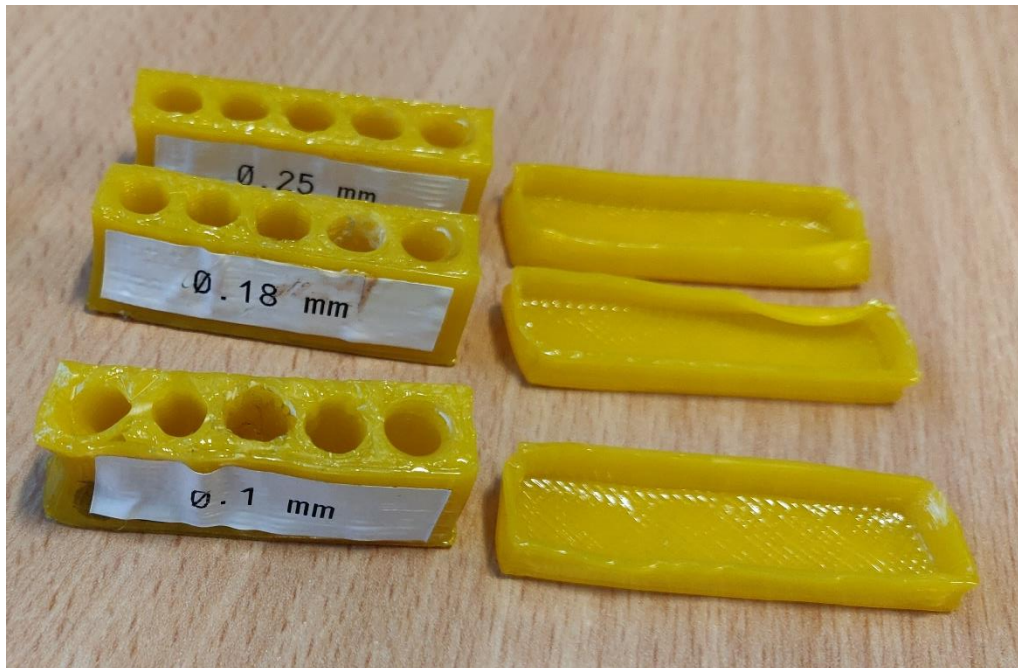


**Figure 6.2 Deformed FDM printed test wells and lids in PET with 0.10, 0.18 and 0.25 mm layer thicknesses after autoclaving at 121°C for 15 minutes.**

HIPS did not deform as significantly as the PET, but bowed under the heat of the autoclave. The deformation of PET and HIPS are almost certainly due to the release of stress as the parts soften at the elevated temperature and pressure of the autoclave.<sup>73</sup> The PLA did not deform in the autoclave but when tested further was not water tight for extended periods of time. PLA prints at a lower temperature (180°C vs. 210°C) and therefore is under less strain than the PET and HIPS, hence less obvious deformation. Instead, it is likely small gaps opened between the print layers, therefore FDM printing was not going to be suitable for this experiment.

SLA printing was next considered. Rather than printing from a coil of thermoplastic, SLA printers use a photosensitive thermoset polymer resin set by

an ultraviolet (UV) laser beam.<sup>74</sup> Photopolymerisation occurs as the monomer carbon chains are activated by the light of the UV laser and become solid as strong chemical bonds are formed, the material is therefore more resistant to heat than the thermoplastics printed by FDM where mechanical bonds are formed between layers.<sup>75</sup> A number of resins are available on the market with varied material properties. Two resins were considered for this study, both manufactured by FormLabs; Clear resin and High-Temp resin. Both were tested in the autoclave and were much more stable than the FDM-printed thermoplastics, no deformation was observed and they remained watertight, Figure 6.3.

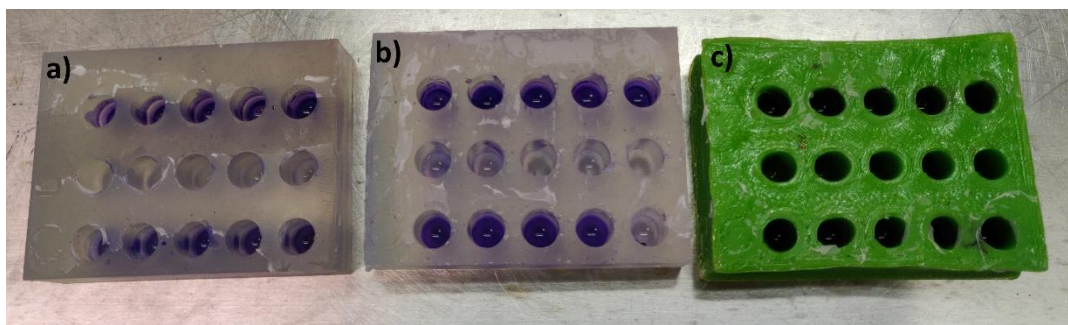


**Figure 6.3** Test prints of a) High temp resin, b) clear resin and c) PLA from FDM printing after autoclaving sterilisation and dyeing PA01 growth with 0.1% Crystal violet.

Another consideration for the material used was how the bacteria interacted with it. For this study, the ideal scenario is negligible adherence of bacteria on the side of the well. A PA01 culture was added to autoclaved test wells printed by SLA in clear and high temp resin and PLA wells printed on the FDM printer (this was investigated in parallel with the autoclaving studies). These materials were tested against a standard polystyrene 96 well plate (packaged sterile). The culture was incubated at 37°C for 24 hours and analysed by a CVA. The results are shown in Figure 6.4.

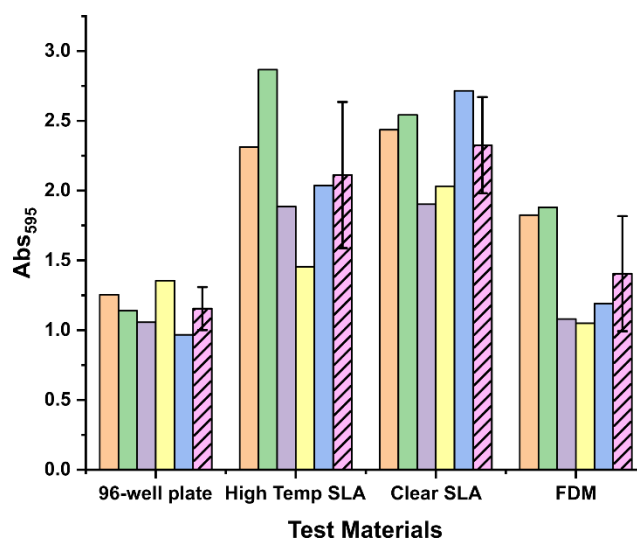


Figure 6.4 CVA absorbance results of biofilm growth in wells printed in the test materials of interest against a standard 96-well plate. The five bars are the individual wells and the striped bar the mean value and the error bars indicate  $\pm 1$  standard deviation.

All of the 3D printed materials showed a higher absorbance than the standard 96 well plate, suggesting there is increased cell attachment to these well walls than the 96-well plate. Interestingly, the FDM printed PLA was most similar to the 96-well plate. This was surprising as FDM prints are typically quite rough due to the individual layers of material extruded on top of each other. Bacteria typically prefer rough surfaces to smooth surfaces as they experience protection from shear forces than can act to remove cells and have an increased surface area.<sup>76,77</sup> The thermoplastics are more likely than the resins to leach into the media, this is a possible explanation for the lower film coverages in the FDM wells. Given the similarities between the high temp and clear resin, in Figure 6.4, and the fact the high temp resin is designed specifically to withstand elevated temperatures, the high temp resin was used for all further studies.

#### 6.4.2 Optimisation of cell design and set up

Once a suitable material was found, the experimental cell design was optimised in line with the following considerations. When undertaking microbiological studies it is necessary to have biological replicates to ensure any variation is due to the variable of interest rather than inherent variability from the bacterial growth.<sup>78</sup> The experimental aim was to investigate the effect of applied potential on bacterial adhesion and biofilm formation on BDD. For each applied potential,



triplicate measurements were needed as a minimum. For every experiment a control set with an applied potential of 0 mV was run alongside two sets with varied applied potentials. To run all experiments together, a minimum of nine BDD electrodes were required with a potential applied to them. This required use of an appropriate multi-channel potentiostat. Additionally, three wells were also used as negative controls with no applied potential, and no bacterial culture present, to ensure the sterility of the experimental set-up. As these wells were not going to have an applied potential they were additional to the main experimental cell to reduce the overall size of the set-up.

In the CH Instrument system available (CHI 1050A) the multichannel potentiostat ran as multiple individual electrochemical cells, each requiring their own reference and counter electrode. In comparison Ivium manufacture a WE32 module which allows control of up to 32 electrodes in a system referenced to a signal reference electrode and the circuit completed with a single counter electrode. The Ivium system was decided to be more cost efficient as it only required one reference electrode; not using a standardised reference has been identified as a limitation of some previous studies trying to utilise a similar concept.<sup>34</sup>

The Sultana et al. review<sup>34</sup> also raised concerns about the positioning of the counter electrode and impact of counter electrode electrolysis products on the bacterial growth process. Also worthy of consideration when working with multiple working electrodes is the impact of depletion effects at the working electrode which could be compounded by biofilm formation. Bacterial cells, once irreversibly attached to a surface, often release signals to other cells to also attach. Isolating the working electrodes within their own bacterial suspensions also prevents preferential formation on one of the electrodes from this signalling behaviour. As a CVA was being used to analyse biofilm formation on the electrode surfaces (Section 1.6.1.3) the BDD electrodes also needed to be easily removable from the set up for analysis, with minimal disturbance of the film on the BDD surface.

The final design was a radial arrangement of nine individual wells on the outside of a larger central well, see Figure 6.5. The central well housed the counter and

reference electrodes which were isolated from the outer wells containing the culture and BDD electrodes, via a conductive membrane, Nafion-212. Nafion-212 is a perfluorinated ion-exchange membrane, nominally 50  $\mu\text{m}$  thick; this was the thinnest form of Nafion available, chosen to minimise the role of membrane resistance as much as possible.

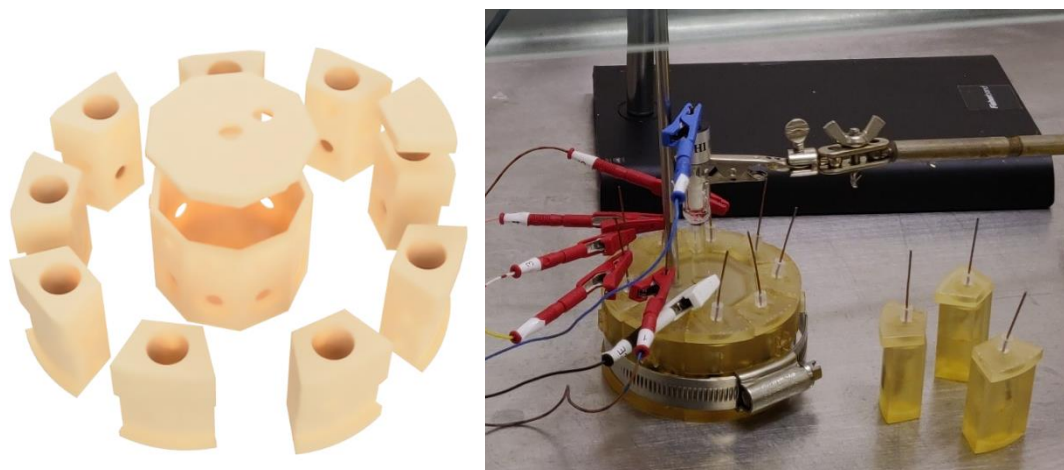


**Figure 6.5** CAD model of the final biofilm design (left) and an optical image of set up in MSC (right). Nine outer wells connect to a central compartment isolated by a Nafion 212 membrane and sealed using rubber gaskets held in place using a hose clamp. Each of the outer wells have a lid through which the BDD electrode is placed. The central well lid has a central hole for the reference electrode and a small hole for the counter electrode and a hole for the thermometer.

As the electrodes needed to be easily removed from the wells for CVA analysis and required an electrical contact to be made, a design where the electrodes could be partially dipped into each of the nine wells was developed (Figure 6.6). The BDD electrode, a disc of 4 mm diameter, had a Ti/Au contact sputtered onto the top 1 mm of the surface. The bottom of the disc was dipped into the culture. A clip was manufactured from copper wire soldered to a Hirshmann measurement crocodile clip. The conducting clip connected to the Ti/Au contact. The copper wire was placed through a small hole in a lid for each well and secured in place with silicon tubing. The lid has multiple purposes, to aid in keeping the experiment sterile by preventing contaminants entering the culture, to reduce evaporation effects and to hold the electrode clips. Once the experiment was completed the BDD could then be removed from the clip and placed into the well of a 96-well plate to be analysed by a CVA. The Hirshmann clip was retracted flush to the lid of the electrode and clipped at the edge of the Ti/Au contact to as

reliably as possible ensure the area of the BDD dipped in solution was constant. The volume of culture in the well was also kept consistent at 1 ml.

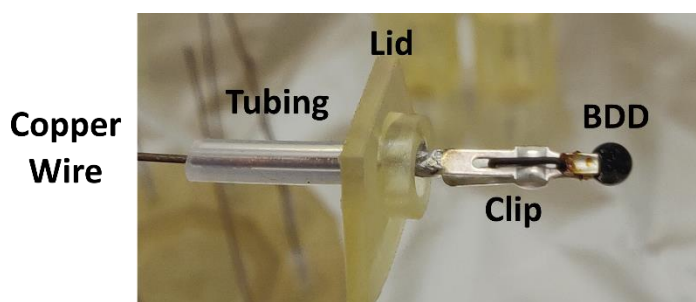
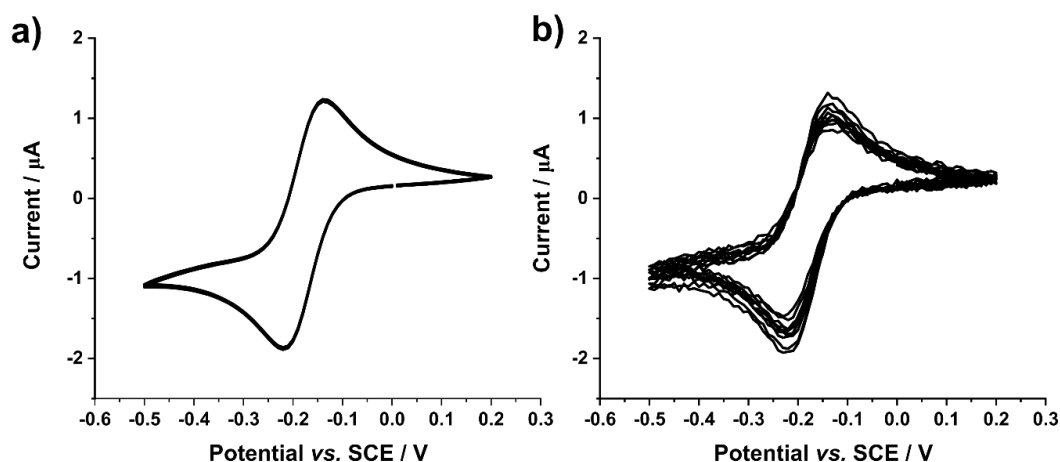


Figure 6.6 Image of the 4 mm diameter BDD round in the clip and lid configuration.

As the BDD was dipped in the culture, both the front and back of the BDD disc and the sidewall were exposed. For these experiments, BDD which had both faces polished to the same finish, nm roughness, was used. The BDD was 500  $\mu\text{m}$  thick. As the disc of BDD is cut from a larger BDD wafer, the cutting procedure produces a slightly rougher sidewall surface. Surface roughness of BDD has been shown to impact cell adhesion.<sup>54</sup> However, compared to the overall area of the BDD, given the smaller area, the sidewall will have a minimal contribution.

#### 6.4.3 Potentiostat testing

A trial experiment to ensure the Ivium compactstat and WE32 module worked as expected was set up. The redox couple ruthenium hexamine ( $\text{Ru}(\text{NH}_3)_6^{3+}$ ; 1 mM in 0.1 M  $\text{KNO}_3$ ), which is well characterised on BDD,<sup>79</sup> was used as a test redox active analyte. Each of the nine channels to be used on the WE32 were checked individually with the same glass sealed BDD macroelectrode by running a CV between +0.2 and -0.5 V vs. SCE. The response on all channels was extremely similar, returning a peak to peak ( $\Delta E_p$ ) separation of 80 mV, Figure 6.7a. The same measurement was taken running all nine channels simultaneously on nine glass sealed macroelectrodes held in a large beaker of solution, Figure 6.7b, which showed slight electrical interference between the electrodes, but still a similar redox couple response.



**Figure 6.7** Response of 1 mm BDD macroelectrode with 1 mM  $\text{Ru}(\text{NH}_3)_6^{3+}$  in 0.1 M  $\text{KNO}_3$  on a) the same electrode on each of the 9 WE32 channels and b) of nine electrodes run simultaneously on the nine WE32 channels. Undertaken with a  $0.1 \text{ V s}^{-1}$  scan rate.

When using the WE32 module for the biofilm experiment the aim is to apply three potentials in triplicate to investigate the effect of potential on cell adhesion and biofilm formation within the same bacterial growth run. The WE32 module connects to a single channel compactstat and effectively amplifies the instructions from a single electrode to multiple electrodes through the WE32 module. To apply different potentials to the working electrodes an offset can be applied to the individual channels on the WE32. This was tested with the nine macroelectrodes and  $\text{Ru}(\text{NH}_3)_6^{3+}$  in a large beaker, three electrodes were offset by  $-200 \text{ mV}$  and three by  $+200 \text{ mV}$ , Figure 6.8a.

The reduction and oxidation peak potentials of the redox couple are  $-0.22 \text{ V}$  and  $-0.14 \text{ V}$ , respectively, from Figure 6.7a. The potential axis in Figure 6.8a is the applied potential with no offset corresponding to the electrodes in green. In the offset channels the potentials of the redox couple are offset by  $+200 \text{ mV}$  (pink) and  $-200 \text{ mV}$  (purple) compared to the axis, so effectively scan a shifted potential range, Figure 6.8b, but the redox process still occurs at the same applied potential. So, for the electrode responses in purple, the reduction reaction peak appears at  $\sim 0 \text{ V}$  on the axis, as the potential is offset but  $-200 \text{ mV}$ , and conversely the pink reduction occurs at  $\sim -0.4 \text{ V}$  but these electrodes are offset by  $+200 \text{ mV}$ . This experiment proves the channels can be offset against each other.

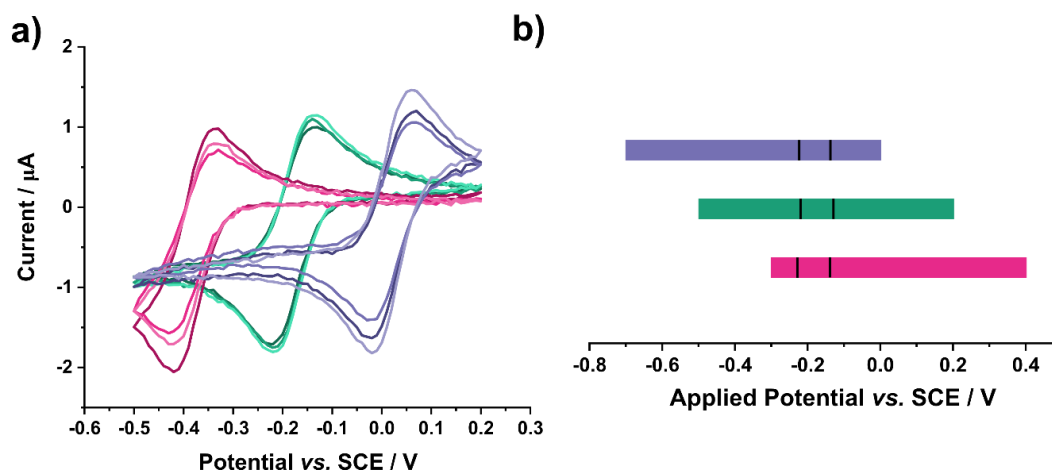


Figure 6.8 a) Current response of nine 1 mm BDD macroelectrodes with 1 mM  $\text{Ru}(\text{NH}_3)_6^{3+}$  in 0.1 M  $\text{KNO}_3$  with no offset (green), a potential offset of -200 mV (purple) and a potential offset of +200 mV (pink) b) shows the applied potential range for the three groups of electrodes, the Black vertical bars align with the redox potentials of  $\text{Ru}(\text{NH}_3)_6^{3+}$  in each case. Undertaken with a  $0.1 \text{ V s}^{-1}$  scan rate.

#### 6.4.4 Membrane

The decision to isolate the counter electrode from the working electrode has already been discussed in Section 6.4.2. The decision to place the reference electrode behind a membrane is more controversial. As highlighted by Sultana et al.<sup>34</sup> the use of a well-defined reference electrode is crucial in knowing the true potential at which adhesion prevention or cell removal occurs. The authors comment that the reference electrode should be placed in the biofilm compartment.<sup>34</sup> This was presumably to reduce the working electrode – reference electrode separation. Increasing this distance results in increased uncompensated resistance,  $R_u$ ,<sup>80,81</sup> which can result in slightly distorted voltammograms. Due to the radial design of the cell there is a significant distance (approx. 24 mm) between the BDD electrodes and the reference electrode. Additionally, the conductive membrane separating the sterile media in the central well from the culture in the outer wells will further add to the resistance. To highlight the added resistance contribution from the membrane, a CV was recorded with the  $\text{Ru}(\text{NH}_3)_6^{3+}$  redox couple in the cell set up (for one glass sealed macroelectrode in one well) with and without the membrane present. The peak separation increased from 78 mV to  $\sim 90$  mV, respectively. These peak to peak separations are slightly higher than the theoretical  $57/n$  mV (at 298 K)<sup>82</sup>. The rationale for keeping the reference electrode out of the wells containing bacteria

was to reduce the risk of fouling on the reference electrode. If the reference electrode fouled, the potentials applied would drift throughout the experiment, which would also be problematic. It is possible that the bacteria could foul the membrane during the course of the experiment. This would result in a further increase in the  $R_u$ , however the membranes were always intended to be single use. No visual evidence of significant biofilm formation on the membranes was ever seen when the cell was dismantled.

#### **6.4.5 Bacterial growth and crystal violet analysis conditions**

To quantify the extent of biofilm formation on each BDD electrode, a CVA was used, where the absorbance ( $Abs_{595}$ ) of a solubilised crystal violet stain is considered proportional to the surface biofilm biomass. The microliter CVA is an established experimental protocol; however optimisation for the exact experimental conditions is important.<sup>83-86</sup> Initially, a growth curve of PA01 was determined to identify the optimal time for cultures in the initial culture to reach mid-exponential growth phase (Figure 6.9a). There is an initial lag phase followed by the exponential growth phase which occurs between approximately 2 and 8 hours. Leaving the cultures to grow for ca. 5 hours should ensure the cells are in the exponential growth phase. By correlating the optical density with colony forming unit (CFU) measurements, determined from LB agar plate counting, the  $OD_{600}$  corresponding to approximately  $2 \times 10^7$  cells  $ml^{-1}$ , can be determined, Figure 6.9b. This was used to ensure the biofilm experiments started with a known and controlled number of cells.

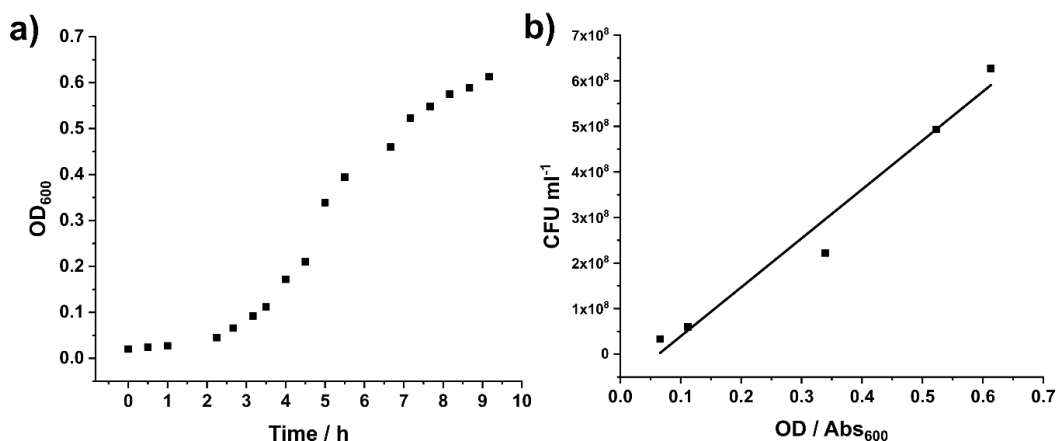


Figure 6.9 a) Growth curve of PA01 with optical density readings taken at multiple time points. b) optical density plotted against colony forming units from serial dilutions of five samples taken during the growth curve. This plot can be used to calculate cell concentrations with relation to optical density.

Significant work was done by Simcox *et al.*<sup>54</sup> to optimise the CVA. This involved investigating solubilisation of the dye with 30% acetic acid and 95% ethanol (both have been used to analyse *P. aeruginosa* strains), and a comparison of results at 0.1% and 0.01% crystal violet concentrations. The optimum was determined to be a 0.1% concentration of crystal violet dye, solubilised with 30% acetic acid as this resulted in absorbance measurements within the optimal region of the photometer.<sup>54</sup> As this study uses the same PA01 strain as the monoculture studies in reference<sup>54</sup> the same conditions were used herein.

#### 6.4.6 Optimisation of experimental set up

Although as much consideration as possible was taken in designing the experimental cell, inevitably, additional issues arose that had not been foreseen. Initially 4 mm diameter BDD rounds were used in the set-up. 1 mm of the top edge was roughened to provide a surface for the Ti/Au contact, which was clip contacted (see Figure 6.6) and dipped into the solution. Although the well volume was set (1 ml) and care was taken in the set-up there was evidence of rusting on the metal clips over a 70 hr period, with additional discolouration of the media (Figure 6.10). Moreover, large currents were passed in the 10's of  $\mu\text{A}$  range (Figure 6.10). This is indicative of solution wetting up to the electrical contact and clip, resulting in larger electrode areas in contact with solution and oxidation or reduction (depending on the applied potential) of the clip.

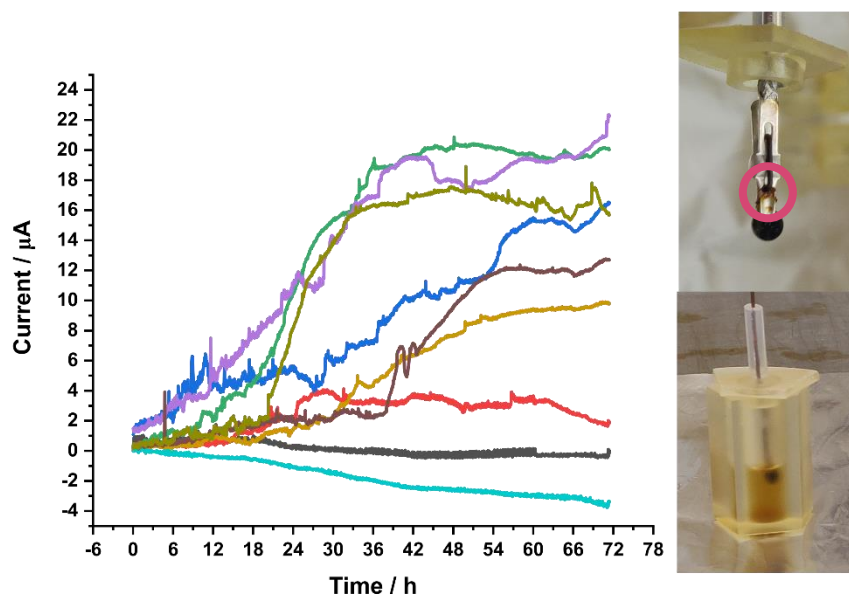


Figure 6.10 Images show discolouration of solution where rusting had occurred and the typical location of the rusting on the Hirshmann clips, inside pink circle. The current time plot shows the large currents passed at 0 mV for nine electrodes in the nine individual wells with the 4 mm BDD rounds used as the electrode.

Whilst the clips are silver plated brass, the silver did not cover the brass where the spring joined the clip, which appeared to be where the majority of rusting occurred. These joints were sealed with nail varnish which helped, but rusting at the bottom of the clip, close to the contact, still occurred. Therefore, larger pieces of diamond were sourced. Rectangular double side polished BDD of 5 mm x 10 mm geometry was used, again roughening 1 mm at the 5 mm edge for a Ti/Au contact, Figure 6.11. A modification of the well lid was made to raise the clip further out of the solution which allowed for the electrical contact to be further away from the culture. This, in conjunction with additional sealing on the metal clips, by applying nail varnish to the join on the spring, resolved the issues with contact wetting and rusting. Currents were measured in the single  $\mu\text{A}$  range, the bottom third (3-4 mm) of the BDD plate was in contact with the culture.



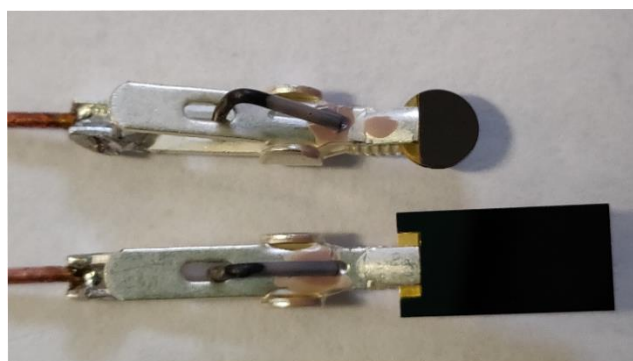


Figure 6.11 image of comparison of the two BDD geometries used, top is the 4 mm round, bottom the 5 x 10 mm piece of diamond. The gold area on both shows the sputtered contact. The purple on the clip by the spring is the nail varnish applied to seal the brass.

An issue was also identified when filling the wells of the set-up. If the liquid was not carefully pipetted into the wells an air bubble could become trapped at the membrane interface, reducing or completely blocking the membrane-solution, a schematic is depicted in Figure 6.12. Membrane blocking would inevitably have implications for electrochemical measurements as the reference electrode would not have solution contact to the BDD electrode and therefore an unknown potential would be applied, and the  $R_u$  would be extremely large. The air bubbles could be excluded by carefully pipetting the solution towards the membrane which forced any trapped air out of the indent to the solution surface.

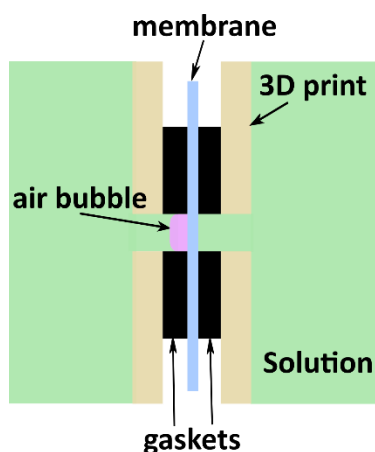


Figure 6.12 Schematic to visualise the entrapment of air against the membrane

After repeated use of the same 3D printed cells, while the issues discussed were resolved, discolouration was observed in the outer wells that had contained the PA01 cultures, Figure 6.13. Despite efforts to clean them the staining appeared to be within the first few layers of the print itself. If the stain was due to residual bacteria the cells would have been inactivated by the autoclaving process. There was no evidence of contamination from the stained wells during sterility experiments, which were undertaken prior to each experiment (incubating the entire set-up at 37°C containing only LB media). The stain could also have been caused by the rusted material produced from the clips in the early experiments. As brass contains copper, which is known to be an antimicrobial agent, it was decided to discard the discoloured cells to ensure this wasn't having an effect on the biofilm growth.<sup>87</sup> The 3D printed components were then used in a semi-reusable manner and replaced after ten uses. No further discolouration was observed.

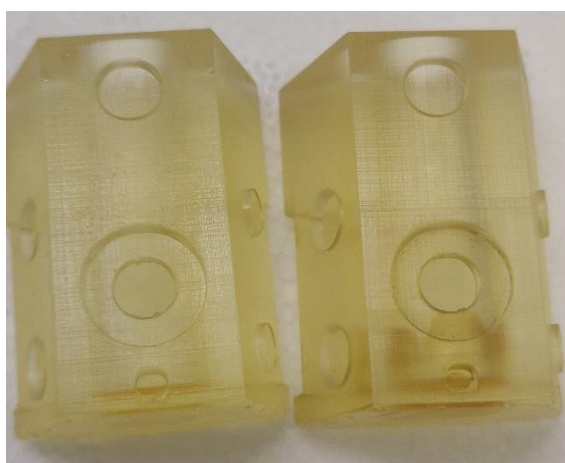


Figure 6.13 Image of unused outer well (left) and a stained outer well (right), height 32 mm.

#### 6.4.7 Optimisation of Crystal Violet assay analysis.

Once all of the practical set up issues discussed above had been resolved, the next challenge was the analysis of the biofilm formation on the BDD. As previously discussed, Simcox et al.<sup>54</sup> had modified the standard crystal violet assay procedure for analysis on 4 mm BDD rounds in a 96 well plate.<sup>54</sup> This procedure assessed biofilm formation on a single surface of the BDD round, however in this experimental set up both sides of the BDD were exposed to the bacterial culture

so growth could occur on both sides. Therefore, both sides needed to be part of the analysis. For the rectangular BDD electrodes, it was possible to stand them in a well in the 96 well elisa plate which exposed both surfaces to the stain, Figure 6.14. The protocol was adjusted to ensure the entire diamond was covered, increasing the volume to 330  $\mu\text{l}$ . After several attempts at this analysis the CVA absorbance values were quite high, often saturating the plate reader. There are two possible explanations for this, there was significant biofilm formation on the BDD or the increased volume of dye at 0.1% was too high.



**Figure 6.14** Difference between positioning of BDD 4 mm round and 5x10 mm rectangle of BDD in the wells of a 96-well plate for crystal violet assay analysis.

PA01 liquid cultures are typically grown in a rotating incubator to increase aeration of the solution to promote growth.<sup>64</sup> In stationary solutions, as in the growth wells used herein, PA01 preferentially grows at the liquid-gas interface of a culture, forming a surface film. This was observed in the culture containing wells for the set up described. Due to the contacting of the BDD and the requirement to connect to the potentiostat it was not feasible to place the set up in a rotating incubator.

The surface film posed a challenge for the analysis as the BDD electrode sat across the liquid surface interface. When the BDD was removed from solution by pulling the BDD up out of the culture, the surface film sometimes collapsed down onto the BDD surface therefore increasing the CVA reading. To reduce this, once the potential had been switched off, the BDD and clip were moved downwards to the bottom of the well, causing the surface film to stick to the clip and or very top

surface of the BDD electrode. To avoid analysing any area which contained surface film deposited biofilm, CVA analysis was carried out only on the portion of the BDD electrode that was in contact with the culture during the experiments. The volume of CVA stain added was thus reduced from 330  $\mu\text{l}$  to 200  $\mu\text{l}$  to accommodate this. Furthermore, to try and ensure the same proportion of BDD electrode was analysed, the BDD plates were carefully oriented in the wells of the 96 well plate. Both these processes aided with differentiation of the CVA between the potentials applied to the BDD and not saturating the plate reader.

#### 6.4.8 Effect of potential on *P. aeruginosa* biofilm formation

##### 6.4.8.1 Determination of potential range

PA01 was grown in LB medium which contains tryptone (10 mg ml<sup>-1</sup>; amino acid source), yeast extract (a mixture of peptides, amino acids, carbohydrate and vitamins), NaCl (10 mg ml<sup>-1</sup>) and NaOH, to neutralise to pH 7. Extended potential windows on a 1 mm diameter disc glass sealed BDD macroelectrode was recorded in (i) LB medium (yellow; solid line) (ii) 0.1 M KNO<sub>3</sub> (purple; dotted line) and (iii) NaCl at 10 mg ml<sup>-1</sup> (blue; dashed line), Figure 6.15 at a)  $\pm 0.8$  V and b)  $\pm 1.5$  V.

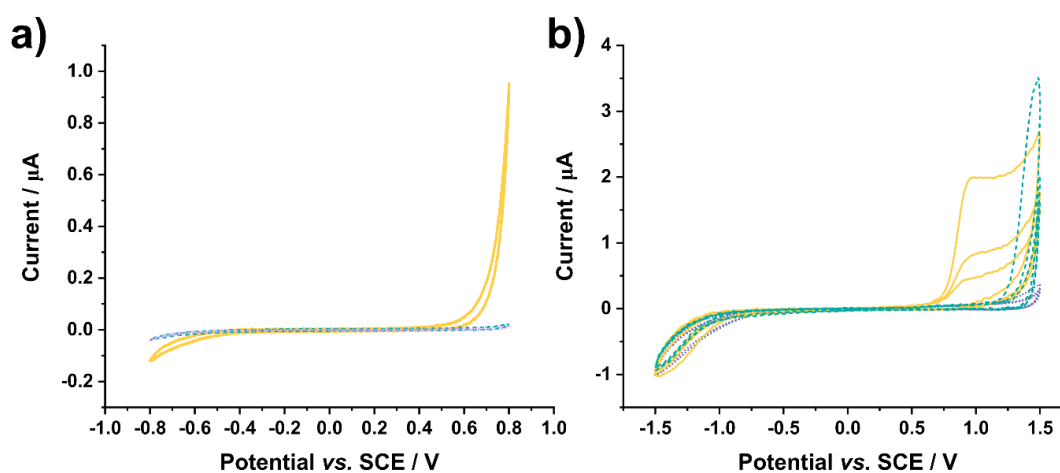


Figure 6.15 Solvent windows (scan rate = 0.1 V s<sup>-1</sup>) performed on a 1 mm diameter disc glass sealed BDD macroelectrode LB medium (yellow; solid line), 0.1 M KNO<sub>3</sub> (purple; dotted line) and NaCl at 10 mg ml<sup>-1</sup> (blue; dashed line) across the potential range a)  $\pm 0.8$  V vs. SCE and b)  $\pm 1.5$  V vs. SCE.

In the LB medium, compared to NaCl and KNO<sub>3</sub>, there is a clear oxidative process, which is not due to water oxidation or chloride oxidation. The latter can be seen in the NaCl solution when scanning out to 1.5 V Figure 6.15b. The LB oxidative

peak occurs at a lower potential than that for chloride oxidation. The exact composition of the yeast extract in the LB medium is not disclosed but is described as a mixture of amino acids, peptides, water soluble vitamins and carbohydrates. The feature at 0.7 V is most likely a vitamin that is present in the yeast extract, as vitamins A, C, D, E, K and the eight B vitamins, are electrochemically active.<sup>88</sup> As the goal is to consider solely the impact of BDD electrode potential on biofilm growth, uncomplicated from faradaic redox reactions, only potentials in the range  $\pm 400$  mV were considered, the non-faradaic current region on the BDD electrode in the LB medium.

#### 6.4.8.2 Effect of application of 0 mV to BDD

In order to collect current information all of the BDD electrodes required an applied potential. An applied potential of 0 mV vs. SCE in triplicate was used in all experiments as a control. A comparison between BDD samples was also made for no applied potential and application of 0 mV, Figure 6.16. When 0 mV was applied increased CVA absorbance readings and optical density readings were recorded compared to the samples with no potential applied.

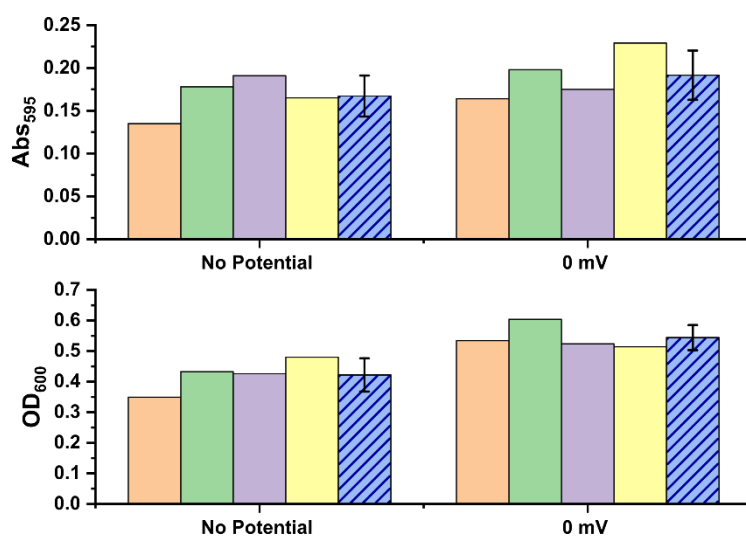


**Figure 6.16 Individual results for CVA (top) and optical density (bottom) from wells with no applied potential and an applied potential of 0 mV, the striped column is the mean of the individual results and the error bars represent  $\pm 1$  standard deviation.**

PA01, along with most bacteria, has a slightly negative zeta potential, the exact value is strongly dependent on the solution pH.<sup>35,43</sup> All surfaces immersed into an electrolyte solution have a charge. At the PZC, where no excess charge prevails, no electrostatic attraction between the surface and bacteria would occur. Due to

the polycrystalline nature of the BDD used, it is impossible to determine the potential of the PZC as it will vary between grains due to crystal structure and dopant density. Taking the assumption that the zeta potential of PA01 in this system is indeed negative, the increase in biofilm formation with the application of 0 mV suggests that the application of 0 mV vs. SCE results in net positive charge on the surface causing electrostatic attraction between the cells and the surface, which in turn encourages biofilm formation.

#### 6.4.8.3 Comparison of applied potentials to biofilm formation on BDD

Within the  $\pm 400$  mV range three pairs of potentials were considered against the controls at 0 mV; + 400 mV and - 400 mV, + 200 mV and - 200 mV and + 50 mV and - 50 mV, each representing one experimental run. Each potential was applied to three BDD electrodes to provide triplicate measurements. The current-time trace for each electrode is shown for each condition. The mean value for each condition with error bars signifying the standard deviation is shown for the triplicate values of the CVA and the growth in the wells ( $OD_{600}$ ) after 72 hours. These will be discussed individually initially.

Given the applied potentials are within the non-faradaic region of BDD in the medium the expected currents should be low. However the influence of the bacteria growing on the surface may result in current changes through either modification of the surface, or the release of redox active metabolites by PA01 *i.e.* phenazines.<sup>89,90</sup> *P. aeruginosa* produces pyocyanin (blue) and pyoverdine (yellow) pigments which give colonies on solid agar a distinctive blue-green colour and turn the liquid culture green, Figure 6.17 a and b, respectively. Other redox active phenazines that could be metabolised include phenazine-1-carboxylic acid, phenazine-1-carboxamide and 1-hydroxyphenazine.<sup>89</sup>

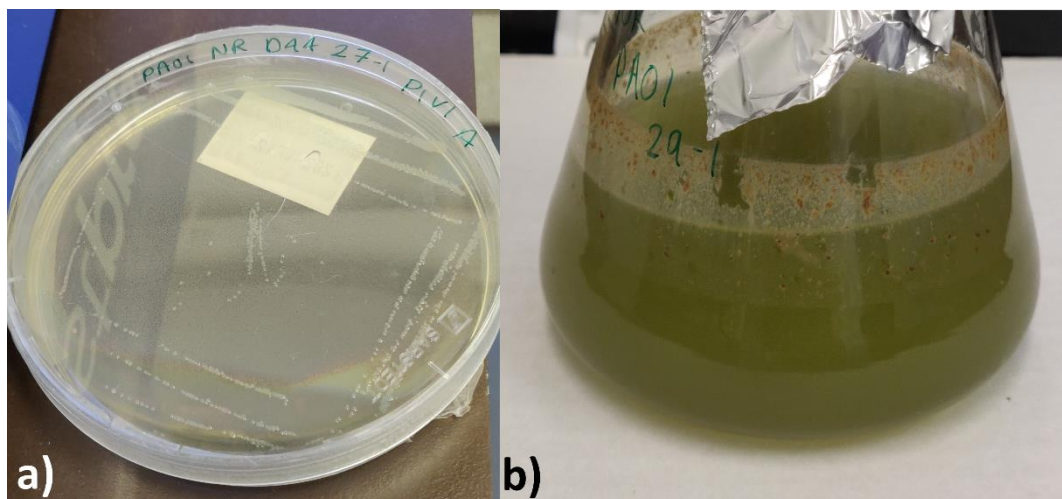
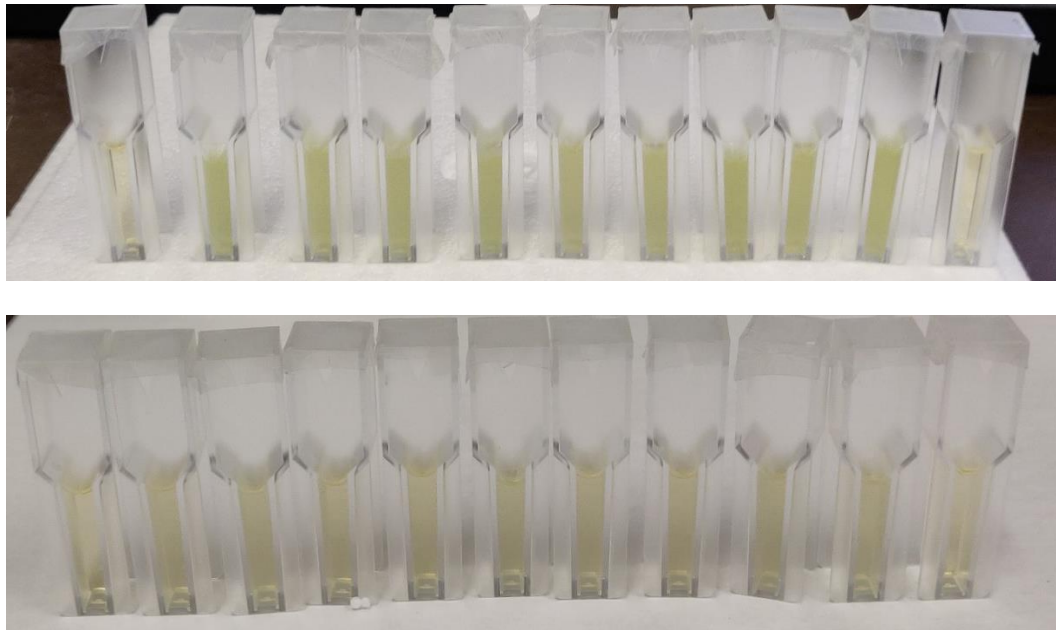


Figure 6.17 a) image of PA01 grown on an LB Agar plate at 37°C for 16 h and b) image of PA01 liquid culture after incubation in a rotating incubator for 72 h at 37°C at 120 rpm.

Pyocyanin redox behaviour has been proposed as a mechanism to identify the presence of *P. aeruginosa* biofilm for rapid diagnostics of infection.<sup>91</sup> Reduction and oxidation of pyocyanin on BDD have been reported at +0.1 and -0.4 V vs. Ag|AgCl, respectively,<sup>55</sup> which fall into the range of the applied voltages considered. Indeed, in some experiments where high growth was observed the final culture from the outside wells, appeared green indicating pyocyanin production, Figure 6.18 top image. However, this was not always observed, some cultures were only cloudy with no distinctive green colouring, Figure 6.18 bottom image.



**Figure 6.18** Both images are of the contents of the outer wells after a 72 h experiment with PA01, the first and last cuvettes contain LB containing no cells for reference. The top image shows a green tint to the culture indicating pyocyanin product, whereas the cultures in the bottom image are not green and appear cloudy which indicates the presence of bacterial cells.

The first experiment considered is the run at applied potentials of  $\pm 400$  mV compared against 0 mV. Figure 6.19a shows the current-time response of the nine electrodes within the set-up, with three BDD samples at each potential. The navy lines are the current traces from the BDD at 0 mV, green at + 400 mV and pink at - 400 mV. Two of the three BDD samples at - 400 mV passed significantly higher currents compared to the other BDD samples, Figure 6.19a. However, there was no obvious evidence of rusting on the clip or contact wetting that would suggest an issue with these measurements. All of the current traces show an initial reduction in the current over the first three hours, a sharp increase is then observed followed by a more gradual decrease in current up to  $\sim 12$  hours. At times  $> 12$  hrs, for + 400 mV and 0 mV a general increase in current is seen, whereas a current decrease is observed in the wells with - 400 mV applied.



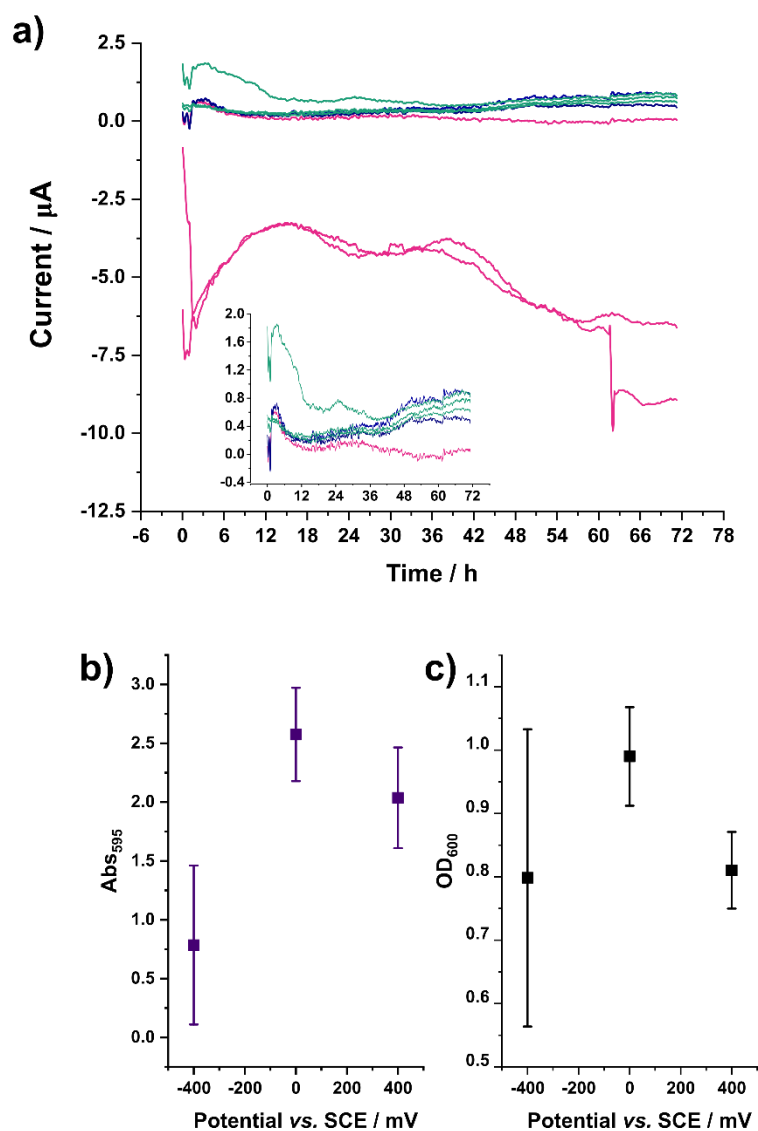


**Figure 6.19** a) Current-time trace of BDD samples at applied potentials of 0 mV (navy), +400 mV (green) and -400 mV (pink) in PA01 cultures, inset is the same graph without the two samples at -400 mV to provide more detail at the lower currents. b) The mean absorbance values of the CVA on the BDD samples averaged from the triplicate samples at each applied potential, error bars represent  $\pm 1$  standard deviation. c) The mean  $OD_{600}$  values averaged from the triplicate well cultures at each applied potential, error bars represent  $\pm 1$  standard deviation.

The CVA analysis and growth analysis in Figure 6.19 b and c, respectively, show the mean value of the triplicate wells at each potential and the error bars represent  $\pm 1$  standard deviation from the mean. At -400 mV, the crystal violet assay shows a reduction in the number of cells on the BDD surface than observed in the control (0 mV) and +400 mV. This is in agreement with the literature, where excess negative surface charge will repulse the negatively charged bacteria from the surface resulting in reduced adhesion and thus reduced biofilm

formation. The larger currents at -400 mV could be due to redox signalling molecule reduction, with possible contributions from oxygen reduction (ORR).

The laser cut edges of the BDD contains  $sp^2$  bonded carbon.<sup>79</sup>  $sp^2$  carbon catalysed ORR can go via the 2 electron pathway producing  $H_2O_2$ ,<sup>92</sup> which could also play a role in inhibiting cell adhesion. Slightly reduced adhesion is also seen at +400 mV, again this could be due to faradaic reactions with oxidation of metabolites damaging the cells surrounding the BDD or unfavourable conditions for cells on the surface. The variation of suspended growth in the wells, Figure 6.19c, also indicates the bacteria were not growing uniformly within the set up despite starting at the same cell concentration ( $2 \times 10^7$  cells  $ml^{-1}$ ). This therefore suggests that the application of a potential may have impacts on suspended bacteria too.

Some suggestions for this include electrochemical interference with metabolites produced by the bacteria and stress to the cell membrane or cellular functions due to the transfer of current through the media. If the potentials are too extreme to promote cellular growth it is possible that the cells could work to modify their membranes or composition of metabolites to try and adjust to the conditions.<sup>89</sup> However if this is unsuccessful and cells die then they will release a greater range of metabolites which could affect the composition of the media for other cells. However, with the limited amount of data available the response of the suspended cells to these applied potentials would require further experimentation. Additionally,  $OD_{600}$  cannot differentiate between live and dead cells, it is likely that after 72 hours the growth has reached the stationary phase so some of the suspended cells will be dead, hence possible overestimation of the number of suspended cells.

The current responses when  $\pm 50$  mV was applied to the BDD samples, and compared against 0 mV, are shown in Figure 6.20a. At -50 mV, two wells showed higher currents than the others but interestingly they were positive currents, this feature cannot be explained by an electrochemical response as a negative potential should pass a negative current, therefore this feature must be attributable to a bacterial influence, either through direct interaction with the electrode or via a redox mechanism. One well at - 50 mV started with a current

at nearly 2  $\mu\text{A}$  which decreased before rising again, the other channel that passed a positive current started with a potential closer to 0 but jumped to the positive currents after  $\sim 24$  hrs. This jump appeared in all the channels but to a lesser extent than the well at - 50 mV. The currents in the other seven wells were fairly similar throughout the experiment.

The CVA again showed a reduction of surface biofilm on the BDD samples on application of -50 mV, although there were sizeable error bars, Figure 6.20b. The CVA results of three wells held at 0 mV were fairly consistent and the CVA on the BDD at + 50 mV was more variable but showed a higher mean value, suggesting more cellular adhesion and biofilm formation than the other two potentials. This could indicate that + 50 mV on the BDD is slightly positive to the cell membrane potential and results in electrostatic attraction between the cells and the electrode surface. The suspended cell growth in the wells was fairly consistent in this run, Figure 6.20, with the most variation shown in the wells at - 50 mV, however the values in all wells were lower than the previous run.

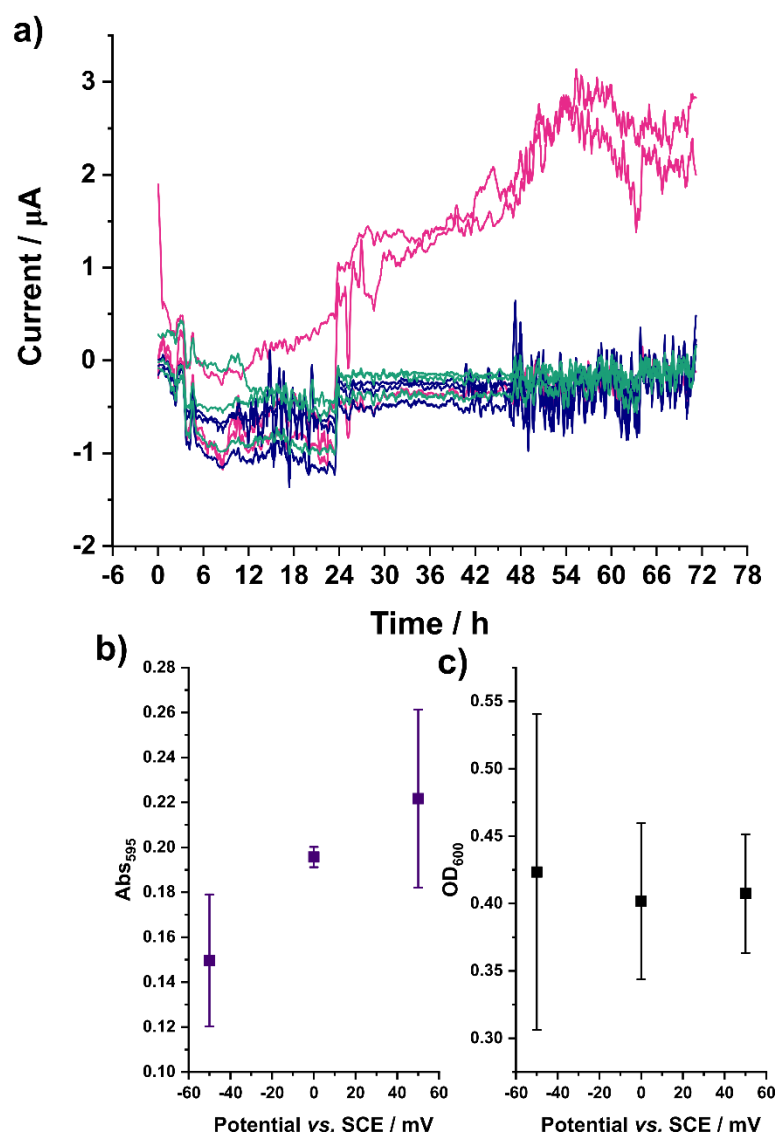


Figure 6.20 a) Current-time trace of BDD samples at applied potentials of 0 mV (navy), + 50 mV (green) and - 50 mV (pink) in PA01 cultures. b) The mean absorbance values of the CVA on the BDD samples averaged from the triplicate samples at each applied potential, error bars represent  $\pm 1$  standard deviation. c) The mean OD<sub>600</sub> values averaged from the triplicate well cultures at each applied potential, error bars represent  $\pm 1$  standard deviation.

Unfortunately, there was an issue with the run at  $\pm 200$  mV. Only very small currents were passed, in the 10's of nA range, Figure 6.21a, very different to the current data obtained above. The CVA absorbance were all observed to be within error of each other and the growth was also fairly similar, Figure 6.21b and c, respectively. This data is included to again highlight the challenges with the set-up of these experiments.

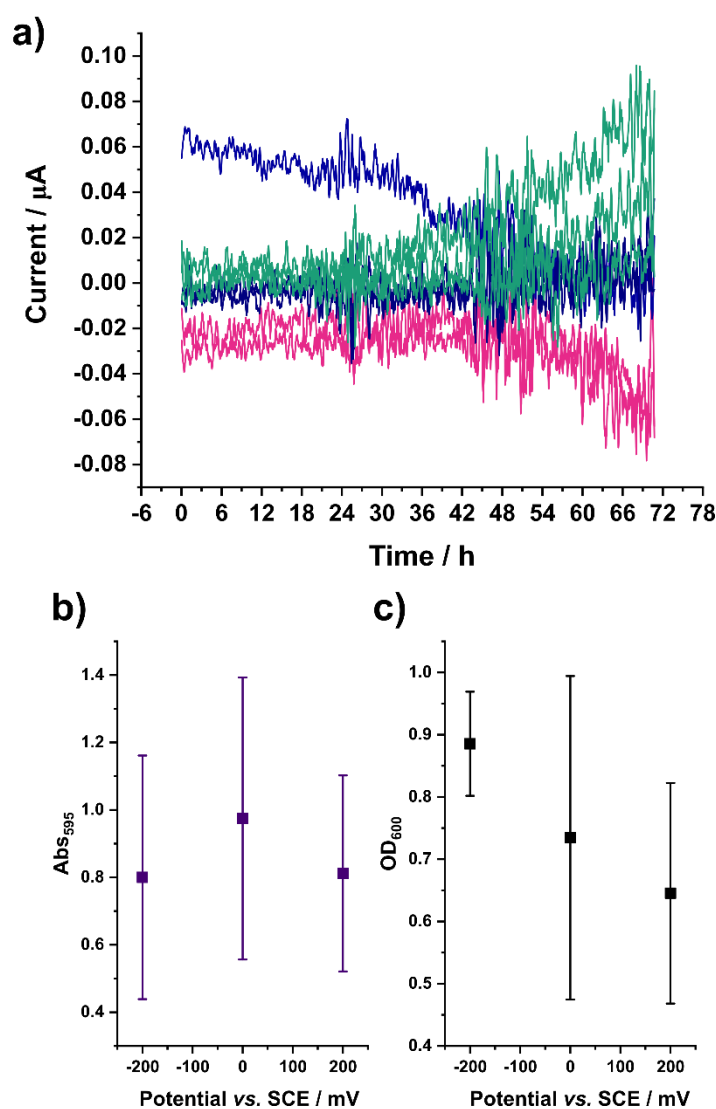


Figure 6.21 a) Current-time trace of BDD samples at applied potentials of 0 mV (navy), + 200 mV (green) and - 200 mV (pink) in PA01 cultures. b) The mean absorbance values of the CVA on the BDD samples averaged from the triplicate samples at each applied potential, error bars represent  $\pm 1$  standard deviation. c) The mean OD<sub>600</sub> values averaged from the triplicate well cultures at each applied potential, error bars represent  $\pm 1$  standard deviation.

Although comparisons between the three electrodes at each of the potentials within an experiment can be easily compared the measured values obtained between experiments was variable, Figure 6.22a. As the experiment was run in the MSC, temperature was not well controlled as would be typical for microbiological studies. The temperature fluctuations for the three runs discussed are shown in Figure 6.22b. Due to the fluctuation and variability in temperature between experiments we are unable to rule out temperature as the

cause of the variability between the runs making interpretation challenging. For example the variation in OD<sub>600</sub> between the runs at  $\pm 400$  mV and  $\pm 50$  mV (Figure 6.19c and Figure 6.20c, respectively) is difficult to compare to aid understanding as the values are so different. Qualitatively the growth looks more uniform when  $\pm 50$  mV is applied than  $\pm 400$  mV which could suggest that the higher potentials are causing more stress to the cells possibly by interfering with metabolites produced by the cells, but further work would be required to verify this.

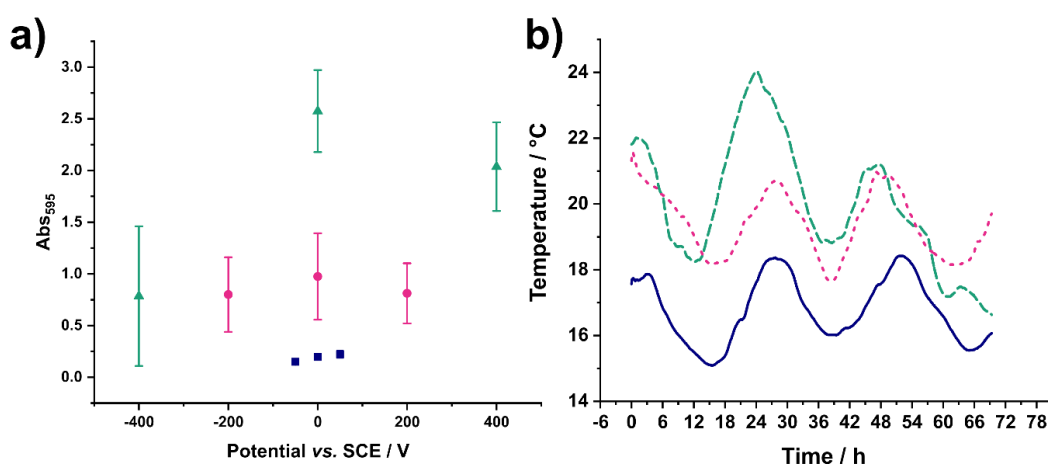


Figure 6.22 a) The mean absorbance values of the CVA on the BDD samples averaged from the triplicate samples at each applied potential for the three experiments considered, pink  $\pm 200$  mV, navy  $\pm 50$  mV, green  $\pm 400$  mV, error bars represent  $\pm 1$  standard deviation b) The recorded temperature across the same three experimental runs pink  $\pm 200$  mV, navy  $\pm 50$  mV, green  $\pm 400$  mV.

Despite showing limited experimental data there was significant advancement in knowledge from this project, particularly with respect to experimental design and problem solving within the set-up. As preliminary work, electrode potential does seem to have some effect on cell attachment and biofilm formation but the analysis was not sensitive enough to fully quantify these changes. The experiment was limited by the amount of BDD electrodes that could be run and the complexity of the set-up. A major challenge was ensuring all the membranes were lined up and the clamp was tight enough to be watertight but not too tight that the 3D print cracked, as occurred a few times. The bacterial growth observed was often variable, possibly related to temperature and the act of passing a current through the medium. The current could impact metabolic processes for the cells and introduce stress affecting growth. That combined with inconsistencies from the placement of the BDD for analysis further contributed

to the variability in the CVA. For some runs the 0.1% dye solution was appropriate but for others it was too concentrated; this was unknown until the dye had been applied. All of these factors contributed to making this experiment very challenging.

Furthermore, in the experiment there was a limited amount of media available to the cells (1 ml) over a relatively long time period, 70-72 hours; this may have also contributed to the higher biofilm formation observed at warmer temperatures when the nutrients would have been consumed at a higher rate which can instigate biofilm formation due to nutrient limitations. The advantage of growing biofilms in flow cells or chemostats are that additional nutrients from media can be added throughout the experiment without disturbing the growth. When designing the experiment a flow cell was discussed, however a significant time period was required to ensure sufficient biofilm was present on the surface for analysis with CVA. Concern was raised about biofilm formation in pipes which could block or change the flow path through the experiment. For this reason a stationary set up was used.

An interesting electrochemical feature was observed in some of the electrochemistry in runs undertaken while refining the experiment. A stepped negative current increase was observed, which remained constant for around 4 hours, and then decreased back to a similar level before the step, Figure 6.23, irrespective of the polarity of the applied potential. The steps always occurred during the first 12 hours of the experiment, although not always at the same time and always returned to a similar current after ~ 4 hours. The increasing negative current therefore suggests that the bacteria were passing electrons to the electrode surface which has previously been observed by Poortinga et al. with *Staphylococcus epidermidis* where both donation and acceptance of electrons from conducting surfaces was observed.<sup>93</sup>

This study showed that where *S. epidermidis* donated electrons the cells were more strongly adhered to the surface than those which accepted electrons.<sup>93</sup> *P. aeruginosa* is not known to depend on direct electron transfer, however a biofilm was formed on the electrode surface so direct electron transfer could have occurred. A study using PA14 (a different *P. aeruginosa* strain) identified the

presence of an unknown redox mediator that consumed electrons from the electrode when biofilm was formed on the electrode.<sup>89</sup> Although beyond the scope of this study understanding this interaction could prove a method for detecting initial cell attachment which could be useful as a biofilm sensor. At the end of the experiment with applied  $\pm 400$  mV the remaining culture in the wells was green, Figure 6.18 (top image), indicating pyocyanin had been produced. The deviation in currents between the three potentials after 36 hours could be due to the reduction (pink), and oxidation (navy and green) of pyocyanin or other redox active metabolites produced by the cells.

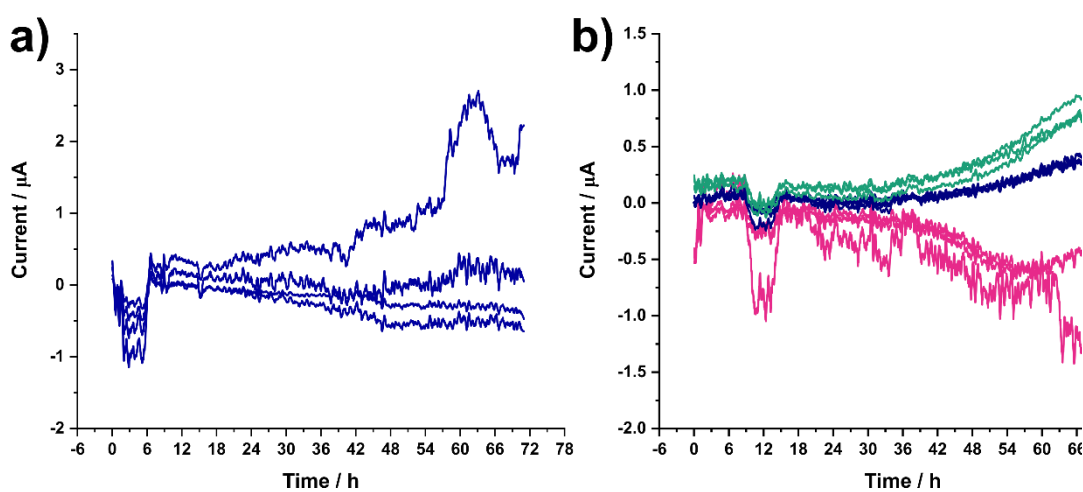


**Figure 6.23 a) Current-time trace with applied potential of 0 mV in PA01 cultures. b) Current-time trace of BDD samples at applied potentials of 0 mV (navy), + 400 mV (green) and - 400 mV (pink) in PA01 cultures**



## 6.5 Conclusions and future work

This was a very challenging experiment requiring aseptic construction of a complex experimental set-up, nine BDD electrodes to function comparably and for bacteria to grow reproducibly. A significant amount of problem solving was required before the experiments of interest could proceed. In terms of material properties and experimental design significant knowledge has been developed. The interpretation of the currents was also challenging as although the region of interest was non-faradaic in the media, the presence of the cells can change this behaviour *i.e.* due to production of redox active metabolites or electron transfer between cells and electrode surface, even pyocyanin production, which could be observed visually was inconsistent between runs. However, from the responses observed throughout the development of the experiment this is certainly an area worth pursuing. The application of a potential could well prolong the lifetime of a sensor, or possibly provide an indication of bacterial attachment that could be monitored.

The intention for these experiments were to compare the effects of potential on biofilm formation with both gram negative (PA01) and gram positive (*Staphylococcus aureus*) bacteria to determine whether the different outer cell structures resulted in a different response. However, given the complexity of the work surrounding the set-up only preliminary work was undertaken with *S. aureus*. Future work should also look to support the CVA results with some form of imaging e.g. scanning electron microscopy or fluorescence microscopy.

Moving forward some recommendations for improvements are to:

- (i) Ensure that temperature control can be implemented: as temperature variations impact growth and removal of this variable would have aided interpretation.
- (ii) Tailor the membrane to the solution conditions. For this work a cation or anion exchange membrane would probably have been better suited as pH was near neutral hence proton availability was limited.
- (iii) The analysis technique: removing the variability in growth with temperature control may improve the variability of CVA between runs in terms of the overall absorbance; however as CVA is a whole surface

technique the issue with the region of the surface remains with the use of a dipping electrode. Imaging techniques, especially with cell stains *e.g.* live dead fluorescence, are improving; however caution should remain depending solely on image analysis to ensure truly representative images are used. *In-situ* analysis during the entire experiment would be the optimum analysis technique; fluorescent tagged bacterial and confocal laser scanning microscopy are probably the best way to do this. With continuous monitoring bias cannot be introduced as the location of the analysis is decided prior to the start of the experiment. However, this is not conducive to biological replicates which should be considered in the analysis of results; a control would be hugely important in this case to be able to draw conclusions between runs.

- (iv) The use of dipped electrodes: although the reasoning was justified in Section 6.4.2 the affinity of PA01 to form a surface film made removal and analysis challenging. Using a free substrate aided the analysis technique utilised, but this again was impacted by the surface film. For *in-situ* sensing, the entire electrode surface would also be in the suspended solution so an experiment with the entire sensor face in the solution would be more representative, and electrode performance would be more reliable and less resistive as a permanent electrical contact could be made. Consideration should be made to the roughness of the packaging material in comparison to the electrode surface and whether preferential adhesion of cells to the packaging occurs. For BDD, if a large enough piece was used and analysed in a way that didn't require the whole surface to be considered then using a sealed electrode may be feasible.
- (v) Monitor suspended cell growth and redox mediator production throughout the experiment: taking small aliquots of the suspended cells throughout the 72 hour experiment would inform on the growth phase of the cells throughout the experiment which could aid understanding. Serial dilution and plating for CFU counts could also be beneficial. Additionally monitoring of redox mediator production may aid with understanding of current time traces and potential stresses on the suspended cells.

(vi) Bacterial strain: PA01 relies on EPS formation early on in cell attachment and subsequently forms a biofilm readily. In comparison PA14, another clinical isolate, does not commit to cell attachment as readily and EPS formation is delayed in comparison.<sup>94,95</sup> Therefore, this study may be more successful with PA14 as a less intense biofilm forming strain allowing the effect of the applied potential to have a greater impact before a biofilm is established.

## 6.6 References

- 1 Z. Khatoon, C. D. McTiernan, E. J. Suuronen, T. F. Mah and E. I. Alarcon, *Heliyon*, 2018, **4**, e01067.
- 2 S. Veerachamy, T. Yarlagadda, G. Manivasagam and P. K. Yarlagadda, *Proc. Inst. Mech. Eng. Part H J. Eng. Med.*, 2014, **228**, 1083–1099.
- 3 J. F. González, M. M. Hahn and J. S. Gunn, *Pathog. Dis.*, 2018, **76**, 1–7.
- 4 O. Ciofu, E. Rojo-Molinero, M. D. Macià and A. Oliver, *Apmis*, 2017, **125**, 304–319.
- 5 T. Bjarnsholt, *APMIS. Suppl.*, 2013, 1–51.
- 6 L. Hall-Stoodley and P. Stoodley, *Trends Microbiol.*, 2005, **13**, 7–10.
- 7 A. Huq, C. A. Whitehouse, C. J. Grim, M. Alam and R. R. Colwell, *Curr. Opin. Biotechnol.*, 2008, **19**, 244–247.
- 8 J. Wingender and H. C. Flemming, *Int. J. Hyg. Environ. Health*, 2011, **214**, 417–423.
- 9 J. A. Lewis, *Mater. Forum*, 1998, **22**, 41–61.
- 10 G. Jones, *Adv. Mar. Antifouling Coatings Technol.*, 2009, 19–45.
- 11 G. D. Bixler and B. Bhushan, *Philos. Trans. R. Soc. A Math. Phys. Eng. Sci.*, 2012, **370**, 2381–2417.
- 12 H. C. Flemming, *Appl. Microbiol. Biotechnol.*, 2002, **59**, 629–640.
- 13 B. Carpentier and O. Cerf, *J. Appl. Bacteriol.*, 1993, **75**, 499–511.
- 14 C. G. Kumar and S. K. Anand, *Int. J. Food Microbiol.*, 1998, **42**, 9–27.

- 15 J. W. Costerton, *Ann. Rev. Microbiol.*, 1987, **41**, 435–464.
- 16 S. Liu, C. Gunawan, N. Barraud, S. A. Rice, E. J. Harry and R. Amal, *Environ. Sci. Technol.*, 2016, **50**, 8954–8976.
- 17 L. Chaves Simões and M. Simões, *RSC Adv.*, 2013, **3**, 2520–2533.
- 18 S. L. Percival, K. E. Hill, D. W. Williams, S. J. Hooper, D. W. Thomas and J. W. Costerton, *Wound Repair Regen.*, 2012, **20**, 647–657.
- 19 C. R. Arciola, D. Campoccia and L. Montanaro, *Nat. Rev. Microbiol.*, 2018, **16**, 397–409.
- 20 J. W. Costerton, L. Montanaro and C. R. Arciola, *Int. J. Artif. Organs*, 2005, **28**, 1062–1068.
- 21 A. Bridier, R. Briandet, V. Thomas and F. Dubois-Brissonnet, *Biofouling*, 2011, **27**, 1017–1032.
- 22 S. Bas, M. Kramer and D. Stopar, *Front. Microbiol.*, 2017, **8**, 1–9.
- 23 I. Liaqat and A. N. Sabri, *Curr. Microbiol.*, 2008, **56**, 619–624.
- 24 I. Banerjee, R. C. Pangule and R. S. Kane, *Adv. Mater.*, 2011, **23**, 690–718.
- 25 M. Kostakioti, M. Hadjifrangiskou and S. J. Hultgren, *Cold Spring Harb. Perspect. Med.*, 2013, **3**, 1–23.
- 26 M. Chen, Q. Yu and H. Sun, *Int. J. Mol. Sci.*, 2013, **14**, 18488–18501.
- 27 H. Gu and D. Ren, *Front. Chem. Sci. Eng.*, 2014, **8**, 20–33.
- 28 A. Tripathy, P. Sen, B. Su and W. H. Briscoe, *Adv. Colloid Interface Sci.*, 2017, **248**, 85–104.
- 29 E. A. Chamsaz, S. Mankoci, H. A. Barton and A. Joy, *ACS Appl. Mater. Interfaces*, 2017, **9**, 6704–6711.
- 30 G. Fleming, J. Aveyard, J. L. Fothergill, F. McBride, R. Raval and R. A. D'Sa, *Polymers (Basel)*, 2017, **9**, 601.
- 31 D. Fikai and A. Fikai, *Prevention of biofilm formation by material modification*, Elsevier Ltd, 2016.
- 32 S. Han, S. Ji, A. Abdullah, D. Kim, H. Lim and D. Lee, *Appl. Surf. Sci.*, 2018,

- 429**, 244–252.
- 33 E. Paluch, J. Rewak-Soroczyńska, I. Jędrusik, E. Mazurkiewicz and K. Jermakow, *Appl. Microbiol. Biotechnol.*, 2020, **104**, 1871–1881.
  - 34 S. T. Sultana, J. T. Babauta and H. Beyenal, *Biofouling*, 2015, **31**, 745–758.
  - 35 A. T. Poortinga, R. Bos, W. Norde and H. J. Busscher, *Electric double layer interactions in bacterial adhesion to surfaces*, 2002, vol. 47.
  - 36 A. C. Smith and M. A. Hussey, *Am. Soc. Microbiol.*, 2005, **1**, 14.
  - 37 T. J. Silhavy, D. Kahne and S. Walker, *Cold Spring Harb Perspect Biol*, 2010, **2**, 1–16.
  - 38 W. W. Wilson, M. M. Wade, S. C. Holman and F. R. Champlin, *J. Microbiol. Methods*, 2001, **43**, 153–164.
  - 39 F. C. Neuhaus and J. Baddiley, *Microbiol. Mol. Biol. Rev.*, 2003, **67**, 686–723.
  - 40 B. Bertani and N. Ruiz, *EcoSal Plus*, 2018, **8**, ecosalplus.ESP-0001-2018.
  - 41 J. Palmer, S. Flint and J. Brooks, *J. Ind. Microbiol. Biotechnol.*, 2007, **34**, 577–588.
  - 42 J. P. Busalmen and S. R. De Sánchez, *Appl. Environ. Microbiol.*, 2001, **67**, 3188–3194.
  - 43 S. Shim, S. H. Hong, Y. Tak and J. Yoon, *Biofouling*, 2011, **27**, 217–224.
  - 44 S. H. Hong, J. Jeong, S. Shim, H. Kang, S. Kwon, H. A. Kyung and J. Yoon, *Biotechnol. Bioeng.*, 2008, **100**, 379–386.
  - 45 S. L. Gaw, S. Sarkar, S. Nir, Y. Schnell, D. Mandler, Z. J. Xu, P. S. Lee and M. Reches, *ACS Appl. Mater. Interfaces*, 2017, **9**, 26503–26509.
  - 46 J. P. Busalmen and S. R. De Sa, *Society*, 2005, **71**, 6235–6240.
  - 47 R. E. Perez-Roa, D. T. Tompkins, M. Paulose, C. A. Grimes, M. A. Anderson and D. R. Noguera, *Biofouling*, 2006, **22**, 383–390.
  - 48 O. Istanbulu, J. Babauta, H. Duc Nguyen and H. Beyenal, *Biofouling*, 2012, **28**, 769–778.
  - 49 E. L. Sandvik, B. R. McLeod, A. E. Parker and P. S. Stewart, *PLoS One*, 2013,

**8**, e55118.

- 50 J. W. Costerton, B. Ellis, K. Lam, F. Johnson and A. E. Khoury, *Antimicrob. Agents Chemother.*, 1994, **38**, 2803–2809.
- 51 J. L. del Pozo, M. S. Rouse and R. Patel, *Int. J. Artif. Organs*, 2008, **31**, 786–795.
- 52 J. Jass and H. M. Lappin-Scott, *J. Antimicrob. Chemother.*, 1996, **38**, 987–1000.
- 53 R. Trouillon and D. O’Hare, *Electrochim. Acta*, 2010, **55**, 6586–6595.
- 54 L. J. Simcox, R. P. A. Pereira, E. M. H. Wellington and J. V. Macpherson, *ACS Appl. Mater. Interfaces*, 2019, **11**, 28, 25024–25033.
- 55 R. E. Wilson, I. Stoianov and D. O’Hare, *Electrochem. commun.*, **71**, 79–83.
- 56 D. Dragoe, N. Spătaru, R. Kawasaki, A. Manivannan, T. Spătaru, D. A. Tryk and A. Fujishima, *Electrochim. Acta*, 2006, **51**, 2437–2441.
- 57 Z. J. Ayres, A. J. Borrill, J. C. Newland, M. E. Newton and J. V. Macpherson, *Anal. Chem.*, 2016, **88**, 974–980.
- 58 T. L. Read, S. J. Cobb and J. V. Macpherson, *ACS Sensors*, 2019, **4**, 756–763.
- 59 T. L. Read, E. Bitziou, M. B. Joseph and J. V. Macpherson, *Anal. Chem.*, 2014, **86**, 367–371.
- 60 L. A. Hutton, G. D. O’Neil, T. L. Read, Z. J. Ayres, M. E. Newton and J. V. Macpherson, *Anal. Chem.*, 2014, **86**, 4566–4572.
- 61 H. E. M. Hussein, R. J. Maurer, H. Amari, J. J. P. Peters, L. Meng, R. Beanland, M. E. Newton and J. V. Macpherson, *ACS Nano*, 2018, **12**, 7388–7396.
- 62 S. Crone, M. Vives-Flórez, L. Kvich, A. M. Saunders, M. Malone, M. H. Nicolaisen, E. Martínez-García, C. Rojas-Acosta, M. Catalina Gomez-Puerto, H. Calum, M. Whiteley, R. Kolter and T. Bjarnsholt, *Apmis*, 2020, **128**, 220–231.
- 63 G. O. Toole, H. B. Kaplan and R. Kolter, *Annu. Rev. Microbiol.*, 2000, **54**, 49–79.

- 64 A. E. LaBauve and M. J. Wargo, *Curr. Protoc. Microbiol.*, 2012, 1–11.
- 65 S. J. Cobb, F. H. J. Laidlaw, G. West, G. Wood, M. E. Newton, R. Beanland and J. V. Macpherson, *Carbon N. Y.*, 2020, **167**, 1–10.
- 66 C. K. Stover, X. Q. Pham, A. L. Erwin, S. D. Mizoguchi, P. Warrenner, M. J. Hickey, F. S. L. Brinkman, W. O. Hufnagle, D. J. Kowallk, M. Lagrou, R. L. Garber, L. Goltry, E. Tolentino, S. Westbrook-Wadman, Y. Yuan, L. L. Brody, S. N. Coulter, K. R. Folger, A. Kas, K. Larbig, R. Lim, K. Smith, D. Spencer, G. K. S. Wong, Z. Wu, I. T. Paulsen, J. Relzer, M. H. Saler, R. E. W. Hancock, S. Lory and M. V. Olson, *Nature*, 2000, **406**, 959–964.
- 67 I. Kukavica-Ibrulj, A. Bragonzi, M. Paroni, C. Winstanley, F. Sanschagrín, G. A. O’Toole and R. C. Levesque, *J. Bacteriol.*, 2008, **190**, 2804–2813.
- 68 C. E. Chandler, A. M. Horspool, P. J. Hill, D. J. Wozniak, J. W. Schertzer, D. A. Rasko and R. K. Ernst, *J. Bacteriol.*, 2019, **201**, 1–18.
- 69 T. Sandle and R. Satyada, *Eur. J. Parenter. Pharm. Sci.*, 2016, **21**, 16–22.
- 70 M. Coakley and D. E. Hurt, *J. Lab. Autom.*, 2016, **21**, 489–495.
- 71 A. J. Capel, R. P. Rimington, M. P. Lewis and S. D. R. Christie, *Nat. Rev. Chem.*, 2018, **2**, 422–436.
- 72 A. Silver, *Agencia Fapesp*, 2019, 5–6.
- 73 J. J. Tully and G. N. Meloni, *Anal. Chem.*, 2020, **92**, 14853–14860.
- 74 A. Su and S. J. Al’Aref, *History of 3D printing*, Elsevier Inc., 2018.
- 75 FormLabs, FDM vs. SLA: Compare the Two Most Popular Types of 3D Printers, <https://formlabs.com/uk/blog/fdm-vs-sla-compare-types-of-3d-printers/>, (accessed 18 October 2021).
- 76 R. M. Donlan, *Emerg. Infect. Dis.*, 2002, **8**, 881–890.
- 77 F. Song, H. Koo and D. Ren, *J. Dent. Res.*, 2015, **94**, 1027–1034.
- 78 G. Bell, *BMC Biol.*, 2016, **14**, 4–5.
- 79 J. V. Macpherson, *Phys. Chem. Chem. Phys.*, 2015, **17**, 2935–2949.
- 80 N. Elgrishi, K. J. Rountree, B. D. McCarthy, E. S. Rountree, T. T. Eisenhart and

- J. L. Dempsey, *J. Chem. Educ.*, 2018, **95**, 197–206.
- 81 A. W. Colburn, K. J. Levey, D. O'Hare and J. V. Macpherson, *Phys. Chem. Chem. Phys.*, 2021, **23**, 8100–8117.
- 82 R. S. Nicholson and I. Shain, *Anal. Chem.*, 1964, **36**, 706–723.
- 83 J. H. Merritt, D. E. Kadouri and G. A. O'Toole, *Curr. Protoc. Microbiol.*, 2015, 1–29.
- 84 J. Chandra, P. K. Mukherjee and M. A. Ghannoum, *Nat. Protoc.*, 2008, **3**, 1909–1924.
- 85 G. A. O'Toole and R. Kolter, *Mol. Microbiol.*, 1998, **28**, 449–461.
- 86 G. A. O'Toole, *J. Vis. Exp.*, 2010, 10–11.
- 87 C. K. Lee, J. Vachier, J. de Anda, K. Zhao, A. E. Baker, R. R. Bennett, C. R. Armbruster, K. A. Lewis, R. L. Tarnopol, C. J. Lomba, D. A. Hogan, M. R. Parsek, G. A. O'Toole, R. Golestanian and G. C. L. Wong, *MBio*, 2020, **11**, 1032–1046.
- 88 M. D. Lovander, J. D. Lyon, D. L. Parr, J. Wang, B. Parke and J. Leddy, *J. Electrochem. Soc.*, 2018, **165**, G18–G49.
- 89 E. M. Bosire and M. A. Rosenbaum, *Front. Microbiol.*, 2017, **8**, 1–11.
- 90 G. W. Lau, D. J. Hassett, H. Ran and F. Kong, *Trends Mol. Med.*, 2004, **10**, 599–606.
- 91 F. A. Alatraktchi, W. E. Svendsen and S. Molin, *Sensors (Switzerland)*, 2020, **20**, 1–15.
- 92 D. San Roman, D. Krishnamurthy, R. Garg, H. Hafiz, M. Lamparski, N. T. Nuhfer, V. Meunier, V. Viswanathan and T. Cohen-Karni, *ACS Catal.*, 2020, **10**, 1993–2008.
- 93 A. T. Poortinga, R. Bos and H. J. Busscher, *Biophys. Chem.*, 2001, **91**, 273–279.
- 94 C. K. Lee, J. Vachier, J. de Anda, K. Zhao, A. E. Baker, R. R. Bennett, C. R. Armbruster, K. A. Lewis, R. L. Tarnopol, C. J. Lomba, D. A. Hogan, M. R. Parsek, G. A. O'Toole, R. Golestanian and G. C. L. Wong, *Mol. Biol. Physiol.*,



2020, **11**, 1–21.

- 95 S. Katharios-Lanwermeier, S. Kasetty, C. D. Nadell and G. A. O’Toole,  
*bioRxiv*, 2021, **1248**.

## 7 Conclusions and Future Work

---

### 7.1 Conclusions

The work in this thesis has led to the design, development and implementation of BDD ring BDD-Q disc electrodes that have the capability of tracking dynamic changes in pH. The pH of the local environment over the disc electrode was decreased through water oxidation at the ring in chapters 3 and 5 and increased due to reduction of oxygen, nitrate and water in chapter 4 on both bare BDD and Cu NP functionalised BDD.

In the presence of a buffer, the time-dependent voltammetric measurement of pH on the BDD-Q disc, which itself contains pH sensitive microspots, has provided an experimental insight into how the pH response varies. Experiments have been verified by FEM modelling. The fact that individual microspots on the BDD-Q disc can experience different local pH environments across the disc results in broad or double peaks being observed in the voltammetric response. In contrast, in unbuffered solutions the pH shift is not inhibited by a buffer species, so the pH becomes uniform across the disc more rapidly. Increasing the buffer capacity acts to slow the diffusion of protons across the disc, resulting in varied pH profiles across the disc then detected in the voltammetric measurement. To avoid the broad and double peaks when data analysing, it was preferred to analyse the rate of pH change between the bulk solution pH and the pH measured once the generated pH front covered the disc and a uniform response was seen. Analysable responses were seen for buffer capacity values  $< 10$  mM. This sensitivity would be adequate for measurement of buffer capacities in fresh and seawater and could be undertaken at source, and with some design adaptations potentially even *in-situ*. Suggestions were given as to how to increase sensitivity of the buffer capacity measurement.

The electrocatalytic effect of Cu NPs on producing local pH changes was considered in Chapter 4. The BDD-Q disc was able to detect local pH increases driven by reactions on the ring electrode. When Cu NPs were present on the BDD ring, compared to the bare BDD ring, larger pH increases were detected at the BDD-Q disc at applied potentials of -2.0, -1.0 and -0.4 V in aerated nitrate and

sulfate solutions, except at -0.4 V in the nitrate solution. In aerated solutions at this potential, ORR is expected on the Cu NPs, which results in local hydroxide production. The fact that in aerated nitrate the pH increase with the presence of Cu NP was less than that on BDD suggests a blocking of the catalytic activity of Cu, possibly due to adsorption of nitrate onto the NP surfaces. The work in chapter 3 and 4 opens up a new technique to track local pH changes for a wide range of applications.

The ring disc electrode work required two individually addressable electrodes to be controlled independently but simultaneously. In chapter 3 this was handled by using an independent galvanostat to control the current on the ring. However, if using a secondary device, understanding of the grounding of the instrument is important as two devices can interfere with each other. When a dual electrode potentiostat was used, it was challenging to perform the experiment and an understanding of how the commercial instrument applied square wave potentials and measured the current was required. These experiments pushed the limitations of the commercial potentiostat and it was essential to understand the behaviour of the potentiostat in order to interpret the data.

In Chapter 5, two techniques were considered for heavy metal sensors, both focused on Cu detection, given Cu is prevalent in the environment. The redesign of the EC-XRF sensor was significantly more user friendly than the original EC-XRF rotating disc electrode. The integration of the BDD into an electrode cap was very successful and had minimal impact on the XRF background of the BDD. The removal of the cap allowed for more uniform hydrodynamic flow of solution across the electrode during rotation as the BDD was not recessed. However, the detection limits reported by Hutton *et al.*<sup>1</sup> were not reached, which was possibly attributable to previous repair of the XRF but also the stability of the deposit on the surface. Deposit stability was found to be dependent on morphology and chemical species, which in turn was controlled by solution composition and deposition potential. This led to variability in the XRF intensity observed between solutions and deposition potentials which was challenging for quantification.

One of the challenges of ASV on solid electrodes is deposition of uniform metallic deposits. Acidification of a solution can aid in the deposition of metals in a metallic form due to the cation being present in a hydrated state. For on-site measurements it is impractical to carry concentrated acids for analysis. Therefore *in-situ* generation of acid is a good alternative and we explored the ring disc electrode geometry for this application. Through water oxidation on the ring the local environment over the disc is acidified and metal deposition can occur. Previous work had shown this effect but for high concentrations of the metal ion in solution, which served well as proof of concept but was not at environmentally relevant concentrations. When the concentration was lowered the situation was found to be complicated by the presence of oxygen also generated at the BDD ring during water oxidation. This effect was explored utilising the sensitivity of the  $sp^2$  carbon spots to pH and oxygen.

Finally, a novel experimental set-up was designed, fabricated and utilised for electrochemical microbial control studies. The aim of this chapter was to determine if the functional lifetime of a BDD sensor could be extended for use *in-situ* by applying small potentials to the sensor surface. The application of small potentials can reduce cellular adhesion due to repulsion between the charge on the cell membrane and the electrode surface. This effect was seen to some extent, when negative potentials (-50 and -400 mV) were applied to the electrode. Interestingly, at +400 mV a reduction in biofilm was also seen compared to a control at 0 mV. At the larger applied potentials ( $\pm 400$  mV), electrochemical interaction between metabolites of the bacteria and the electrode surface are more likely and could have caused stress to the cells, stalling growth and adhesion. At lower potentials ( $\pm 50$  mV) the effects of electrostatic attraction and repulsion between the BDD surface and the cells are more likely to be the cause of the variation. This data was challenging to interpret due to variation in bacterial growth, possibly due to temperature variations. However, the initial results suggest that application of a potential can reduce biofilm formation on BDD electrodes.

## 7.2 Future Work

The BDD-Q integrated ring disc opens significant potential avenues to explore. Electrocatalytically induced local pH changes of any metal NP that can be electrodeposited on the ring could be investigated using this technique. Directly following on from the work presented here the electrocatalytic effect of different morphologies of Cu deposits could also be considered, such as Cu<sub>2</sub>O cubes which show promise as a catalyst for CO<sub>2</sub> reduction.<sup>2</sup> Additionally, it could be interesting to determine what effect the electrocatalytic reactions have on deposit morphology; this information could inform about the lifetime of catalysts. Suggested techniques for this include scanning electron microscopy (SEM) combined with energy-dispersive X-ray (EDX) spectroscopy or identical location transmission electrode microscopy for more in depth consideration. These techniques would require modification of the current electrode design.

The spatial variation of the generated pH in the presence of buffer was an interesting result. Modifications could be made to the electrode arrangement which may improve sensitivity in buffered solutions, paving the way for a more sensitive buffer capacity sensor. Possible suggestions include;

- (i) A smaller diameter disc and ring; to reduce the diffusion path over the disc.
- (ii) Variation of the ring thickness.
- (iii) Variation of the sp<sup>2</sup> carbon region on the disc.
- (iv) Parallel electrodes with a thin channel between.
- (v) Generator electrodes either side of a detector electrode to introduce H<sup>+</sup>/OH<sup>-</sup> from two directions. This would create a uniform pH distribution more quickly. The design could be in the form of bars in a defined channel or a ring-ring disc type arrangement. These designs would require optimisation and verification of BDD-Q pH sensing performance in a format other than a disc.

Future work on the ring disc electrode in strong buffer solutions using a complementary spatial measurement of pH distribution *i.e.* confocal laser fluorescence microscopy with a fluorescent dye could also help elucidation of the voltammetric response. As the sensitivity in the current arrangement is adequate

for freshwater and seawater environments, future work would look to apply this sensor in actual environmental samples.

In the area of EC-XRF, further work could consider how reliably metal deposits can form under the conditions likely found in environmental samples, and what happens when multi-metals are present. If EC-XRF were to be used as a semi quantitative multi-metal technique it would require understanding of metal-metal interactions during deposition. This could be achieved through analysis of deposits by SEM and EDX to identify the distribution of the metals, *i.e.* discrete deposits or combined. Controlled deposition from individual solutions *i.e.* deposition in a Cu solution followed by deposition in a Zn solution could also provide some insight and a possible way to consider the XRF response. XRF technologies can now map a surface on the microscale to identify location of elements which could also be a useful technique. A semi-quantitative technology could be useful for suspected pollution events where a relatively quick measurement to determine the heavy metals present can inform on the response to the pollution event.

To continue the work on locally controlled pH reactions some alternative sensing applications could benefit, e.g. free chlorine sensing where the local pH could be controlled to move the species into a more readily electro-analysable form. If work was to continue for metal sensing a better understanding of the role of oxygen generation during water oxidation would be useful. This initial work shows promise *i.e.* through careful control of the generation current an optimum environment can be achieved. However, the lower the metal concentration the more challenging this is. Additionally this technique could be more successful with a species other than Cu as Cu is very sensitive to oxygen.

For any future electrochemical control microbiological experiments my recommendations include:

- (i) Implementation of temperature control to reduce variability between runs.
- (ii) Tailoring the membrane to the solution conditions.
- (iii) Consideration of the analysis technique: CVA, live/dead staining *etc.*

- (iv) Consideration of the electrode designs: using electrodes that can be fully submerged may be more informative for future sensor development.
- (v) Monitor suspended cell growth and pyocyanin production throughout the experiment.
- (vi) Continuation of this work should also include consideration of a Gram positive bacterial strain such as *Staphylococcus aureus* to determine the effects of potential on the other common bacterial cell membrane structure.
- (vii) Consideration to bacterial strain characteristics, *e.g.* PA01 vs. PA14.

### 7.3 References

- 1 L. A. Hutton, G. D. O. Neil, T. L. Read, Z. J. Ayres, M. E. Newton, J. V. Macpherson, G. D. O'Neil, T. L. Read, G. D. O'Neil, Z. J. Ayres, M. E. Newton and J. V. Macpherson, *Anal. Chem.*, 2014, **86**, 4566–4572.
- 2 F. S. Roberts, K. P. Kuhl and A. Nilsson, *Angew. Chemie*, 2015, **127**, 5268–5271.